Segregation in High Concentration Flows

Georgina Williams

The University of Leeds
Centre for Doctoral Training in Fluid Dynamics

Submitted in accordance with the requirements for the degree of
Doctor of Philosophy

December 2020

The candidate confirms that the work submitted is his/her own and that appropriate credit has been given where reference has been made to the work of others.

Acknowledgements

First and foremost I would like to express my gratitude to my somewhat extraordinary supervisory team. I thank Jeff for constantly reminding me to do actual science, yet providing no end of amusement along the way and ultimately making the science infinitely better. Rob and Gareth for your continual emotional support, wine, places to hide, tolerance and fixing of terrible maths/breaking of physics/really rather long sentences and countless other ridiculous duties that are way beyond the usual supervisory job description. I am extremely grateful.

I would like to thank Helena of the Sorby Lab for being my hands when H&S declared it too dangerous for me to stand on a step. But mostly for making the many months, possibly years, of laboratory work an absolute delight. I hope the ballotini is finally out of your hair.

I would like to thank Dominik and the other members of the waLBerla team at FAU-Erlangen whose support in setting up the models was invaluable and who were excellent hosts.

I thank Claire and the other members of the CDT in Fluid Dynamics for all their efforts and support during my time at Leeds. Also to the rest of the cohort for being such excellent colleagues, making the whole experience both memorable and enjoyable and vastly improving my cryptic crossword skills.

I would like to thank Fran for providing rock art on demand and Lydia for providing exceptional moral support, my Mum and Dad for always assuming I would get to this point and for frequently stepping in for life stuff when I had to focus on this work.

To Aaron, thank you for being an excellent husband, I simply would not have got this far without you.

And finally to my wonderful Rowan, thank you for being the absolute best reason not to quit (I’m afraid I am insisting on Dr. Mum from now on).

Abstract

Sand injectites are observed in a wide range of locations and settings, both modern and ancient but little is known about the processes controlling their formation. The scale of these injections range from mm to km in size and represent the forceful injection of fluidised sand into host strata. Due to the difficulty of observing in-situ events and relative paucity of outcrop data interpretations, understanding of the flow processes during fluidisation pipe formation is lacking. Existing fluidisation models provide mechanisms for fluidisation but remain simplistic and do not capture the full dynamics nor the range of characteristics which are observed to vary both spatially and temporally across the system during the formation of sand injectites. Fluidisation theory relies on an understanding of both the velocity characteristics and the concentration characteristics of a fluidisation event but comprehensive evidence of these quantities has not previously been available.

The novel application of experimental techniques in both two dimensions and three dimensions in this thesis provides both high resolution velocity data for the formation and quasi-steady state of fluidisation pipes along with high resolution concentration data for the first time. Complementing this, the novel application of numerical modelling provides insight into the early stages of void formation and demonstrates a new methodology for investigating flow processes during fluidisation. The products of the fluidisation events modelled are presented providing a direct link between fluidisation processes and products for reference in interpreting outcrop data. Residual morphologies are evidenced resulting in explanations of the poor detection rate of sand injections. New models of fluidisation and void formation are presented based

on the extensive characterisation of a fluidisation event achieved across multiple methodologies.

Table of Contents

List of Tables

List of Figures

Nomenclature

A	projected area
Ar	Archimedes number
c	lattice speed
$\boldsymbol{c}_q$	lattice velocity in direction q
C	contact point
$\mathcal{C}_{a,b}$	set of contacts for particles a and b
C_d	drag coefficient
d	diameter
d_p	particle diameter
e_n	dry coefficient of restitution
f	pre-collision particle distribution function
$\tilde{f}$	post-collision particle distribution function
f^{eq}	local equilibrium particle distribution function
$\boldsymbol{F}$	force matrix
$\boldsymbol{F_c}$	total contact force
$\boldsymbol{F}^n_{c,ij}$	normal contact force
$\boldsymbol{F}^t_{c,ij}$	shear contact force
g	acceleration due to gravity
I	identity matrix
K	constant describing properties of a suspension
k_n	normal stiffness constant
l	characteristic length scale
m_{ij}	reduced particle mass for the particles i and j
$\boldsymbol{M}$	quaternion matrix function
$\boldsymbol{n}_{ij}$	normal direction unit vector for particles i and j
N_p	number of particles
$p_{i,j}$	particle

q direction of particle distribution function

$\boldsymbol{Q}$ orientation matrix of particle

Re Reynolds Number

t time

$\boldsymbol{t}_{ij}$ tangential direction unit vector for particles i and j

$\boldsymbol{T}$ torques matrix

u_{mf} minimum fluidisation velocity

$\boldsymbol{u}$ fluid velocity

$\boldsymbol{u}_{r,ij}$ relative velocity vector for particles i and j

$\boldsymbol{u}_{p,ij}$ particle velocity vector for particles i and j

U characteristic velocity

V volume

$\boldsymbol{V}$ translational velocity matrix

w_q weighting factors

$\boldsymbol{W}$ rotational velocity matrix

$\boldsymbol{x}$ lattice location

$\boldsymbol{x}_{p,ij}$ location of the centre of particles i and j

$\boldsymbol{X}$ position matrix of particle

$\widehat{\boldsymbol{X}}$ point of contact

δ_{ij} overlap length between particles i and j

δt timestep

ε error reduction parameter

$\boldsymbol{\lambda}$ contact reaction

μ dynamic viscosity

μ_f dynamic viscosity of the fluid

μ_c friction coefficient

μ_{sample} attenuation coefficient of a sample

μ_{water} attenuation coefficient of water

ξ_n	normal damping constant
ξ_t	tangential damping constant
ξ	contact distance
ρ_f	density of fluid
ρ_p	density of particle
τ	characteristic collision time
υ	kinematic viscosity
υ_f	kinematic viscosity of a fluid
υ_s	kinematic viscosity of a suspension
$[\nu]$	intrinsic viscosity of a particle
ϕ	particle fraction
$\boldsymbol{\omega}_{p,ij}$	angular velocity vector of particles i and j
Ω	inter-particle collision operator

Abbreviations

CT	Computed Tomography
DEM	Discrete Element Method
HCSITSS	Hard Collision Semi-Implicit Time-Stepping Solver
HU	Hounsfield Unit
LBM	Lattice Boltzmann Method
PIV	Particle Image Velocimetry

1 Thesis context, significance and structure

1.1 Thesis rationale and objectives

Sand injection occurs when fluidised sand is forced into host strata (Hurst et al., 2011). The forceful injection of an unconsolidated sand can occur in all directions and requires a parent body of sand and a mobilised fluid, although identification of a parent bed to the injected structures is often a challenge (Cartwright and Santamarina, 2015; Cobain et al., 2018). When sand injections breach the surface of the host strata, they are termed extrudites, sand volcanoes, blows or vents (e.g., Hurst et al., 2011; Ross et al., 2013). The remaining geological feature, visible as a depression on the sea-bed, is referred to as a pockmark (Andresen, 2012), a term that has been used to describe hydrocarbon, water and gas-fluidised events (Judd and Hovland, 2009). Both injectites and extrudites are highly permeable and therefore increase reservoir complex connectivity, can provide permeability pathways to the sea floor and can also be a valuable hydrocarbon store in themselves (Hurst et al., 2011; Ross et al., 2014; Ravier et al., 2015). The correct identification and depth of understanding of such features is critical to the safe and responsible exploitation of deep-sea sedimentary basins (Huuse et al., 2010).

Sand injectites are known to span a number of scales, outcrop datasets have been shown to span four orders of magnitude (Figure 1-1, Wheatley at al., 2019) and exhibit preserved flow features such as flow pathways, particle size sorting and segregation, and wall geometries which are used to

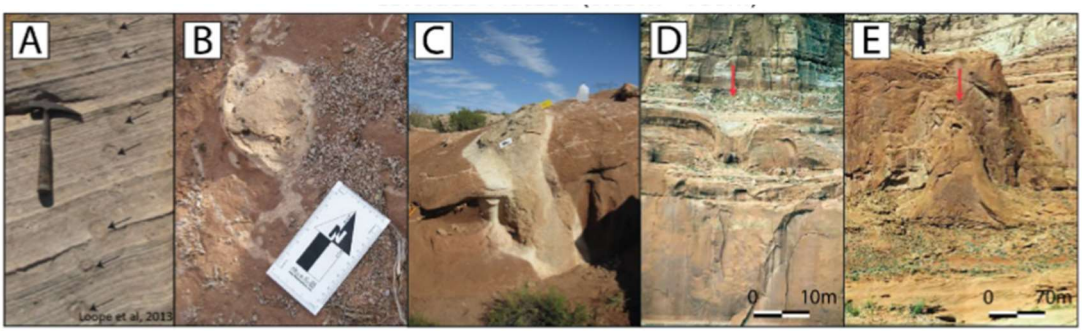

Figure 1-1. Fluidisation pipes in outcrop showing the range of scales from 0.03 m to 100 m. Composite image reproduced from Wheatley at al., 2019. Outcrop examples are from the Colorado Plateau. Image A is modified from Loope et al., (2013) – Zion National Park, Utah), images D and E are modified from Chidsey et al., (2012) - Glen Canyon National Recreation Area.

interpret the flow conditions at emplacement (Ross et al., 2014; Cobain et al., 2015). Dynamic properties of the flow during development are more difficult to determine and the propagation direction also has been the subject of much wider debate (Peterson, 1968; Taylor, 1982; Obermeier, 1998; Duranti, 2007; Hubbard et al., 2007; Hurst et al., 2011; Sherry et al., 2012; Ross et al., 2014; Cobain et al., 2015). Seismic examples of injections and fluidised pipes are observed known to span 10s to 100s of meters in width and commonly hundreds of meters in height (see Table 1, Cartwright and Santamarina (2015), included in Figure 2-4 of this thesis) and the large-scale architecture of the sea-floor examples of fluidisation pipes is evidenced in the seismic data sets (Figure 1-2 and also: Hurst et al., 2003; Huuse et al., 2004; Cartwright et al., 2008; Vigorito et al., 2008; Szarawarska et al., 2010; Jackson et al., 2011). Despite the outcrop and seismic evidence of injections it is noted that, understandably there is no observational evidence of an active fluidisation process and so, the examples summarised thus far have been documented and interpreted after the event. It is critical then, that for the accuracy of those interpretations that the fluidisation processes present in fluidisation pipes are well categorised and that the resulting structures and

characteristics of the fluidisation processes be linked back to their formation structures. Despite previous investigations having experimentally modelled fluidisation events (Nichols et al., 1994; Frey et al., 2009; Ross et al., 2011), modelling permeable layers alternated with a less permeable seal to create an overpressure in the bed. There have been no experimental observations specifically considering the flow dynamics of pipe formation nor extrusion vents. This thesis aims to investigate the flow dynamics by providing quantitative data for the characterisation of fluidisation events and the variations observed both spatially and temporally in such processes.

The mechanical behaviour of the fluidisation of granular materials applies to

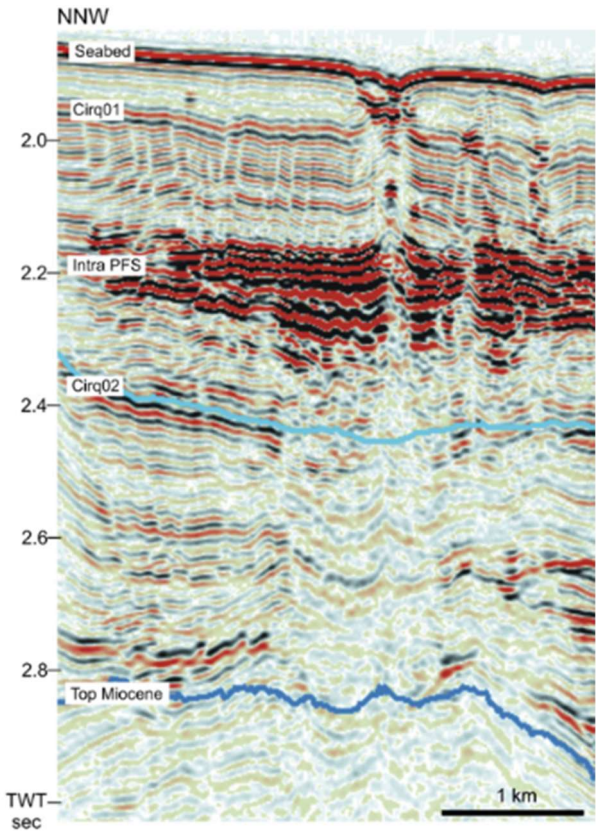

Figure 1-2 Example of a seismic expression of a fluidisation pipe from the Lower Congo Basin West Africa. The pipe terminates in a typical "pockmark" at the seafloor. Reproduced from Andresen and Huuse (2011).

both industrial and geophysical processes (Rigord et al., 2005) and the

process of fluidisation is known to be influential in a range of geological features (Ross et al., 2011). Studies on monodisperse beds describe three flow regimes for localised flow through a bed: static flow through the bed, where particles remain stationary, the cavity regime where part of the bed is fluidised but is overlain by a layer of static bed , and the chimney regime where a fluidisation pipe reaches the surface (Zoueshtiagh and Merlen, 2007; Philippe and Badiane, 2013; Mena et al., 2017). Fluidisation theory suggests more complex systems, such as bidisperse and polydisperse systems, can be modelled through a pseudofluid approach. A pseudofluid is where the fluid and the smallest particle class are treated as a single fluid and properties of that pseudofluid are assumed to be that of the suspension (Di Felice, 2010). Such an approach is necessarily dependent on knowing the concentration of the particles in the suspension in order to assign the properties of the pseudofluid as accurately as possible. Therefore this research aims to measure the concentration of a fluidisation event and provide understanding of how this changes with bed characteristics and through the different stages of fluidisation.

Recently, geological models of pipe formation have been suggested by Ross et al. (2011) and Cartwright and Santamarina (2015). Ross et al. (2011) outlined the stages of pipe formation when a less permeable seal overlies more permeable sediment and developed a model showing the broad stages of pipe development. In contrast, Cartwright and Santamarina (2015) propose four modes of fluidisation pipe formation in a sediment bed: hydraulic fracture, erosive fluidisation, localised sub-surface volume loss and syn-sedimentary pipe formation (Figure 1-2). Both models cover the overarching dynamics of the formation of pipes but models for the range of

geomorphological and sedimentological features documented in fluidisation pipes, and mechanisms for the formation of common pipe and extrudite features, are not proposed. This research will propose new models for fluidisation, capturing the spatial and temporal variation of the events, and suggesting how this influences characteristics commonly observed at outcrop and their interpretation.

Seismic data (Gay et al., 2007; Moss and Cartwright, 2010; Løseth et al., 2012; Maestrelli et al., 2017), experimental data (Nermoen et al., 2010; Ross et al., 2011; Bureau et al., 2014) and outcrop interpretations (Ross et al., 2014; Cobain et al., 2015; Wheatley et al., 2016; Chan et al., 2018) all contribute to the developing understanding of sand injectites and fluidisation. However, a previously unexplored avenue for investigation within sand injectites is the application of computational modelling to further understand the parameters affecting fluidisation. This research aims to demonstrate the feasibility of such approaches, specifically a two-way coupled Lattice Boltzmann Method and Rigid Body Solver. How the technique can be successfully implemented will be explored and the further understanding that can be gained beyond the measurements possible with existing experimental techniques.

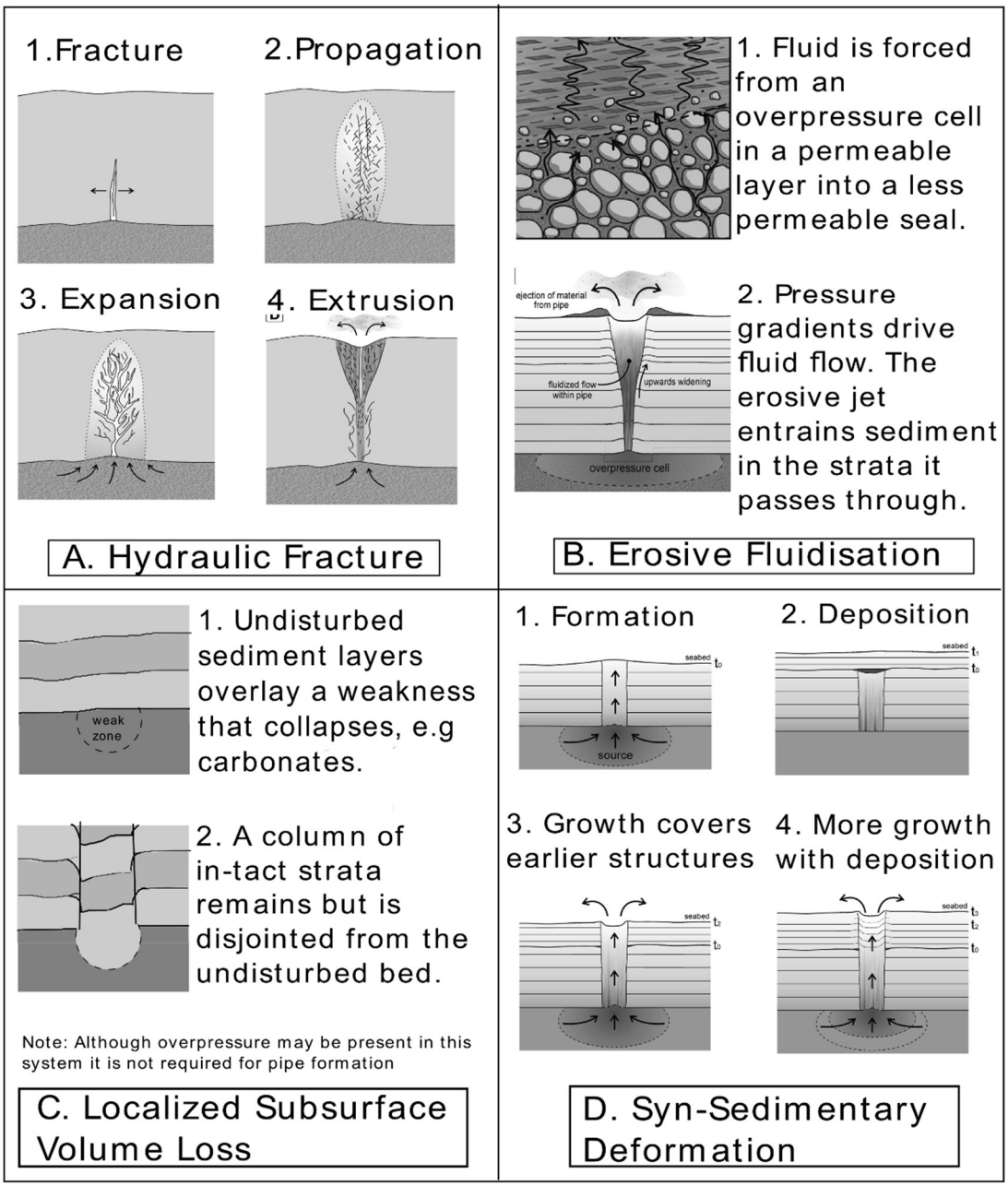

Figure 1-3 Summary of fluidisation mechanisms proposed by Cartwright and Santamarina (2015). A. Hydraulic fracture. A.1 - The overpressure exceeds the tensile strength of the bed and a fracture occurs, fluid rushes into the fracture expanding the fracture. A.2 the overpressure causes more fractures surrounding the initial fracture and a network of fractures propagates. A.3 The network of fractures expands as more fluid is pushed in. A.4 The network reaches the surface and extrusion occurs. B. Erosive fluidisation. C. Localised sub-surface volume loss. D Syn-sedimentary deformation.

1.1.1 Research Aims

1) ***What are the processes governing the formation of fluidisation pipes and how do the bed properties affect the formation?***

   This question will be investigated using experimental modelling of flow processes across high porosity and low porosity beds and fast and slow inlet velocities. (Chapters 4, 6 and 7).

2) ***What are the flow regimes present within a fluidisation event and how do the regimes affect the observed formation?***

   Flow regimes are known to be governed by the velocity and concentration of the fluidisation event. High resolution data of both the velocity and concentration fields across bed porosities are presented and used to determine flow regimes (Chapters 4, 5)

3) ***What sedimentological structures are formed in the bed during fluidisation and how are these structures ap after the cessation of flow?***

   The formation of typical geological structures such as laminations, structureless sediments and presence of clasts are frequently used to interpret outcrop data. Here we will present evidence for the formation mechanisms of these structures and the residual structures linked to the formation (Chapters 4, 5 and 6).

1.2 Thesis structure

The thesis is structured in 8 chapters:

1 Introduction. The research aims and objectives are presented alongside an introduction to the research themes covered in this thesis and a brief outline of each chapter is provided.

2 Literature Review. A literature review providing the background theory for the research conducted in this thesis and describing the current knowledge around sand injection systems and fluidisation events. A brief consideration of the governing parameters of the flow features of fluidisation events is given and the implications for injectites explained.

3 Quantitative analysis of the influence of porosity and permeability on flow fields and injectite dynamics in bidisperse sediment beds. The methodology and instantaneous velocity results of two-dimensional experiments of bidisperse bed fluidisation are presented. Data were collected using Particle Image Velocimetry for high porosity and low porosity beds fluidised with fast and slow inlet velocities and the velocity features during formation and in the quasi-steady state are described. The results of the PIV data are analysed in terms of the flow regimes present in the fluidisation event and a flow regime categorisation for fluidisation events is proposed. The PIV data are used in a force balance approach to track particle paths through the fluidisation event and present a range of possible clast sizes that could be supported by the flow.

4 Particulate concentration during fluidisation events. This chapter presents the methodology and results of three-dimensional experiments

using Computed Tomography. Time series are presented showing the raw CT data for every 0.5 s from the initiation of fluid flow. The characteristics of the wall regions are considered. Residual structures after the cessation of flow are given and a comparison to established fluid flow features and implications for detectability of in-situ fluidisation events studied. The three-dimensional data are shown to have very similar geometry to the two-dimensional experiments. The first concentration profiles of fluidisation events are given and discussed in the context of the velocity data.

5 Formation sequences of fluidisation pipes for a range of porosity beds and the implications for in-situ injectites. The qualitative data collected from the two-dimensional experimental arrangements is outlined and the fluidisation sequences for different porosity beds are detailed. The flow regimes in the system are analysed and new models of fluidisation processes and products are developed and discussed.

6 Numerical simulations of a bidisperse bed using a two-way coupled approach. The two Lattice Boltzmann implementations used in this thesis are outlined and the results generated using the Viper High Performance Computing facility are presented. The influence of bed heights on void development are considered and the velocities of the separate fluid and particle phases are presented in the early phases of fluidisation. The numerical model is shown to be a promising avenue for future research and understanding of fluidisation events.

7 Synthesis and Conclusions. The synthesis chapter brings together all of the data sets presented in Chapters 4 – 7 and discusses the data in the context of the broader themes of: initial stages of fluidisation, the

development of geomorphological features, and the residual features formed from fluidisation events. Further avenues for research are proposed.

2 Literature Review

2.1 Outline of the problem(s)

There are numerous examples of sand injections, fluidised sands, intruding into host strata, and they occur over scales ranging from millimetre scale (Best, 1989) to kilometre scale (Løseth et al., 2012). Academic interest in injectites has increased as their significance for petroleum systems has been realized (Cobain et al., 2015). Injections of fluidised sand can serve as both hydrocarbon reservoirs and also form fluid migration pathways between less permeable host strata in marine environments (Hurst et al., 2011; Ross et al., 2014; Ravier et al., 2015). However fluid-escape structures have been documented in every sedimentary environment and may be damaging and costly such as sand volcanoes (also known as boils or blows) occurring close to rivers (Guhman and Pederson, 1992), damaging dams or levees (Li et al., 1996) or as a result of seismic activity (Quigley et al., 2013). The overall process of injection is widely accepted. However, the hydrodynamic processes during injection are not well understood and very few physical models of such processes are available (Rodrigues et al., 2009; Ross et al., 2011). Determining the fluid dynamic behaviour of injected sand-fluid mixtures is critical to modelling the emplacement of sand injectites and is of great interest to basin analysis as a means to determining the fluid budget required to fluidize and inject sand (Vigorito and Hurst, 2010).

Fluid escape structures are characterised by size segregated sediments – typically fines depleted cores surrounded by walls made up of finer particles (Hurst el al., 2009, Ross et al., 2014). The mechanisms of segregation in

such structures have thus far been documented and subject to multiple theories such as inertial migration, size segregation in high concentration – slow moving flows, and incorporation of bed particles at flow edges (Cobain et al., 2015). In the field of granular dynamics mechanisms such as axial size segregation, spontaneous stratification and percolation are well documented when mixed sizes of grains are in motion (Makse et al., 1998), but such approaches have not been applied to injectites. The segregation of different particle classes in fluidisation events is likely to be influential in the dynamics and evolution of fluidisation events.

2.2 Geological studies of multiphase flows

Sand injections have been documented in a wide range of sedimentary environments: glacial, lacustrine, deltaic, tidal, shallow marine, deep-water marine fans and turbidites (Jolly and Lonergan, 2002 and references therein). By comparing the literature documenting these structures, Jolly and Lonergan (2002) showed that these fluidisation structures appear significantly more frequently in deep-water marine channels and turbidites than in any other sedimentary environment, although no explanation for this was offered. Liquefaction and fluidisation are two related processes that are responsible for the formation of fluid escape structures (Mount, 1993). Liquefaction is the collapse of the grain structure in a bed due to the (rapid and temporary) increase in pore fluid pressure and subsequent loss of shear resistance. It is usually induced by cyclic loading of relatively high frequency (e.g., seismic tremors or machinery vibrations) (Craig, 2004). Fluidisation occurs when the drag forces on particles exceeds the submerged weight, and can occur during liquefaction processes or due to

flow through a bed from some underlying flow unit. Mount (1993) states that most water escape structures occur through cases of partial fluidisation (e.g., dish and pillar structures). Within a geological setting, full fluidisation results in complete disruption of the primary sedimentary structures (Duranti and Hurst, 2004). There are two types of fluidisation: particulate in which the suspension remains homogeneous, and aggregative in which heterogeneous instabilities are generated (Lowe, 1975; Roche et al., 2001). In particulate fluidisation, at very low velocities the bed is stable and pore-fluid flow is governed by Darcy's law. At slightly higher velocities, the bed expands smoothly, heterogeneities are negligible until the threshold minimum fluidisation velocity, u_{mf}, is reached, at which point the entire bed becomes fluidised (Richardson, 1971, Roche et al., 2001). Particulate fluidisation is only possible in monodisperse or very weakly polydisperse materials when the density difference between particles is small (Richardson, 1971, Roche et al., 2001). Some instabilities result in channelling of the fluid phase and the formation of vertical pipes. Pipe stability is affected by the polydispersivity of the granular material and the minimum fluidisation velocity. Segregation of the granular material is common and enhances the stability of pipes. It is most effective when the ratio of the minimum fluidisation velocity of the coarse particles to that of the fine particles is greater than 2 (Richardson, 1971, Roche et al., 2001).

All injectites are a result of the fluidisation of sediment (Jonk, 2010). For sediment to become fluidised, and hence remobilised, there must be a migrating interstitial fluid providing sufficient driving force (e.g., drag, lift) to overcome any forces resisting the movement of the particle (e.g., gravity, apparent cohesion or fluid-particle friction). The fluid is driven by a pressure

gradient caused by the over-pressuring of the pore fluid and its subsequent dissipation. The overpressuring is frequently ascribed to seismicity, rapid fluid migration into parent sands, rapid burial, or instability of overlying sediments (Cobain et al., 2015 and references therein). Cobain et al. (2015) suggested that these mechanisms for fluidisation remain relatively shallow and small scale, and that deeper, often larger scale, injections occur as a result of overpressuring due to fluid migration into a sealed sandstone body or compaction.

The cohesive properties of the sediment are known to have an influence on the fracturing and initial formation of fluidisation structures (e.g Cosgrove, 1995, 2001). More recently, blast test studies have demonstrated that sediments with cohesive properties are resistant to liquefaction and prohibited the formation of sand blows and volcanoes (Fontana et al., 2019). As such, this work focusses on cohesionless sediments that are more easily and predictably susceptible to fluidisation. Despite the resistance of cohesive sediments to fluidisation, it is suggested that once initial fracturing has occurred many of the flow processes associated with these structures can be expected to show similarities (Ross et al., 2011).

As the vast majority of literature available on sand injectites is derived from outcrop studies and seismic data there are very few observations of the effects of changing the properties in the system on the fluidisation processes observed (Hurst et al., 2011; Cartwright and Santamarina, 2015). As a result, there is a lack of laboratory-derived evidence to provide a clear link between observed sediment qualities and the processes of fluidisation events, that in turn can provide analogue evidence for the processes inferred

from outcrop. These links can additionally be probed using numerical simulations to further constrain and expand the parameters tested in the laboratory.

2.2.1 Injection Structures

Hurst et al. (2011) provides a clear categorisation of the distinctive types of intrusion structures observed in geological settings (Figure 2-1). The intrusion features are commonly divided into four constructs: parent units; dykes; sills; and extrudites. Parent units (yellow arrows; Figure 2-1) are bodies of depositional sandstones that form an interconnected system of sandstones with sandstone intrusions. They often display features of post-depositional sand and fluid mobilization. Sandstone dykes (red arrows; Figure 2-1) and sills (blue arrows; Figure 2-1) are intrusive structures that cross cut the host strata in the case of dykes and are generally concordant with the host strata in the case of sills. Dykes can take high or low angles to the host bedding and vary geometrically as linear pipes, bifurcating, bulbous and curved, tapering and planar (see Ross (2013) and references therein). Sills are generally tabular, although they may show some discordant bifurcating or stepped features relative to the host strata. Extrusive sandstones (or extrudites, green arrow; Figure 2-1) are where intrusive structures have vented sand onto the surface (e.g., the seafloor or Earth's surface). Extrudites can vary vastly in size from sand extrusion sheets identified on seafloor basins, representing 10000 km^2 (Løseth et al., 2012) to sand volcanoes (also known as boils, springs or blows; Guhman and Pederson, 1992; Quigley et al., 2013), representing centimetre to metre scales.

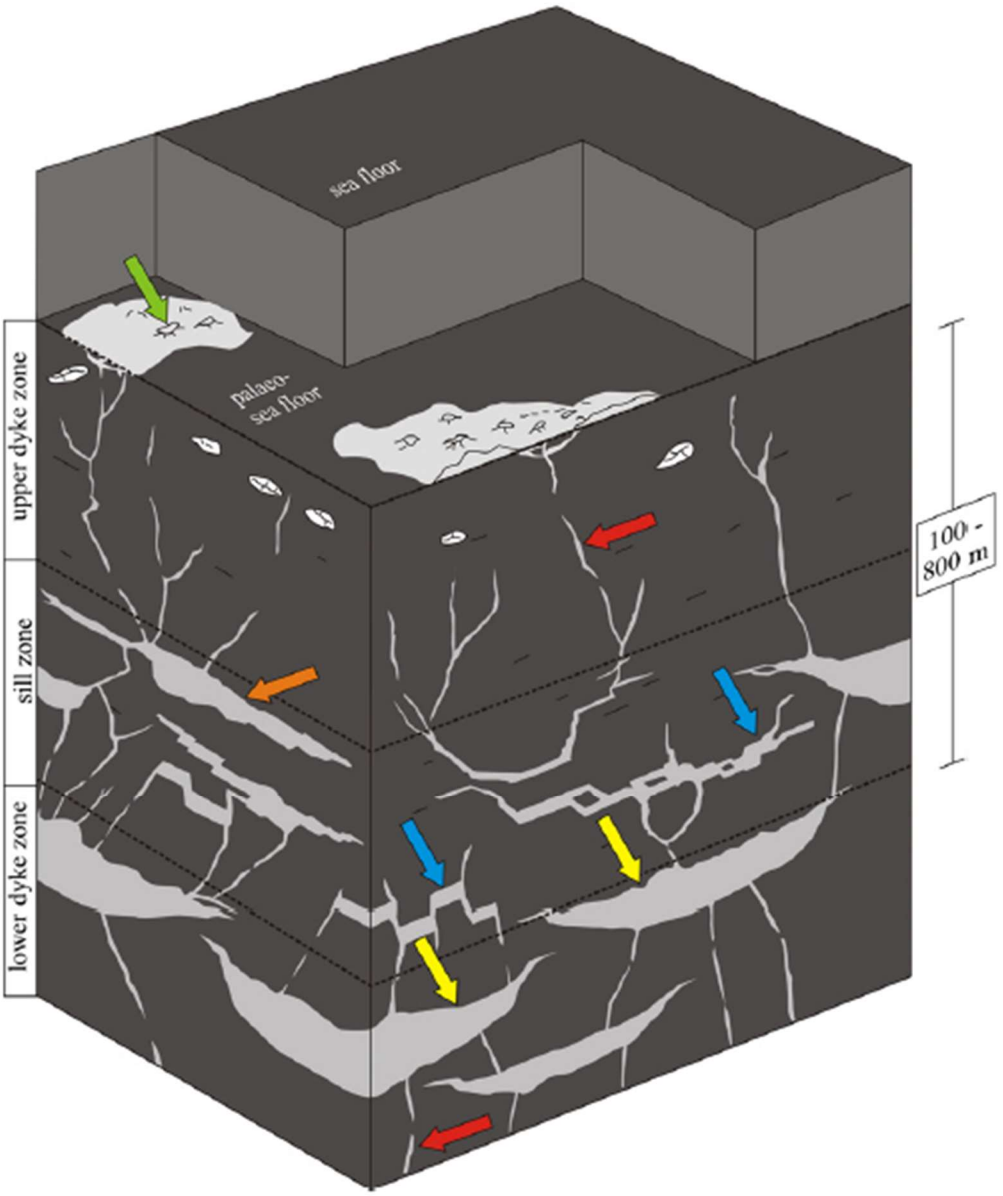

Figure 2-1 An example sand injectite complex (light grey) based on outcrop and subsurface observations in host rock (dark grey). Remobilized parent sandstone units (yellow arrows); sandstone dikes (red arrows) and sills (blue arrows); irregular sandstone intrusions (orange arrow); sandstone extrudites (green arrow), overlaid by the sea floor typically unconsolidated sediments (modified from Hurst et al., 2011).

Large-scale architecture of injections is often identifiable in seismic datasets (Hurst et al., 2003; Huuse et al., 2004; Cartwright et al., 2008; Vigorito et al., 2008; Szarawarska et al., 2010; Jackson et al., 2011). Some flow features, such as flow pathways, particle size sorting and segregation, and wall geometries are also identifiable in outcrop data sets (Ross et al., 2014; Cobain et al., 2015). However, the propagation direction and the dynamic

properties of the flow during fluidisation pipe development are more difficult to determine and therefore more widely debated (Peterson, 1968; Taylor, 1982; Obermeier, 1998; Duranti, 2007; Hubbard et al., 2007; Hurst et al., 2011; Sherry et al., 2012; Ross et al., 2014; Cobain et al., 2015). Previous investigations have experimentally modelled fluidisation of layered beds (Nichols et al., 1994; Frey et al., 2009; Ross et al., 2011), whereby more permeable layers are alternated with a less permeable seal to create an overpressure in the bed. However, there have been no experimental observations specifically considering the flow dynamics of pipe formation and the resulting sedimentary structures, nor extrusion vents.

2.2.2 Vertical Fluid Escape Structures

Cartwright and Santamarina (2015) summarised the seismic studies that have clearly identified vertical or sub-vertical fluid escape pipes (associated with both injectites and extrudites) detected in three-dimensional seismic data. The published studies show that pipes range dramatically in size but that the detection of short pipes in this manner is limited by the vertical resolution of the data. The same restrictions apply when identifying pipe diameters as the smallest identified are at the lateral resolution minimum (i.e., a few tens of metres). Generally, the pipes were observed to have a circular or elliptical cross section, interpreted from the coherency, amplitude or dip in the seismic data (Gay et al., 2007, Moss and Cartwright, 2010; Andresen et al., 2011). Identifying the root zone may help to make inferences about the fluid composition in the fluid escape pipes. Commonly vertical pipes terminate at a surface pockmark, but many also terminate in convex upwards structures or paleo seafloor mounds, with some pipes

simply terminating upon meeting a surface that cannot be penetrated or deformed (Cartwright and Santamarina, 2015).

2.3 Common Features and Inferences

2.3.1 Grain Size and Distribution

Roche et al. (2001) showed experimentally that vertical pipes are observed to be sorted vertically (as is observed in the industrial studies of fluidized beds) and, when unconfined, take the form of an upward flaring funnel. At higher velocities, the entire bed was shown to segregate vertically with larger particles remaining at lower elevations after fluidisation and fines migrating upwards.

As well as the vertical migration of fines, fines are often observed to migrate radially outwards from the axis of fluid flow and are observed as "elutriation bands" or "haloes" interfingering the host strata (Hurst et al., 2011; Ravier et al., 2015). The migration of fines is often observed after emplacement and dewatering as a depletion of fines in the injection structure. Marchand et al. (2015) observed that the particle segregation and resulting fines content in the particle distribution directly effects the porosity and permeability of hydrocarbon reservoirs, directly affecting the productivity of the reservoir and the tendency to cause overpressuring, which could in turn cause triggering of fluidisation vents and rupture of the reservoir. The segregation of particles observed in injection structures can cause the fines depleted structures to act as high permeability conduits between strata, provide leakage pathways through hydrocarbon seals and facilitate pathways for gas migration thereby hindering carbon sequestration (Cartwright and Santamarina, 2015).

2.3.2 Grain Orientation

For non-spherical sediments or particles, grain orientation can have a significant effect on the permeability of the injected rock. Sherry et al. (2012) observed laminations (segregated layers of particle classes) in outcrop proposed to be solely due to grain orientation-related permeability differences. At grain scale, the only observable differences between the clearly identifiable laminations were the grain orientations of the long axis of the grains. It was suggested that the alignment of the grains was altered after the termination of fluidisation and caused a feedback loop where higher permeability channels allowed more pore-water percolation, further aligning the grains in these regions to allow better fluid flow. Diggs (2007) also observed preferential grain alignment with the inferred direction of fluid flow and attributed this to a laminar flow regime causing traction at the walls. Ravier et al. (2015) observed both clasts and grains showing preferential alignment with the direction of fluid flow and also interpreted this as evidence for long periods of traction during injection. Hurst et al. (2011) states that there is scant coverage of observations of grain-alignment in the literature and that there is no unequivocal evidence that grain alignment is indicative of any particular flow regime, with evidence proposed for both laminar and turbulent cases. It remains that the factors that develop or inhibit grain alignment during injection are not well understood and in-situ observation of the development of grain alignment features, either experimentally or numerically, would greatly contribute to the understanding of the micro-structures observed in outcrop.

2.3.3 Laminae and Banding

Laminae and banding have been observed in outcrop studies of injectites (Hubbard et al., 2007; van der Meer et al., 2009; Scott et al., 2009; Sherry et al., 2012; Ross et al., 2014) and reproduced experimentally (Ross et al., 2011). Laminae and banding structures are distinct layers of segregated particle classes. They are frequently observed to run parallel or sub-parallel to the margins of the injectite and can be identified by sharp boundaries between distinct microstructure features of the lamination (such as grain size or alignment, or presence and concentration of clay size particles). However, the interpretation of the cause of laminations and banding are wide and varied. From outcrop studies, the mechanisms of segregation leading to laminations have been ascribed to multiple episodes of injection (Diggs, 2007; Scott et al., 2009), migration of clay-sized particles (Ross et al., 2014), waning flow velocities (Scott et al., 2009) and differing viscosities of carrier fluids (Sherry et al., 2012). Experimentally, laminations have been observed to result from the movement of a dynamic injectite, recording the path and advancement of the fluidised sediments (Ross et al., 2011). Jonk (2010), however, suggests that most injectites are devoid of sedimentary structures associated with the transport and settlement of high-concentration geological flows and that most laminations observed in outcrop are related to processes occurring after the cessation of the flow. Sherry et al. (2012) observe that the extent of the laminations in the Yellow Bank Creek complex are exacerbated by such processes in a feedback loop between small permeability differences and grain alignment during the de-watering process. Determining the mechanism for the segregation of particle classes leading to the formation of laminae and

banding is important as the interpretations imply very different flow regimes (Hurst et al., 2011). Laminae have been ascribed to flows with very different rheological characteristics and driven by different processes and without more extensive experimental observations of the laminae formation the origins and influences remain poorly constrained.

2.4 Fluidisation Pipes and their formation

2.4.1 Initialisation of Water-Escape Structures

To mobilise a sediment particle, the driving forces provided by the migrating fluid must exceed the resistive forces acting on the particle. In the ideal case of monodisperse spheres, this requires only one minimum fluidisation velocity, u_{mf}, and the transition to fluidisation is abrupt. In practice, the transition to fluidisation is gradual and is termed “incipient fluidisation". Incipient fluidisation occurs through the variability in particulate properties observed both in the field and in laboratory experiments. Nevertheless, the minimum fluidisation velocity of a single particle can be approximated by (Richardson and Zaki, 1954; Gibilaro, 2001; Jonk, 2010):

$$u_{mf} = K(\rho_p - \rho_f)d^2 g/\mu \qquad \text{for the viscous flow regime, } Re \sim 1 \qquad (2.1)$$

$$u_{mf} = K\sqrt{(\rho_p - \rho_f)dg/\rho_f} \qquad \text{For the inertial flow regime } Re > \sim 1000 \qquad (2.2)$$

where Re is the Reynolds number (defined in section 2.5.1) ρ_p and ρ_f are the density of the sediment particle and the fluid respectively, d is the particle diameter, g is the acceleration due to gravity, μ is the dynamic viscosity of the carrier fluid and K is a constant incorporating other properties of the suspended phase including the drag coefficient of the particles.

There is extensive literature investigating the effects of fines on the behaviour of soil samples under loading but this research is limited to triaxial stress tests and geotechnical properties such as shear strength and porewater pressure (Lade and Yamamuro 1997; Yamamuro and Lade, 1999; Chien et al., 2002;Ozener et al., 2009; Wand and Wang, 2010; Monkul and Yamamuro, 2011). Such tests measure deformation and pore water pressures under quasi steady loadings. However, fluidisation and liquefaction are dynamic processes. Yamamuro and Lade (1999) tested natural sands for their liquefaction potential and showed that there was a strong positive correlation between fines content (silts) and liquefaction potential. Further, it was concluded that neither void ratio nor density of sand should be used as an indicator of liquefaction potential. Nevertheless, at present evidence for the role of fines in liquefaction and fluidisation is limited and there is scope to investigate the effects of fines and the validity of the established equations in the context of initiation of fluidisation.

2.4.2 Propagation and Stability Controls

Cobain et al. (2015) provide a diagrammatic representation (Figure 2-2) of the interaction of a propagating injection with the host strata, in this case, mudstone. Figure 2-2 shows that a propagating injection continually interacts with the host strata to determine the structure and development of the injection. It is expected that propagation controls also vary with the material of the host strata and observations of propagation in a sand bed will differ from those in mudstone due to the lack of tensile strength in a sand body. In a mudstone body, the propagation of the injection advances as long as the hydraulic pressure gradient exceeds the tensile strength of the fracture (Davies et al., 2012). In cohesionless sediment there is no tensile

strength and so the propagation of the injection persists as long as the hydraulic pressure gradient persists and fluid velocity exceeds the minimum settling velocity of the sediment. This leads to rapid rupturing processes in cohesionless sediments (Ross et al., 2011). Ross et al. (2011) showed experimentally that, for sand extrusions in cohesionless sediments, pipes can take a variety of distinct morphologies: (i) vertical and narrow; (ii) vertical and wide; (iii) a funnel shape that widens towards the top; (iv) subvertical; (v) sinuous showing a dyke and sill, or stepped morphology; or (vi) a poorly defined, yet wide, zone of fluidized sediment. It was observed that once venting had occurred the flowrate in the pipe increased significantly. Further, the morphology obtained during fluidisation is not fixed and may transition from one form to the other throughout fluidisation. Some pipes were seen to migrate, leaving extensive areas of structureless sediment behind them. Ross et al. (2011) also observed that the pipe walls were often lined with fines, an observation made in outcrop by Mount (1993). Mount (1993) asserted that the stability of pipe walls is increased by the elutriation of fines radially out from the fluidised zone. It is suggested that when finer particles migrate away from the centre of the fluidisation zone and into the surrounding bed the porosity in these regions is reduced, reducing flow leaking out of the pipe and thus intensifying the flow within the pipe and sustaining the fluidisation process.

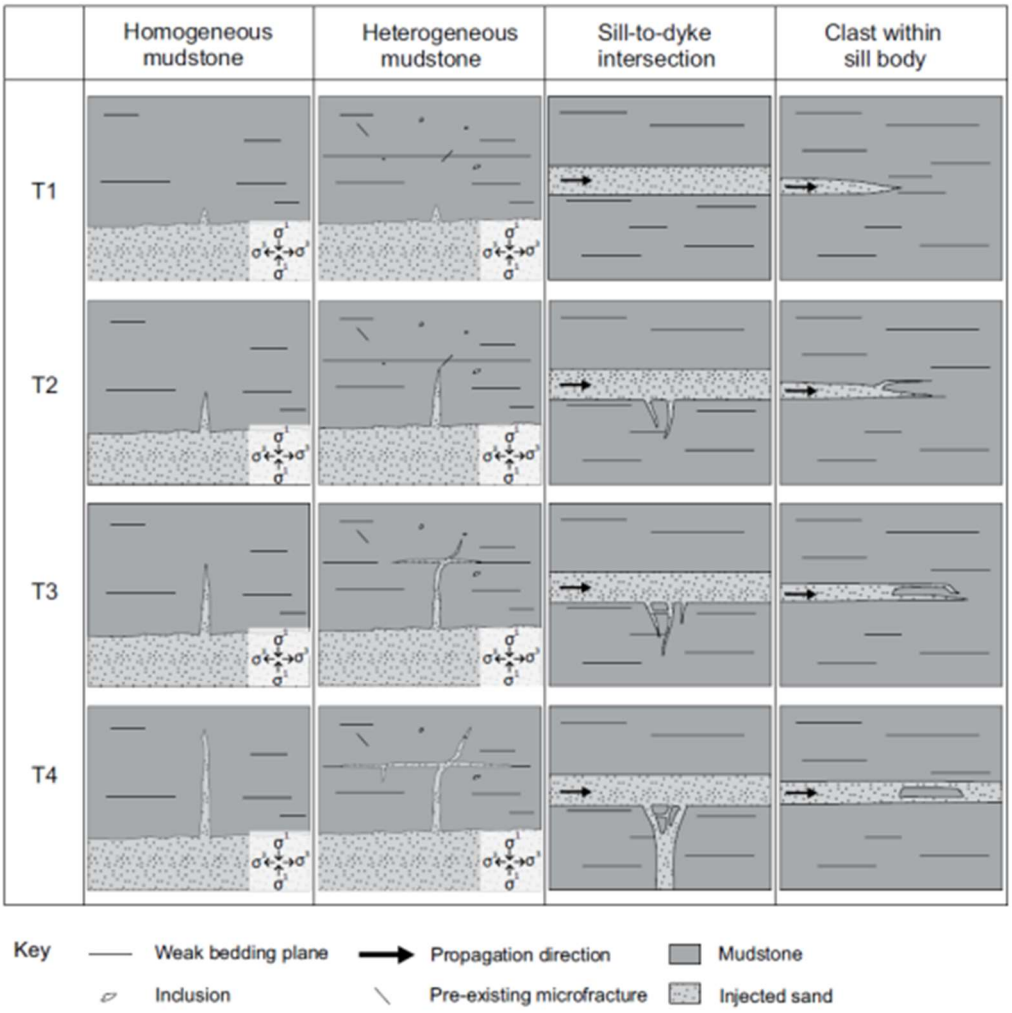

Figure 2-2 Interactions of propagating injections with heterogeneities in host strata (reproduced from Cobain et al., 2015)

2.4.3 Termination of Fluidisation Pipes

Best (1989) identified examples of fluidisation pipes terminating both before and after the injection was vented. Since fluidisation is driven by a hydraulic pressure gradient, it follows that the termination of an intrusion occurs when this gradient is dissipated. Best (1989) suggested a possible mechanism for the cessation of fluidisation is the local variation of the minimum fluidisation velocity caused by deviations in grain properties of the bed or indeed through the venting of the pressure as a sand volcano. Further, the dissipation of the gradient is inherently linked to the triggering mechanism; a sudden stop in the driving pressure will indicate the impending termination of

the injection. Jonk (2010) proposed that this sudden dissipation of the fluid-pressure contributes to the observable structure of sand-injectites in outcrop. As the pressure-drop reduces below the effective stress of the fracture it is asserted that the fracture walls contract, effectively freezing the grains of the fluidised area in place and providing a frictional force, preventing further particle migration.

2.5 Flow Regimes during Injection

2.5.1 Classical approaches

Fully laminar flow conditions are characterised by a stable and predictable system where at any point in space the velocity of the fluid remains the same over time. Within a laminar system, instabilities can arise, seemingly spontaneously, causing the flow to become unsteady and to display chaotic features, sensitive to the system conditions, that propagate over time and space (Tritton, 2012).

Turbulent flow conditions are characterised by the chaotic advection of kinetic energy through rapid and irregular fluctuations of velocity in space and time (Tritton, 2012). In order to determine when dynamically similar systems can be expected, the Reynolds number is used to quantify the influence of the governing parameters and the characteristics of the flow that can be expected for that system. The Reynolds number is defined as:

$$Re = \frac{Ul}{\upsilon} \tag{2.3}$$

where U and l are typical length and velocity scales of the system and υ is the kinematic viscosity ($\upsilon = \mu\rho$). It is important to note that there are no time scales included in the determination of dynamical similarity through a

Reynolds number approach as steady imposed conditions are assumed; any resulting unsteadiness in the system is related to the length and time scales therein and is not independent. This approach also assumes geometrical similarity between the systems to be compared. Generally speaking, flow is fully laminar only at very low Reynolds numbers and can begin to display instabilities as a result of the system conditions as low as $Re \approx 40$, with more frequent instabilities and transitional regimes observed at around $Re \approx 400$. Fully turbulent conditions can be expected from $Re \approx 2000$ (Tritton, 2012).

The classification of dynamical similarity is not absolutely determined by the Reynolds number if there are other influencing factors within the system. For example, convection problems must consider temperature fluxes and may not have a characteristic system velocity and so the Rayleigh number is a more appropriate measure of dynamical similarity. Injectites are known to be systems driven by pressure gradients (Hurst et al., 2011), a parameter that drives the fluid velocity of the system; temperature variations in the system are considered negligible. However, injectite systems contain density differences between the solid and liquid phases and this must therefore be accounted for in the consideration of dynamical similarity.

The Archimedes number characterises the fluid flow due to density differences and is calculated as:

$$Ar = \frac{d_p^3 \rho_f (\rho_p - \rho_f) g}{\mu_f^2} \tag{2.4}$$

where d_p represents the particle diameter, ρ_f and ρ_s the density of the fluid and the sediment particles respectively, g represents the acceleration due to gravity and μ_f represents the dynamic viscosity (Di Felice, 2010).

The fluid dynamics of systems with $Ar < 10$ is dominated by viscous forces characterising the laminar flow regime, whereas systems with $Ar > 105$ are dominated by inertial forces (turbulent flow regime) (Di Felice, 2010). The minimum fluidisation condition of the suspension is shown graphically as a function of the terminal (or particle) Reynolds number and the Archimedes number in Figure 2-3. For systems falling below the dashed line, the system cannot suspend the particles and fluid flow is termed "seepage". For systems between the two lines, the flow is a suspension and for systems above the black line, the drag force on particles exceeds the particle weight, which is only possible in fully confined systems.

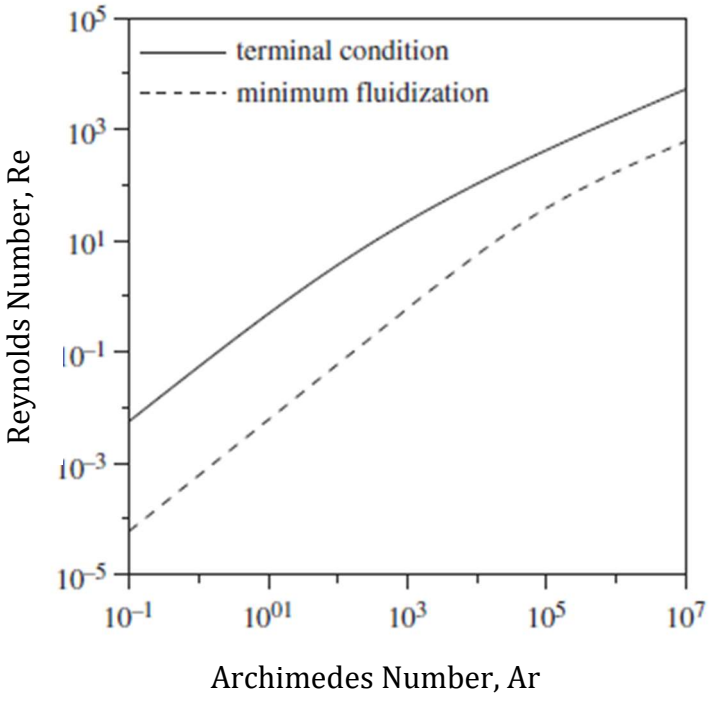

Figure 2-2 Minimum fluidization and terminal Reynolds number as a function of Archimedes number (reproduced from Di Felice, 2010).

2.5.2 Alternative flow regime categorisation

The mechanical behaviour of the fluidisation of granular materials applies to both industrial and geophysical processes (Rigord et al., 2005). Fluidised

bed studies have identified three flow regimes for localised flow through a bed that are not categorised by dimensionless numbers (Zoueshtiagh and Merlen, 2007; Philippe and Badiane, 2013; Mena et al., 2017): static flow through the bed (also known as Darcian flow), the cavity regime, and the chimney regime. The static regime is well categorised in all contexts and represents the case where the fluid passes through a bed without exerting sufficient drag force on the particles to cause their entrainment into the flow. Bed flow is governed by Darcy's equation and the bed behaves as a saturated porous medium. The Darcy regime, as defined by Zoueshtiagh and Merlen (2007), allows for some dilation of the bed at the onset of fluid flow but no further particle movement. The other two regimes represent the cases where the fluid flow through the bed exerts sufficient drag force to cause particle motion. The cavity regime exists only for a very narrow range of fluid discharges (Zoueshtiagh and Merlen, 2007; Philippe and Badiane, 2013; Mena et al., 2017). It occurs when the drag force exerted on the bed particles is sufficient to cause fluidisation and expansion of some of the bed but dissipates with bed height so that the bed does not become fluidised to the surface; there exists a fluidised region overlain by a static bed governed by Darcian flow. The chimney regime comprises the case of bed fluidisation where a central chimney forms over the inlet, carrying particles up through the bed to the surface where they then move outwards and away from the central jet to settle out.

2.6 Governing parameters and range of scales in injectite systems

Injectites are formed from the fluidisation of sediment particles in water. It is this interaction between the solid and liquid phases that drives the complexity in accurately confining the flow regime when compared to a homogeneous fluid. Further complexity is added from the polydispersivity of particles, varying densities and shape factors contained within the sediment class. As a result, the system must be simplified and characteristic parameters are often chosen that approximate the system as accurately as is reasonable.

2.6.1 Length Scales

The two prevailing sources of injectite data are incidences of fluidisation pipes and extrudites in outcrop and identification from seismic data. Summaries of the published data are provided by Cartwright and Santamarina (2015) and Hurst et al. (2011) and are reproduced in Figures 2-4, 2-5 and 2-6. Typically, the most appropriate length scale to use in determining the flow regime is the cross-sectional diameter of the conduit through which the flow is moving (Tritton, 2012), which is the pipe diameter for fluidisation pipes. Fluidisation pipes are shown in Figure 2-5 to have been identified at length scales of centimetres up to tens of metres and at seismic scales (Figure 2-4) from tens of metres to hundreds of metres, thus demonstrating that geological fluidisation features can span at least three orders of magnitude.

Using the pipe cross-sectional diameter is relatively simple in slowly varying pipe structures but extrudites often do not demonstrate a regular cylindrical structure and often display conical or domed structures (Figure 2-6). Further,

the use of a fixed length scale in this manner does not account for the geometrical development of the system over time, which will be influenced by the flow regime of the system. For some systems, the result of such changes will be negligible as the flow regime will remain the same throughout the system and for the duration of the intrusion, however it is important to consider these points as they contradict the assumptions upon which the principles of assessing dynamical similarity are based. This has the implication that for other systems the flow regime may vary within the geometry and possibly over time.

2.6.2 Viscosity

For many fluids, the dynamic viscosity is not a constant but is a function of the shear rate. For dilute suspensions, the effect of the presence of particles is well established in the equations of Einstein (1905) for dilute suspensions and Batchelor and Green (1972) for extensional flows. The Einstein equation neglects the influence of other particles and defines the viscosity of the suspension as:

$$\nu_s = \nu_f(1 + \frac{5}{2}\phi) \tag{2.5}$$

where the subscripts s and f represent the suspension and the fluid respectively and ϕ remains the particle fraction or concentration. Batchelor and Green (1972) account for the presence of a higher fraction of particles by including higher order terms in ϕ. This introduces significant errors when ϕ is not appropriately constrained. There are no analytical solutions to the problem of high concentration flows. An averaging approach, assuming the effect of all the particles in the suspension is the sum of adding all the particles sequentially, has been applied by Ball and Richmond (1980) and

gives an equation effectively identical to the Kreiger-Doherty equation when accounting for particle shape:

$$\nu_s = \nu_f(1 - \phi/\phi_{max})^{-[\nu]\phi_{max}} \quad (2.6)$$

where the subscript max denotes the maximum packing fraction and $[\nu]$ is the intrinsic viscosity of the particle, taken as 2.5 for a single smooth sphere. By assuming a pseudo-fluid approach, where the carrier fluid and the smaller particle class are treated as a single fluid with augmented properties, equation 2.6 can be used to predict the viscosity of a binary suspension:

$$\nu_s = \nu_f(1 - \phi/\phi_{max,1})^{-[\nu]\phi_{max,1}}(1 - \phi/\phi_{max,2})^{-[\nu]\phi_{max,2}} \quad (2.7)$$

Location	Height (range in m)	Width (range in m)	Top at surface	Reference
Offshore Nigeria			Y	Løseth et al., 2011
Offshore Ireland	<1500	200–600	N	Van Rensbergen et al., 2007
Offshore Mauretania	140–340	<200 m?	N	Davies and Clarke, 2010
Offshore Namibia	50–1100	30–450	Y	Moss and Cartwright, 2010a
Offshore Norway	600–1200	200–600	N	Hansen et al., 2005
Hikurangi, New Zealand	250–600	100–300	Y	Netzeband et al. 2010
Offshore Vancouver Is. Canada	100–200	<100	Y	Zuhlsdorff and Spiess, 2004
Offshore Norway	80–700	50–915	Y	Hustoft et al., 2010
Offshore Angola	25–450	60–300	Y	Andresen et al., 2011
Offshore Angola	200–700	50–300	Y	Gay et al., 2007

Figure 2-4 Table adapted from Cartwright and Santamarina (2015) showing the published literature on fluidisation pipes identified from seismic data.

Author (s)	Location	Age	Geometry	Injectite margins and internal sedimentary structures
Hannum (1980)	Kane County, Utah.	Jurassic.	Circular in plan view. Pipe diameter exceeds 1 m.	Pipe fill comprises homogenized sandstones and centimeter- to metre-scale blocks of host strata.
Mount (1993)	Adelaide, South Australia.	Lower Cambrian.	Circular in plan view. Pipe diameter ranges from 1 to 6 cm. Base grades into the surrounding rock.	Concentric internal structure. Central core of very fine sand and a cylindrical to irregular outer halo devoid of fines.
Netoff (2002)	South central Utah.	Middle Jurassic.	Circular in plan view. Pipe diameter of up to 60 m. Cylinders are near-vertical, pillar-like structures.	Irregular and deformed subhorizontal bedding and lamination (5–15 cm wide). Abundant breccian blocks of host strata.
Huuse et al. (2005)	South East Utah.	Middle Jurassic.	Circular to oval in plan view. Pipe diameters exceed tens of metre. They cross >100 m host strata.	Sandstone beds locally bend up along the pipe margins. Pipe fill comprises homogenized sandstones and centimeter- to meter-scale blocks of dune sandstone.
Chan et al. (2007)	Colorado Plateau.	Lower to Middle Jurassic.	Circular in plan view. Pipe diameter ranges from cm.size to >10 m. Base flares into the surrounding rock.	Pipe margins have sharp boundaries. Deformed, irregular, near-horizontal bedding and lamination. Drag structures found close to the margins.

Figure 2-5 Table reproduced from Hurst et al. (2011) summarising the published literature on fluidisation pipes identified at outcrop.

Author (s)	Location	Age	Geometry	Margins and internal sedimentary structures
Obermeier (1996)	New Madrid, Missouri.	Holocene.	Coned. Thickness between 0.3 and 0.7 m. Extends laterally for 5 to 20 m.	Normal gradation of coarse claystone clasts from feeder dike. Planar to wavy laminae dipping away from vent.
Takahama et al. (2000)	Karasu River district, Japan.	Late Quaternary.	Mounded to ring type structures.	Vertical alignment of tabular grains. Angular soil and pumice clasts.
Boehm and Moore (2002)	Santa Cruz, California.	Upper Miocene.	Up to 3 m thick. Extends laterally up to 100 m. Sheet structure.	Parallel laminae and cross bedding. Bioturbation.
Hildebrandt and Egenhoff (2007)	Cienega and Vitichi, Bolivia.	Ordovician.	Thicknesses between 0.1 and 1.2 m. Basal margins are downward convex. Upper margins are sharp and flat. Extends laterally 100 to 2000 m.	Angular and platy claystone clasts. Laminated sandy clasts aligned in distinct layers.
Hurst (2004)	Santa Cruz, California.	Upper Miocene.	Irregular lower basal surface. Sheet structure.	Parallel laminae and cross bedding. Rounded shale clasts. Mudstone breccias. Bioturbation.
Hurst et al. (2006)	Santa Cruz, California.	Miocene.	Up to 5 m thick. Shallow inclined upper surface. Irregular basal surface.	Low angle laminae and cross bedding. Bioturbation. Shale clasts and breccias.
Glennie and Hurst (2007)	Hopeman, Scotland.	Late Permian.	Thickness between 0.2 and 0.3 m. Cone-shaped.	Low angle laminae (<15°) that dips away from a central vent. Angular clasts of laminated sandstone.
Jonk et al. (2007)	County Clare, Ireland.	Carboniferous.	Domed. Up to 0.4 m thick. Up to 1.5 m diameter.	Cratered centre with runnels on the dome's slope.
Jonk et al. (2007)	Freagh, County Clare, Ireland.	Carboniferous.	Domed. Up to 0.2 m thick. Diameter between 0.3 and 0.4 m.	Undulose laminae.
Jonk et al. (2007)	County Clare, Ireland.	Carboniferous.	Domed. Thickness between 0.1 and 0.45 m. Diameter between 0.3 and 1.8 m.	Cratered centre with runnels on the dome's slope.
Pringle et al. (2007)	County Clare, Ireland.	Carboniferous.	Coned. Up to 0.75 m thick. Up to 3 m diameter.	Inclined shale and sand laminae. Cratered centre with runnels on the domes' slope.

Figure 2-4 Table reproduced from (Hurst et al., 2011) summarising the published literature on extrudites from outcrop.

where the subscripts 1 and 2 differentiate between the two classes of particulate.

Polydisperse suspensions are more challenging as the effectiveness of equation 2.7 is limited by the need to appropriately evaluate the maximum packing fraction for each particle size class (Stickel and Powell, 2005). Therefore, effectively constraining the viscosity of the fluidising suspension during injections is next to impossible due to the need to account for the properties of all of the particle classes present and their respective concentrations within the suspension. The elutriation of particles from the system and the migration patterns of particles of different sizes and shapes indicate that the concentrations are also temporally and spatially dependent so the viscosity at the start of injection is almost certainly different to the viscosity at a later time. The challenge of defining a representative viscosity for geological settings is a contributing factor to the lack of agreement within the literature around the flow regimes that occur in injectites.

2.6.3 Velocity

Defining a characteristic velocity of the system poses yet more challenges since systems are often interpreted from outcrop data (post-event) or seismic data (largely consisting only of length scale data). A common approach defines the characteristic velocity as the minimum fluidisation velocity necessary to fluidise the largest particle observed in the system. The minimum fluidisation velocity of a single particle can be approximated by equations 2.1 and 2.2 (Richardson and Zaki, 1954; Gibilaro, 2001; Jonk, 2010). For the inertial flow regime, the minimum fluidisation velocity is independent of the suspension rheology and dependent only on the density of the fluid and the particle properties. However, the fluid viscosity must also be well defined for the laminar and transitional flow regimes when viscous forces are important.

2.7 Application of the discussed approaches

2.7.1 Varying the viscosity as a function of concentration across multiple length scales

By using a pseudofluid approach, Reynolds numbers have been calculated for a range of particle concentrations (Figure 2-7). The calculations have assumed a monodisperse suspension of 0.4 mm particles at a range of concentrations from 0.15 to 0.54 and the viscosity calculated using equation 2.6. The exponent taken as –1.5, as derived empirically by (Ferreira and Diz, 1999). The characteristic velocity was chosen to be the minimum fluidisation velocity calculated using equation 2.2, taking $K = \frac{4}{3C_d}$ and the drag coefficient $C_d = 0.5$, which is appropriate for rough spheres (Sherry et al., 2012). The resulting Reynolds number-concentration curves show that for

large scale pipe structures the flow is always turbulent, yet at metre scale the flow regime is laminar above ϕ = 0.35. For the exact same suspension moving at the same characteristic velocity, this does not seem logical, particularly as the packing limit is approached. Using the suspension theory approach for the same suspension gives an Archimedes number of Ar = 103 and particle Reynolds numbers as shown in Figure 2-8. Plotting these values on Figure 2-3 shows that the suspension is expected to be static at higher concentrations, and the fluid motion would occur as seepage through the stationary bed (Figure 2-9). Since the Archimedes number is less than 105, the system is expected to always be in the laminar flow regime (Di Felice, 2010). Once again, this is not an appropriate prediction of the system dynamics since, for an injectite system, density differences do not drive the flow dynamics, although they will significantly affect it. The driving mechanism is the pressure difference exerted on the fluid, which in turn exerts a drag force on the suspended particles. Therefore, Reynolds number must also be considered when determining if the flow can be expected to be turbulent since the velocity term that encompasses the driving pressure. However, the values of particle Reynolds number at which each regime is well established have not been determined in the published literature.

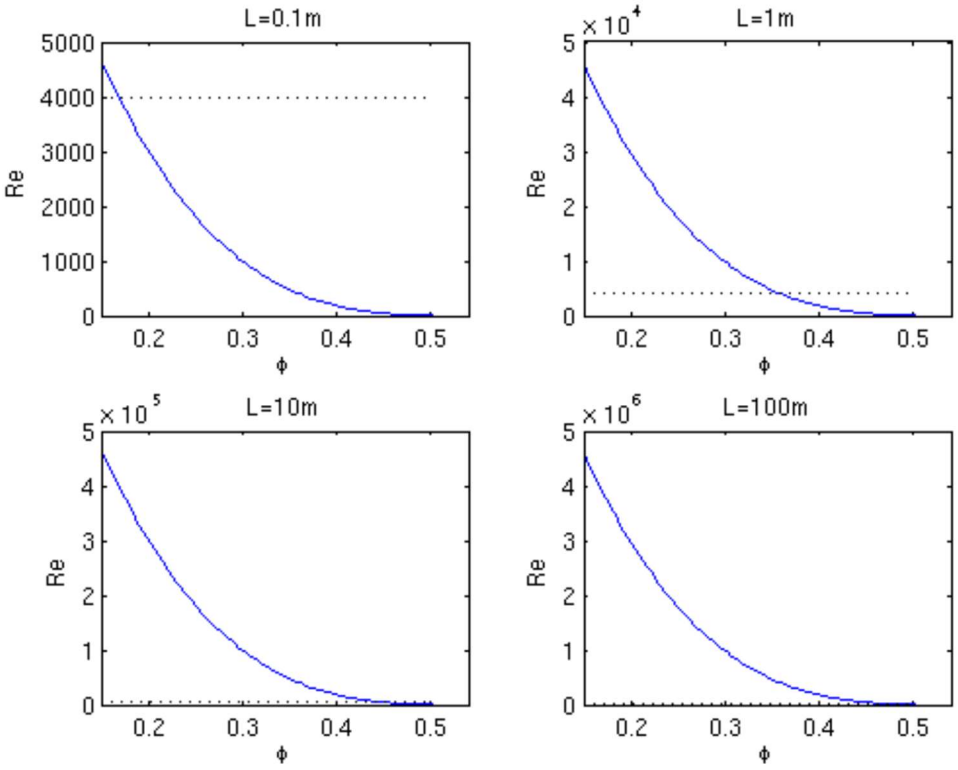

Figure 2-5 Examples for Reynolds number calculation using a range of conduit widths (L) and concentrations (ϕ) for a monodisperse suspension made up of d_p = 0.4 mm, u_{mf} calculated using equation 2.2, $K = 4/(3C_d)$ as applied by (Sherry et al., 2012) and taking the drag co-effcient as C_d = 0.5 for a rough sphere. Dotted line shows the transition to turbulence at Re ~ 4000

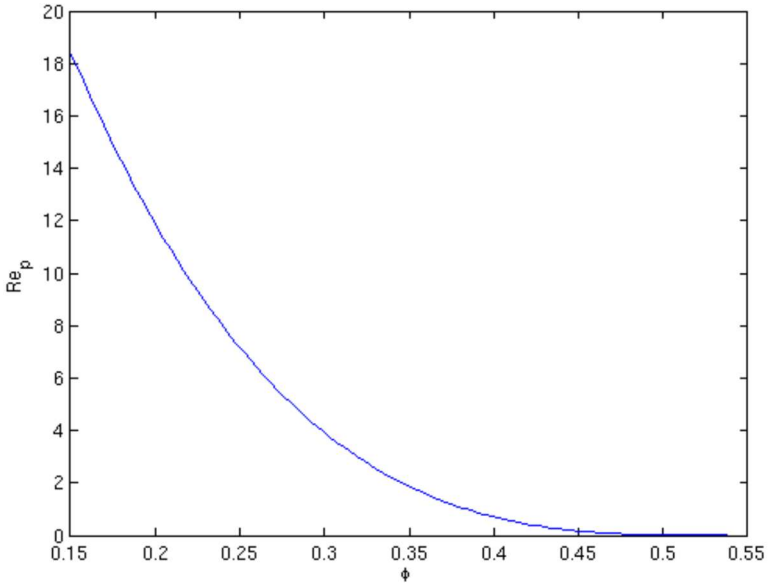

Figure 2-7 Concentrations (ϕ) for a monodisperse suspension made up of d_p = 0.4 mm, u_{mf} calculated using equation 2.2, $K = 4/(3C_d)$as applied by (Sherry et al., 2012) and taking the drag co-effcient as C_d = 0.5 for a rough sphere.

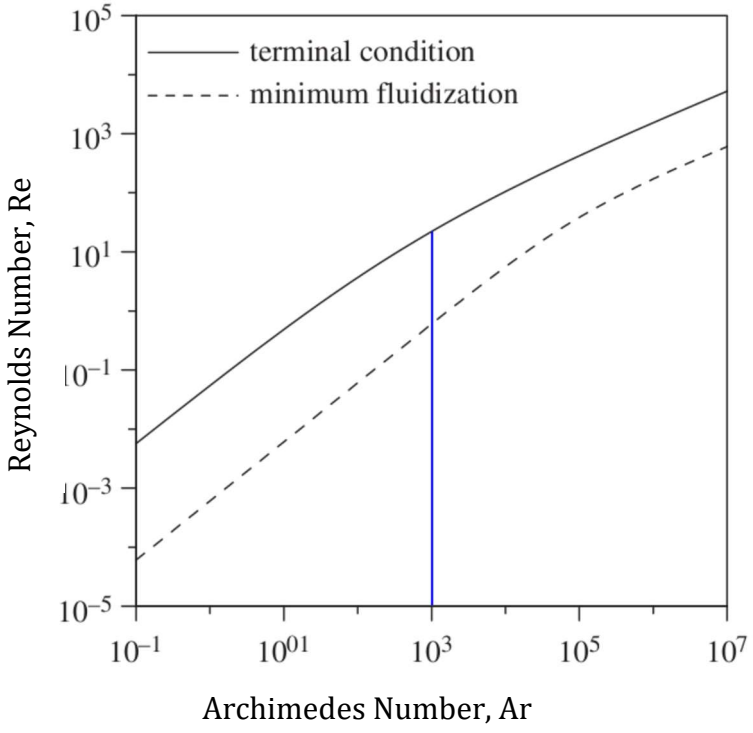

Figure 2-6 Plot showing the range of values expected for the example suspension using a suspension theory approach. Blue line represents range of Re_p values obtained by varying the concentration ϕ and augmenting the suspension viscosity as before. The sediment is expected to be fluidised at ϕ < 0.4, for higher concentrations the bed is stationary.

2.8 Implications for Injectites

Categorising dynamically similar systems is rarely attempted in the geological literature and is generally attempted using the assumption that suspensions can be treated as pseudofluids and through the calculation of the Reynolds number. The use of a pseudofluid assumes that all of the multiphase dynamics can be approximated with the use of an augmented viscosity. Although this rheological approach is often used in the fluidised beds literature (Di Felice, 2007), this applies to small scale laboratory experiments and unequivocally contains empirical assumptions relying heavily on small scale experimental data. It is therefore questionable whether such an approach is suitable for field-scale injectites. Further consideration should be given to the choice of the length scale when using this approach, as demonstrated in section 2.7.1. Clearly, at a certain system scale the pipe diameter is no longer the appropriate length scale to represent the flow dynamics of the system. The use of a particle Reynolds number and the Archimedes number considers the system at particle level and therefore is more appropriate in the determination of local scale dynamics. However, both the Reynolds number and the Archimedes number assume that an augmented viscosity can represent particle-fluid and particle-particle interactions, which still requires investigation. Although the augmented viscosity has been shown to be a reasonable approximation in some experimental work, it is used much more broadly than is suitable. Moreover, due to the nature of the Kreiger-Doherty equation (Equation 2.6), often the approximations for the particle properties contained in the

exponent are derived in unrepresentative experimental systems and used to circumvent the derivation of the rheological properties of the system at hand.

The analysis of the rheological properties of geological flows is non-existent and without this this approach cannot be shown to accurately reflect the dynamics of the system. Di Felice (2010) asserts that the use of an Archimedes number fully characterises the flow dynamics in geological suspensions and states that flows with $Ar > 105$ are turbulent and flows with $Ar < 10$ are fully laminar. In reviewing the Archimedes equation, it is clear that the Archimedes number alone cannot possibly determine the flow regime as injectites are pressure driven systems and the Archimedes number has no factor containing this property of the system. Although this is well known to be appropriate for buoyancy driven-systems, density differences between phases will certainly influence the flow dynamics during injection but cannot determine the system dynamics. Both approaches make the assumption that a choice of velocity scale is suitable for determining the system properties however velocity can be highly variable across the system.

Figure 2-10 shows the common conical shape typical of extrusive systems where velocities will be significantly higher at the pipe inlet and much reduced at the vent and across the radial cross section of the vent. Flow rate would provide a more suitable characterisation for specific points within the system as this could account for the geometric variation. However using the flow rate does assume that flow rate is a conserved property of the system which will not be the case for systems in porous host strata.

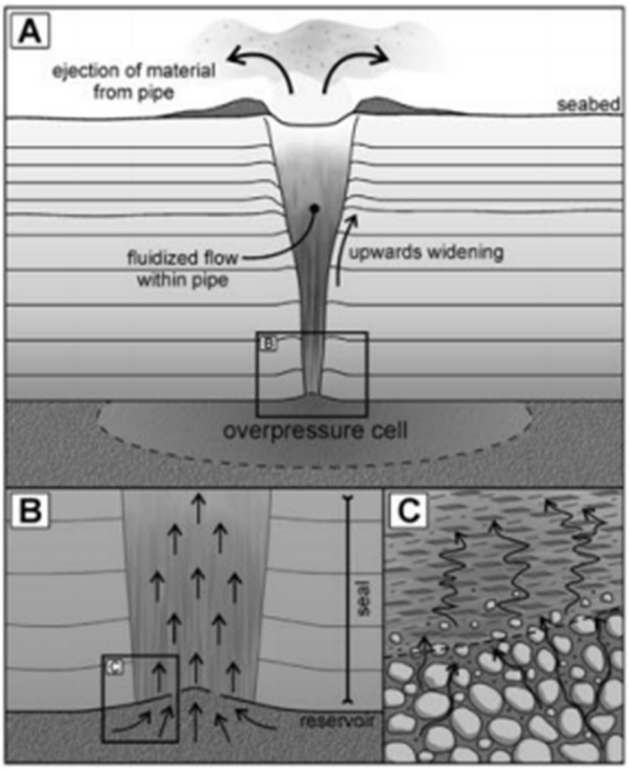

Figure 2-10 Diagram representing the general stucture of an extrudite (reproduced from Cartwright and Santamarina (2015)). A) shows the overall non-uniform geometry common for extrudites. B) Shows flow at the initiation point of the injection. C) Shows seepage flow dynamics at injection.

Cartwright and Santamarina (2015) acknowledged that the flow regime is highly dependent on the composition of the injecting fluid but noted that the identification of the root zone in seismic data is difficult because of the loss of imaging accuracy with depth. Also, the identification of unambiguous feeder structures is rare. However, some studies do find this data and, in these cases, more accurate assumptions can be made about the fluid properties in the fluid escape structure. Outcrop data is yet more challenging as, although particle properties can be well defined for the analysis section, the whole system has been dewatered. Concentration data, and therefore importance of particle-particle interactions, cannot then be inferred.

Outcrop data also makes use of deformation features to determine if the flow regime was likely to be turbulent and erosive or laminar and traction based.

Reynolds number calculations based on the fall velocity of the largest clasts observed have been used to determine turbulent flow regimes (Scott et al., 2009; Sherry et al., 2012; Ross et al., 2014; Cobain et al., 2015) and erosive features also suggested to indicate turbulent regimes (Cobain et al. (2015) and references therein). Laminations have been interpreted as in favour of both regimes (Hurst et al., 2011). Diggs (2007) suggests grain alignment at the walls of clastic dykes is indicative of a traction-based system and therefore a laminar process of injection. This approach often leads to much debate about the flow regimes involved during injection and much further investigation of active flow dynamics is needed.

2.9 Scaling in Experiments

Classical scaling analysis suggests that for an experimental model to be considered successful, it should be geometrically, kinematically and dynamically similar to its natural prototype (Hubbert, 1937; Rodrigues et al., 2009). Geometrical similarity means that corresponding lengths are proportional and kinematic similarity means that corresponding time intervals are proportional (Rodrigues et al., 2009). As discussed in Section 2.5.1 dynamical similarity means that forces at corresponding points should have the same direction and proportional magnitude. The proper scaling of experiments is widely acknowledged to be near impossible in most experimental arrangements (Hubert 1937; Peakall et al., 1996; Rodrigues et al., 2009; Mourgues et al., 2012) The power of such scaling (if achieved) is that any measurement taken from a perfectly scaled experiment could then be converted to that of the natural analogue by means of an algebraic transformation (Paola et al., 2009). However, using scaled experiments to

predict measurements in the natural analogue is not the only benefit of experimental models. Despite, most experiments not being dynamic scale models, they appear to capture the essence of many important processes in natural systems, this is termed “unreasonable effectiveness” by Paola et al. (2009).

In order to successfully represent natural processes and mechanisms through an experimental analogue it is necessary in the design of the experimental arrangement to consider the processes which are to be observed and their relevant scales (Mourgues et al., 2012). Some qualities of the prototype and the natural event are scale invariant – such as sediment properties (density, particle size etc.) and the fluidising medium. As a result the minimum fluidisation velocity of a single particle is invariant across scales. There is however, a kinematic difference between the model and the natural event. Due to the difference in modelled and natural bed depths, the depth of the bed influences the fluid dissipation rates, any fluid seepage through the bed and the resistance of the bed to fluid flow. These properties then directly influence the pressure build up required to initiate a fluidisation event and also the temporal evolution of the fluidised flow through the bed.

Experimental models are known to greatly speed up process times in comparison to large scale systems, for many variables (Peakall et al., 1996, Paola et al., 2009) due to the differing length scales. Figure 9.7 of Peakall et al. (1996) demonstrates that some variables may be faster in the model than in the prototype, examples from their analysed fluvial models being sediment transport and vertical erosion, whereas other quantities such as fall velocity and grain motion during saltation were shown to be slower in the models

than the prototype. This has the impact that the morphology observed in the models may be distorted in comparison to the natural analogue. It is also of note that natural events tend to be intermittent while experiments, by their nature, are more tightly controlled and often reach a steady state quickly which is not likely to happen in a natural event (Paola et al., 2009). Therefore, different scales are likely to influence the different processes and mechanisms observed in experimental fluidisation events and as such the interpretation of observed measurements, particularly temporal measurements and results and resulting morphologies, should be carefully considered.

2.10 Conclusions

It is likely that a range of dynamical regimes occur across injectite systems and, in some cases, within the same system. It is the exact properties of the system that determine the dynamical properties of the flow and the resulting geological features after cessation. Classical approaches to dynamical similarity make use of many assumptions that are simply not valid for high concentration geological flows. Existing alternative approaches also use classification systems that consider the whole fluidisation event and do not capture the likely spatial and temporal variability within events. The approaches used are sensitive to changes in concentration and the resulting rheology of injection, which can vary temporally and spatially. Significantly more information is needed about the velocity and concentration properties of geological flows if these approaches are to continue to be the standard approach, or alternative methods of classification derived that accurately constrain injection systems.

3 Quantitative analysis of the influence of porosity and permeability on flow fields and injectite dynamics in bidisperse sediment beds

3.1 Introduction

Most of the known characteristics, in terms of large-scale morphology, of sand extrusions and fluidisation pipes have been inferred from high resolution seismic datasets (Cartwright and Santamarina, 2015). However, seismic reflection data rarely capture small-scale sedimentary structures and tend not to resolve steep features such as fluidisation pipes (Briedis et al., 2007; Cobain et al., 2020). Furthermore, geometry is often poorly constrained when structures are of the order of the spatial resolution limits of seismic reflection data (Hurst et al., 2011). Nevertheless, analysis of seismic data suggests some common characteristics of fluidisation pipes (Table 3-1). Especially helpful are cases where: i) the root zone is identified, indicating the triggering mechanism; ii) where fluidisation pipes are large enough to be identified, the clustering of pipes or exclusion zones between pipes indicating shared fluid sources or drained root zones respectively, iii) large pockmark features indicate explosive or rapid events; or iv) diffuse terminations are present which are suggested as indicators of a sedimentary collapse or dissipation of flow where highly permeable layers are present (Table 3-1, taken from Cartwright and Santamarina, 2015). However, beyond these “indicators” of broader characteristics, seismic datasets are unable to provide detailed characteristics of the beds, the particle size, type and distribution within the pipe nor of the transporting fluid.

Table 3-1 Observed characteristics of fluidisation pipes from seismic datasets and their implication for fluidisation pipe genesis (modified from Cartwright and Santamarina, 2015)

Observed Characteristics	Implication for pipe genesis
Formation in layered, clay-dominated sedimentary basins	Low vertical hydraulic conductivity
Either single-time formation event or episodic formation	Sustained overpressure generation and sporadic release events
Decisive vertical orientation	Gravi-tropic guided formation mechanisms
May exhibit pronounced 10:1 slenderness	Length-persistent formation mechanism
Often linked to high-pressure root zones, sometimes related to gas accumulation	Fluid driven mechanisms
Apparent exclusion distance between neighbouring pipes	Drained root zone
Some pipes form above collapse structures	Not fluid driven
Possible regional clustering	Shared formation mechanism
Alignment may reflect subsurface features	Associated to fluid flow conduits or local strains that favour pipe nucleation
Termination may take place at pockmarks or mounds on the seafloor or at similar palaeo-features within the sediment	Vigorous fluid flow and sediment erosion/transport
Diffuse termination within the sediment	Pipe genesis associated to a deep cavity collapse at the root zone, or a fluid-driven pipe formation that gradually dissipates into a highly permeable layers and can no longer sustain pipe growth
The structure of the host sediment may be preserved -at least in large pipes-	Fluid driven mixing is not enough to eradicate the sedimentation structure or formation does not involve high fluid flux
Intermediate layers may be missing within pipes	Selective fluid-driven removal

Similarly, outcrop examples are scarce and often discontinuous or small in comparison to field-scale events (Hurst et al., 2011). Further, interpretations of those examples offer both the laminar (Dott, 1966; Peterson, 1968; Taylor, 1982; Sturkell and Ormö, 1997) and turbulent (Duranti and Mazzini, 2005; Obermeier et al., 2005; Hubbard et al., 2007; Scott et al., 2009) flow regimes as potential explanations for observed characteristics, with some characteristics offered as evidence for both regimes (e.g., the contrasting interpretations of grain-size variation in sandstone dikes; Hurst et al., 2011). Early research cited normal grading in the walls of clastic dikes as evidence

of a laminar flow regime because of the presence of graded layering (Peterson, 1968), but more recent research has cited normal grading as evidence of fluid turbulence during sand injection (Hubbard et al., 2007). Some studies have attempted to use the Reynolds number, parameterised using velocities estimated based on the largest transported particles, to identify the likely flow regime and resolve this apparent dichotomy (Scott et al., 2009; Ross et al., 2014) however such approaches rely on the estimation of the flow concentration which is largely unknown. Aside from the question of whether the formative flow was indeed laminar or turbulent, additional processes inferred from outcrop evidence of fluidisation events remain unresolved, such as the cause of size segregation of fluidised particles and the movement of larger clasts through pipe systems towards the walls, with inertial lateral migration and local incorporation of the clasts being suggested as explanations (Segré and Silberberg, 1962a,b; Hogg, 1994; Macdonald and Flecker, 2007; Hurst et al., 2011; Cobain et al., 2015).

Physical modelling offers the opportunity to further investigate flow processes and is able to shed light on characteristic behaviours of fluidisation events (Mörz et al., 2007; Zoueshtiagh and Merlen, 2007; Rodrigues et al., 2009; Ross et al., 2011; Philippe and Badiane, 2013; Philippe et al., 2017). Multiple experimental methodologies have been used to address the problem of visibility in high concentration systems: quasi-two dimensional configurations (e.g., Nichols et al., 1994; Nichols, 1995); three-dimensional configurations with views at the surface and wall interface (Mörz et al., 2007; Zoueshtiagh and Merlen, 2007; Rodrigues et al., 2009; Ross et al., 2011); and three-dimensional configurations using newer experimental technologies such as refractive index-matched fluids and particles to aid

visibility (Philippe and Badiane, 2013; Mena et al., 2018). Previous experimental work can further be subdivided by the type of sediment used: monodisperse studies have provided a simple insight into basic fluidisation processes (Mörz et al., 2007; Philippe and Badiane, 2013; Mena et al., 2017), while layered bi-disperse approaches have modelled “seal” failure and observed some segregation phenomena (Nermoen et al., 2010; Ross et al., 2011). Here, for the first time, the influence of a homogenous bi-disperse bed on fluidisation processes is assessed in order to understand the role of more realistic sediment and porosity variations on injectite dynamics and morphology. Furthermore, quantitative data of the flow fields are collected and integrated alongside observations of segregation and morphodynamics.

This chapter will consider the velocity characteristics measured across laminar and turbulent fluidising conditions and high and low porosity systems, varied by changing the mixture of particles forming the bed. During the experiments reported herein, bi-disperse beds were locally fluidised while high speed imaging was used to capture observations of particle segregation behaviours and processes and to enable the extraction of high-resolution Particle Image Velocimetry-derived velocity fields. These velocity fields are interrogated to draw conclusions about the turbulence characteristics that could be present in field fluidisation events. Section 4.2 outlines the experimental approach used, with Particle Imaging Velocimetry data presented in section 3.3. The implications for fluidisation pipe flow characteristics are discussed and compared to the monodisperse data available in section 3.4 and the resulting conclusions are summarised in section 3.5.

3.2 Methodology

The experiments presented herein were conducted in the Sorby Environmental Fluid Dynamics Laboratory at the University of Leeds. To enable the full characterisation of the fluidisation process in a high concentration system and to ensure reliable, high-resolution velocity measurements the opacity of the fluidised medium must be addressed. It has been demonstrated that it is possible to investigate high concentration fluidisation events using Particle Imaging Velocimetry (Nermoen et al., 2010; Ross et al., 2011).

Particle Imaging Velocimetry (PIV) is a technique for measuring the velocity of a fluid flow. Velocity vectors are determined by comparing the displacement of “tracer” particles at two well-defined time instances (Adrian and Westerwheel, 2011). Each image is divided into interrogation regions and the displacement of the seeding particles in each interrogation region is measured by cross-correlating the images of the first and second frames to find the mean displacement that gives the maximum correlation (Westerwheel et al. 2011). Commonly PIV is applied to dilute flows and a Laser is used to provide a light sheet to enable the tracking of the tracer particles. In high concentration particulate systems this is not possible, due to the obscuration of individual particles, and as the particles have a different refractive index compared to the fluid phase. For these reasons it is not possible to use Laser illumination. Instead 20% of the coarse sediment class was dyed blue, this dyed fraction acted as the seeding particles. A constant LED light source with a red filter illuminated all the particles in the experiment. The combination of red light and blue particles distinguished the

dyed particle fraction from the non-dyed particles providing significant contrast for the dyed particles to tracked by the PIV software .

This set of experiments used a similar approach to that of Nermoen et al. (2010) (Figure 3-1) to ensure a predictable point of fluidisation and to enable imaging of the fluidised area with high speed cameras. Using a two-dimensional flat-walled cell removes the need to correct for cylindrical distortion in the images at the analysis stage.

3.2.1 Experimental arrangement

The arrangement consisted of a quasi-two-dimensional Perspex® tank (0.5m wide x 0.5m high x 0.02m deep) with a central circular inlet (diameter 0.008m) at the base of the tank. Drainage at a height of 500 mm from the inlet was included to maintain a constant water surface elevation. Water was pumped in by gear pump to ensure a steady water discharge and each bed was 250 mm thick. A flow meter was used to maintain constant discharge for the duration of the experiment.

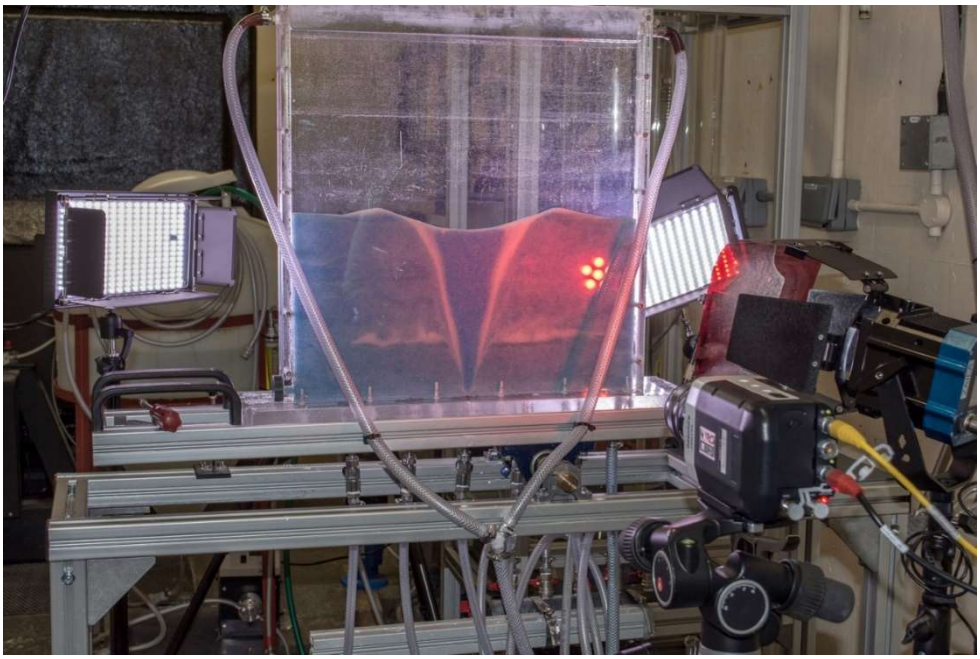

Figure 3-1 Laboratory arrangement showing tank and drainage system, lighting arrangement and high-speed camera

3.2.2 Fluidised medium

Solid glass spheres with a density of 2650 kg m^{-3} were used as the host strata since their density is equivalent to natural sand, the fluidised material in field fluidisation events. Unlike natural sands, however, solid glass spheres have a uniform sphericity (in this case 0.91) and narrow size distribution, allowing for greater control of experimental parameters. The friction angle of glass spheres is typically 24 – 26°, whereas angular granular materials have a much broader range, 24-35° (Makse et al., 1998; Klinkmüller et al., 2016).

The particle size distributions and sphericities of the four classes of particle tested were measured using a Retsch Camsizer XT particle shape analyser

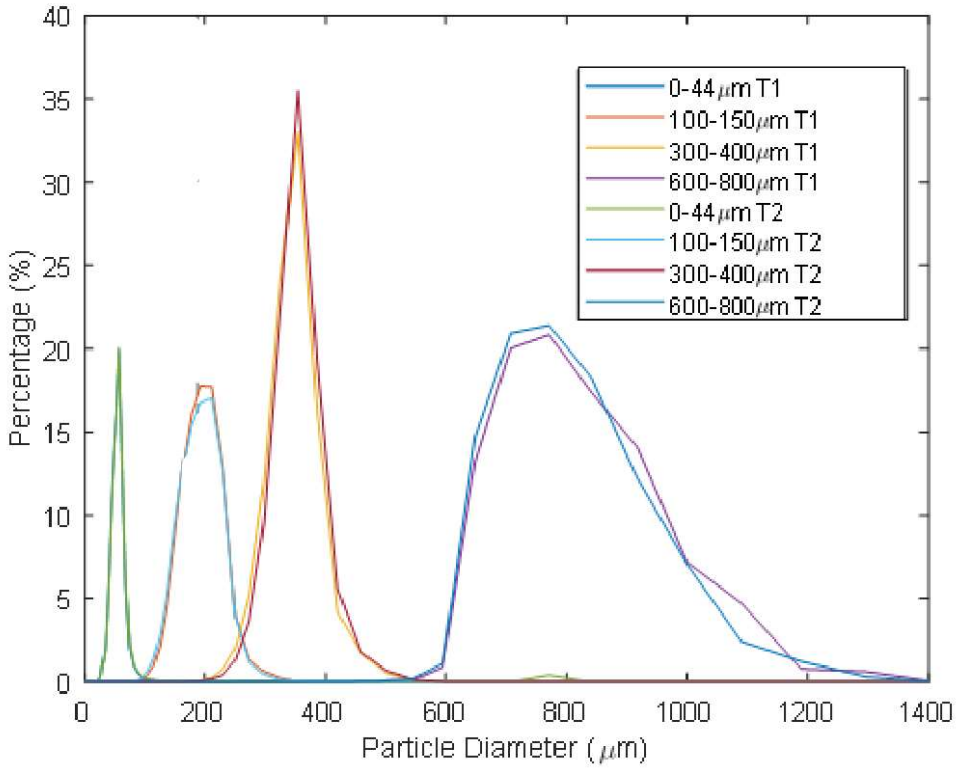

Figure 3-2 Particle Size distributions for individual particle size classes of sediment used to make bed mixtures in experiments (see table 4-2 for mixtures). T1 and T2 refer to the test number for the particle size measurements.

(Figure 3-2). Three bidisperse bed mixtures of solid glass spheres (40% fine

particle class, 60% coarse particle class) were tested to consider the effect of varying porosity on fluidisation (Table 3-2). Twenty percent of the coarse particle class were dyed blue to aid visualisation of the fluidisation event and optimise the contrast in the high-speed images.

In order to generate a repeatable and homogeneous bed, a specific mixing protocol was developed: First, the tank was initially filled with 10 mm of water. Second, the weighed particle classes were combined and mixed until evenly distributed. Third, small batches of the mix were saturated and transferred into the tank through a funnel and filling pipe. Fourth, the layer was agitated until it became level across the tank and homogeneity was achieved. Agitation also served to remove any trapped air present in the saturated mixture. Five 50 mm-thick layers were built up in this manner until the complete mix had been transferred into the tank. Total bed thicknesses were 0.25 m ± 3.6%. The tank was then filled slowly with water from above so as not to disturb the homogeneous level bed until water reached the outflow pipes at the top of the tank. Each experimental run used a new set of sediment to ensure the correct ratios and volume of particle sizes as sediment lost to elutriation could not be quantified.

3.2.3 Experimental parameters

Experimental parameters for each run are summarised in Table 3-2. The flow rates at the inlet were chosen to represent a laminar flow regime and a turbulent flow regime when calculated as discussed in Sections 2.5 and 2.6. A pseudo-fluid approach was used for the *a-priori* calculations of Reynolds number across the range of possible concentrations and using the inlet diameter as the length scale. It was not possible to fluidise the beds

consistently at lower velocities than those sed for the slow inlet velocty cases.

Table 3-2 Experimental parameters

Configuration ID	Fines Class Median Particle Size (μm)	Coarse Class Median Particle size (μm)	Porosity of undisturbed bed	Flow Rate at inlet ($m\ s^{-1}$)	Reynold's number range for pseudofluid
LS (low porosity-slow flow velocity)	51	754	0.247	0.317	~350-2500
LF (low porosity- fast flow velocity)	51	754	0.247	0.919	~1800-7000
HS (high porosity- slow flow velocity)	181	754	0.325	0.362	~350-2500
HF (high porosity- fast flow velocity)	181	754	0.325	0.919	~1800-7000
VF (Very high porosity- fast flow velocity)	330	754	0.377	0.919	~1800-7000

3.2.4 High-speed data capture

High speed videos were collected at 400 frames per second using a Vision Research Phantom Miro M120C camera. Red lighting was used to provide additional contrast for the blue dyed portion of the particles. A calibration image was acquired prior to the commencement of each experimental run, facilitating the later conversion of each 1080 × 1920 pixel frame to SI units. The pixel resolution varied between 0.206 mm and 0.228 mm dependent upon the exact set-up of the camera per run (exact frame sizes shown in Table 3-3). The filling procedure outlined in Section 3.2.1 ensured a homogenous bi-disperse bed that was fully saturated.

Three 10 s-long videos were collected at 0 s, 150 s, and 300 s from the onset of fluid flow, giving ~4000 frames per collection. The selection of these periods captures the development of the fluidisation structures at initialisation and two periods of quasi-steady flow.

Table 3-3 Frame sizes and mm per pixel for each run

Run	X (mm)	Z (mm)	Mm/pixel
HS	438	246.6	0.228
HF	427.8	240.7	0.222
LS	395.9	222.7	0.206
LF	401.7	225.9	0.209

3.2.5 Particle Image Velocimetry (PIV)

PIV was carried out on the collected video clips. Image sets were transferred as cine files from the camera to Dantec Dynamic Studio version 6.4. PIV vectors were generated using the adaptive PIV algorithm (Dantec Dynamics, 2015). A grid step size of 16 pixels was used in the horizontal and vertical directions giving velocity vector maps comprising 64 × 117 vectors in the x and z directions, respectively (z being the dominant direction of fluid flow). The minimum and maximum specified interrogation areas were 64 × 64 pixels and 128 × 128 pixels, respectively. Vector data were exported as .csv files and imported into Matlab. Raw vector data(U, V and Velocity Magnitude) were stored as matrices in x,z,t format and scaled using the calibration images acquired prior to the commencement of fluid flow. Since the PIV algorithm commonly produced unrealistic velocity vectors at the edges of image frames, five velocity vectors were discarded from each of the four edges of the dataset. A simple threshold was applied to the remaining data in each of the three matrices, removing any vectors with a magnitude greater than twice the inlet velocity in the dominant direction of flow (U and Velocity Magnitude) and half the inlet velocity in the cross stream direction of

flow (V). The incidence of spurious vectors removed from each data collection is shown in Table 3-4.

Table 3-4 Velocity vectors removed from each dataset by range validation.

Dataset	Number of velocity vectors removed	As a percentage of velocity vectors collected (%)
HF 10s	169901	0.001848
HF 150s	5763	0.000063
HF 300s	82172	0.000894
HS 10s	18657	0.000203
HS 150s	36197	0.000394
HS 300s	20388	0.000222
LF 10s	22386	0.000243
LF 150s	544758	0.005925
LF 300s	410912	0.004469
LS 10s	8249	0.000090
LS 150s	257279	0.002798
LS 300s	400695	0.004358

3.2.6 Sources of Uncertainty

Uncertainty or “error” is inherent in all experimental work. The sources of error can be split into two types: human error due to the limit of accuracy in operating measurement equipment and systematic error introduced in the processing of the raw data through PIV algorithms or other manipulation of the raw data sets. Sources of human error in this set of experiments include: mass of particles added to the system (± 0.005 kg), height of the bed produced in the tank (± 0.005 m), timing of data collection triggering (± 1 s), mass of seeding particles added to the system (± 0.005 kg).

The error introduced by the PIV algorithm is more complex and also can propagate through into velocity statistics and derived quantities (Sciacchitano and Wieneke, 2016). The main sources of error in the PIV system are camera calibration, camera orientation, seeding density and out-

of-plane particle motion. Error associated with differences in camera calibration (i.e., differences in object-space pixel sizes between experiments) was minimised by calibrating the camera prior to each run and applying each resulting scaling in post-processing. Discrepancies in camera orientation were minimised during experimental set-up by levelling both the camera and the tank independently. Unlike typical PIV arrangements, where a measured fluid is seeded with tracker particles, the present experiments track the fluidised bed particles in the flow field. It was therefore not possible to optimise the seeding density for the measurements.

The out-of-plane motion of the particles is the most significant source of error in the PIV system (Nobach and Bodenschatz, 2009), and also is independent of the seeding density in the system (Nobach and Bodenschatz, 2009; Wieneke, 2015). The uncertainty contributed by the out-of-plane motion varies with the proportion of out-of-plane motion, size of interrogation area and particle-image size (Figure 7 and 10 of Wieneke, 2015). Taking Wieneke's worst-case scenario of 30% out of plane motion, the associated error in between-frame particle displacement is 0.14 pixels. Error estimates for 10, 20 and 30% are given in Table 3-5, showing a range of possible uncertainties of the velocity measurements of the PIV datasets for each experimental arrangement. The significance of the error in the velocity measurements varies across the experimental domain. In the high velocity regions, the error in the measurements ranges from 0.3% to 15%. However, in the slow velocity regions, the potential error in the measurements is of the same order of magnitude as the measured velocity.

Table 3-5 Approximate error in PIV measurements of velocity due to out of plane motion using quantities from (Wieneke, 2015) [1)]

Run	Size of pixel (mm/px)	10% out of plane motion		20% out of plane motion		30% out of plane motion	
		Approximate Error (px)	Error in Velocity (mm/s)	Approximate Error (px)	Error in Velocity (mm/s)	Approximate Error (px)	Error in Velocity (mm/s)
HS	0.228	0.04	1.824	0.08	3.648	0.14	6.384
HF	0.222		1.776		3.552		6.216
LS	0.206		1.648		3.296		5.768
LF	0.209		1.672		3.344		5.852

[1)] Instantaneous velocity measurements in the central core range from 0.036 m s^{-1} to 1.67 m s^{-1} but in the slow flowing regions are of the order mm s^{-1}, giving a range of uncertainty varying from the order of magnitude of the instantaneous velocity measurement to 0.3% of the instantaneous velocity measurement.

3.3 Results (PIV Vector Output)

3.3.1 Instantaneous Velocity

3.3.1.1 Velocity features in Void Development

The full velocity vector dataset is perhaps best viewed in an animated format (See Supplementary Material – HS_0s.avi, HS_150s.avi, HS_300s.avi, HF_0s.avi, HF_150s.avi, HF_300s.avi, LS_0s.avi, LS_150s.avi, LS_300s.avi, LF_0s.avi, LF_150s.avi, LF_300s.avi). However, example frame sequences have been extracted for the purposes of this thesis. The high resolution velocity data are able to capture the flow velocities inside the expanding void space (examples shown in

Figure 3-3 and 3-4). The injected fluid propagates upwards and is deflected along the intact bed. The fluid is then deflected downwards at the edges of the void space (Figure 3-3 and 3-4). Although the jet is central in the example cases shown, the void spaces formed were not of a regular geometry and, as a result, the deflected velocities are not symmetrical. The irregular void expansion is likely due to small heterogeneities in the bed at the earliest fluidisation.

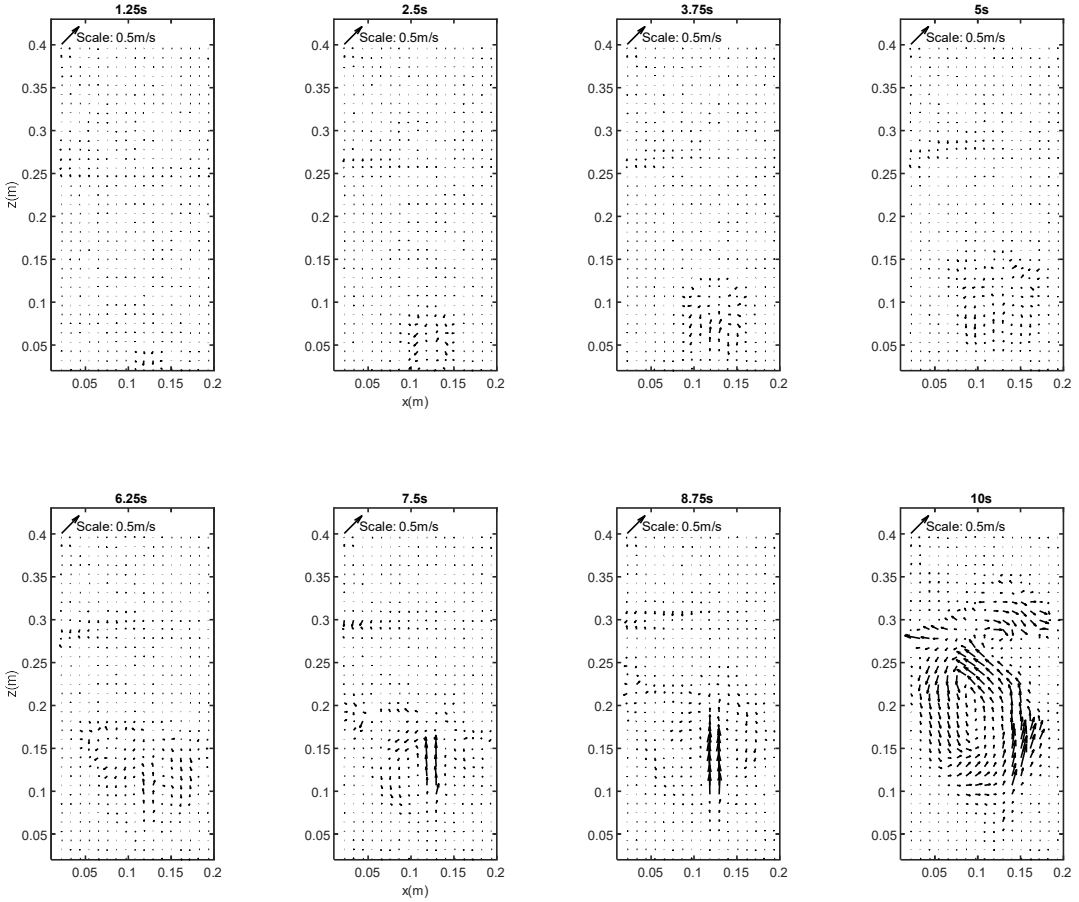

Figure 3-3 Instantaneous velocities during void space development in High porosity - fast velocity (HF) bed.

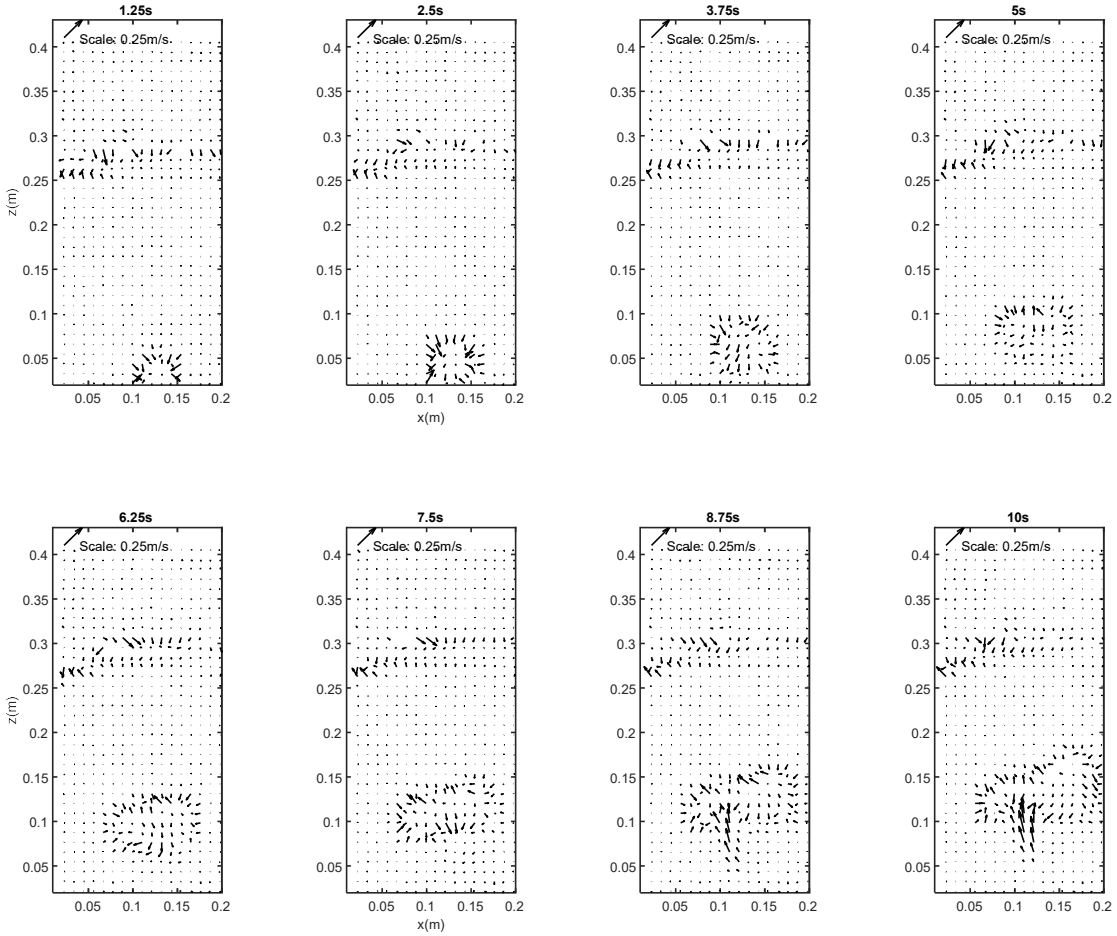

Figure 3-4 Instantaneous velocities during void development for High porosity - slow velocity (HS) bed

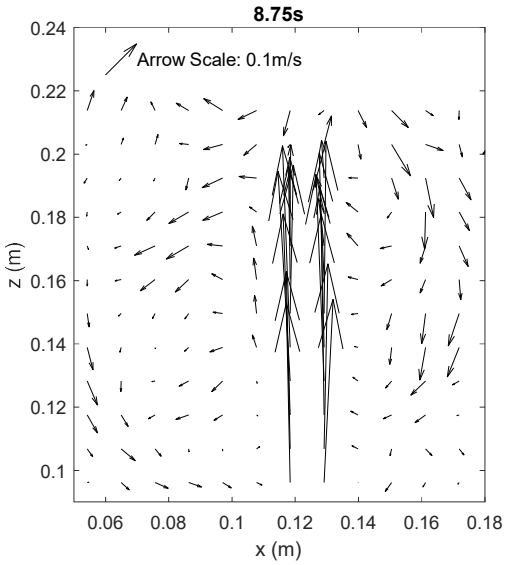

Figure 3-5 Instantaneous velocities focussed on the void space for High porosity - fast velocity (HF) bed at 8.75 s

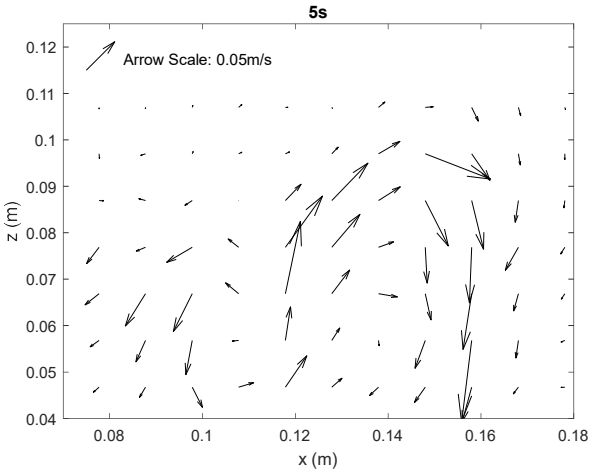

Figure 3-6 Instantaneous velocities focussed on void space for Low porosity - fast velocity (LF) bed at 5 s

3.3.1.2 Quasi-steady state velocity core

At 150 s after the onset of fluidisation, all of the test cases reach a quasi-steady state. The time series of each dataset recorded in the quasi-steady state are shown in Figures 3-7 – 3-15. All of the cases show a steady central core, defined as the region above the inlet where the velocity vectors are dominated by vertical upward velocities with little lateral motion. For context

example vectors have been overlain on the original high speed image in Figure 3-7.

For the high porosity - fast inlet velocity case, the series of measurements commencing at 150 s after the onset of fluid pumping shows a steady central core approximately ranging from 0.02 m (Figure 3-8, 157.5 s) wide to 0.04 m wide (Figure 3-8, 153.75 s) and varying in height from 0.13 m from the inlet (Figure 3-8, 151.25 s) up to 0.17 m from the inlet (Figure 3-8, 157.5 s). The width of the central core is calculated by choosing the widest point of the central core vectors in each plot and subtracting the X co-ordinates of the two vectors, the vectors are spaced 0.0109 mm apart. The fastest velocities are 0.59 m s^{-1}. At 300 s after the onset of fluidisation, the properties of the central core are broadly the same as those for 150 s; the lateral spread of the core varies from 0.02 m (Figure 3-9, 302.5 s) to 0.03 m (Figure 3-9, 305 s) and in height from the inlet from 0.13 m (Figure 3-9, 310 s) to 0.17 m (Figure 3-9, 307.5 s). Maximum velocities remain at 0.58 m s^{-1}.

The similarity between the two sets of measurements indicates that a quasi-steady state has been reached by 150 s after the onset of fluidisation, in line with the qualitative observations in Chapter 6.

For the high porosity - slow inlet velocity case (Figures 3-10 and 3-11), the geometric properties of the central core are largely similar to the fast inlet velocity cases (Figure 3-8 and 3-9). The width of the core varies from 0.02 m (Figure 3-10, 156.25 s) to 0.03 m (Figure 3-10, 158.75 s) and the height of the core varies from 0.13 m above the inlet (Figure 3-10, 151.25 s and 156.25 s) to 0.18 m above the inlet (Figure 3-10, 157.5 s). As expected, maximum

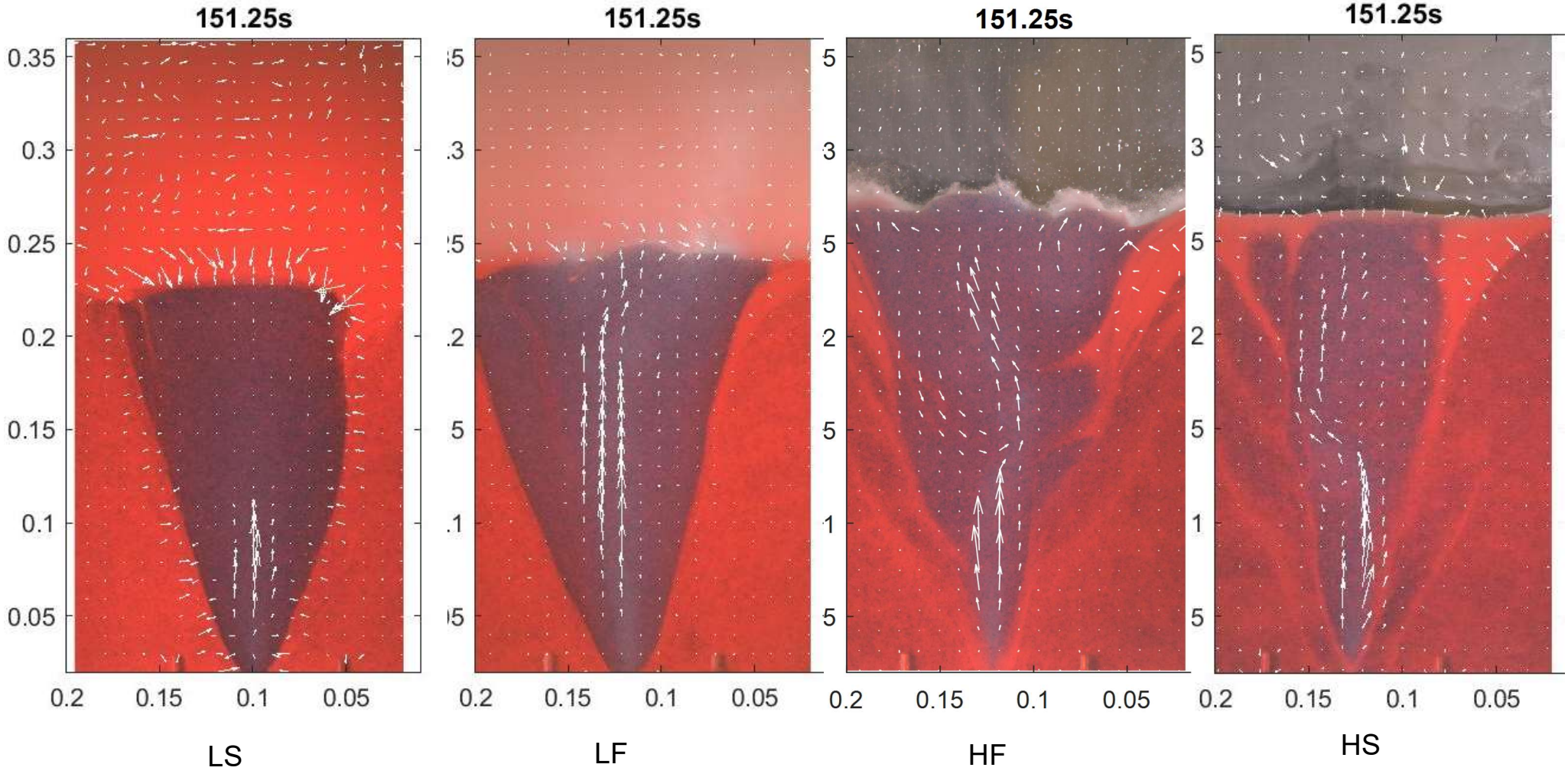

Figure 3-7 Instantaneous velocities of the quasi-steady state overlaid on the original image file for all bed types at 151.25s after the initiation of the fluid flow.

velocities are slower than those observed in the fast inlet velocity case at 0.29 m s^{-1}.

At 300 s, however, the steady core shows little variation in maximum width, with all instances displayed in Figure 3-10 showing a maximum core width of 0.03 m. The height of the core also shows significantly less variation, with the minimum at 0.13 m from the inlet for all displayed instances except for 301.25 s and 302.5 s when the height of the core is 0.15m from the inlet. The maximum velocity observed in the core is also slightly reduced at 0.27 m s^{-1}.

Interestingly, the low porosity - slow inlet velocity case also follows very similar geometric properties (Figures 3-12 and 3-13) to the high porosity – slow inlet velocity cases (Figures 3-10 and 3-11), with a 0.03 m maximum width core evident in all displayed instances for both sets of measurements. The maximum height of the central core is slightly reduced to 0.11 m above the inlet (again for all displayed instances in Figures 3-12 and 3-13). The maximum velocity is 0.18 m s^{-1} for the dataset recorded from 150 s after the onset of fluidisation (Figure 3-12) and 0.17 m s^{-1} for the dataset recorded from 300 s after the onset of fluidisation (Figure 3-13). This shows a significant reduction in observed velocities relative to the corresponding high porosity - slow inlet velocity case.

The low porosity - fast inlet velocity case shows a clear consistent jet to the bed interface with the overlying water column (Figures 3-14 and 3-15 all instances). The central core maintains the consistent width of 0.03 m but appears slightly narrower in Figure 3-14 since the vectors are reduced at the edge of the central core in comparison to the dataset taken at 300 s (Figure

3-15). Smaller vectors at the edge of the central core imply that the exact width of the core is narrower than for a central core with large vectors at the edges. The true location of the edge of the core must fall within 0.0109 mm of the vector point. There are strong upward-focussed vectors, in some cases reaching the free surface (Figure 3-14, 153.75 s, 155 s and 156.25 s), which implies that the central core reaches the free surface in these cases. At 151.25 s and 152.5 s, the jet appears slightly deflected from the central equilibrium position at 0.2 m from the inlet indicating a slight heterogeneity in the flow field. For the dataset recorded from 300 s after the onset of fluidisation (Figure 3-15), all cases have strong upward velocities reaching the overlying water column but most cases show a distinct narrowing of the central core at a height of approximately 0.17 m above the inlet. The maximum velocities for the instances displayed are 0.55 m s^{-1} for the 150 s dataset and 0.53 m s^{-1} for the 300 s dataset which is a slight reduction in maximum velocity from the equivalent high porosity cases (0.59 m s^{-1} and 0.58 m s^{-1}, respectively).

It is clear from the geometric properties of the central jet core that inlet velocity has little control on the width of the central jet since this is consistent across all cases presented. It is likely then that this property is governed by the inlet diameter as this is also a consistent geometric property across all the observed cases (0.008 m inlet diameter). The maximum height of the steady core is governed by the inlet velocity as demonstrated. Furthermore, it is shown that the dynamics of the jet, governed by the inlet velocity and inlet diameter, are the greatest control on the velocities evident in each case. In contrast, bed porosity plays a less influential role. It is interesting,

however, that the effect of the porosity on the jet height is not consistent between fast and slow inlet velocities. For the slow inlet velocity, a lower porosity bed has the effect of reducing the maximum height of the central core in comparison with the equivalent high porosity case. In contrast, for the fast inlet velocity, a lower porosity bed has the effect of increasing the maximum height of the central core in comparison with the equivalent high porosity case.

3.3.1.3 Quasi - steady state far from inlet

Above the established central core, the jet within the slow inlet velocity cases for both porosities has a tendency to dissipate to very small velocities. This occurs in all instances for the dataset captured from 300 s after the onset of fluidisation for the high porosity - slow inlet velocity case (Figure 3-11) and for all instances recorded in the quasi-steady state for the low porosity - slow inlet velocity case (Figures 3-12 and 3-13). The high porosity - slow inlet velocity case from 150 s after the onset of fluidisation (Figure 3-10) shows a tendency for the jet to deflect from the equilibrium position then dissipate with distance from the inlet but some cases have visible jets reaching the interface with the overlying water column (Figure 3-10, 151.25 s and 152.5 s). This reflects the qualitative data recordings for this case (Chapter 5.4.2), where the jet was observed to be very mobile above the central core and there were regular instances of fast moving parcels of fluid reaching the interface with the overlying water column as the jet migrated. The dissipation of the central jet is observed as a decrease in magnitude of the velocity vectors, this occurs in a small spatial region immediately above the central core. In the low porosity case the vertical distance over which the

dissipation of the velocities occurs is smaller than the high porosity case which exhibits a more gradual dissipation (see Figure 3-16, which has been magnified for clarity).

In the region far from the inlet it appears the porosity of the bed has a much greater influence on the velocity profile than is evident in the near-field. For the fast inlet velocity cases, all datasets show clear jets reaching the surface (Figures 3-8, 3-9, 3-14 & 3-15). However, the high porosity datasets are much more prone to deflections of the jet from the equilibrium position above the central core (Figures 3-8 and 3-9). These deflections are characterised by changes in lateral movement of the jet (e.g. see Figure 3-17). Figure 3-17 also captures the re-entrainment of downward-moving fluid into the upward moving jet. As noted in Section 3.3.1.2, the low porosity case does not demonstrate the same tendency of the jet to deflect and the central jet does not deviate from the equilibrium position (Figures 3-14 and 3-15). This tendency to maintain a central upward jet with minimal deviations is consistent with the broader qualitative observations in Chapter 6.

Despite the tendency to remain in the equilibrium position for the low porosity - fast inlet velocity case, there is a stronger recirculation of the particles on the left of the central jet, which is demonstrated more clearly in Figure 3-16. This is due to a heterogeneity in the developed fluidised zone not visible in the vector dataset but shown in the qualitative image in Figure 3-19.

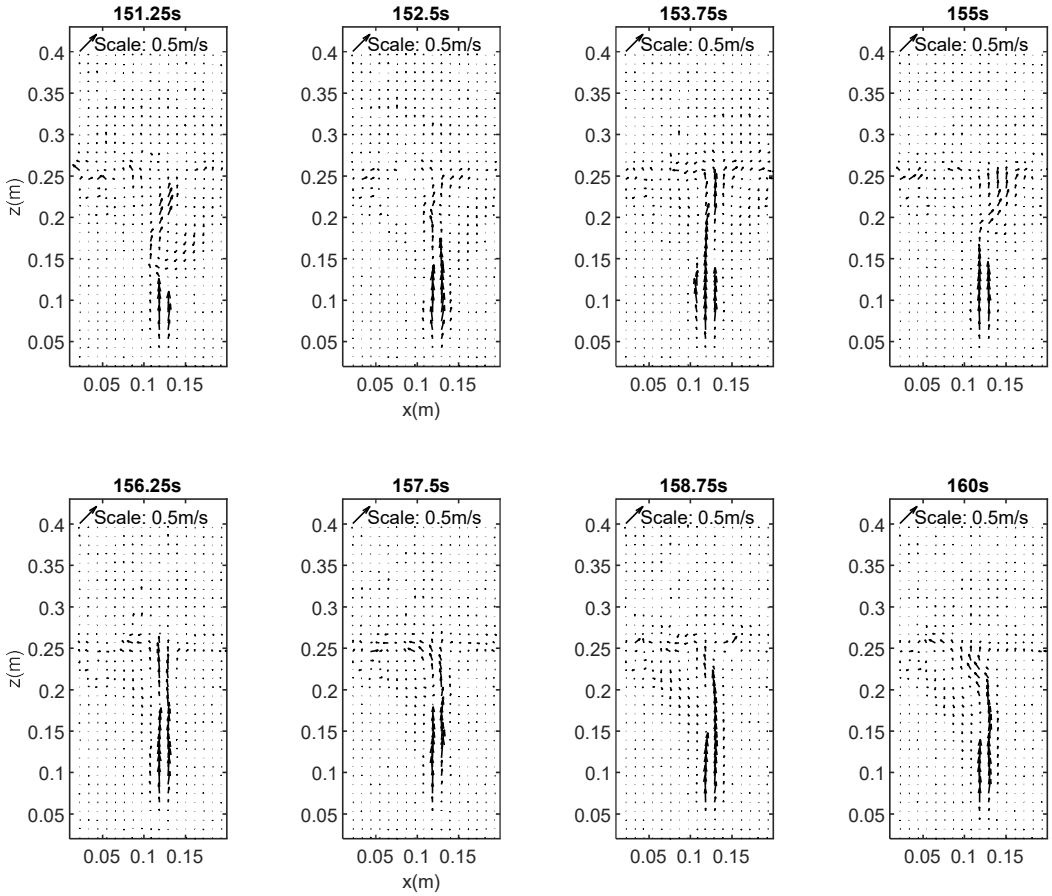

Figure 3-8 Instantaneous velocities of the quasi-steady state for high porosity - fast velocity bed (HF) commencing at 150s after the initiation of the fluid flow.

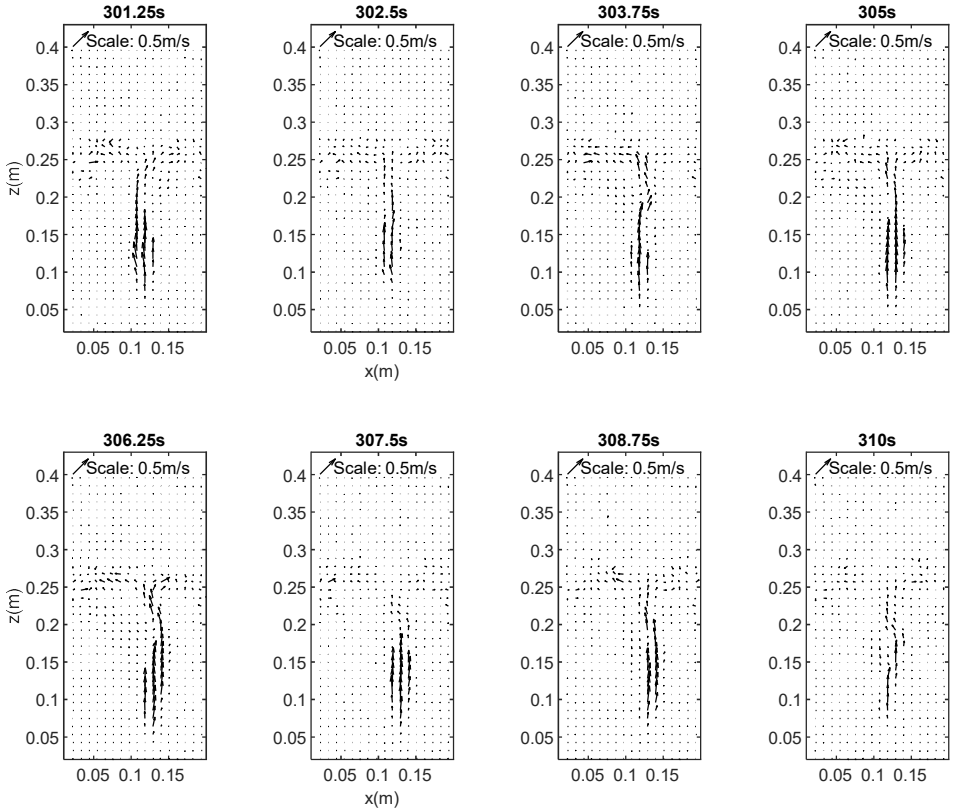

Figure 3-9 Instantaneous velocities of the quasi-steady state for high porosity - fast velocity bed (HF) commencing at 300s after the initiation of the fluid flow.

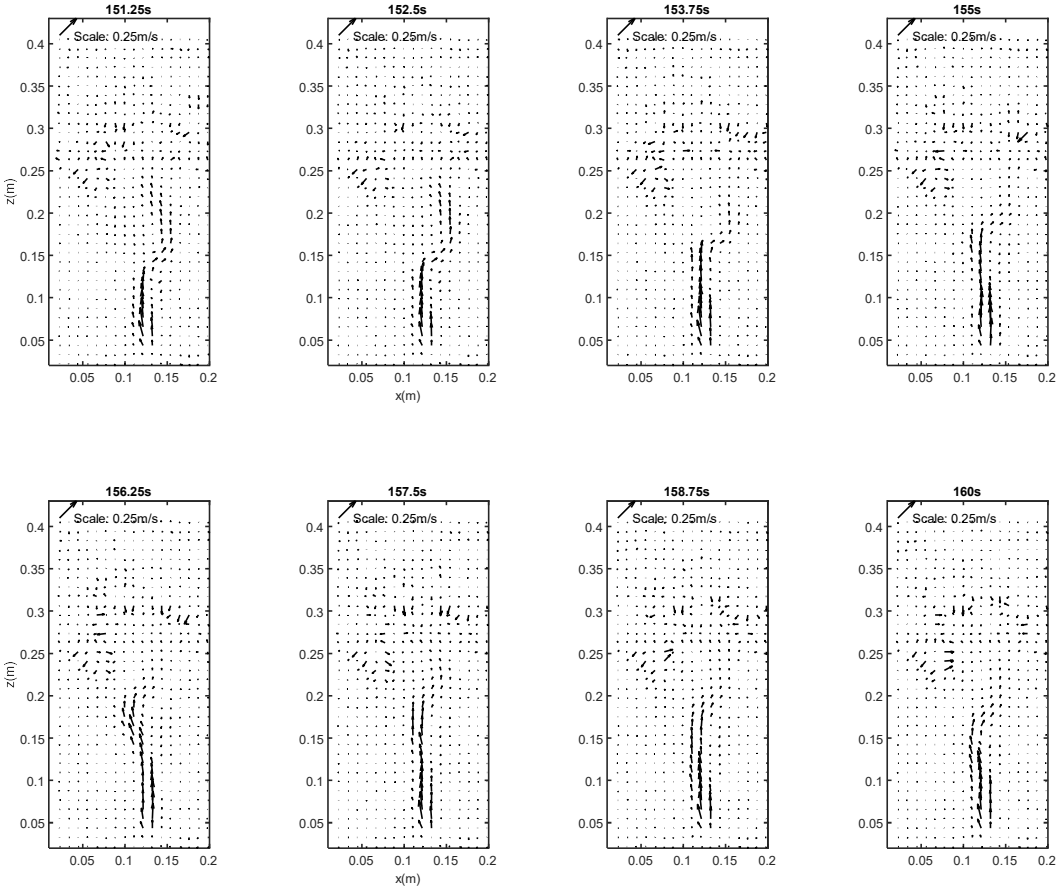

Figure 3-10 Instantaneous velocities of the quasi-steady state for high porosity - slow velocity bed (HS) commencing at 150s after the initiation of the fluid flow.

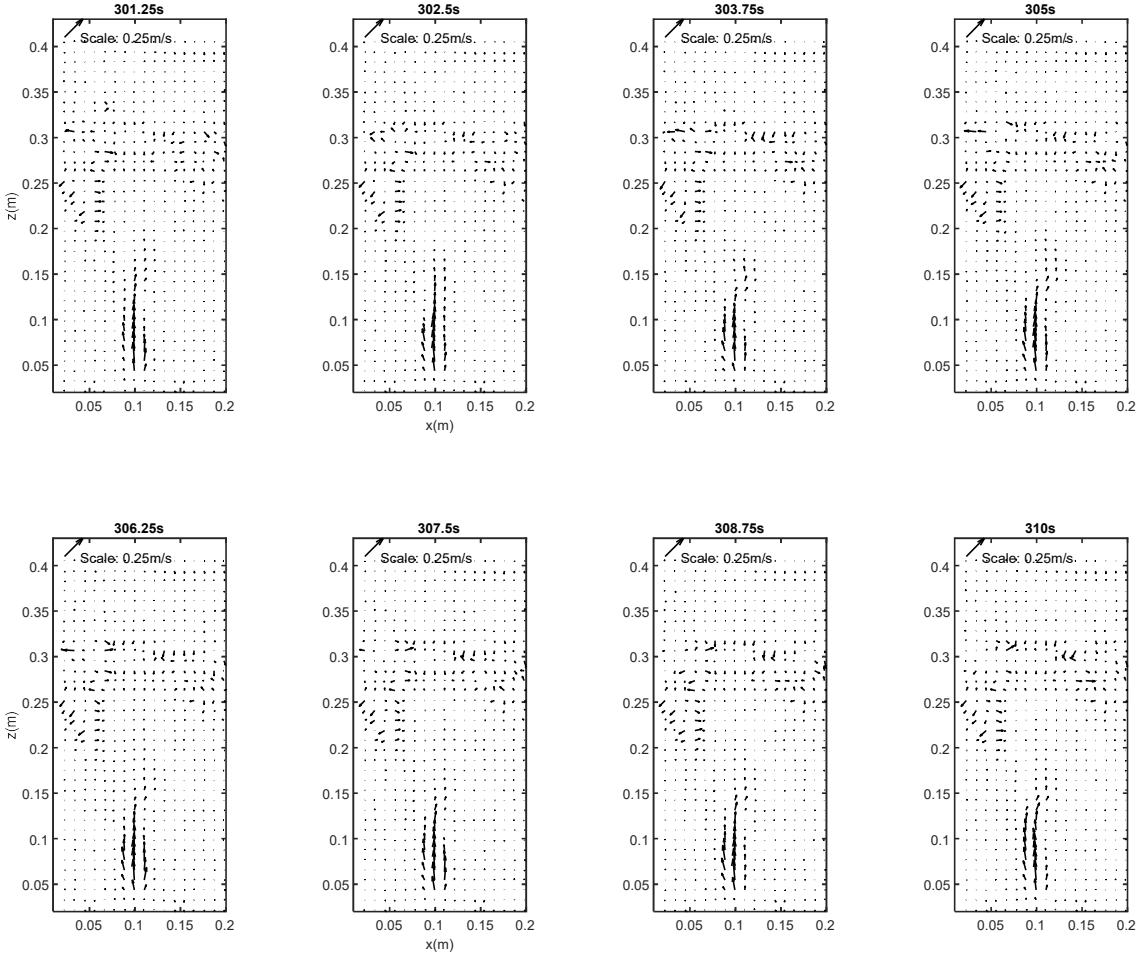

Figure 3-11 Instantaneous velocities of the quasi-steady state for high porosity - slow velocity bed (HS) commencing at 300s after the initiation of the fluid flow.

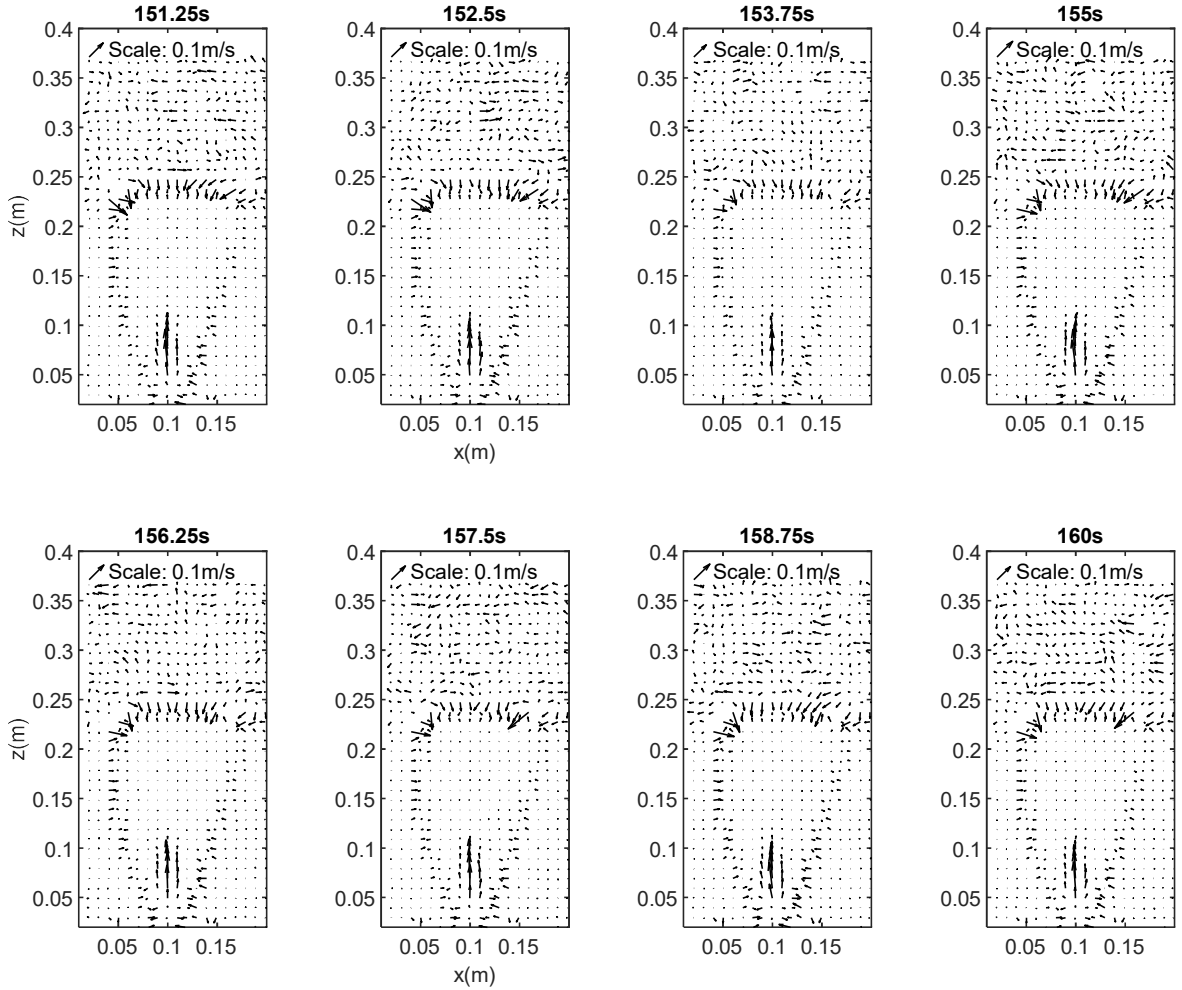

Figure 3-12 Instantaneous velocities of the quasi-steady state for low porosity - slow velocity bed (LS) commencing at 150s after the initiation of the fluid flow.

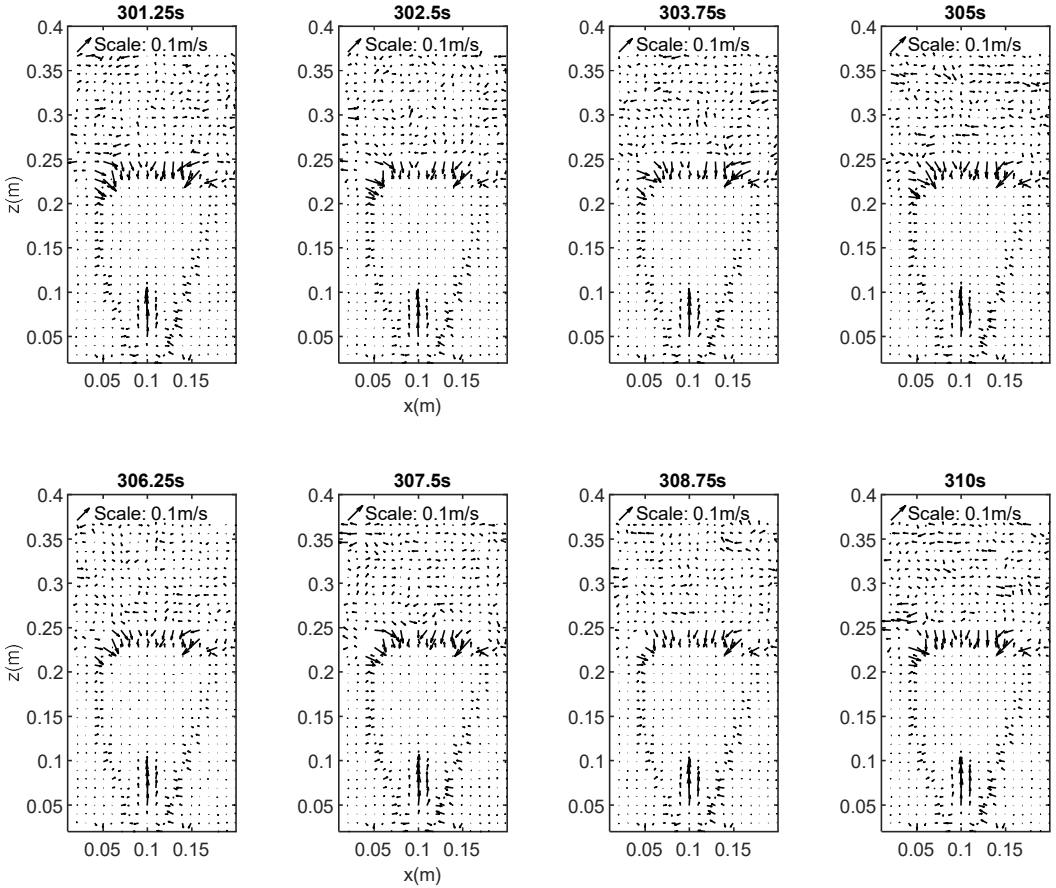

Figure 3-13 Instantaneous velocities of the quasi-steady state for low porosity - slow velocity bed (LS) commencing at 300s after the initiation of the fluid flow.

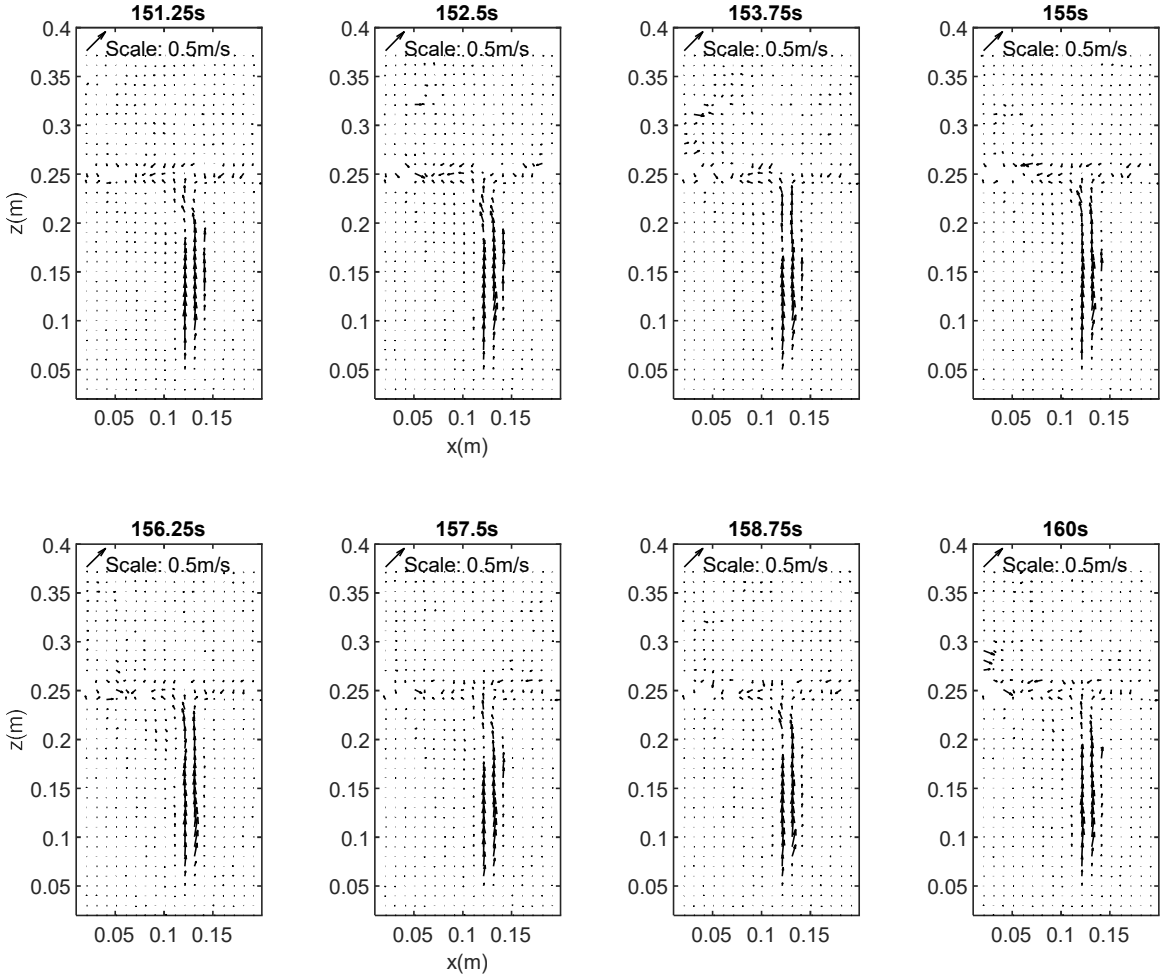

Figure 3-14 Instantaneous velocities of the quasi-steady state for low porosity - fast velocity bed (LF) commencing at 150s after the initiation of the fluid flow.

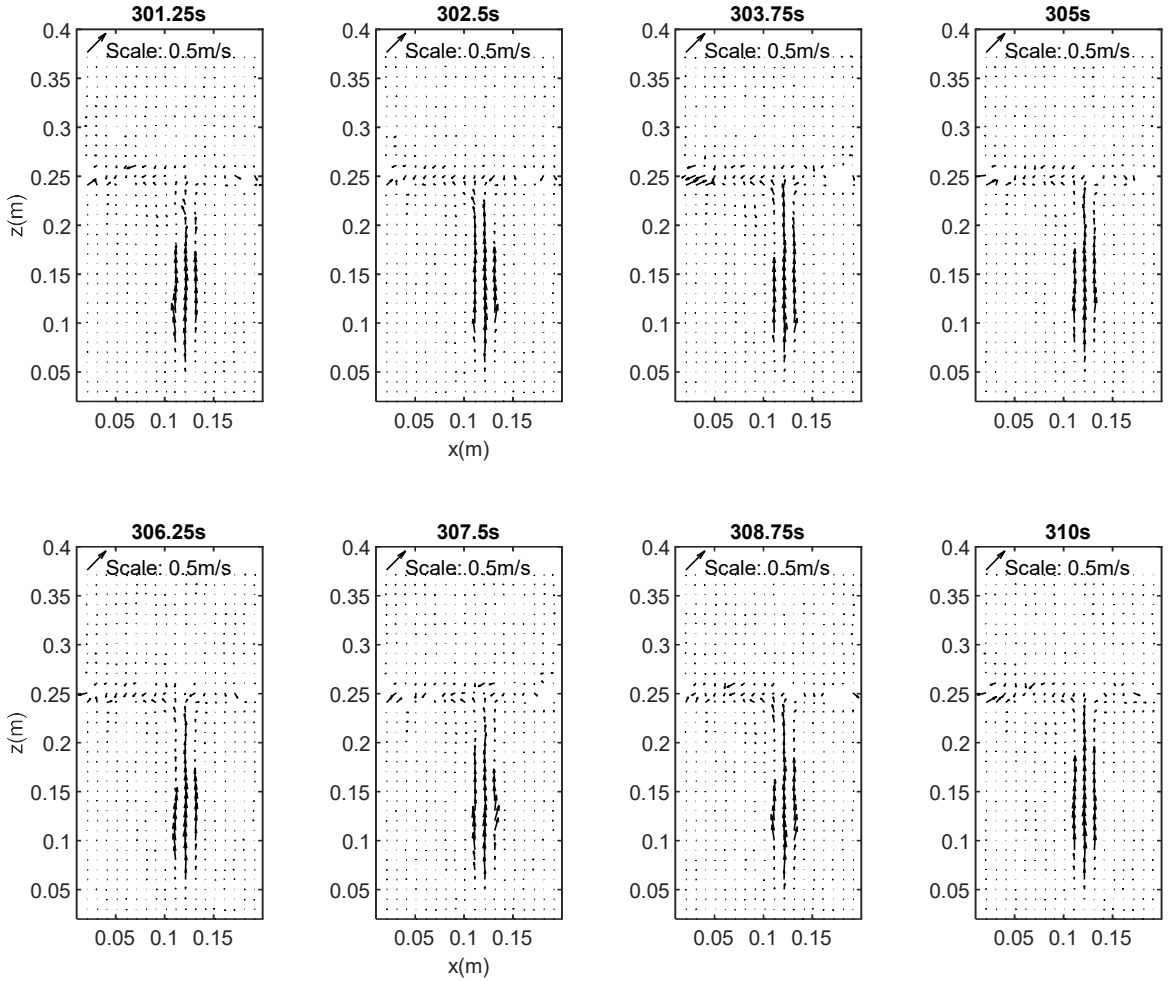

Figure 3-15 Instantaneous velocities of the quasi-steady state for low porosity - fast velocity bed (LF) commencing at 300s after the initiation of the fluid flow.

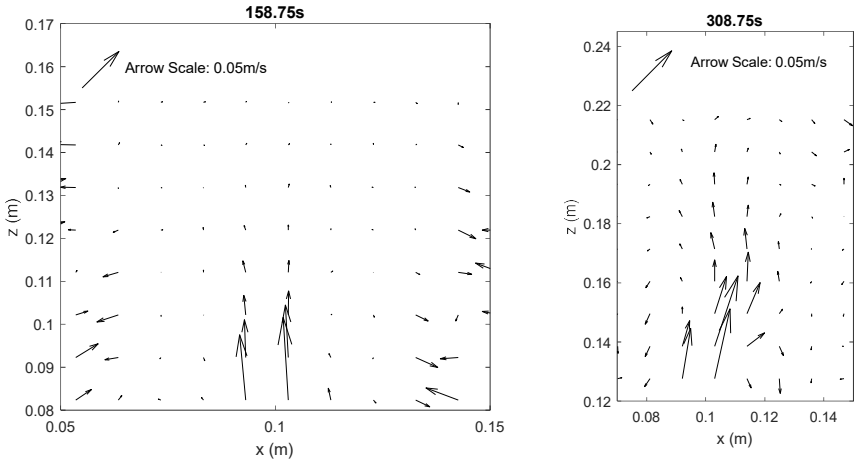

Figure 3-16 Instantaneous velocities for the quasi-steady state of the low porosity - slow inlet velocity case (LS) left and the high porosity - slow inlet velocity case (HS) right showing the top of the visible jet and the dissipation of the central core.

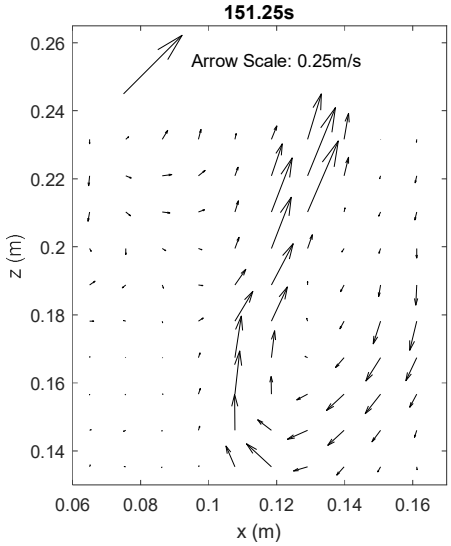

Figure 3-17 Instantaneous velocity vectors for high porosity - fast inlet velocity case showing a deflection of the central core at 0.18 m from the inlet.

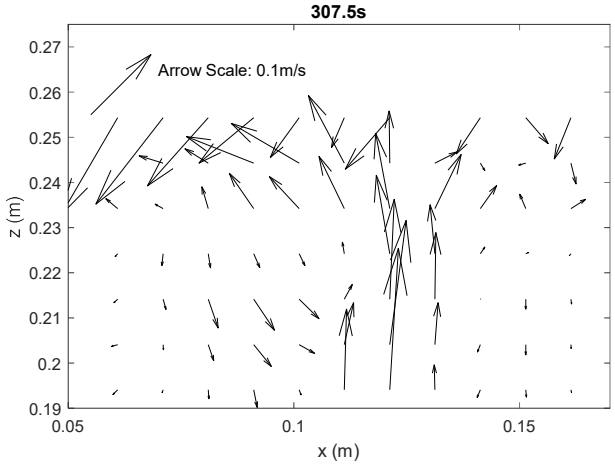

Figure 3-18 Instantaneous velocities for the quasi-steady state of the low porosity - fast inlet velocity case (LF) showing the recirculating flow at the interface with the overlying water column.

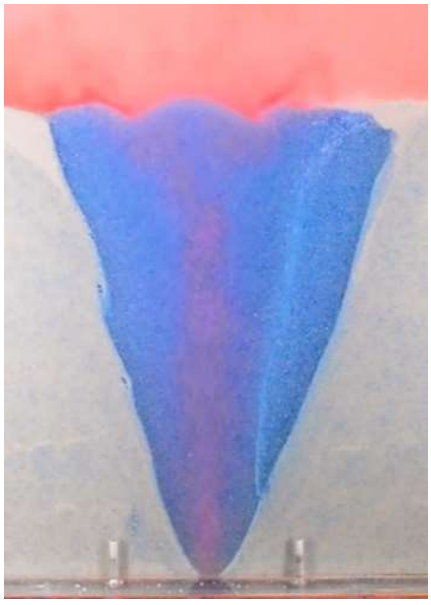

Figure 3-19 Image of the low porosity fast inlet velocity case showing the developed heterogeneity in the fluidised zone taken at 300s after the onset of fluidisation.

3.3.2 Mean Velocity Profiles.

When the flow reaches a quasi-steady state it is possible to characterise the velocity through mean velocity profiles. Velocities averaged over 10 s are presented in Figure 3-20 for 50, 100, 150, 200 and 250 mm above the inlet. One standard deviation from the mean is shown as an error bar on each of the plots. Velocities have been normalised by the mean inlet velocity measured by the flow meter and the radial position from the centre of the inlet by the inlet diameter. Across all runs, it is clear that the maximum velocity decreases with increasing height in the fluidised zone (Figure 3-20). However, for the fast inlet velocity cases, the mean velocities at 50 mm are significantly slower than those at 100 mm (Figures 3-20 HF_150s and 3-20 HF_300s).

The low porosity runs at both inlet velocities (LS and LF) exhibit negative velocities at a height of 250 mm at both 150 s and 300 s after the onset of fluid pumping (Figures 3-20 LS_150s, LS_300s, LF_150s and LF_300s). These runs showed high levels of elutriation of fine particles after extrusion, causing a reduction of the thickness of the fluidised zone. Therefore, the interface between the particle bed and the overlying fluid is no longer at 250 mm for the low porosity runs and the measurements taken at 250 mm are in a dilute flow above the fluidised zone. It is likely that negative velocities are larger particles falling back out of the dilute zone above the bed and into the fluidised zone again. Negative velocities are often visible to either side of the central high velocities, quantifying the downward recirculation of particles identified in Section 5.2.6. The magnitudes of the negative, downward-

directed velocities are significantly smaller than the upward-directed velocities (e.g., Figures 3-20 LF_150s and 3-20 HF_150s).

Interestingly, for the low porosity - slow velocity case, the velocity profile shows no upward velocity in the central fluidised zone at heights of 150 mm and 200 mm from the inlet (Figures 3-20, LS_150s and 3-20 LS_300s). This could be indicative of the cavity regime, where a fluidised cavity is overlain by a static particle bed (Philippe and Badiane, 2013). However, small positive mean velocities are evident at 0.04 m on the x-axis which could also indicate an asymmetrical fluidised region (Figure 3-20, LS_150s and LS_300s). The fastest velocities are recorded at 100 mm from the inlet for both of the high velocity cases (Figures 3-20, LF_150s and 3-19 LF_300s), whereas the fastest mean velocities are recorded at 50 mm from the inlet for the low velocity cases (Figures 3-20, LS_150s and 3-19, LS_300s).

In addition, for both bed porosities, the mean velocity profiles captured 300 s after the onset of fluid pumping show a reduction in velocities in comparison to mean velocity profiles captured 150 s after the onset of fluid pumping. This is barely perceptible for the low porosity - fast inlet velocity case (Figure 3-20, LF_150s and LF_300s) but is much more obvious on the high porosity - fast inlet velocity case (Figures 3-20 HF_150s and 3-19 HF_300s).

The mean velocity profiles shown in Figure 3-20 are comparable to typical velocity profiles obtained for a jet discharging into a fluid ambient (e.g. Pope, 2000; Cushman-Roisin, in press; Fig. 9.3 therein). Moving from proximal to the jet orifice to distal to the jet orifice, a typical turbulent jet initially has a potential core, with length 6-10 times the orifice diameter (Albertson et al., 1950), in which the fluid velocity is unchanged from that within the nozzle.

The shape of the velocity profile thus approximates a top hat. Downstream of the potential core, or “zone of flow establishment” (Albertson et al., 1950), the maximum velocity decreases exponentially with distance from the orifice (Fischer et al., 1979; Papanicolaou and List, 1988) and the velocity profile can be approximated by a Gaussian distribution multiplied by a stretching factor (Papanicolaou and List, 1988; Cushman-Roisin, in press). Entrainment of ambient fluid, enhanced by the formation of coherent turbulent structures at the shear layer between the jet and the surrounding fluid, dominate the flow processes in this “zone of established flow” (Albertson et al., 1950; Fischer et al., 1979; Papanicolaou and List, 1988). In the present experiments, only small scale turbulence is present since these large turbulent coherent structures are damped significantly by the high particle concentrations. Circular jets typically widen linearly with distance from the jet orifice (see Fischer et al., 1979 and many other studies), but the opposite occurs in the present study (Figure 3-20), with the high velocity region narrowing with distance. This, again, is attributed to the influence of the particles in the system. As the particles have a negative buoyancy in the system, the fluid velocity must exert sufficient drag force on the particle to exceed the buoyant weight of the particle. Thus the velocity profile is necessarily damped at all points where particles are present. Once the jet velocity has diffused to a point where the velocity acting in the dominant upwards direction is less than the required velocity to carry a particle the velocity profile becomes negative as at these points the particles are falling (Figure 3-20, HF-150 the profile at 200 mm demonstrates this particularly well).

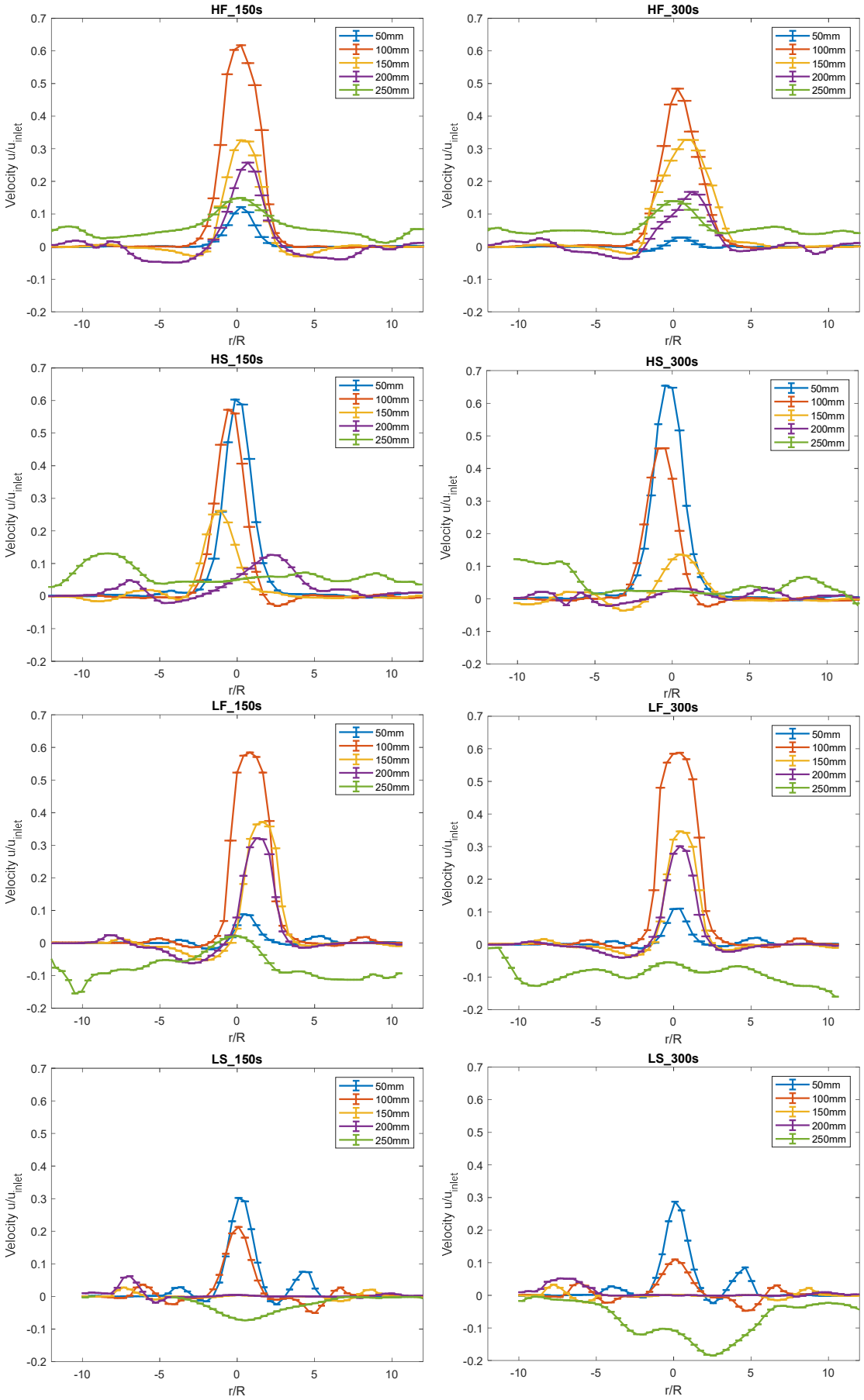

Figure 3-20 Mean velocity profiles over 10 s for the quasi-steady state taken at 50 mm, 100 mm, 150 mm, 200 mm and 250 mm from the base of the tank. One standard deviation error bars are shown.

3.3.3 Peak velocity and propagation of the fluidisation event

The temporal evolution of the location of each peak velocity within the initial bed height was identified (Figure 3-21). During the void development phase (HS_0s, HF_0s, LS_0s, LF_0s), the peak velocity occurs within the void space. The location of the peak velocity subsequently propagates upwards, tracing the advancement of the void (shown most clearly in LF_0s). HF_0s has a shorter time to extrusion so also captures the advancement of the peak velocity following the void space and the beginning of the turbulent mixing phase (See Chapter 5.2.1). Figure 3-22 shows the height of the fluidisation event over time, this is measured as the greatest height at which a fracture or propagating void space can be identified in the bed. Both of the slow inlet velocity cases (HS and LS) show a broadly linear propagation of the void space over the 10 s measurement period. The low porosity – fast inlet velocity case (LF) follows the same propagation rate as the slow inlet velocity case (LS) for the first 2.2 s before the rate of propagation increases steeply. At 5.2 s and 6 s the rate of increase slows marking points at which the void space expands laterally. The high porosity – fast inlet velocity case (HF) advances linearly until 7.2 s where the rate of propagation increases with proximity to the free surface. It is noted that, when comparing Figure 3.21 and 3.22 the peak velocity is often at a lower height than the advancing fluidisation front indicating that the peak velocity is within the jet channel or void not at the interface between the jet or void and the undisturbed bed.

The quasi-steady state cases (150 s and 300 s from onset of fluid pumping) show that the location of the peak velocity is confined to a small region in each case. The peak velocities show some variability in the lateral direction

and fall within 10-36 mm of the central axis of the inlet (approximately 1 to 4 times the inlet diameter) (Table 3-6). The greater spread of the location of the peak velocity in the lateral x-direction is seen in the faster inlet velocity cases (e.g. Figures 3-21, LF and HF). It is evident that the peak velocities in the quasi-steady state can only occur in the central core, as described in section 3.3.1.2. The regions where the peak velocity can occur outline the central core and this could be used as a means of determining the location in the fluidised zone where the dynamics are governed by the characteristic properties of the jet rather than the bed characteristics.

Table 3-6 Mean and standard deviations of the vertical distance of the peak velocity from the inlet and the horizontal range of the peak velocity for each dataset.

Run	Mean vertical distance of Peak Velocity from inlet (m)	Standard deviation of vertical distance of peak velocity from inlet (m)	Range of location of peak velocity in the X direction (m)
HS_150s	0.0720	0.0095	0.015
HS_300s	0.0657	0.0069	0.015
LS_150s	0.0642	0.0042	0.010
LS_300s	0.0643	0.0053	0.010
HF_150s	0.1009	0.0153	0.029
HF_300s	0.1182	0.0152	0.036
LF_150s	0.1060	0.0106	0.017
LF_300s	0.1021	0.0112	0.027

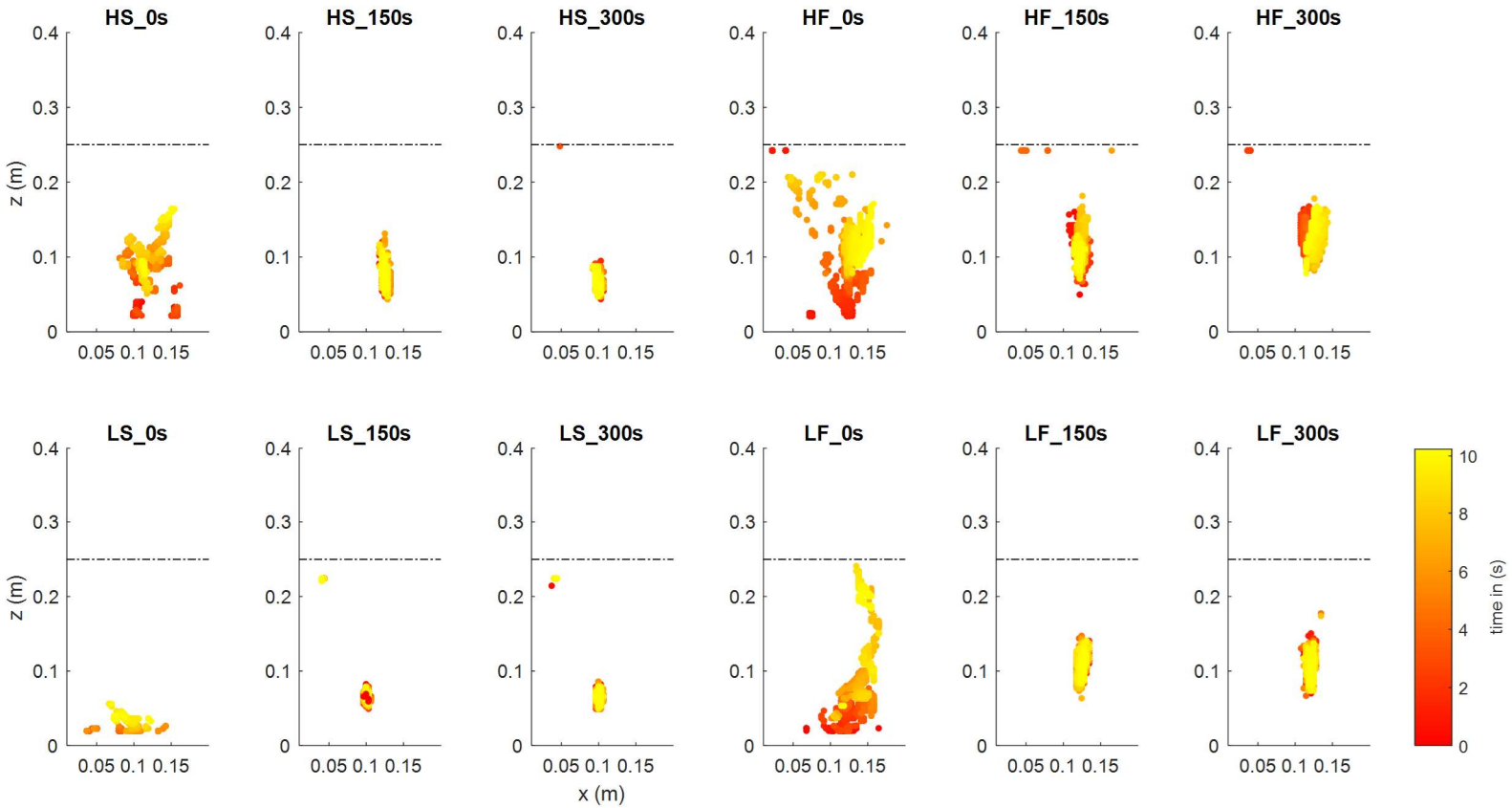

Figure 3-21 Locations of the peak velocity within the original bed height. Points are coloured by timestamp with earliest points coloured red and latest timestamps yellow. Dashed-dotted black line indicates initial height of sediment bed at the start of the experiment.

3-

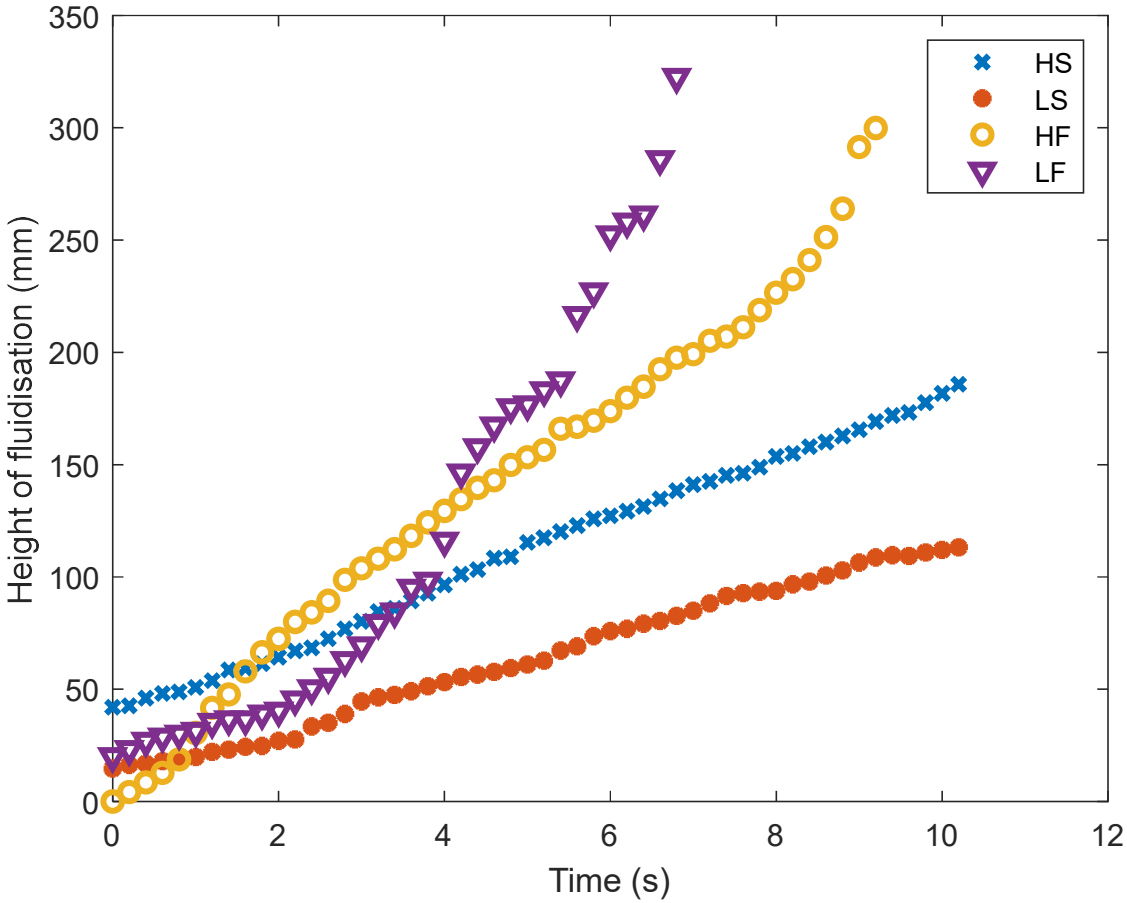

Figure 3-22 Height of fluidisation event against time. HS and LS did not reach extrusion over the 10 s measurement period.

3.4 Turbulence analysis

3.4.1 Local Reynolds number

Reynolds number is often used to determine the flow regime within a system and is calculated as $Re = \frac{\rho U l}{\mu}$, where ρ is the density of the fluid (kg m^{-3}), U is a characteristic velocity (m s^{-1}), l is a characteristic length scale (m) and μ is the dynamic viscosity of the fluid (kg $m^{-1}s^{-1}$). As the system has multiple zones of fluid flow, the local time-averaged velocity has been used to calculate a local Reynolds number at each data point in the system. The time-averaged velocity is only meaningful once the system has reached a quasi-steady state and so spatial variations of local Reynolds number are presented for the 10 second duration datasets taken at 150 s and 300 s for each configuration (Figure 3-23).

The high porosity - fast inlet velocity (HF) case shows a region of higher Reynolds number, indicating higher turbulence in the turbulent zone, at 150 s than in the wider turbulent zone visible at 300 s (Figures 3-23, HF_150s and HF_300s). Although the low porosity - fast inlet velocity (LF) case shows comparable Reynolds numbers (Figure 3-23, LF_150s and LF_300s), the turbulent zone does not widen over time and as such the turbulence is of comparable intensity at 300 s as at 150 s (Figure 3-23, LF_150s and LF_300s). The LF cases also show turbulence of a greater intensity at a greater distance from the inlet in comparison to the high porosity case (HF) (Figure 3-23, HF_150s and HF_300s). Conversely, there is a greater intensity of turbulence in the high porosity cases (HS) than the low porosity cases (LS) for the slow inlet velocity cases and this persists for a greater

height from the inlet (Figure 3-23, HS_150s, HS_300s, LS_150s and LS_300s).

It is noted that a single length scale has been used across the system as is usual with a Reynolds number approach (Di Felice, 1995; Tritton, 2012). As the length scale is the inlet diameter this is consistent across all experimental runs, as is the density and viscosity properties of the particles and the fluids respectively. The local Reynolds plots are therefore a scaling of the local velocity. Using an alternate Reynolds number, such as the particle Reynolds number, would have the same effect. The particle Reynolds number uses the particle diameter as the length scale. The particle Reynolds number varies from 62 for the smallest particles to 499 for the coarsest particles used herein. It Is noted that this approach defines two particle Reynolds numbers for each system measured however still does not sufficiently describe the localised dynamics. Further, as the Re_p in all cases is much greater than unity, and the surrounding flow is not dilute an alternate dynamical number, such as the Stokes number which describes creeping or viscous flow, will also not sufficiently describe the localised flow regimes.

The system is known to vary in space and time. Consequently, the appropriate length scales and pseudo-fluid viscosity also vary across the system and so a local Reynolds scaling to characterise this system should be able to account for the local variations characteristic of each of the measured beds. It is proposed that for a system similar to those measured herein, with multiple particle classes and localised fluid behaviours an appropriate scaling would be able to define both the local pseudo-fluid viscosity and an appropriate local length scale. To quantify the pseudo-fluid

viscosity using the equations in Section 2.6.2 would require knowledge of the concentrations of each of the particle classes in a particular region. For a local characteristic length scale, an average separation distance between particles could be appropriate. However, the measurement of both such quantities would require an experimental arrangement capable of distinguishing between the two species of particle in the concentration data and tracking large volumes of particle locations. This could possibly be achieved through refractive index matching and particle laser induced fluorescence methods but is not attainable through the experimental arrangements detailed herein.

.

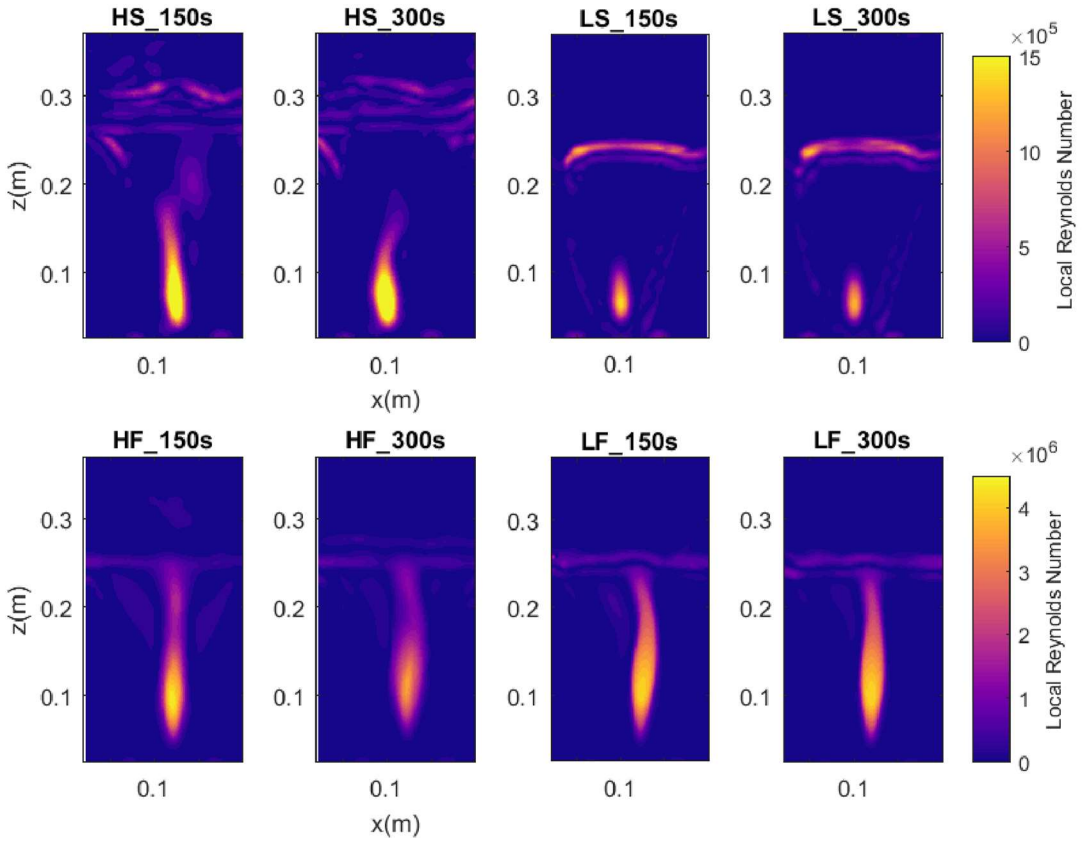

Figure 3-23 Plots showing the local Reynolds number for the quasi-steady state datasets. Note the differing contour scales across the slow and fast inlet velocities.

3.4.2 Lateral velocity gradients in the quasi-steady state

The lateral velocity gradients are shown as a positive or negative velocity gradient (Figures 3-24 to 3-31). The sign of the velocity gradient indicates if the velocities are increasing or decreasing laterally with left to right representing the positive direction. The maxima of the velocity gradients for the low porosity, fast inlet velocity cases demonstrate the region of transition between the fast upward moving flow and the much slower falling particles (Figures 3-24 and 3-25). The minima between the two maxima in each frame represents the location of the maximum velocities in the upward moving jet. The central minima of the jet is not a consistent width across the flow field, for example at 151s in Figure 3-24 the region of minimum velocity gradients is approximately 3 mm at 0.11 m from the inlet but then narrows above this region. The location where the velocity gradient is a minimum between the two regions of maximum velocity gradients demonstrates the locations in the flow field where the upward moving flow is more homogenous and there is little variation in the velocity field.

There is also variation in the regions of maximum velocity gradients, 154 s is a good example (Figure 3-24). A narrow region of positive velocity gradient maxima is shown in red. The negative gradients, shown in blue, are much wider and show more variation in the intensity of the lateral velocity gradients. The wider region of velocity maxima shows where there is greater turbulent mixing on this side of the jet and more entrainment of the downward falling slow particles with the rapid upward moving jet.

The low porosity cases in Figure 3-24 and 3-25 show little variation in the magnitude of the velocity gradients with height from the inlet, however for the high porosity fast inlet velocity cases (Figures 3-26 and 3-27) some timestamps show much more variation with height, though interestingly, not all. Figure 3-26, 151 s – 153 s shows similar characteristics to the low porosity cases in the region closes to the inlet, however in the upper half of the bed (above 0.11 m from the inlet at 151 s and above 0.18 m above the inlet for both 152 and 153 s) we see variations in the behaviour. At 151 s the velocity gradient maxima have lower magnitude than the lower bed and the edges of the higher magnitude gradients are less clearly defined. At 152 s, above approximately 0.18 m from the inlet, the regions of the maxima follow a clearer path but show significantly lower magnitudes than the velocity gradient magnitudes close to the inlet. At 153 s a wider region of high magnitude velocity gradients is visible and also higher magnitudes in comparison to the previous timestamp at 152 s. Following this, at 154 s, the velocity gradients behave much more like the channelised flow of the low porosity fast inlet velocity cases (Figure 3-24 and 3-25). This shows that in the upper bed of the high porosity fast inlet velocity case there is a lot of variation in the jet behaviour, notably In terms of the rate of change of the velocities across the flow field. At 152 s (Figure 3-26), there is a low rate of change of velocity across the flow field, whilst at 154 s there are rapid and large rates of change of velocity in the upper bed. This reflects the points where the chaotic jet in the upper bed is more spread laterally across the flow field and thus more diffuse, and when it is narrower and focussed, respectively. These temporal changes in the bed far from the inlet are due to the interaction of the upward moving jet with the heterogenous particle field.

Furthermore there is a variation between the 150 s data set and the 300 s data set for the high porosity fast inlet velocity case in that at 300 s (Figure 3-27) the behaviour of the velocity gradients is less variable between timestamps and more closely aligned to the low porosity fast inlet velocity case (Figures 3-24 and 3-25). This indicates that the chaotic jet becomes more stable between 150 s and 300 s and there is less interaction between the falling particles and the upward moving jet. The gradual reduction in chaotic behaviour of the jet likely indicates that between 150 s and 300 s the particle migration of the smaller particle class becomes less dominant on the flow behaviour.

The high porosity slow inlet velocity cases (Figures 3-28 and 3-29) also demonstrate different behaviours in the lower and upper bed. Between 150 s and 155 s the velocity gradients marking out a strong channel in the jet region grow in height from the inlet over time. At the top of the jet region is a deflection from the equilibrium position. The deflected jet is marked out by regions of visible velocity gradients but they are significantly lower in magnitude than in the jet region. The deflected jet behaviour in the 300 s dataset (Figure 3-29) is greatly reduced in comparison to the dataset collected at 150 s. Slight deflections of the jet from the equilibrium position are visible in the gradients but above the first visible deflection point of the jet there are barely any distinct areas of velocity gradients indicating the upper bed has stabilised into a homogenous region of diffuse flow (Figure 3-29).

Distinct from the previously discussed cases the low porosity slow inlet velocity shows little development between 150 s (Figure 3-30) and 300 s

(Figure 3-31) datasets. The magnitudes of the velocity gradients displayed are smaller and the maximum height at which the channelised jet region reaches is 0.1 m from the inlet. Above the jet region there are no distinct regions of velocity gradients indicating homogenous diffuse flow in this area. This is mostly due to the much higher particle concentration in this case acting to diffuse the velocity gradients across the bed.

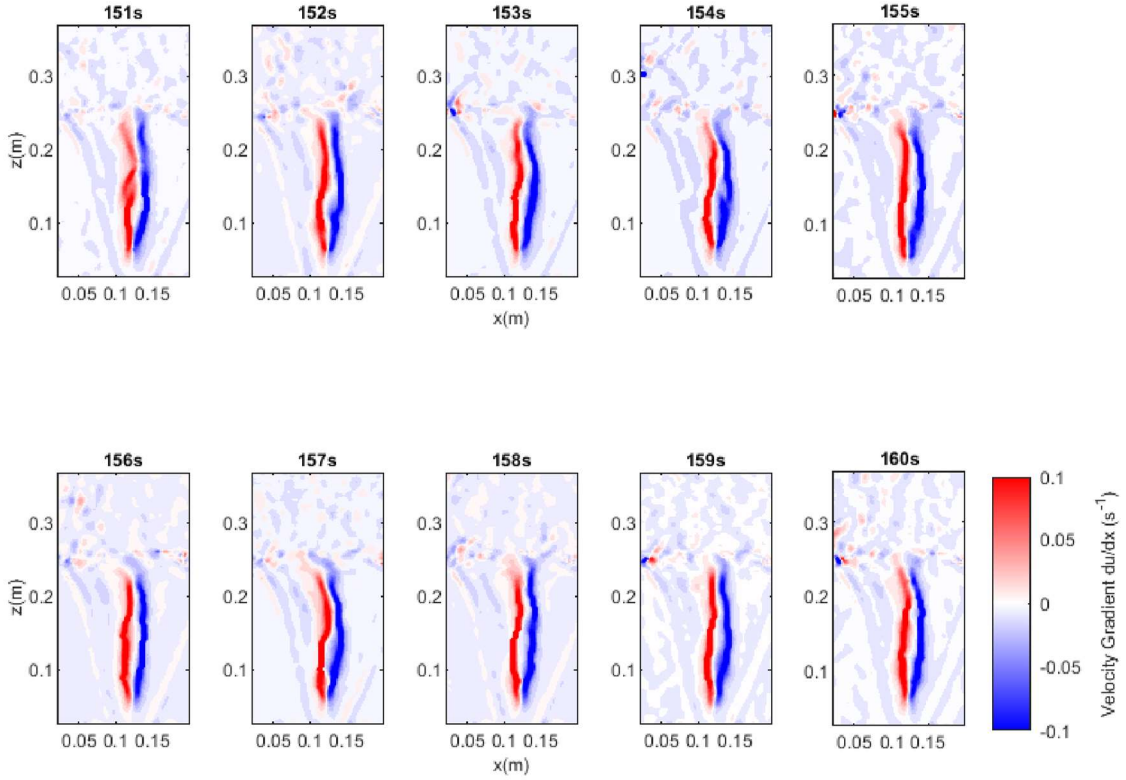

Figure 3-24 Velocity gradients for the low porosity, fast inlet velocity case between 150 and 160 seconds after initiation of fluid flow (LF_150s).

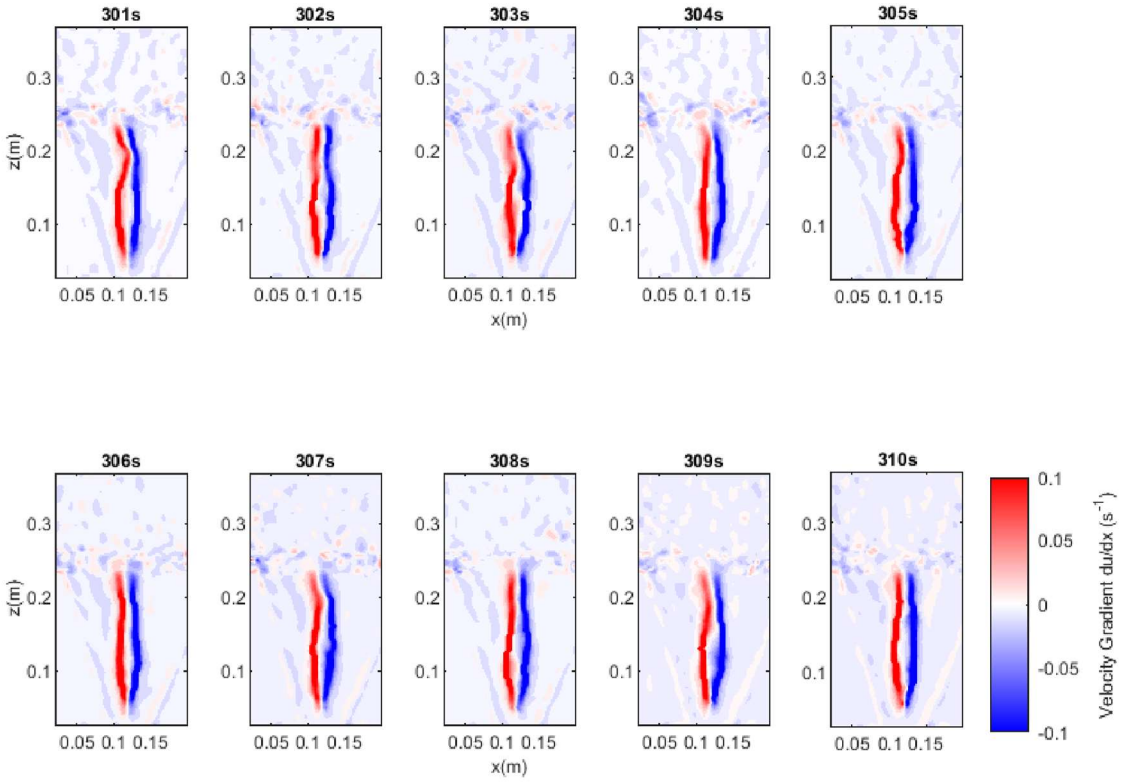

Figure 3-25 Velocity gradients for the low porosity, fast inlet velocity case between 300 and 310 seconds after initiation of fluid flow (LF_300s).

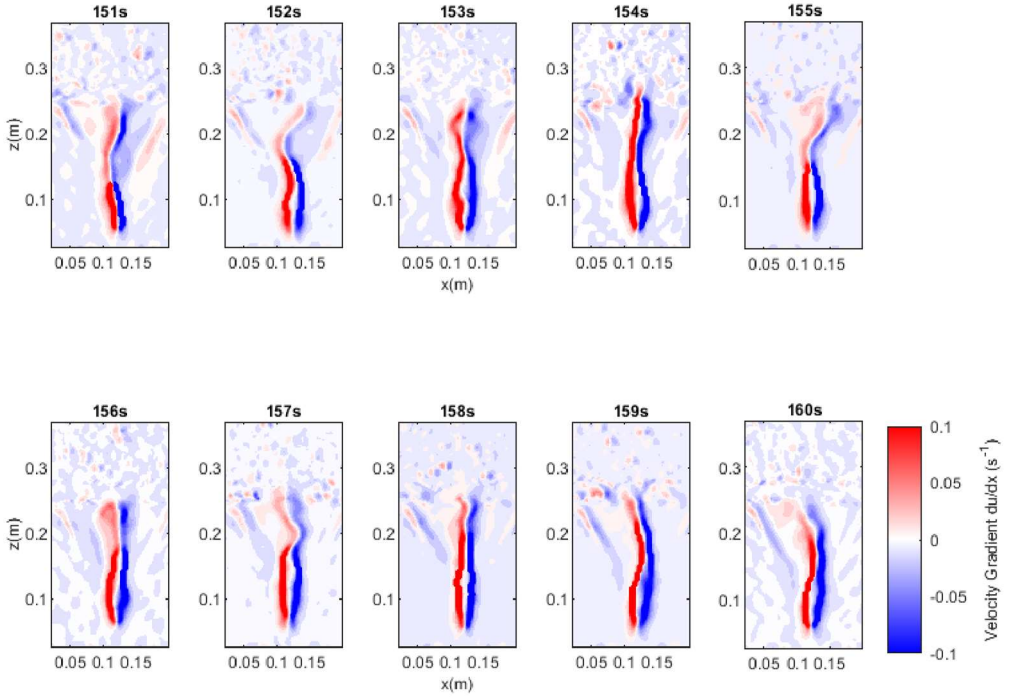

Figure 3-26 Velocity gradients for the high porosity, fast inlet velocity case between 150 and 160 seconds after initiation of fluid flow (HF_150s).

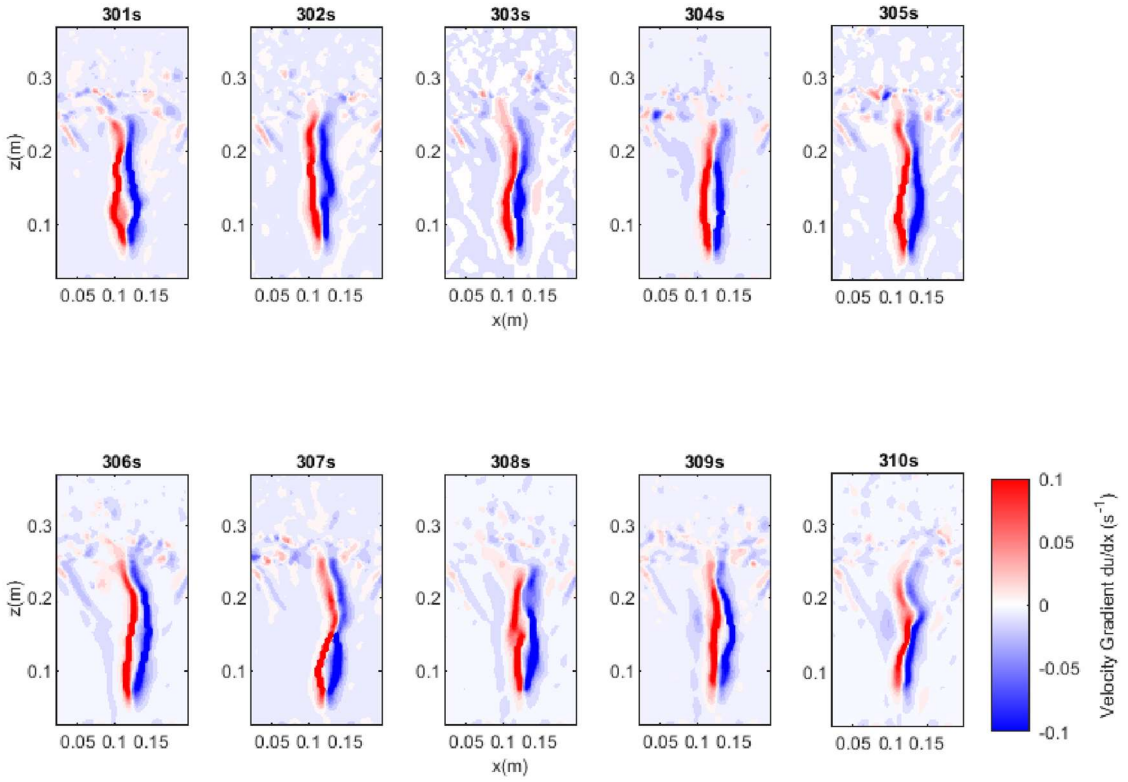

Figure 3-27 Velocity gradients for the high porosity, fast inlet velocity case between 300 and 310 seconds after initiation of fluid flow (HF_300s).

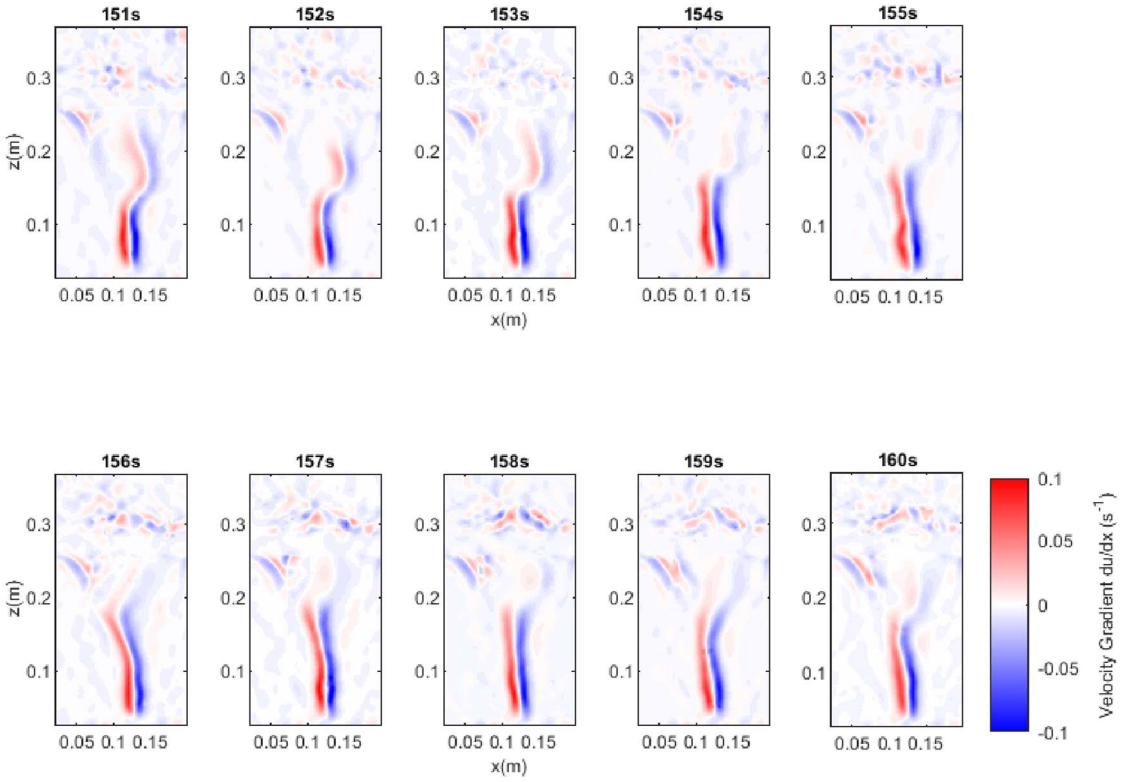

Figure 3-28 Velocity gradients for the high porosity, slow inlet velocity case between 150 and 160 seconds after initiation of fluid flow (HS_150s).

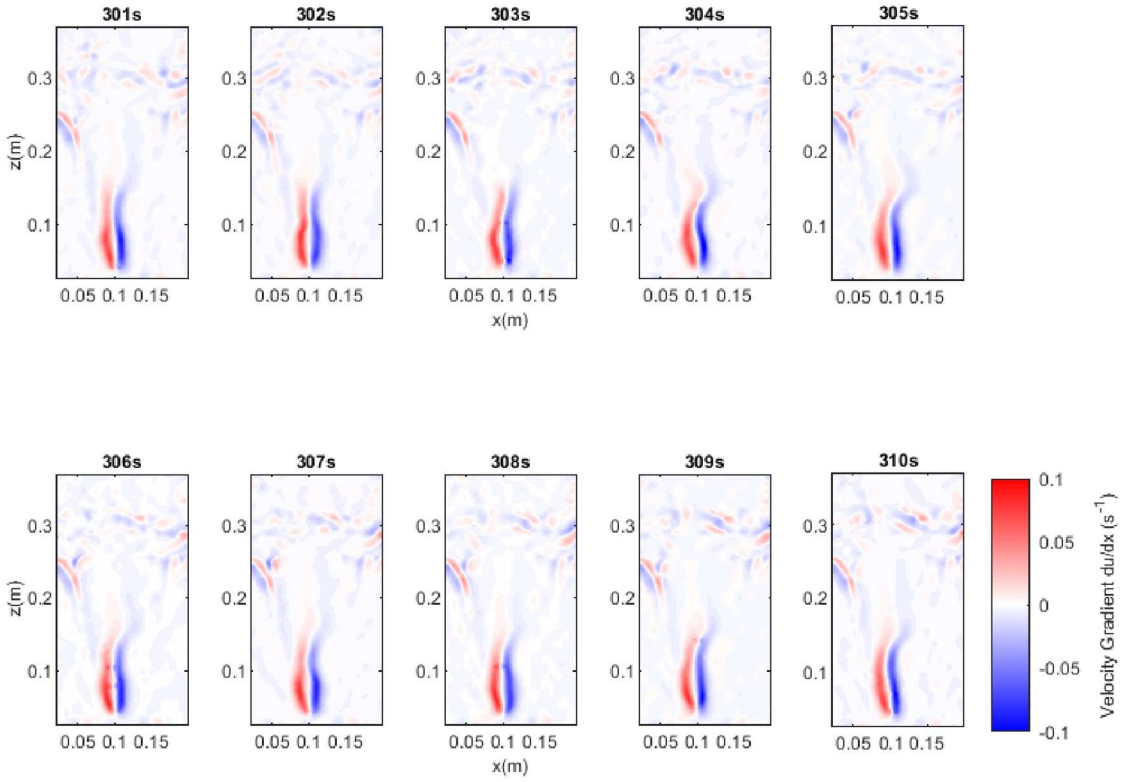

Figure 3-29 Velocity gradients for the high porosity, slow inlet velocity case between 300 and 310 seconds after initiation of fluid flow (HS_300s).

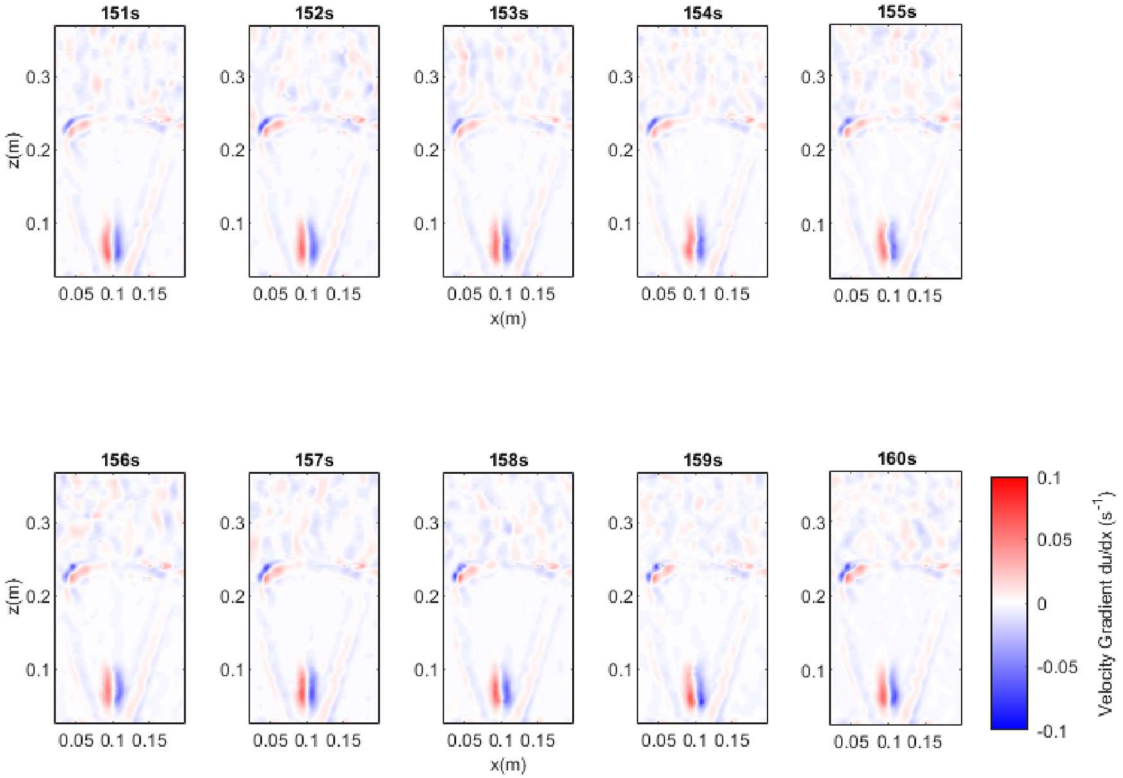

Figure 3-30 Velocity gradients for the low porosity, slow inlet velocity case between 150 and 160 seconds after initiation of fluid flow (LS_150s).

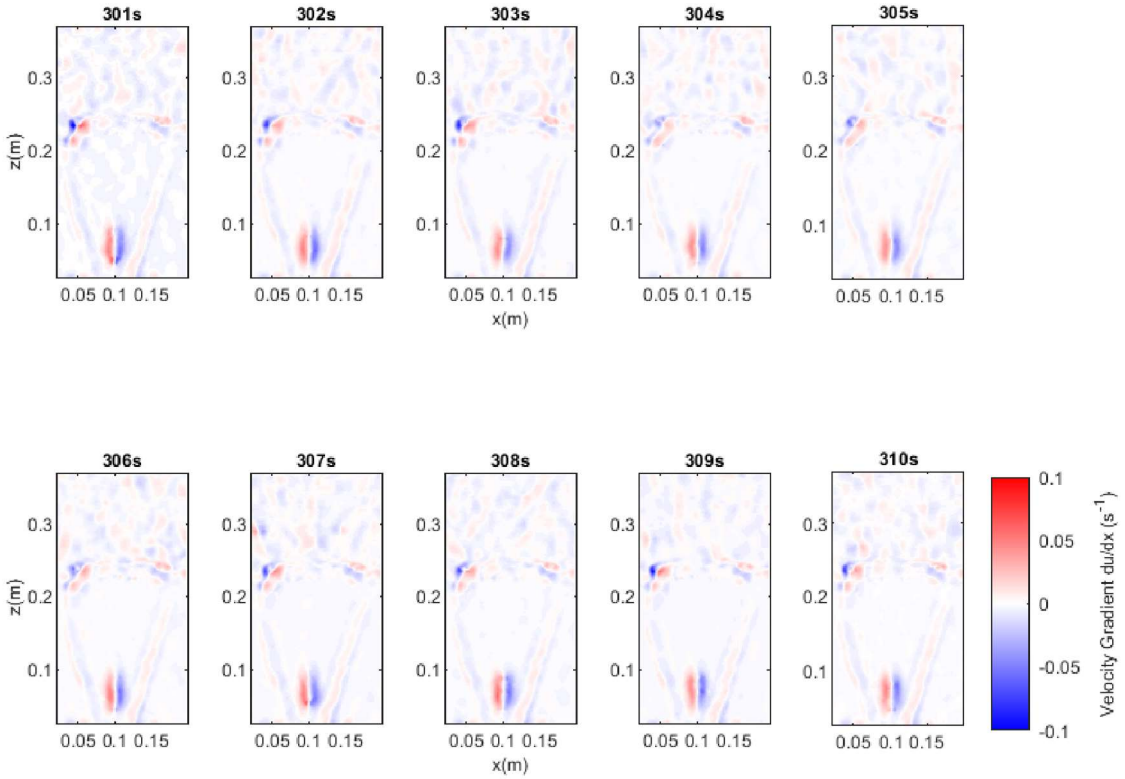

Figure 3-31 Velocity gradients for the low porosity, slow inlet velocity case between 300 and 310 seconds after initiation of fluid flow (LS_300s).

3.5 Discussion

3.5.1 Flow regimes in the fluidised zone

In the case of monodisperse unconfined beds, three fluidisation regimes are acknowledged in the literature: the “static” regime, the “cavity” regime and the “chimney” regime (Philippe and Badiane, 2013; Mena et al., 2017, 2018). The static regime occurs when there is a slight expansion of the bed initially then flow occurs exclusively through the pore spaces. The cavity regime has a region of particles in motion directly above the inlet but only for a proportion of the bed and the remainder of the bed is in the static regime. The chimney regime has a column of moving particles from the fluid inlet to the free surface above the bed. The works of Philippe and Badiane (2013) and Mena et al. (2018) represent the onset of fluid flow in a monodisperse bed, and also demonstrated that the cavity regime was in itself, transient and if left for a sufficiently long period of time would develop into the chimney regime (Mena et al., 2018).

In the geological literature, the debate focusses around evidence for turbulent or laminar flow regimes in the particle bed during fluidisation (Scott et al., 2009; Ross et al., 2011; Hurst et al., 2011; Cobain et al., 2015). The cases tested in this set of experiments demonstrate much more heterogeneity across the fluidised region than can be captured by attributing a single regime across a whole bed. There is both an observable difference in the turbulence characterised by the Reynolds Number that can be demonstrated across the flow field laterally (Figure 3-22) and differences in the characteristics across the flow field with distance from the inlet

demonstrated by the velocity fields (Figures 3-7 to 3-14) and the velocity gradients (Figures 3-23 to 3-30). The variations across the flow field exhibit behaviours more akin to jet dynamics in the near field region and more variable regimes in the far field region with the variability attributed to the bi-disperse bed mixtures and the influence of the changing porosities within the bed spatially and temporally.

In all cases, there was a region of fast, upward-moving, turbulent flow close to the inlet. Only in the low porosity - fast inlet velocity case did this zone reach the interface with the overlying water column and establish something comparable to the “chimney” regime (Figure 3-13 and 3-14). The low porosity - slow inlet velocity case perhaps most resembled the “cavity” regime, displaying a turbulent core overlain by a very slow velocity zone between the “cavity” and the interface between the fluidised bed and the overlying water column (Figure 3-11 and 3-12). However, the particles were still in motion, albeit orders of magnitude slower than within the turbulent zone (Figure 3-15).

Intuitively it would be expected that the bi-disperse beds that resemble more closely a monodisperse bed would behave more like the experiments of Philippe and Badiane, (2013) and Mena et al., (2017). Herein, it is observed that the low porosity bed mixes behave comparably to the monodisperse experiments and the high porosity bed mixes do not. This is attributed to the changing concentrations across the bed over time, which adds more complexity to the system than can be observed in a monodisperse bed. Consequently, the previously observed regimes can only partially describe the flows across the whole domain in a bi-disperse bed.

Here the regimes present within a fluidisation event are analysed by flow region, in order to assess the influence of bed type. The flow is broken down into three characteristic regions: a jet region, a supra-jet region and a recirculating region.

3.5.1.1 Jet region

The geometry of the inlet and the velocity of the fluid flowing into the system appears to dominate the flow near the inlet in all cases. That is, the diameter of the inlet characterises the maximum width of the fast upward-moving flow (Section 3.3.1), and the mean velocity at the inlet characterises the maximum height of the fast upward-moving turbulent flow (Section 3.3.1), herein referred to as the “central core”. Bed porosity has a secondary influence on the height of the central core (Section 3.3.1). The central core occurs in all the observed cases of fluidisation to a greater or lesser extent – it was not possible in this set of experiments to fluidise the bed without a turbulent central core.

The central core is identified as the region of fast moving upward flow, with a central minimum in velocity gradient flanked by a region of velocity gradient maxima to either side, demonstrating the boundary of the fast upward moving flow with the slow moving falling particles. The peak velocity of the fluidisation event occurs only after the quasi-steady state has been reached; the calculated Reynolds number indicates that the flow in this region is firmly in the turbulent regime. The scale and dynamics of the central core are governed by the dynamics of the jet at the inlet to a much greater extent than any characteristics of the bed.

In Chapter 5, it is shown that the initiation of fluidisation varied across porosities, with low porosity beds displaying behaviour resembling hydraulic fracture and void development and high porosity beds showing more turbulent mixing and entrainment. Despite large differences caused by the porosities in the early development of the fluidised bed, porosity does not appear to have a large influence over the central core behaviour once the quasi-steady state has been reached. This is most easily evidenced by the similarities between the HF and LF velocity field characteristics (Figures 3-7 and 3-8 and Figures 3-13 and 3-14 respectively), mean velocity profiles (Figure 3-19), peak velocity locations (Figures 3-20 and 3-21) and the velocity gradients near the inlet (Figures 3-23 and 3-24 for the low porosity fast inlet velocity and Figures 3-25 and 3-26 for the high porosity fast inlet velocity). However, these two examples differ in that the low porosity case has a central core that meets the free surface and the high porosity case does not.

Although all cases can be seen to have a central core demonstrating the characteristics discussed above, the low porosity slow inlet velocity case shows reduced magnitudes over all of these velocity characteristics in comparison to the other cases. It is considered that this is the influence of the porosity for this case. In Chapter 5.2.4, it was observed qualitatively that significantly more particles of the smaller size class left the fluidised zone and formed layers or mounds to either side of the fluidised region over the unfluidised areas of the bed in the low porosity high velocity case than in the low porosity slow inlet velocity case. This implies that, after initial fluidisation, the concentrations and thus porosities in the two beds are no longer comparable to each other and the slow velocity case has much higher

particle concentrations in the fluidised zone than the high velocity case once the quasi-steady state has been reached. Therefore, the higher particle concentrations in the low porosity slow inlet velocity case dampen the velocity field significantly in comparison to the other observed cases.

3.5.1.2 Supra-jet region

The region above the central core, where the flow field is no longer dominated by the jet dynamics, appears to be influenced more significantly by the porosity of the bed. In high porosity beds (Figure 3-7), above the central core the jet deviates from the equilibrium lateral position over the inlet and is deflected to a greater extent than in low porosity beds (Figure 3-13). When the inlet velocity is fast in the high porosity bed, the supra-jet region above the central core is characterised exclusively by a fast upward-moving turbulent jet that is very mobile laterally across the upper bed; this is captured in both the velocity vectors (Figure 3-7 and 3-8 to a lesser degree) and the qualitative observations (Chapter 5). The mobility of the chaotic jet decreases between the two quasi-steady datasets (150 s and 300 s from the onset of pumping). It is only by comparison with the qualitative data that it becomes clear that the chaotic jet motion in the supra-jet region is caused by deflections of the jet through the interactions of the jet with regions of dilute flow and concentrated particle flows. This also explains why the chaotic jet behaviour decreases over time as the segregation of the particles becomes more pronounced. It is also interesting to note that there have been no reported observations of a migrating or mobile jet in monodisperse experiments but pipe mobility has been observed in layered experimental work (Mörz et al., 2007; Ross et al., 2011).

For the high porosity slow inlet velocity cases, deflections are clear at the top of the central core (Figures 3-9 and 3-10) but then become more diffusive in nature with distance from the inlet. Regions of re-entrainment of falling particles into the flow are highlighted by larger regions of high velocity gradients (Figure 3-27 155 s). In the low porosity slow inlet velocity case, the supra-jet region, above the central core, is dominated by diffusive flow. Despite there being particle movement, the region above the central core is more homogenous (demonstrated by the minima in the velocity gradients; Figure 3-29 and 3-30). Velocities in this region are minimal and the bed more closely resembles a liquefied bed (loosely packed particles with no shear strength due to the pressure exerted by fluid in the pore spaces); there is little measurable particle movement in this region, although it is observed qualitatively. The diffusive flow is characterised by small velocities, laminar regime Reynolds numbers, and very low velocity gradients. The inlet jet has dissipated in this region and fluid flow is spread homogenously across the supra-jet region.

The ability of a fluidisation event to elutriate particles is of critical importance to the flow regimes observed in the bed. In the low porosity fast inlet velocity case, the bed is characterised almost exclusively by the central core that extends to the interface between the fluidised bed and the overlying water column. This channelization of the flow in the upper bed is caused by both low porosity of the surrounding bed and also the very high porosity of the fluidised region (Chapter 5.2.6). The very high porosity observed in the “low porosity” case is only evident through comparison with the qualitative observations of the very high elutriation from this case. Therefore, counter intuitively, the flow that is more heterogeneous at the commencement of

fluidisation (low porosity has bigger difference between particle classes) behaves more like the homogenous monodisperse flows observed in the literature once a quasi-steady state has been reached. Conversely, the equivalent porosity but reduced inlet velocity case has a much reduced capacity to elutriate particles and therefore the regime observed is vastly different.

Therefore, it is likely – yet unquantifiable from the present dataset – that, long after the onset of fluidisation, the “low porosity” bed has been reworked to such an extent that its porosity is significantly greater than that of the “high porosity” bed. It is therefore crucial for the advancement of our understanding of fluidised flows to quantify the concentration characteristics of fluidisation events.

3.5.1.3 Recirculation region

The upward-flowing regimes only represent one portion of the flow dynamics during fluidisation events. All of the cases presented herein also demonstrate regions of recirculation of particles and slow moving, downward, flow at the margins of each fluidised zone. When considering the low Reynolds numbers (Figure 3-22), small downward velocities (Figures 3-7 to 3-14) and small velocity gradients (Figures 3-23 to 3-30), these regions can be characterised as exhibiting laminar flow. This demonstrates a distinct deviation from previous debates in the literature about the flow regimes evident in fluidisation events (Scott et al., 2009; Hurst et al., 2011; Cobain et al., 2015). Both the qualitative and quantitative data presented herein exhibit a fast moving turbulent core surrounded by slow moving laminar zones (Section 3.5.2 and 3.5.3). Slow inlet velocity cases exhibit laminar flows in both the upwards (supra-jet region) and downwards directions (recirculating

region) while fast inlet velocity cases exhibit a turbulent upward-directed core surrounded by laminar downward-directed margins where particles recirculate.

The work in this chapter is limited by the measurement of the velocity of only the largest particles. Therefore, it cannot be determined whether the observed downward-directed motion is representative purely of falling particles or whether the suspending fluid is also directed towards the inlet. That is to say, it is not possible to determine at what point particle motion becomes decoupled from the fluid motion. Further work capable of measuring both the velocity of the fluid and the velocity of the particles and the coupling between the two would greatly enhance the understanding of such flow events. Additionally, as previously mentioned, quantification of the concentration characteristics of the flow at all locations during a fluidisation event should lead to improved understanding of the flow characteristics and the interaction between the concentration of the flow and the flow regimes observed in each zone in a fluidisation event.

3.5.2 The presence of clasts in the fluidised zone

The ability of a fluidisation event to carry or support a clast is often used as a method to estimate the minimum fluidisation velocity of that event (Scott et al., 2009; Sherry et al., 2012; Ross et al., 2014). The ability of a flow to support a measured clast is dependent on the concentration of that flow at the time of fluidisation (Di Felice, 2010) and therefore fluidisation velocity estimates have previously been calculated across a range of flow concentrations. However, all previous attempts of calculating the minimum fluidisation velocity from the size of the largest clast present have made the

assumption of a homogenous upward flow throughout the extent of the fluidisation pipe (Scott et al., 2009; Sherry et al., 2012; Ross et al., 2014). It is therefore of interest to consider the motion of a hypothetical clast in the flow regimes discussed in section 3.5.1.

3.5.2.1 Force balance

In order to simulate the motion of a hypothetical clast subjected to measured flow regimes, it is necessary to consider the force balance on that clast. Herein, a simplified version of the Maxey-Riley equation (Maxey and Riley, 1983) was utilised, in which the drag, weight, buoyancy and pressure gradient terms were retained and all other terms, including those with non-zero temporal derivatives are neglected. In addition, particle-particle and particle-wall collisions were approximated using the approach outlined by Matuttis and Chen (2014), in which the magnitude of repulsion forces are approximated as the amount of particle-object overlap multiplied by Young's modulus and the direction of repulsion forces are estimated as ratio of the overlap and the vector norm of the overlap. The force balance can therefore be written as:

$$v\rho_s \frac{dU_f}{dt} = v\,\rho_f \left(\frac{\partial U_f}{\partial t} + V_f \frac{\partial U_f}{\partial x}\right) + v\left(\rho_s - \rho_f\right)g - \frac{1}{2}AC_D\rho_f(U_f - U_s)\left|U_f - U_s\right| \quad (3.1a)$$

$$v\rho_s \frac{dV_f}{dt} = v\,\rho_f \left(\frac{\partial V_f}{\partial t} + U_f \frac{\partial V_f}{\partial z}\right) - \frac{1}{2}AC_D\rho_f(V_f - V_s)\left|V_f - V_s\right| \quad (3.1b)$$

Where v is a representative volume of a particle, ρ_s and ρ_f are the density of the sediment and the fluid respectively, U_f and V_f represent the velocity of the fluid in the dominant (z) and cross stream (x) directions, g is the acceleration due to gravity, A is a representative surface area of a sediment particle and C_D is the drag coefficient.

3.5.2.2 Particle tracking

Equations 3.1a and 3.1b were coded within Matlab and solved using the ode45 function (Shampine and Reichelt, 1997). Hypothetical particles (diameter 100 μm) were added to the instantaneous velocity fields recorded for each data set and the flow path plotted in each case (Figure 3-31). The particle size was chosen to represent a particle likely to be easily entrained into the flow field. The recirculation of the particles in the supra-jet region is evident for the high porosity fast cases and the high porosity slow inlet velocity at 150 s (at 300 s the movement of the particle is slower so it does not leave the jet until late in the tracking).

Interestingly, regardless of seeding position and although the simulated particles were smaller than the largest particles present in the experimental system, none of the flow fields were able to elutriate the simulated particle out of the top of the vent (Figure 3-31). The lack of elutriation may explain the very limited evidence available for extrudites in the field (Hurst et al., 2011; Ross et al., 2013). Therefore, the reason that extrudites may be so infrequently documented is because even high velocity systems with high channelization may not be sufficient to extrude material after the first initial explosion. The capacity of a flow to support larger particles and clasts must be considered.

The size of the clast will necessarily determine the ability of the fluidisation event to support the clast. If the clast is too great to be supported by the system it will either sediment and deflect the flow or sediment and block the flow completely – forcing another fluidisation event in a different location. However, if the clast is of a size that can be supported by the flow, the only

possible escape of a clast in this system is for the clast to sediment at the wall of the system.

Assuming that a clast is small enough to be supported by the jet it will then either be moved around the supra-jet region by the deflecting jet if the flow behaviour is similar to the high porosity fast velocity cases, or be pushed to the side and sediment into the wall in slower velocity or highly channelised cases. It is unlikely that any significantly sized clasts would fall into the jet region as the geometry of the system is so much narrower in this region and the concentrated static bed is much closer to the flowing region. Also, in the jet region the transition between fluidised and non-fluidised is much narrower in the direction perpendicular to the flow, so that two possibilities are more likely. First, since the transition region is narrow, it is less likely that a clast would be re-entrained and therefore more likely that it will deposit in its location. Second, if a clast enters the jet region, it is more likely that it would become re-entrained into the flow. If multiple large clasts (re-)entered the system, this would further complicate the system, leading to a critical condition where the flow is unable to continue in this location and so fluidisation occurs elsewhere, or flow could become more channelised around the clasts.

Since the particle tracking here (Figure 3-31) monitors the path of a single hypothetical particle in the velocity field there is no resistance or impediment to the particle motion due to the concentration of the particles present at any particular point in the system – including regions of undisturbed bed. The model therefore likely under predicts the extent to which a particle initially seeded in the centre of the jet would recirculate. In addition, re-entrainment

is likely to be less well modelled in the low porosity cases since particle concentration is significantly more heterogeneous in these cases and a particle is therefore unlikely to be able to free-fall at the margins of the fluidised zone (see Figure 3-31).

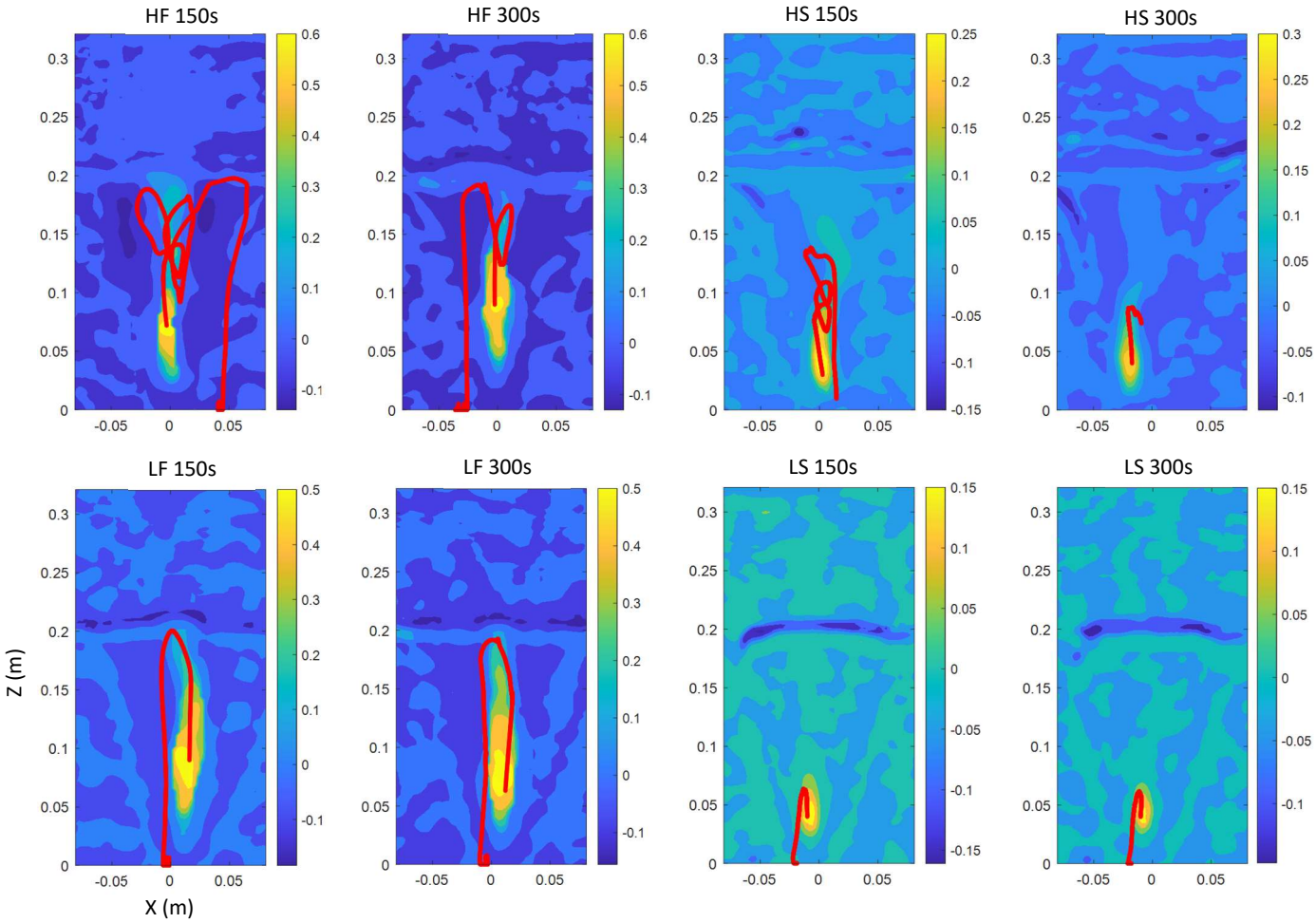

Figure 3-32 Particle tracking through the velocity domain.

3.5.2.3 Limiting clast size in the fluidised zone

From the preceding discussion, velocity fields alone are not sufficient to predict the ability of a fluidisation event to support a clast or particle of a given size; we must know both the flow velocity and the density of the supporting fluid – in this case assuming a pseudo-fluid model. Simplifying equation 3.1a by assuming that, in the dominant direction of flow, the buoyant weight of the clast and turbulent drag are the only forces acting on the clast, it is possible to write:

$$\rho_p va = \left[\frac{1}{2}AC_d\rho_f(U_f - U_p)|U_f - U_p| - gV\left(\rho_p - \rho_f\right)\right] \quad (3.2)$$

where ρ_s is the mass density of the clast, which takes a value of 2650 kg m^{-3} for silica sand, V is the volume of the clast (m^3), a is the acceleration of the clast (m s^{-2}), A is the projected area of the clast perpendicular to the z direction (m^2), C_d is the drag coefficient, which takes a value of 0.47-0.48 for spheres with Reynolds numbers ranging from 1×10^3 to 1×10^5 (Mikhailov and Freire, 2013), ρ_f is the mass density of the supporting fluid, which takes a value of 1000 kg m^{-3} for pure water to 2000 kg m^{-3} for a suspension with concentration of 0.6 (Di Felice, 2010), U_f is the velocity of the fluid (m s^{-1}), U_p is the velocity of the clast (m s^{-1}) and g is the gravitational acceleration, which takes a value of 9.81 m s^{-2} at Earth's surface.

If it is assumed that the particles are spherical (i.e., projected area, $A = \frac{\pi}{4}d^2$, and volume, $V = \frac{\pi}{6}d^3$), that there is no net vertical acceleration of the clast (i.e., $a = 0$) and the clast is stationary (i.e., the weight of the clast is supported by the fluid and $U_p = 0$), then:

$$\frac{\pi}{8}d^2C_d\rho_f{U_f}^2 = g\frac{\pi}{6}d^3\left(\rho_p - \rho_f\right) \quad (3.3)$$

Rearranging gives,

$$d = \frac{\frac{3}{4} C_d \rho_f {U_f}^2}{g(\rho_p - \rho_f)} \quad (3.4)$$

Substituting typical values for C_d,

$$d = \frac{0.3525 \rho_f {U_f}^2}{9.81(2650 - \ _f)} \quad (3.5)$$

Note that equation 4.4 is independent of the inlet dimensions; it describes the maximum particle velocity that can be supported by fluid within the central core. To arrive at equation 3.4, it has still been necessary to assume that the velocity field of the pseudo-fluid is steady in space and time, which is certainly not the case at the commencement of fluidisation (Figures 3-3 and 3-4 for example) and is highly unlikely in the supra-jet region once the quasi-steady state has been reached (Figures 3-7 to 3-14). Since the concentration is the main variable in modelling a pseudo-fluid density, this must be established. Further, to fully understand particle motion and behaviour in a fluidisation event, it is necessary to model the two-way coupled interaction of the particles and the flow field. As previously established, the concentration of particles and interaction of the particle field is of fundamental importance to understanding the capacity of a fluidisation event to support clast material and affects the minimum fluidisation velocities required in a system.

The above outlined approach is comparable to that used by Ross et al., (2014), yet has applied across a range of concentrations and velocities to identify possible clast sizes, where they used the clast size to determine the possible velocity for a range of concentrations. Figure 3-32 demonstrates the range of particle sizes a flow is able to carry when calculated using equation 3.4. For a fluid composed purely of water with no particle concentration the particle size supported is 0.2 mm for a flow velocity of 0.1 m s^{-1} to 20 mm for

a flow velocity of 1 m s^{1}. For a highly concentrated flow with a pseudo-fluid density of 2000 kg m^{-2} the maximum particle size that could be supported ranges from 1.2 mm to 100 mm for the same range of flow velocities.

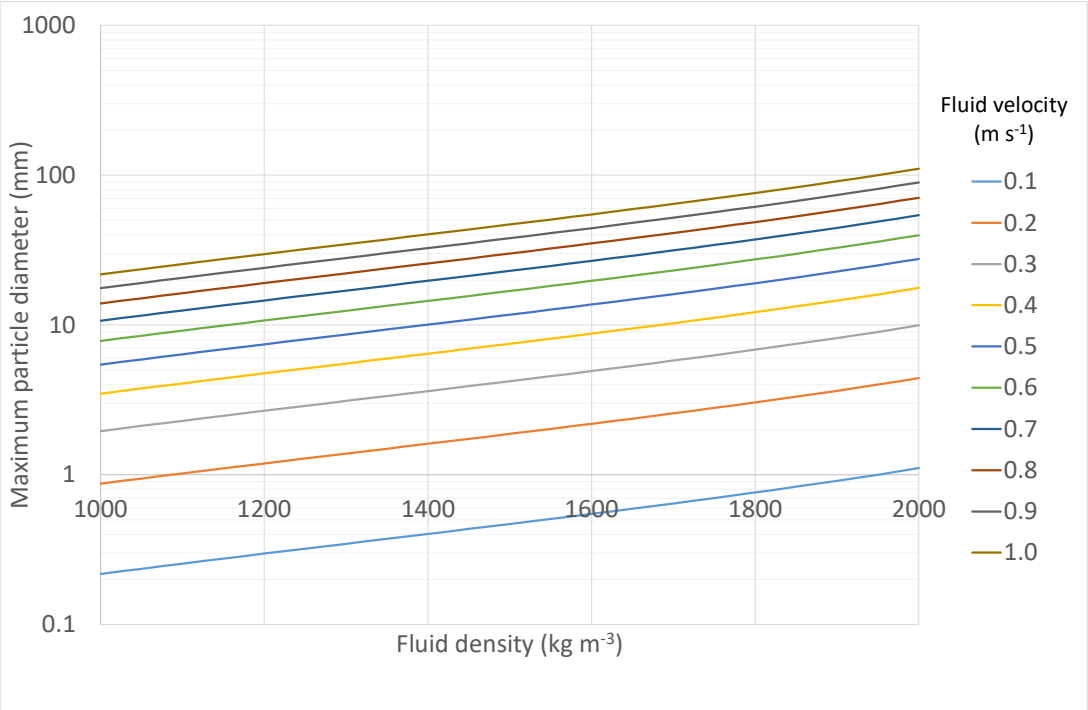

Figure 3-33 - Plot of relationship between clast or particle size, fluid density and velocity of the pseudo-fluid.

3.6 Conclusions

The quantitative analysis shows that a single flow regime cannot fully characterise the flow conditions of a fluidisation event into a bi-disperse bed. Further, laminar conditions are observed in recirculating and supra-jet regions and turbulent conditions are observed in the jet region. The different regions characterised herein (jet, supra-jet and recirculating), are influenced by both the inlet velocity and as a secondary influence in the supra-jet region the porosity. The previous attempts to characterise field observations in this way are therefore too simplified, and when considering the characteristics evident in the field the flow region should be identified. These data provide

the first quantification of both laminar and turbulent flow regimes within the same fluidisation event.

Observing velocities alone in these systems is not sufficient to fully characterise the fluidisation properties of a fluidisation event – to do so would lead to erroneous conclusions about the nature of the geological properties observed in the field. These observations of the velocity field only make sense when considered in concert with the particle behaviours and so the locations of the particles during the fluidisation event must be quantified. Furthermore the surrounding bed is observed to not be an indicator of likely flow concentration during a fluidisation event, as the low porosity bed was shown to behave more like a mono-disperse bed than the high porosity case.

The minimum fluidisation velocity is shown to be dependent on a number of inter-dependent factors and the largest clast size is likely to be insufficient to gain a reasonable understanding of the flow field alone. But in consideration with the flow region and concentration the particle size could be an indicator of flow velocity. The ability of an established flow to elutriate even small particles is demonstrated to be significantly lower than would otherwise be expected due to the diffusion of the flow velocities in the supra-jet region. It is proposed that this is likely the reason there are less examples of large extrusion events in the field than would be expected.

4 Particulate concentration during fluidisation events

Given the lack of any direct observations of natural injectites and extrudites, there are no data on concentration. Instead, assumptions about concentration span large ranges, from low concentration right through to values approaching the packing limit (Scott et al., 2009; Ross et al., 2014). Similarly, experimental work has previously left the measurement of concentration unaddressed (Morz et al., 2007; Zoueshtiagh and Merlen, 2007; Rodrigues et al., 2009; Mourgues et al., 2012; Phillippe and Badiane, 2013; Mena et al., 2017), likely due to the limitations of the experimental techniques available. Thus, estimation of concentration remains a major challenge.

The effects of particles in a fluid flow are known to be significant and attempts have been made to provide empirical relationships between flow behaviour and particle concentration (Di Felice, 1995 and references therein). Perhaps the most recognised of these is the Richardson-Zaki equation, which asserts that the velocity of a suspension can be quantified as a function of the settling velocity of a single particle and the voidage of that suspension (Richardson and Zaki, 1954; Di Felice, 2010). The Richardson-Zaki equation has previously been used to deduce flow characteristics from geological features and outcrops (Duranti and Hurst, 2004; Sherry et al., 2012; Ross et al., 2014; Cobain et al., 2015). It is valid for concentrated suspensions (up to 0.6) but only for those that can be classified as mono-disperse (Di Felice, 2010). For the relationship to hold across multiple particle classes, a pseudo-fluid approach is needed, where the properties of the fluid itself, in terms of density and viscosity, are artificially augmented by the presence of the smallest

particle class (Gibilaro et al., 2007; Di Felice, 2010). By assuming that the smallest particles and the fluid are one continuous phase, the Richardson-Zaki equation holds for multiple particle phases and has been shown to be a reasonably good approximation of suspension behaviour and characteristics (Di Felice, 2010). To employ such an approach, one must then know the voidage or volume fraction of particles present and particle sizes contained in the suspension to be studied.

However, in the absence of any observations, there are no data on concentration and particulate properties during natural fluidisation pipe formation and extrusion events (Scott et al., 2009). Previous attempts to use Richardson-Zaki (1954) based relationships in order to make inferences about the flow conditions of fluidisation events have countered the lack of knowledge of the flow concentration by using a range of values and thus obtaining a range of flow conditions which could be applicable (Scott et al., 2009; Sherry et al., 2012; Ross et al., 2014; Cobain et al., 2015).

Work on fluidised beds suggests that the fluidised suspension can in some circumstances have an apparent viscosity which is higher than that of the fluidising medium (Gibilaro et al., 2007). It follows then that this higher viscosity pseudo-fluid can support much larger clasts or particles than the equivalent particle-free fluid. To use a viscosity based on a pseudo-fluid to estimate the likely velocity or fluidisation characteristics of an injection assumptions must be made about that fluidised suspension. Usually such assumptions are made from characteristics derived from outcrop data (e.g Cobain et al., 2015) or inferred from empirical relations (Scott et al., 2009; Ross et al., 2014). However to date, there have been no measurements that

quantify the concentration properties during a sand injection or extrusion event. Further it is noted that when such characteristics are estimated or inferred by using a single concentration to characterise the fluidisation there is an assumption of homogeneity across the fluidisation event (e.g Scott et al., 2009; Ross et al., 2014). It is likely that such an assumption is erroneous and a vast oversimplification of the concentrations that actually occur in subsurface sand remobilisation.

Establishing the likely concentration at the time of sedimentary structure formation is almost impossible from outcrop and seismic data (Sherry et al., 2012; Pau et al., 2014). By providing an experimental analogue of a bidisperse suspension undergoing fluidisation, pipe formation, extrusion and subsequent settling following the cessation of flow, the present work can establish a range of likely conditions to support interpretation of dewatered outcrop injectites and the injectites observed in seismic data, in the future and identify the limits of past approaches to understanding fluid flow conditions.

Chapter 3 quantified the velocity characteristics of the different flow regions using high speed imaging. In this chapter, a non-intrusive experimental approach is used to quantify the concentration characteristics of a fluidisation event in three dimensions and compare this to the findings from previous chapters. Specifically, a Computerised Tomography (CT) scanner operating at 2 Hz is used to capture the previously unquantified concentration within the fluidisation process. Furthermore, the CT scanner enables the temporal variation of the concentration to also be assessed.

By again varying the ratio of particle sizes in the bidisperse unconfined bed, the influence of bed porosity on fluidisation characteristics will be further

understood and contribute to a more holistic picture of the physical characteristics of fluidisation events. Final scans of the residual morphology following the cessation of flow provide clarity on the assumptions about what can and cannot be deduced about fluid flow from residual morphologies.

4.1 Methodology

This set of experimental runs were conducted in the Wolfson Multiphase Flow Laboratory at the University of Leeds. A GE Brivo CT386 CT scanner was used to collect the raw data. A cylindrical tank was designed to reduce the likelihood of interference due to the container shape (see partial-volume effects, Goldman, 2007). Three identical tanks were produced to enable the quick changeover of beds in the CT scanner and thus increase measurement efficiency. The tanks had an internal diameter of 145 mm and a longitudinal length of 180 mm. The centre of the inlet was located at 90 mm in the longitudinal direction. The front face of the tanks were transparent in order to aid the filling procedure.

A single inlet was continuously fed by a BVP-Z Standard Gear Pump with a Z-201 pump head and a flow meter to monitor the discharge rate. The gear pump was located outside of the room housing the CT scanner and connected by long hoses to ensure that the experiment could be started at the same time as the scanner. Outflow pumps (Watson Marlow 520Du/R) maintained the fluid height throughout the experiment. Beds were created using the same procedure outlined in section 3.2.2 to a total bed height of 70 mm (Table 4-1).

Table 4-1 Sediment mixtures used to create bidisperse beds for experimental observations

Run	Fine Particle Median (μm)	Coarse Particle Median (μm)	Percentage Fines (%)	Velocity measured on flow gauge (ms^{-1})
Low Porosity (0-10 mm)	51	749	40±2.7	0.53
Low Porosity (10-20 mm)	51	749	40±2.7	
Low Porosity (20-30 mm)	51	749	40±2.7	
High Porosity (0-10 mm)	180	749	40±2.7	0.69
High Porosity (10-20 mm)	180	749	40±2.7	
High Porosity (20-30 mm)	180	749	40±2.7	
Very High Porosity (0-10 mm)	333	749	40±2.7	0.6
Very High Porosity (10-20 mm)	333	749	40±2.7	
Very High Porosity (20-30 mm)	333	749	40±2.7	

* Measurements in brackets correspond to the volume scan distance from the centre of the inlet in the longitudinal direction.

The filled tanks were then placed into a long container box through which the inlet hoses were connected (Figure 4-1). The box was then sealed to ensure no fluid from the overflows could make contact with the scanner.

The GE Brivo CT385 is a 16-slice scanner manufactured by GE Medical Systems (GE Medical Systems, 2018). The slice resolution was 0.625 mm, which allowed the simultaneous collection of 10 mm sections (i.e., 16 × 0.625 = 10 mm). Each image produced by the CT scanner comprises 512 × 512 pixels, with each pixel representing 187.5 μm x 185 μm, yielding a total field of view of 96 × 96 mm. A full set of axial scans of the length of the bed was completed before the commencement of fluid flow. An axial scan is a scan where the reconstructed image is in the plane perpendicular to the axis of rotation of the gantry; with the gantry in the present set up in a vertical orientation. A cine scan takes repeated sets of 16 axial scans of the same 10

Figure 4-1 Experimental arrangement. Three identical filled tanks were placed in the unsealed container box before the commencement of CT data collection.

mm volume for the duration of the scan. Cine scans were used during fluidisation events. Scans were completed at 2 scan volumes per revolution and the scanner completed revolutions at a rate of one revolution per second. Twenty six complete volumes were collected per complete cine scan, representing a time period of 13 s. Flow was allowed to continue for a further 150 seconds to ensure the full development of the fluidisation feature before cessation of flow. Another set of axial scans covering the full length of the bed was then taken, showing the settled bed after the cessation of flow. Each sediment mix was fluidised three times, on a new unfluidised bed in a new tank for each fluidisation event (See Procedure 4-1). The first cine scan of each set scanned the volume from 0-10 mm from the centre of the inlet during a fluidisation event. The next cine scan, comprising the same bed mix in a new tank, would scan the volume corresponding to 10-20 mm from the centre

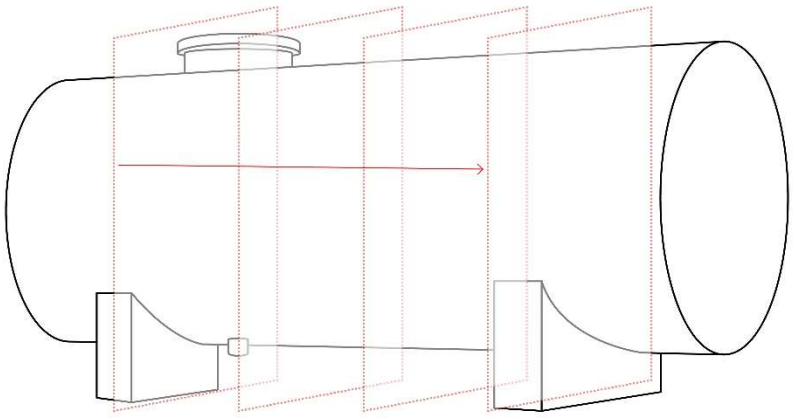

Axial scan – slices taken consecutively through the

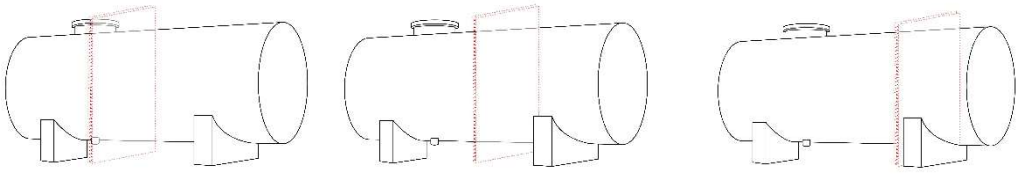

Cine scan – 16 slice scans taken repeatedly over the same volume for 13 s. Repeated for three volumes (see Procedure 4-1)

Figure 4-2 Diagram of scan procedure for axial scans (top) and cine scans (bottom).

of the inlet during a fluidisation event. The third cine scan would then be taken over the volume corresponding to 20-30 mm from the centre of the inlet, again recording a new fluidisation event. Thus the three separate fluidisation events yield three adjacent 10 mm long volumes but over independent fluidisation events of the same sediment mix. This gives the combined datasets a total coverage of 30 mm. The data collection volumes rely on the assumption that the flow field will be axisymmetric. The full list of runs completed is shown in Table 4-1 and the procedure for a “set” of runs is outlined in Procedure 4-1.

CT scanners measure the attenuation of X-rays and store the recorded values in Hounsfield Units, represented as relative grey scale values per pixel (Hounsfield, 1973; Reilly et al., 2017). The attenuation of X-rays is a function of both the density and atomic number, but the measurement of X-ray

attenuation can also be affected to a much lesser degree by surface properties, proximity of material interfaces to the measurement zone, and the size of the object (Bolliger et al., 2009). The materials used in this study were kept consistent; the atomic number of the particles and the material density remained constant across varying particle sizes. It is therefore assumed that a reduction in CT attenuation, and consequent Hounsfield Unit, corresponds to a reduction in the proportion of glass spheres present in the measurement zone.

Hounsfield Units are defined relative to the attenuation coefficient (μ) of water, which is by definition 0.

$$HU = (\mu_{sample} - \mu_{water})/\mu_{water} \times 1000$$

The resolution of the CT scanner used in the present experiments was 187.5 μm per pixel. For the very high porosity sediment mixes, the particle size of both particle classes used in the mixture was greater than the pixel resolution. For the high porosity mix some of the fines class is about the same resolution as the scanner and for the low porosity mix the fine particle class is much less than the resolution of the scanner (particle size distributions for each separate particle size class are shown in Figure 4-3), and so some pixels may be resolved as entire particles. Where and when the particles are smaller than

the pixel resolution or a void space is present, the Hounsfield Unit recorded represents the average radio-density over that pixel (Mena et al., 2015). The

Procedure 4-1 – The procedure undertaken for each set of bed mixtures for recording fluidisation events in the CT scanner.

Experimental Procedure – to be repeated for each bed mix:

- Fill 3 identical tanks with the same bed mix, Tanks 1, 2 & 3
- Place tanks in protective box for scanning and place box on scanning table (See Figure 4-2)
- Move the scanning table so Tank 1 is in the focus of the scanner
    - Full set of axial scans Tank 1 - unfluidised bed
    - Set scanner to scan volume from 0 – 10 mm from the inlet in longitudinal direction.
    - Simultaneously commence fluid pumping and start cine scan of volume (0-10 mm from inlet)
    - Allow fluidisation to run for 150 s
    - Stop fluid pumping
    - Full set of axial scans Tank 1 residual bed
- Move the scanning table so Tank 2 is in the focus of the scanner
    - Full set of axial scans of Tank 2 – unfluidised bed
    - Set scanner to scan volume 10 – 20 mm from the inlet in longitudinal direction.
    - Simultaneously commence fluid pumping and cine scan of volume (10-20 mm)
    - Allow fluidisation to run for 150 s
    - Stop fluid pumping
    - Full set of axial scans of Tank 2 – residual bed
- Move the scanning table so Tank 3 is in the focus of scanner
    - Full set of axial scans of Tank 3 – unfluidised bed
    - Set the scanner to scan volume 20 – 30 mm from the inlet in longitudinal direction.
    - Simultaneously commence fluid pumping and cine scan of set volume (20-30 mm)
    - Allow fluidisation to run for 150 s
    - Stop fluid pumping
    - Full set of axial scans of Tank 3.
- Empty all three tanks and refill each with next bed mixture.

recorded Hounsfield units in this study are used as an indicator of relative density to inform discussions about typical relative concentrations of regions throughout the stages of fluidisation. To enable relative densities across each bed to be examined, a linear scaling was applied to the recorded Hounsfield Units. The mean HU for water was thus set to 0 for each new run and the mean HU of the saturated sediment bed prior to fluidisation, was set to 1. This assumes that the maximum particle concentration occurs prior to fluidisation (i.e., prior to the expansion of any interparticle void spaces caused by excess pore-water pressures). Therefore, in the foregoing, this normalised Hounsfield Unit scale will be referred to as the relative concentration. CT Scanners produce large volumes of data that are stored in the DICOM file format (Mena

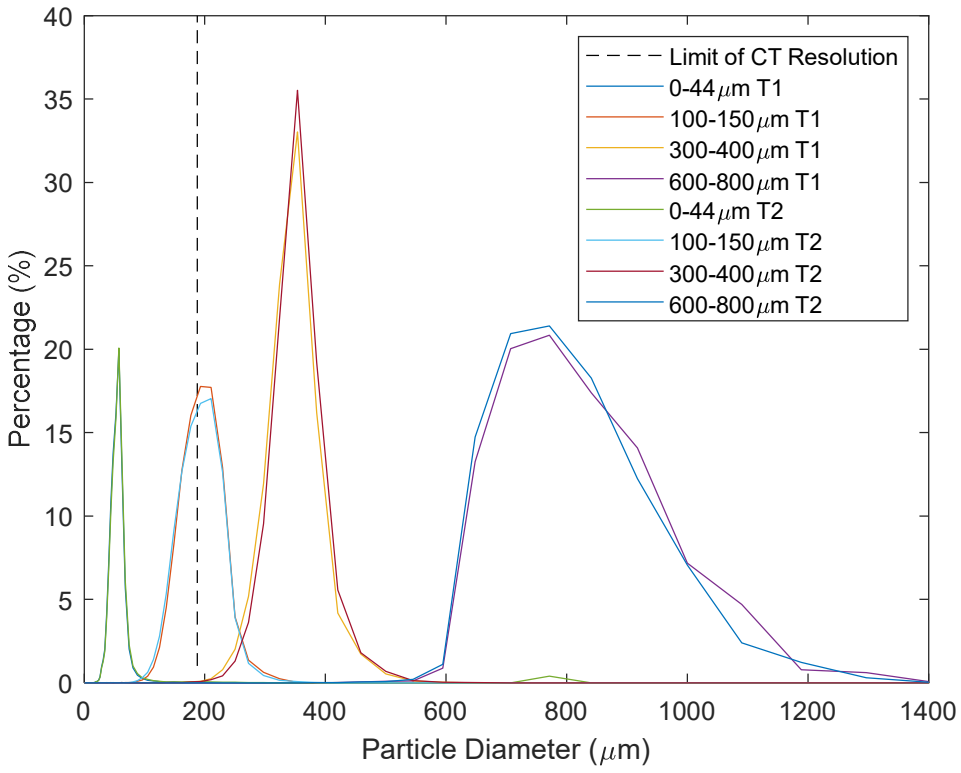

Figure 4-3 Particle Size distributions for individual particle size classes of sediment used to make bed mixtures in experiments (see table 4-1 for mixtures). Dotted line shows the limit of the resolution of the CT scanner indicating some of the fine particles are smaller than the resolution of the scanner. T1 and T2 refer to the test number for the particle size measurements.

et al., 2015). These files were exported from the scanner and subsequently imported into Matlab for post-processing. DICOM data files retain both the recordings of the Hounsfield Units for each pixel interrogated but also store information detailing scan settings and pixel locations. This allows the reconstruction of the spatio-temporal position of the recorded pixels into Matlab matrices and the visualisation of the recorded Hounsfield Units. Since the matrices generated were square images with dimensions 512 × 512 pixels but the scanner recorded a circular diameter interrogation area, pixels that lay outside of the interrogation area were assigned a blanking value of −2000.

4.2 Results

4.2.1 Raw CT data

Raw CT datasets are shown in Figures 4-4, 4-5, 4-6 for different bed types 9 s after the onset of fluid pumping. For all sediment mixes at 0 mm from the centre of the inlet there was a dilute region corresponding with the centre of the upward-directed fluid flow. This dilute region is more visible in raw CT plots for the low porosity mixture (Figure 4-4) than the high porosity mixture (Figure 4-5) because the smaller particle class in the low porosity mixture had a median diameter of 51 μm, that is much smaller than the resolution of the scanner at 187.5 μm (Figure 4-3). For the high porosity mixture the smaller particle class had a median diameter (180 μm), that was in the region of the resolution of the scanner (187.5 μm) and the smaller particle class for the very high porosity mix had a diameter (333 μm), that was much greater than the resolution of the scanner (187.5 μm). Therefore, where the particles had a scale around or less than the resolution of the scanner the pixel values plotted

represented an average x-ray attenuation for the sample area. By virtue of a majority of particles being larger than the scanner resolution, more individual particles were visible in the very high porosity mixture than in the lower porosity mixtures (Figures 4-6). The low porosity and high porosity mixtures appear more homogenous in the raw data due to the pixel averaging over the smaller particles classes used in these mixtures (Figures 4-4 and 4-5 respectively). However it is noted that the lack of clearly defined particles does not necessarily mean an area devoid of particles. The dilute regions visible in the channels in Figure 4-4 are much darker – indicating there are indeed fewer particles present whereas the dilute regions in Figure 4-5 are lighter indicating greater particle presence.

The morphologies visible for the low porosity set of experiments appears to vary between the three runs (corresponding to the three sample volumes 0 – 10 mm, 10 – 20 mm and 20 – 30 mm). At 0.625 mm (Figure 4-4, A) the fluidised zone shows a wider “bulb” mostly dilute with few particles detectable in the HU measurements. The bulb measures approximately 32.4 mm in diameter at the widest point 38 mm above the inlet, the fluidised zone then narrows to a diameter of 21.9 mm (assuming the fluidised zone is approximately axisymmetric) 53.6 mm above the inlet. At 6.875 mm longitudinally from the centre of the inlet (Figure 4-4, F), the widest part of the bulb remains at approximately the same diameter (32.3 mm) at a height of 35 mm above the inlet. However in the zone above the dilute bulb significantly more particles are visible in the HU measurements. This dilute region above the bulb has a typical funnel shaped geometry, and is characterised by a higher number of particles than the dilute bulb but still visibly less than the

Table 4-2 Mean attenuation of X-rays (Hounsfield Units) for the mixed sediment beds

	Mean ± 1 standard deviation attenuation of X-rays (Hounsfield Units)	
Run	**Sediment bed**	**Overlying water**
Low Porosity (0-10mm)	2326.3 ± 197	1064.1 ± 0.0
Low Porosity (10-20mm)	2729.0 ± 179	978.0 ± 0.0
Low Porosity (20-30mm)	2721.1 ± 193	986.3 ± 0.0
High Porosity (0-10mm)	2269.5 ± 135	1057.6 ± 0.0
High Porosity (10-20mm)	2650.0 ± 140	973.2 ± 0.0
High Porosity (20-30mm)	2647.8 ± 125	976.4 ± 0.0
Very High Porosity (0-10mm)	2487.1 ± 126	979.3 ± 0.0
Very High Porosity (10-20mm)	2515.0 ± 105	984.4 ± 0.0
Very High Porosity (20-30mm)	2493.1 ± 112	984.1 ± 0.0

undisturbed bed. The diameter of this supra-jet region narrows to 19.9 mm, at a height of 52.9 mm above the level of the inlet but widens to approximately 50 mm at the bed surface. The dilute bulb is narrower at the last slice location for this bed, 9.375 mm longitudinally from the centre of the inlet, with the widest point measuring 30 mm in diameter 27.2 mm in height from the level of the inlet. The supra-jet region shows similar particle concentrations above the bulb to the undisturbed bed, but closer to the surface the top of the funnel is visible as a very slightly more dilute region of particles at the bed surface in comparison to the undisturbed bed. This indicates that the bulb is wider closer to the inlet and narrows closer to the surface with some parts of the bulb overlain by undisturbed bed. Furthermore, the geometry of the fluidisation event is approximately axisymmetric. A bulb overlain by undisturbed bed is

evident in each of the three volumes tested for this bed mix despite different morphologies between the 10-20 mm volume and the other two. The columnar void observed in Figure 4-4 I-N still narrows in proximity to the surface, and a much wider void space is shown in Figure 4-4 Q – V with no connection to the surface observed in these slices. This morphology would indicate that in the low porosity cases the extrusion occurs via a narrow pipe propagating from the much larger void space, this mechanism is addressed in more detail in Chapter 6.

In comparison to the low porosity case, at 0 mm longitudinally from the centre (Figure 4-5, A) the high porosity case shows significantly higher concentrations of particles in the fluidised zone. The dilute zones itself is much harder to define in the raw data set as the boundaries between the dilute and concentrate regions are more diffuse. Approximately, the dilute region is 10.9 mm wide just above the inlet, widening to a 22.5 mm diameter at 28.7 mm from the inlet and a 32.6 mm at the top of the bed. The dilute zone with very few visible particles in only persists for the first 6.4 mm above the inlet and there are no points with very dilute spaces in a scan slices taken more than 2.5 mm longitudinally from the centre of the inlet (i.e. Figure 4-5 D–X). Aside from the very dilute zone, the morphology shows very little difference with longitudinal distance from the centre of the inlet for the first 8.75 mm (Figure 4-5, A-H); there is a gradual increase in particle concentration around the edges of the fluidised zone with increasing distance of the measurement slice away from the centre of the inlet. From 10 mm to 15 mm from the centre of the inlet there is decreasing visibility of any dilute regions (Figure 4-5, I – J, note these data are from a separate fluidisation event) and from 16.25 mm

onwards (Figure 4-5, N-X) there is very little evidence of the fluidised zone and so it is likely that this area remains undisturbed.

The very high porosity case has the narrowest fluidised zone of the three sediment mixtures tested (Figure 4-6), and shows the least variation in width of the dilute zone with height from the inlet. At 0 mm from the centre of the inlet (Figure 4-6, A), the pipe ranges from 9.75mm in diameter 17.1 mm in height from the inlet, to 17.81 mm in diameter at the top of the bed. There is little variation in the longitudinal direction for the first 3.75 mm (Figure 4-6 A-D), after this point however the measurement slices have reached the edge of the pipe and there is reduction in the size of dilute regions with distance from the centre. At 8.75 mm (Figure 4-6, H) there is only a small dilute region visible in the upper bed. At 10 mm onwards in the longitudinal direction there is only a small region of particle disturbance visible at the interface of the bed with the overlying water indicating the pipe is not located in this region. This shows that at this timestamp for the pipe formation in the very high porosity case the pipe already has the typical geometry of a funnel with a narrow base widening with proximity to the surface.

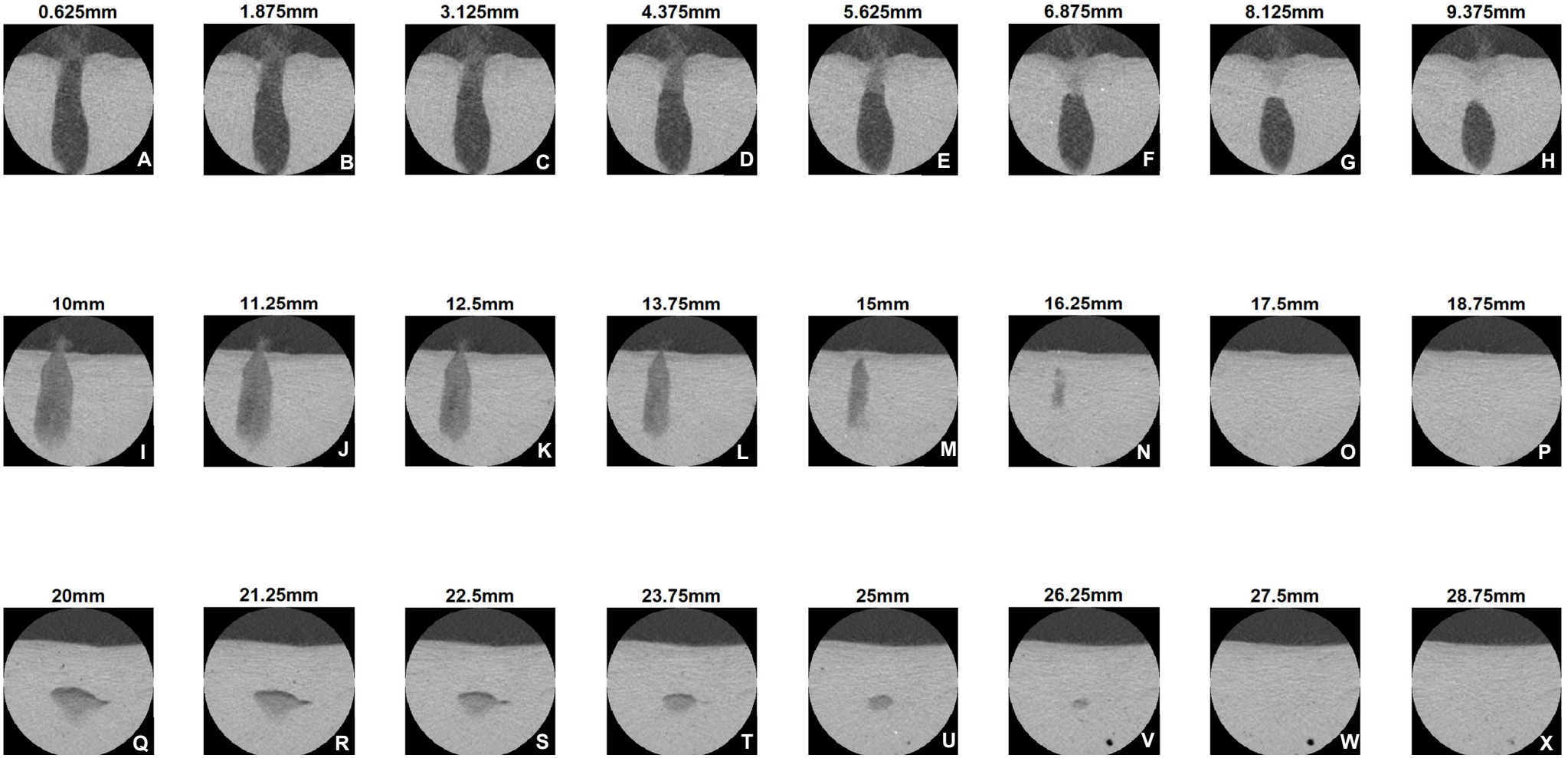

Figure 4-4 Raw CT data showing Hounsfield Units for low porosity bed mix 9s after onset of fluid pumping. 0 -10 mm (A-H) shows a bulb formation of the void space which narrows with height from the inlet. 10 mm – 2 0 mm(I-P) shows the void space or channel forming away from the assumed equilibrium position. 20 - 30 mm (Q-X) shows the edge of a void formation which appears to be overlain by undisturbed bed.

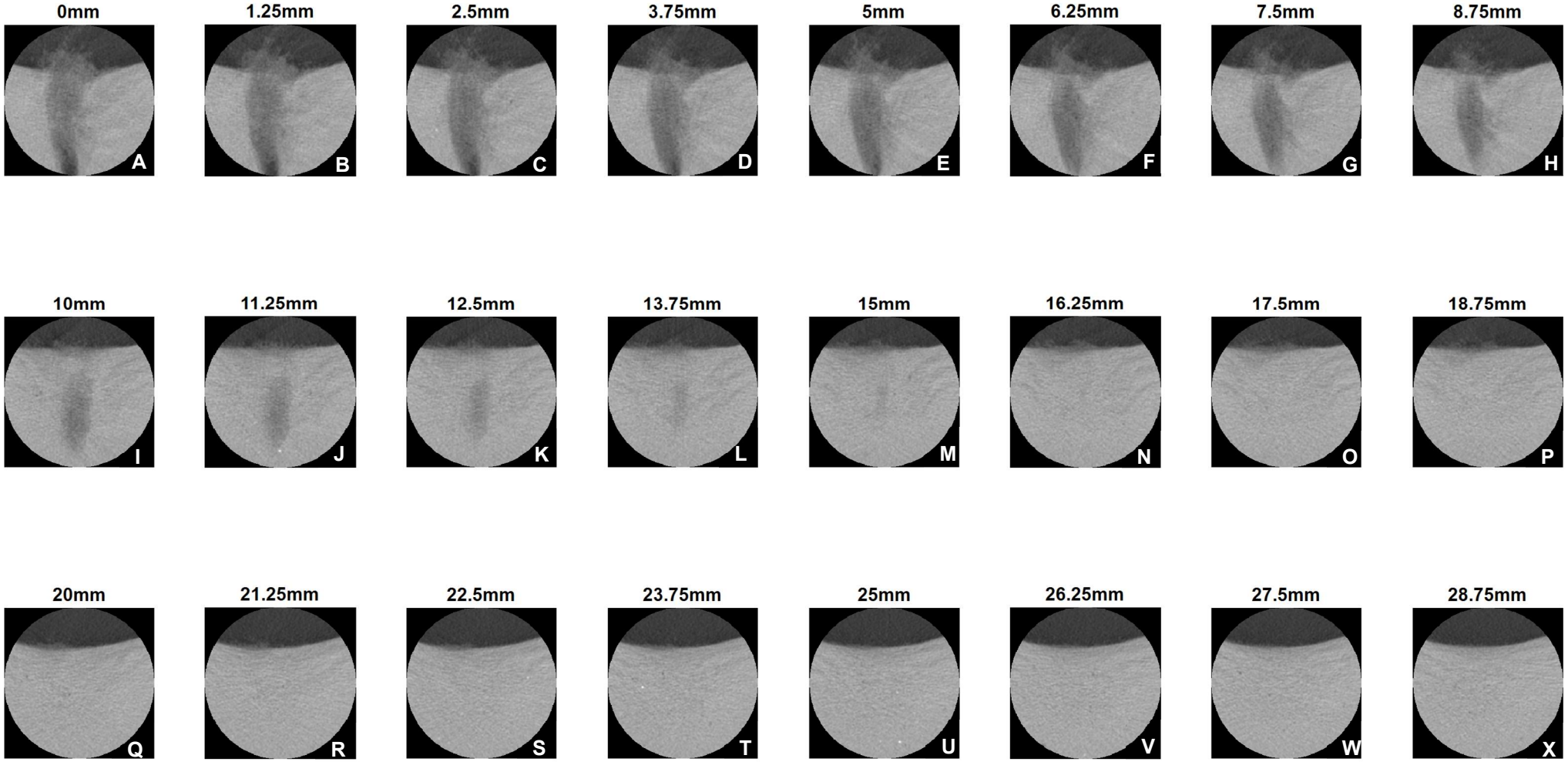

Figure 4-5 Raw CT data showing Hounsfield Units for high porosity bed mix 9s after onset of fluid pumping. A – H show an asymmetrical pipe indicating the fluidised zone has been deflected .I-J show laminations indicative of particle size segregation to either side of the dilute zone. Some layers of segregated particles visible at the very top of the bed in Q-S, Q-X does not show the fluidised zone as this is beyond the diameter of the pipe and is mostly undisturbed bed.

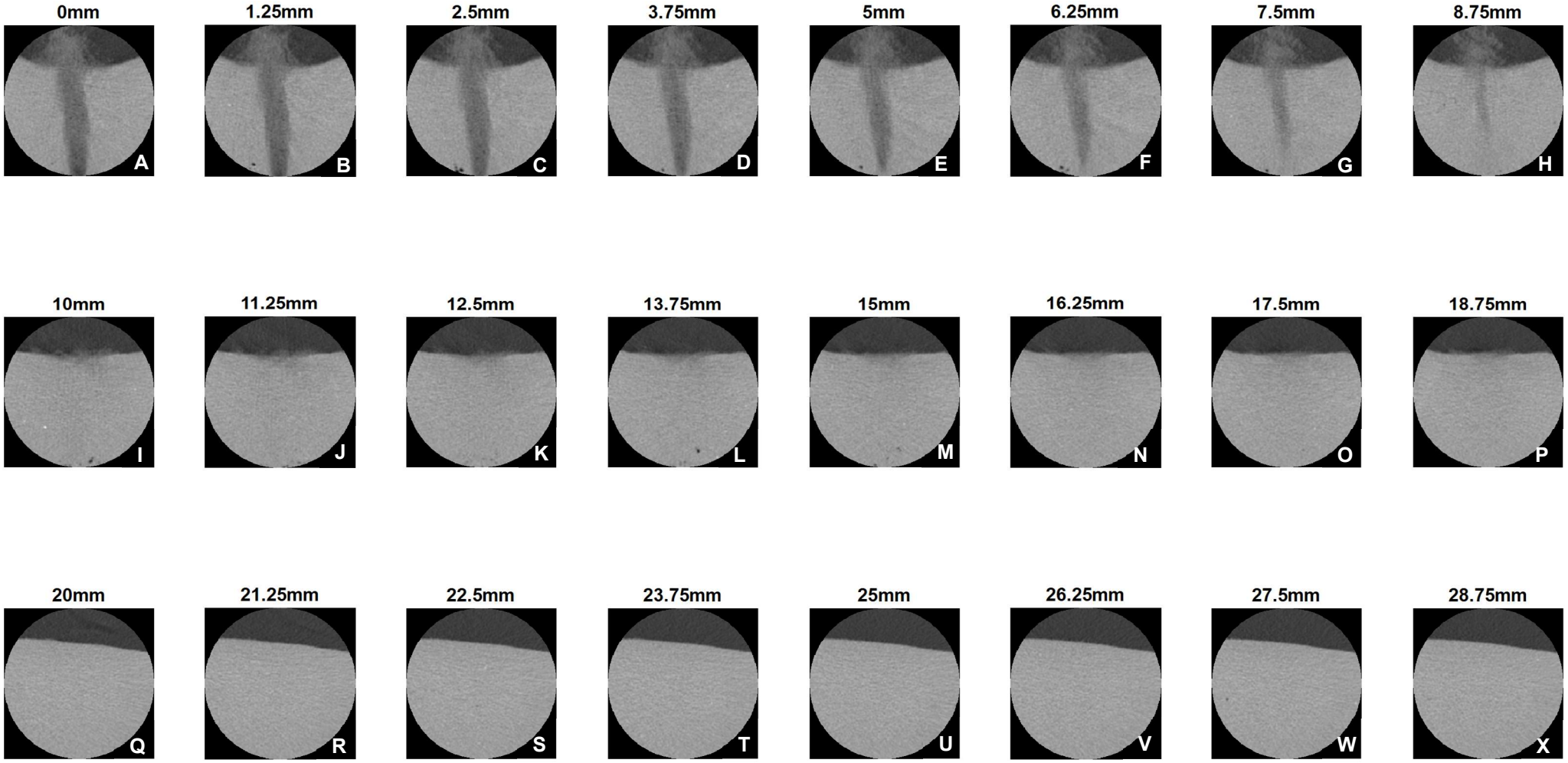

Figure 4-6 Raw CT data showing Hounsfield Units for very high porosity bed mix 9s after onset of fluid pumping. A much narrower fluidisation pipe is observed in A-H . I -P show surface disturbances at the top of the bed indicative of the top of the funnel or surface disruption of particles. Q-X is undisturbed bed as this is far from the fluidisation pipe.

4.2.2 Time series

Time series of the bed concentrations (normalised Hounsfield Units) are shown for each run at the point closest to the centre of the inlet (0 mm, 10 mm and 20 mm for each porosity) (Figure 4-7 to 4-9). The normalised HU values a normalised against the mean HU value of the undisturbed bed as calculated from the initial axial scans pre-fluidisation, the HU value of water is 0 in these plots. Therefore any individual pixel with a HU value greater than the mean bed value will have a normalised HU value greater than 1m, this is not uncommon in pixels completely or mostly filled with a single particle and therefore is also more prevalent in the very high porosity bed (as most of the particles in these runs are greater in size than a pixel).

4.2.2.1 Low porosity bed mixture

In Chapter 3 (and in more detail in Chapter 5 to follow), it was observed that the low porosity bed mixtures began the fluidisation process with a process that appeared similar to hydraulic fracture. This was expected to be observed in the 0 mm set of CT Slices (Figure 4-7). However, in the present experiments, the start of the fluidisation occurred away from the central point of the inlet (Figure 4-7, 0 – 4.5 s). At 5 s, a plume of particles appeared above the bed (Figure 4-7, 5 s), indicating that extrusion had occurred. In the following timestep (Figure 4-7, 5.5 s), a fluidisation pipe that reached the top of the bed is visible. It is likely that between these time steps, the pipe moved longitudinally into the focus of the CT scanner. However it is possible the original fracture was slightly offset from the centre but was very narrow and as the pipe expanded over time the dilute flow reached the focus of the

scanner similar to the advancement of the fracture recorded in the qualitative 2 dimensional case. At 5.5 s there were very few particles in the centre of the pipe and more particles were entrained into the centre of the fluidised pipe in the subsequent timesteps.

As observed in the raw data at 9 s, the pipe that formed in the low porosity bed at 0 mm had an interesting morphology, with a bulb shape in the lowest part of the bed that narrowed with height (Figure 4-7, 5.5 -12 s). This morphology became wider over the time period but retained this form. The slices of raw data shown in figure (4-4, A-H) show that the bulb shape is approximately axisymmetric. The pipe continued to develop by becoming wider over time (Figures 4-7, 6 – 12 s) expanding from 15.9 mm at the widest part of the bulb (12 mm in height from the inlet) at 5.5 s to 33.2 mm wide at the widest part of the bulb (36.8 mm high from the inlet) at 12.5 s after the onset of fluid pumping. Also notable in the low porosity run is that the transition from the bed to a relatively homogenous dilute zone was fast, especially in the “bulb” which echoes observations of the wall regions for this mixture reported in section 6.2.6. In addition, there was a region of increased concentration in the dilute zone above where the bulb narrowed, indicating that there is more recirculation of particles in the flow in this region (Figure 4-7, 10–12 s).

The low porosity bed data that were captured at 10 mm from the centre of the inlet (Figure 4-8) show the fluidised pipe again widening over time and emerging into the focus of the scanner. Interestingly this pipe has stabilised offset from the centre of the inlet in the lateral direction. And although this pipe expands over time as seen in the dataset at 0 mm (Figure 4-7), it does not migrate laterally to the centre of the inlet. At 10 mm longitudinally from the

centre of the inlet (Figure 4-8) from 7 s to 9 s the pipe is expanding and entraining more particles into the fluidised region. From 9.5 s onwards the expansion of the pipe appears to slow and more particles are entrained into the pipe lower down the bed. Without velocity data it is unclear if this is a region still flowing but with a higher concentration of particles such as a recirculation zone or if the particles have settled and the morphology in the longitudinal direction has changed.

At 20 mm from the centre of the inlet in the longitudinal direction, the development of the very edge of a bulb type morphology can be seen (Figure 4-9). At 3.5 s a small dilute zone is visible approximately 37.1 mm in height from the inlet and 10.9 mm in diameter, the centre of the dilute zone has a concentration relative to the original bed concentration of 0.26. At 4 s the dilute zone expands laterally and vertically, before decreasing in size again for the next three time steps (4.5, 5 and 5.5 s). The dilute zone then expands again until 8.5 s becoming much larger in the vertical direction (21.6 mm at the maximum depth) and from 9 s onwards the lower part of the dilute zone again becomes more concentrated with particles. At this longitudinal distance from the centre of the inlet it is assumed the observations are at the edge of the fluidised zone and in the recirculation zone. It is likely these temporal changes are showing small fluctuations in the number of recirculating particles in this spatial location as the jet stabilises.

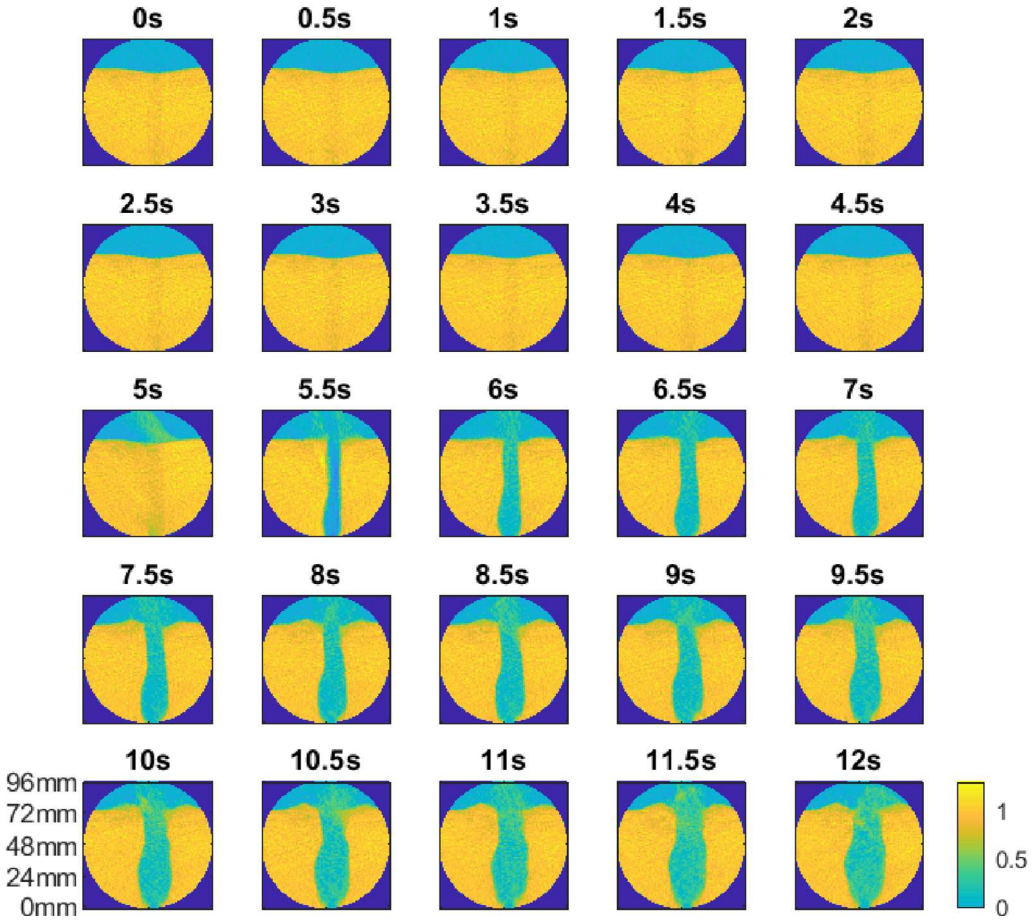

Figure 4-7 Normalised Hounsfield units low porosity bed at 0 mm from the centre of the inlet. From 0s to 4.5s after the onset of pumping there is no effect on the bed at this measurement point. 5s shows particles in the fluid above the bed indicating extrusion has occurred away from the centre of the inlet. 5.5s to 12s shows the bulb morphology developing over time.

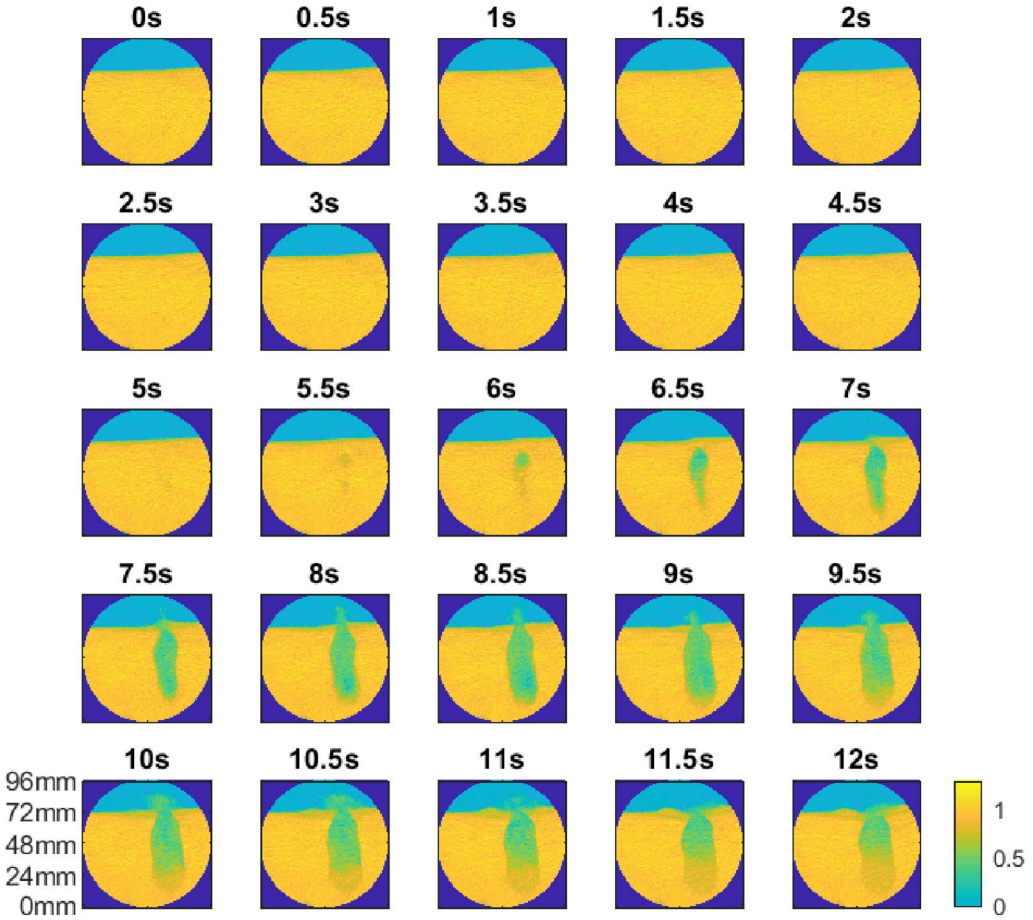

Figure 4-8 Normalised Hounsfield units low porosity bed at 10 mm from the centre of the inlet. 0s to 5 s shows little evidence of fluidisation despite fluid pumping 5.5 s to 12 s shows the development of a fluidisation pipe offset from the centre of the inlet.

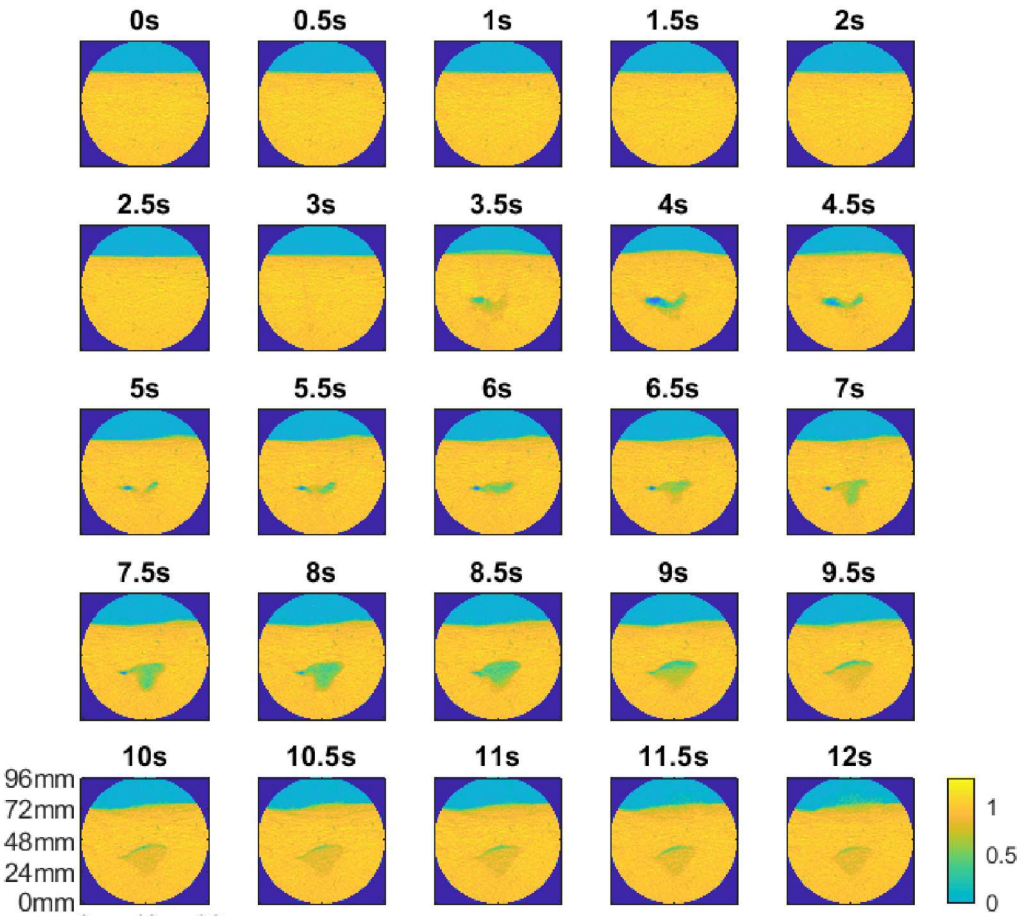

Figure 4-9 Normalised Hounsfield units low porosity bed at 20 mm from the centre of the inlet. 3.5 s onwards shows the formation of a void space. After 8.5 s the void space appears to begin refilling with particles indicating the void space is either moving out of the focus of the scanner or becoming smaller as particles and fluid are elutriated from the system after extrusion.

4.2.2.2 High porosity bed mixture

Void development is visible for the high porosity run (Figure 4-10, 0.4-2 s & Figure 4-11, 1-3s). As previously seen, the void expansion then develops into turbulent mixing and chaotic jet features. This is evident In the sinuous pipe features captured in Figures 4-10, 3-6 s and 4-11, 3.4-5.5 s. For both examples, after 6 s the pipe becomes more central. In Figure 4-10 6 s onwards the concentration is characterised as being dilute at the base of the pipe – close to zero and having a greater concentration of particles higher up the bed at approximately 0.4 of the unfluidised bed average. The high porosity mix shows less stability than the low porosity pipe, as seen in previous chapters. This is likely due to the falling streams of particles that were observed to characterise this bed mix and are discussed in more detail in Chapter 6. The diameter of the high porosity pipe varies between 10.9 mm and 22.8 mm at the centre of the inlet (0 mm in the longitudinal direction once the pipe develops; Figure 4-10). The data set collected at 20 mm from the inlet is at the very edge of the pipe boundaries. The data in Figure 4-12 show a dilute zone fluctuating in and out of the focus of the scanner between 1.5 s and 7 s. This is the very edge of the turbulent mixing zone entering the focus of the scanner as the pipe develops. After 7 s, the pipe is much more stable and in this data set the pipe no longer deviates from the equilibrium position significantly enough to come back into the focus of the scanner.

After extrusion particles can be seen in the overlying water column at all timestamps plotted when measurements are taken close to the centre of the inlet (Figure 4-10). They are particularly visible at 7s, here it is observed that the fluidisation velocity is sufficient to carry the particles above the original bed

height however they do not travel far from the vicinity of the fluidisation event. Therefore it is likely that the particles are fluidising upwards and falling back into the fluidised zone in very close proximity. Further from the centre of the inlet (Figure 4-11 and 4-12) fewer particles are observed in the overlying water column, however where the jet is observed to be breaching the bed surface in the focus of the scanner particles are once again observed (e.g. Figure 4-11, 5.5 and 10 s and 4-11 , 2.5 , 5, 5.5 s).

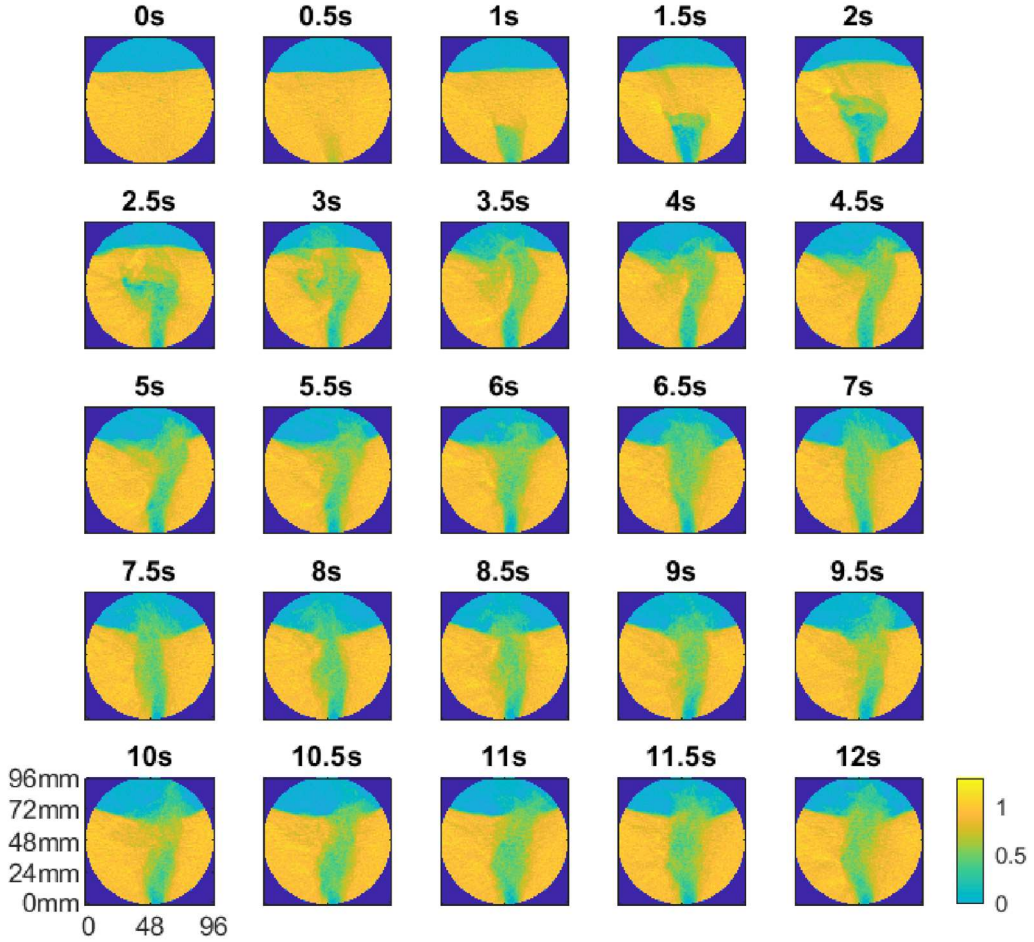

Figure 4-10 Normalised Hounsfield units high porosity bed at 0 mm from the centre of the inlet. Turbulent mixing observed until extrusion at 3.5 s, 4 s - 12 s shows chaotic jet behaviour.

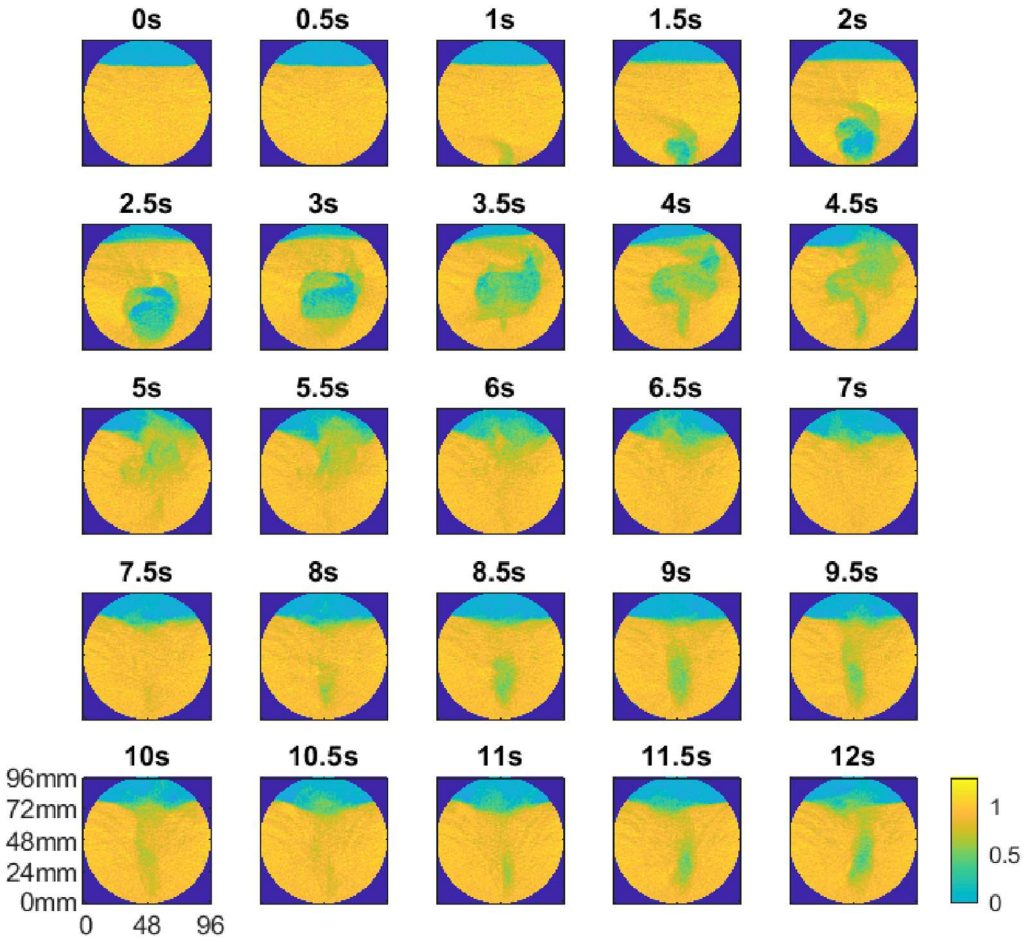

Figure 4-11 Normalised Hounsfield units high porosity bed at 10 mm from the centre of the inlet. Turbulent mixing observed before extrusion at 3.5 s. Particle segregation is visible at 4 s. From 5 s the jet moves out of focus of the scanner however bed disturbance is visible at the surface of the bed. The jet returns to the focus of the scanner in the lower bed from 8 s.

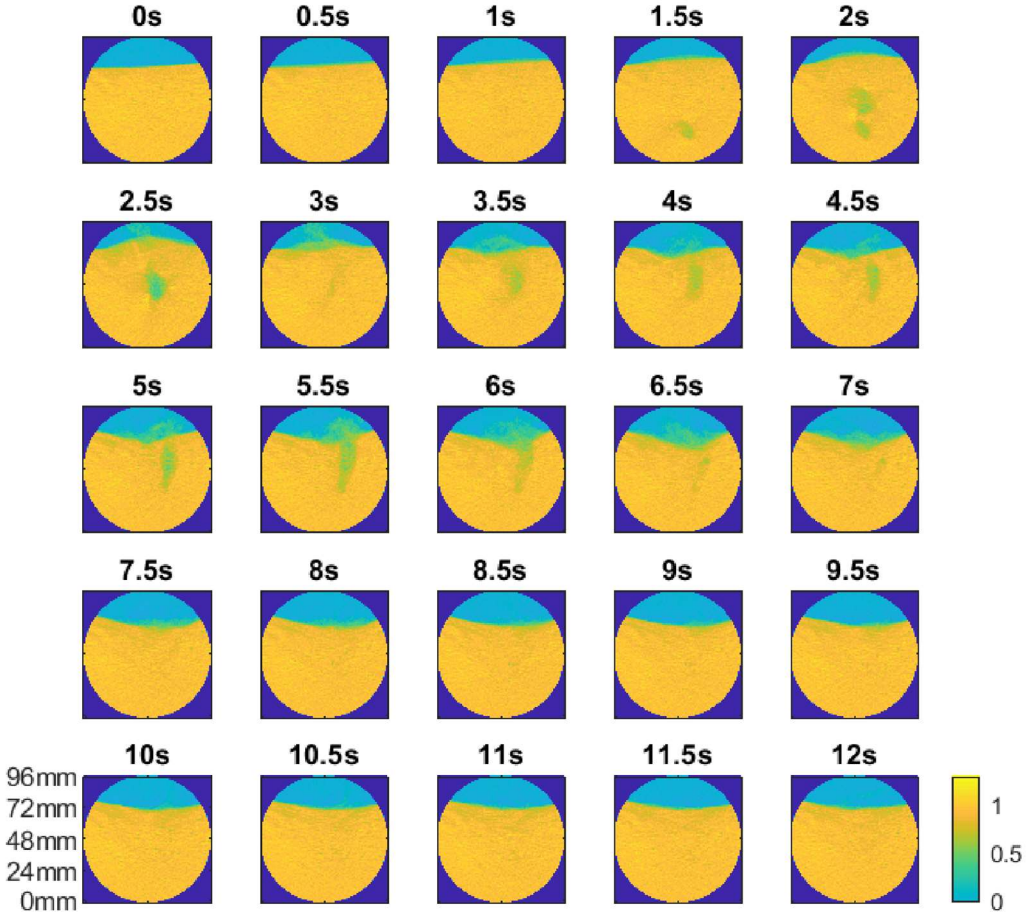

Figure 4-12 Normalised Hounsfield units high porosity bed at 20 mm from the centre of the inlet. The edges of the turbulent mixing are visible from 1.5 s to 2.5 s. At 2.5 extrusion is visible at the surface. Some edges of the chaotic jet visible from 3.5 s to 6.5 s.

4.2.2.3 Very high porosity bed mixture

The very high porosity runs do not show a void developing, more a vertical pipe propagation directly to the surface with little sinuosity or deviation from the central axis (Figure 4-13, 7-12 s). This is characteristic of mono-disperse beds (Philippe and Badiane, 2013). There is some small movement visible in the 10 mm time series (Figure 4-14), representing more dilute regions passing in and out of focus of the measurement point but this is significantly less obvious than for the high porosity bed and not as self-stabilising as the low porosity bed. Interestingly at the 20 mm longitudinal measurement point the pipe is not detectable at all (Figure 4-15). This could be that any movement was focussed in the opposite longitudinal direction, however as the dilute zone in this fluidisation pipe is only between approximately 10 – 18 mm wide when measured in the field of view shown in Figure 4-6 and assuming axisymmetry, it is likely that the bed is actually undisturbed in this measurement region.

In comparison with the high porosity case, particles are again observed to be persistent in the water column above the fluidised zone. The particles appear to be immediately above the dilute zone and do not travel away from the vent. If particles were travelling away from the vent, layers of settling particles would be expected to be observed over the undisturbed bed (Figure 4-13 8 s onwards, 4-14, 5 – 8.5 s). This lack of layers of vented sediment implies that, although the particles are travelling higher in the water column than the original bed height, they are not elutriated from the system. Instead the particles are recirculated in close proximity to the vent.

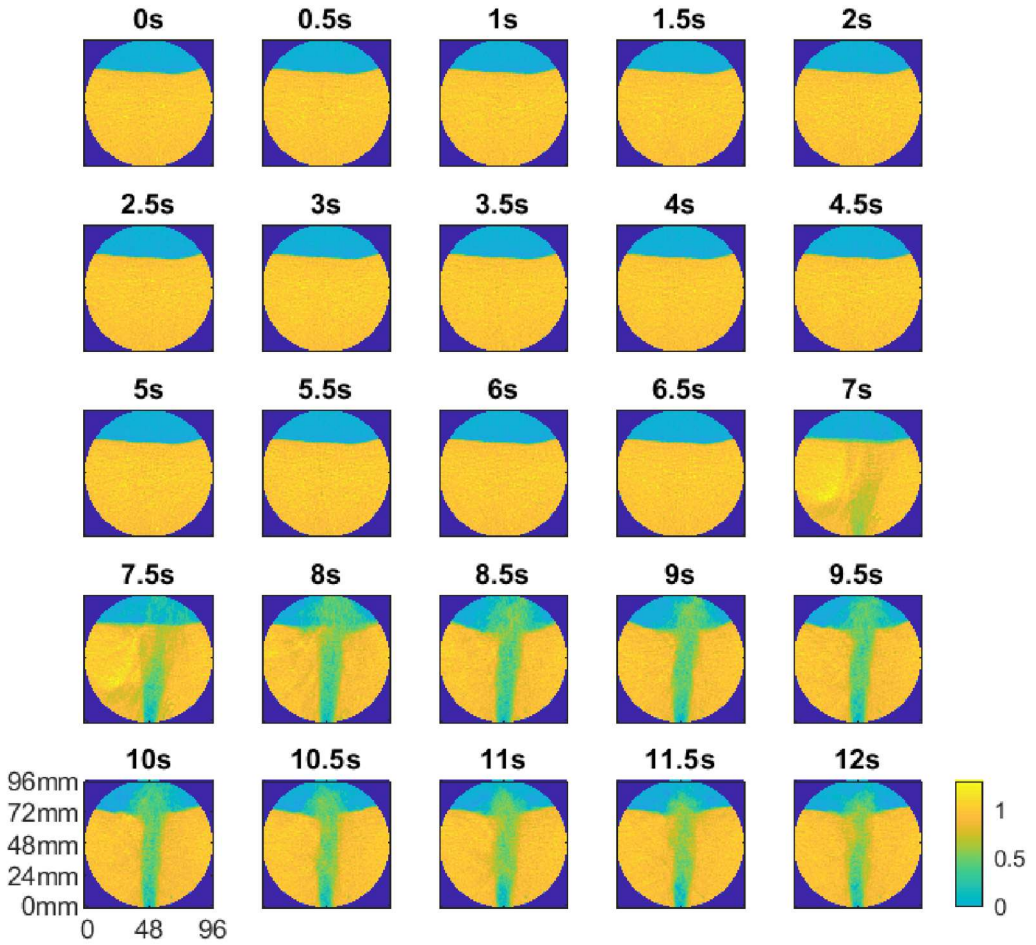

Figure 4-13 Normalised Hounsfield units very high porosity bed at 0 mm from the centre of the inlet. No fluidisation is evident until 7 s. The pipe forms rapidly from 7 s and is very stable with little deflection.

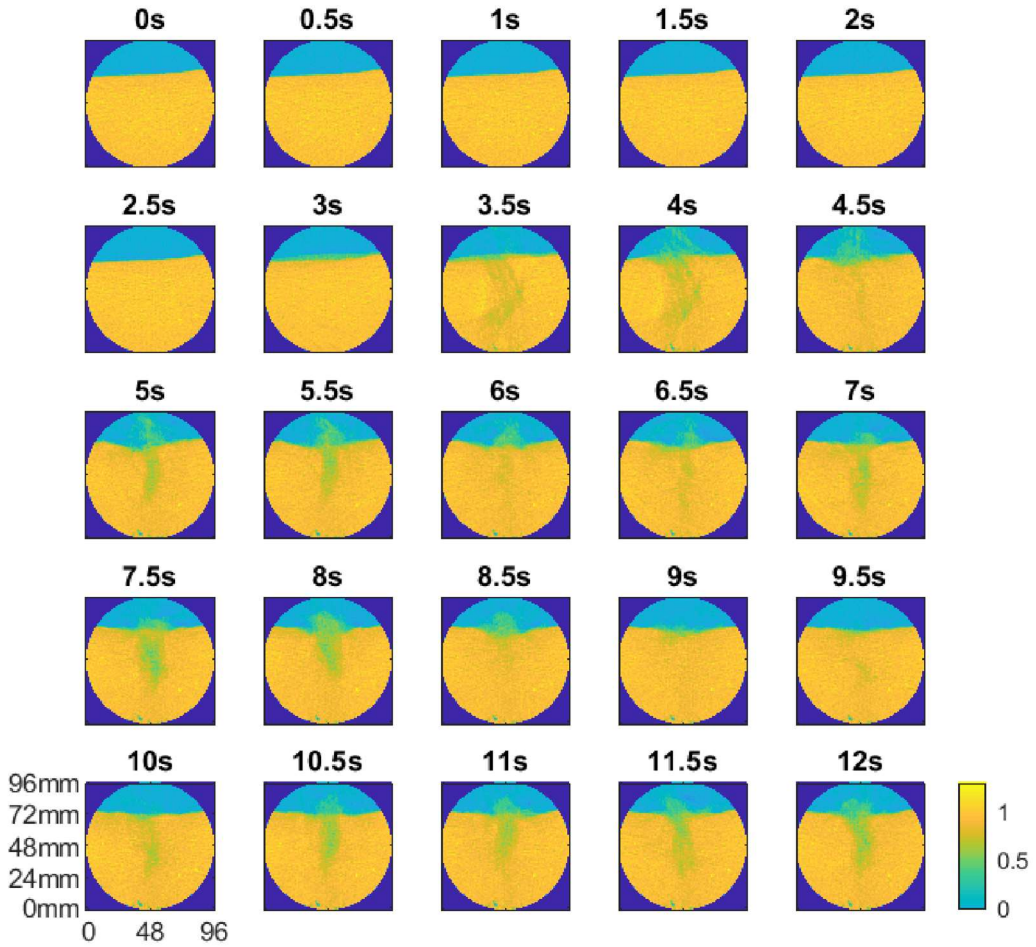

Figure 4-14 Normalised Hounsfield units very high porosity bed at 10 mm from the centre of the inlet. Some turbulent mixing is visible at 3.5 and 4 s. The top of the fluidisation pipe is visible in the upper bed from 5 s onwards.

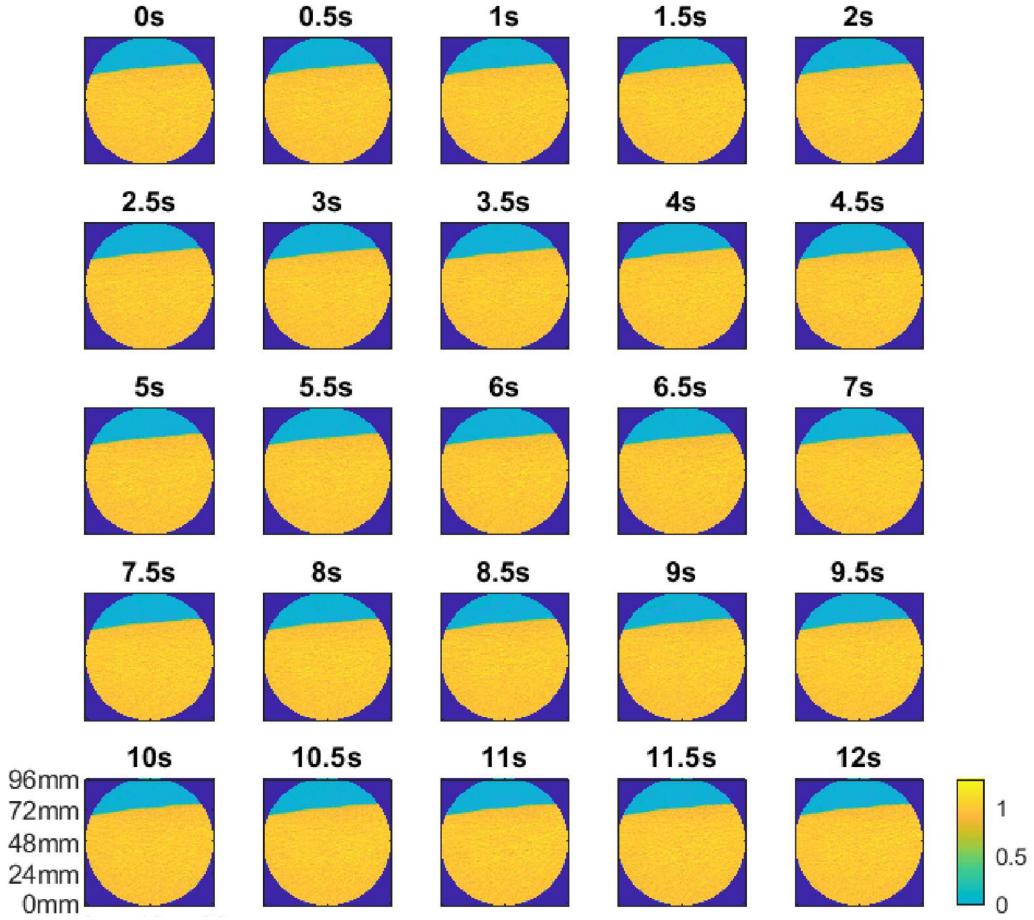

Figure 4-15 Normalised Hounsfield units very high porosity bed at 20 mm from the centre of the inlet. Pipe diameter is only 10 mm for the other measured cases therefore it is likely these data represent the undisturbed bed in this fluidisation event.

4.2.3 Wall regions

The wall regions in each of the characteristic fluidisation pipes have distinctive characteristics for each porosity (Figure 4-16). In the very high porosity pipe, the edges of the pipe have a region more concentrated with particles at approximately 0.65 of the mean value of the unfluidised bed (Figure 4-16 A). The width of this transition to undisturbed bed varies but is roughly of the order of a few millimetres, and contrasts with a more dilute fluidised central region with a HU of around 0.3-0.5 of the mean unfluidised bed. However this is not consistent across the height of the pipe. Above 60 mm the wall boundaries become less clear and there is a greater concentration of particles across the whole diameter of the pipe.

The high porosity bed (Figure 4-16 B) shows a much more gradual transition in the wall region back to undisturbed bed than for the other observed bed mixes. The centre of the pipe is around 0.5 of the HU value of the undisturbed bed and the wall regions approximately 0.6 – 0.8 of the HU value of the unfluidised bed. The thickness of the wall region ranges from approximately 3 mm wide to 6 mm. The very dilute central fluidised zone is present only for the first 24 mm above the inlet, above this there is a greater concentration of particles in the fluidisation pipe. The region of higher porosity in the central zone is much more variable than for other bed mixes and ranges between 10 mm and 20 mm diameter implying that the walls in this sediment mix are significantly less stable for this case at this stage of fluidisation.

The low porosity bed (Figure 4-16 C) has the most distinct wall formation observed within a pipe, showing an abrupt change between an undisturbed bed and a fully dilute flow region that narrows with height. The dilute region

towards the top of the narrowing pipe does not appear to have a greater concentration of particles than is observed lower down the pipe – as is evident in the higher porosity cases. This shows an abrupt difference in wall structure and dilute region characteristics between the low porosity and the higher porosity cases.

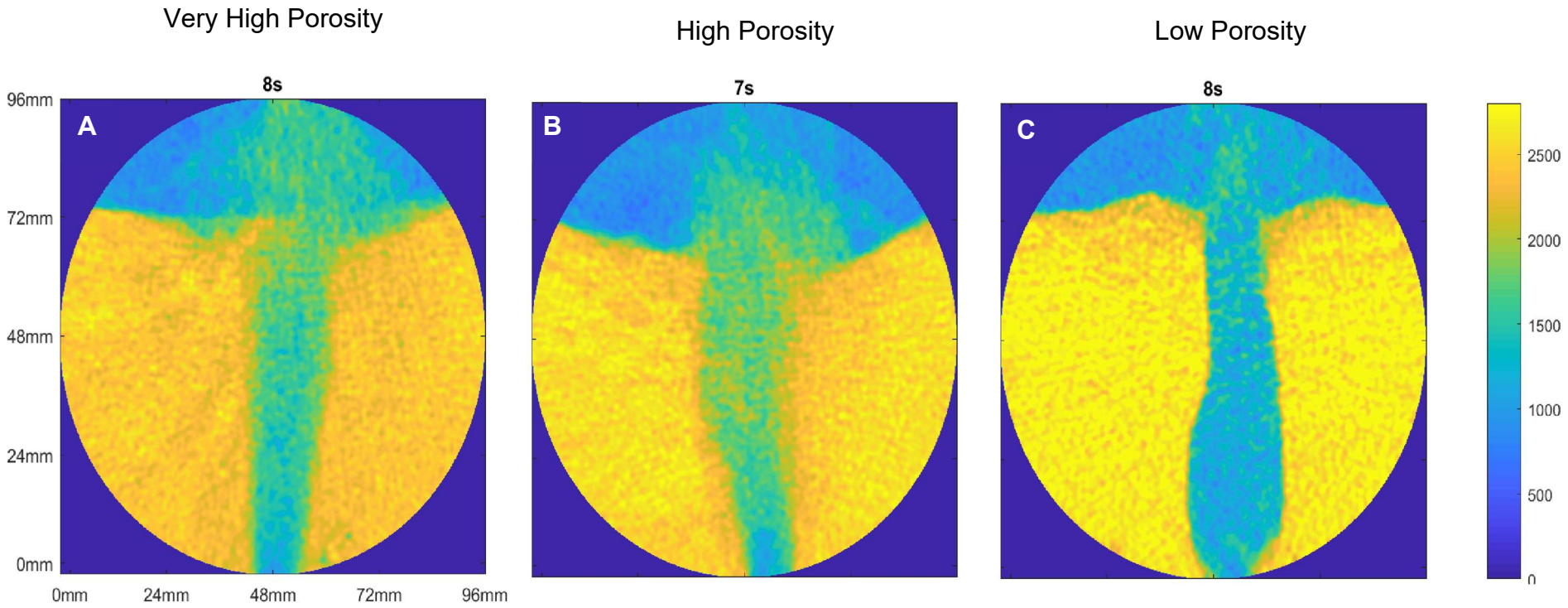

Figure 4-16- Zoomed CT data measured at 0 mm from the centre of the inlet in the longitudinal direction for all bed mixes, A – Very high Porosity bed mix at 8 s, B – High porosity bed mix at 7 s , C – Low porosity bed mix at 8 s.

4.2.3.1 Temporal variation in wall dynamics

In comparison with the time series of the Hounsfield Unit data (Figures 4-7, 4-10 and 4-13) it is observed that the process of pipe formation and thus wall formation is different for each sediment mix. The low porosity bed shows a pipe that expands by eroding the undisturbed bed and thus the transition between fluidised zone and undisturbed bed is sharp and coherent. Temporally the wall is moving laterally across the fluidised zone as more bed is entrained however the location is relatively predictable. In contrast, the high porosity mixture fluidises by turbulent mixing and for the time period measured (0-12.5 s) the pipe has not fully stabilised and thus the structures at the walls of the pipe are less clear in these data. The transition between dilute flow and undisturbed bed is difficult to determine likely as the walls are not yet stabilised and it is postulated herein that this mix is likely to have more easily identifiable wall structures much later in the flow sequence. The chaotic mixing and chaotic behaviour of the jet in the upper bed of the high porosity case mean the high and low concentrations of particles within the fluidised zone are moving frequently and so the walls of this pipe are unstable and unpredictable. The very high porosity mixture fluidised in a similar manner to a mono-disperse bed, as an advancing turbulent jet with little chaotic mixing, as such the higher concentration walls are visible and relatively stable across the temporal evolution of the pipe yet are wider than the low porosity walls indicating a region od segregated particles of the fine particle class at the interface between the fluidised zone and the undisturbed bed.

4.2.4 Residual morphologies

4.2.4.1 Surface depressions

Axial scans were taken after the cessation of fluid flow capturing the full volume of the sediment mixture in order to observe the structures that remain in the fluid bed after a fluidisation event. The surface views showed discernible differences between the remaining surfaces of the plots (Figure 4-17). These plots are analogous to what is visible on the sea floor following a sand injectite event reaching the surface and also bear similarities to seafloor features termed “pockmarks” formed from fluid flow (Hovland et al., 2010). Very high porosity beds - where the two particle sizes used in the bidisperse bed were the closest in size - showed the smallest surface depressions for both diameter and depth (Figure 4-17 A-C). High porosity cases showed the largest diameter surface depressions with sharply angled ridges surrounding the central depression (Figure 4-17 D-F). The depression itself appeared smooth. The low porosity case showed the most uneven surface depressions with rings of particles visible in the depression and the most variation between repeats (Figure 4-17 G-I). The low porosity run capturing the volume from 10 mm to 20 mm from the centre of the inlet in the longitudinal direction shows a lateral offset from the centre indicating that the fluidisation pipe stabilised in the offset position for the duration of the fluidisation and dewatering.

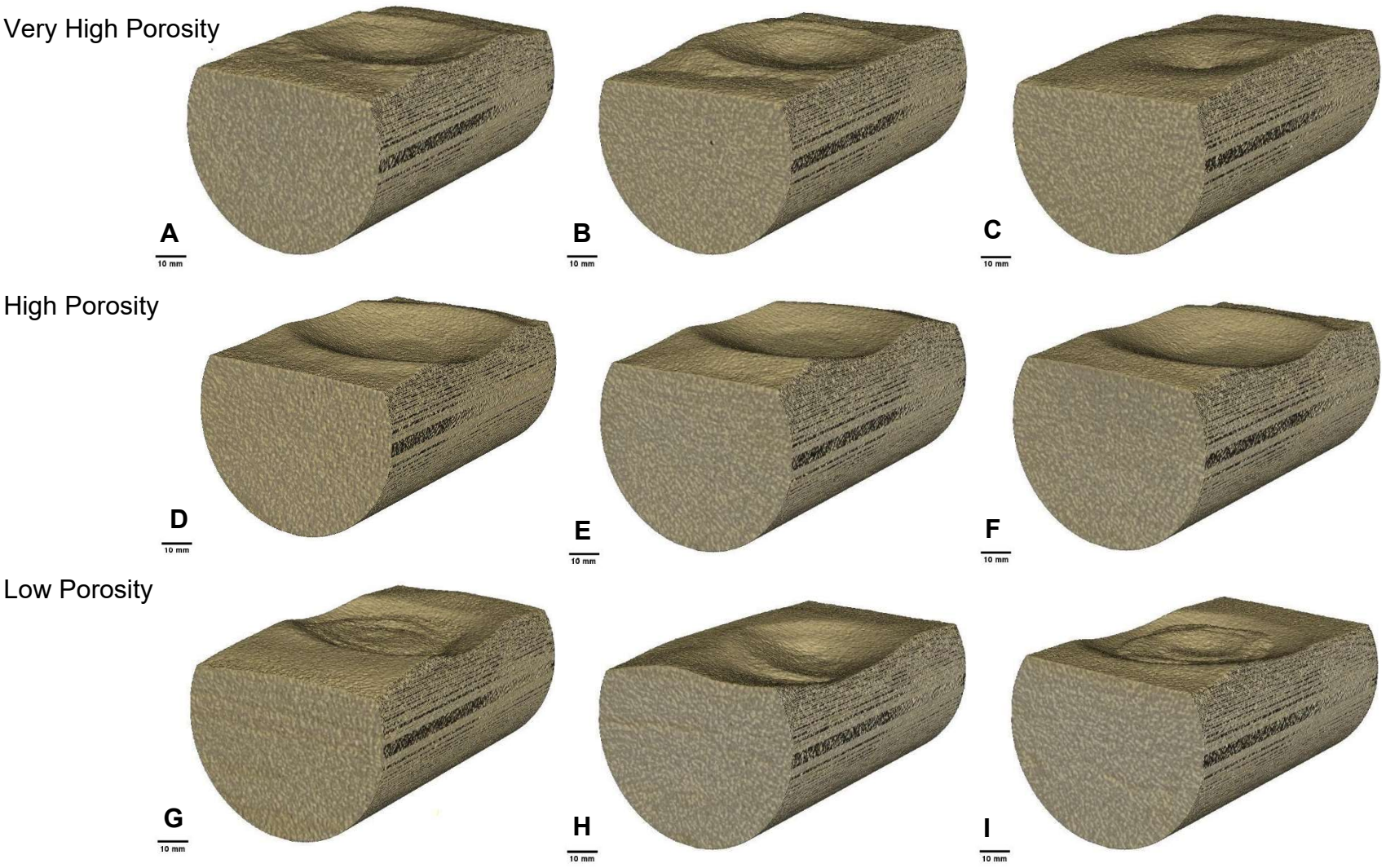

Figure 4-17 Residual morphologies visible from the bed surface

4.2.4.2 Interior structure of residual morphology – low porosity bed mixture

Contour plots of the interiors of the beds after the cessation of fluid flow show that the residual structure is not geometrically similar to the structure during the first 12.5 seconds of fluidisation for the low porosity runs (Figure 4-18, 4-19, & 4-20). The low porosity runs had very steep almost vertical walls within the first 12 s of flow that had an abrupt change between dilute flow and the wall of the fluidised pipe with a bulb at the base narrowing with height (Figure 4-7). In contrast the residual beds show an easily identifiable region of disturbed bed where the bed concentration is significantly lower, this region is narrow at the base and widens at the surface. This is likely to be partly to do with the duration of the fluidisation event captured. Qualitative observations in the two dimensional arrangement for the low porosity bed showed the stages of a fluidisation event (Chapter 5.2.1). For the low porosity case with a high inlet velocity, extrusion occurred at 9 s but geometry was only fully regular after several minutes of fluidisation (Figures 5-2 and 5-3). Therefore the residual upward flaring funnel morphology developed between the end of the CT recording and the cessation of flow 2.5 minutes later.

The low porosity runs capturing the 10 – 20 mm and 20 – 30 mm volumes both show evidence of asymmetry in the flow. The 10 - 20 mm dataset shows the residual morphology is offset as was the flowing region recorded which implies the flow stabilised here and did not migrate to the central position (Figure 4-19). This is interesting in itself as after 2.5 minutes it would be expected that the fluidised zone would migrate to the central position over the inlet due to the inlet position being fixed and the erosive nature of the upwards

jet (Chapter 5.2.6). Further the axial scan of the residual morphology of the run capturing the 20 - 30 mm volume shows that this fluidisation was also offset but in the longitudinal direction (Figure 4-20), evidenced by the visible porous region being much larger from -20 - 0 mm than from 0 -18.75 mm. For this run the measured region during fluidisation was 20 - 30mm in the positive direction. The asymmetry of this flow in the opposite direction to that which was measured explains why there is very little visibility of the fluidised zone in Figure 4-9.

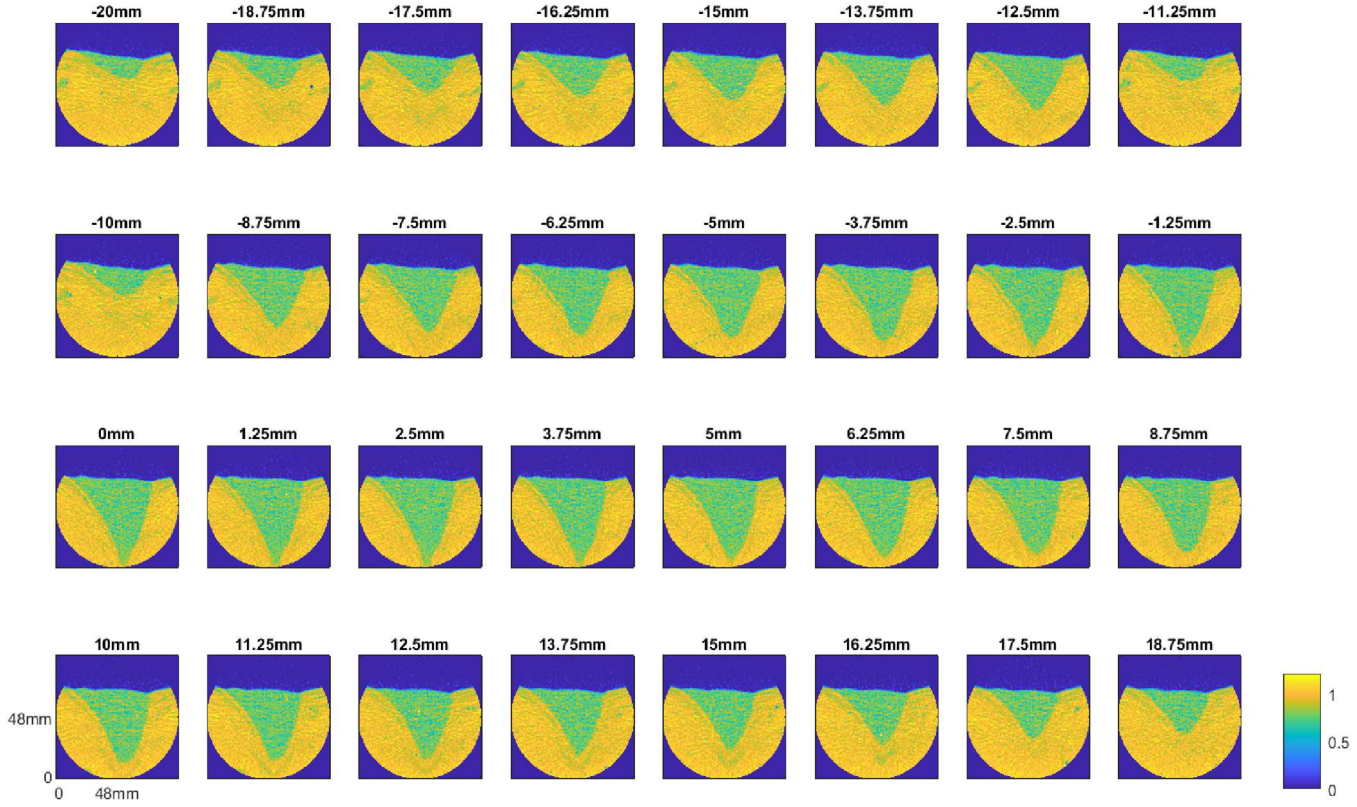

Figure 4-18 Axial scan of the residual morphology for the low porosity run that captured 0 – 10 mm volume during fluidisation.

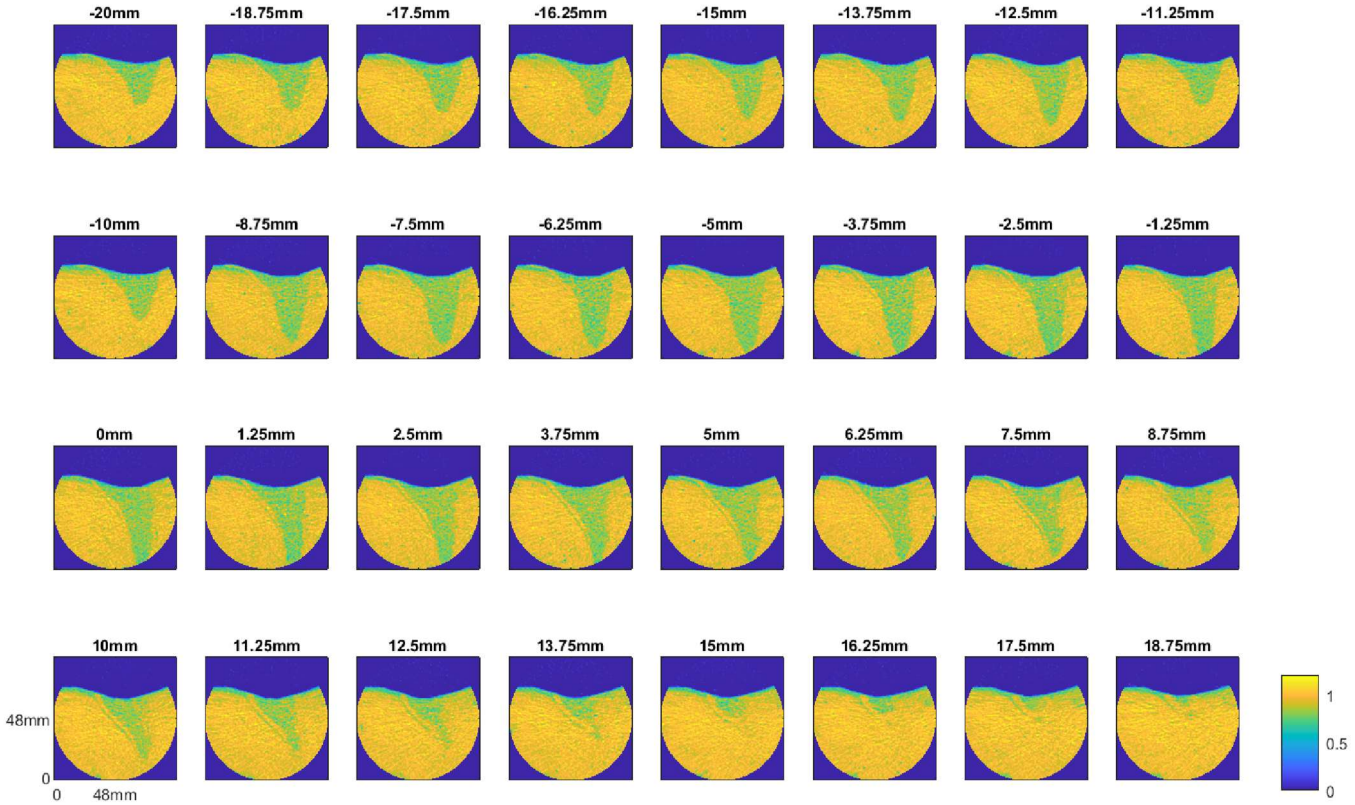

Figure 4-19 Axial scan of the residual morphology for the low porosity run that captured 10 – 20 mm volume during fluidisation.

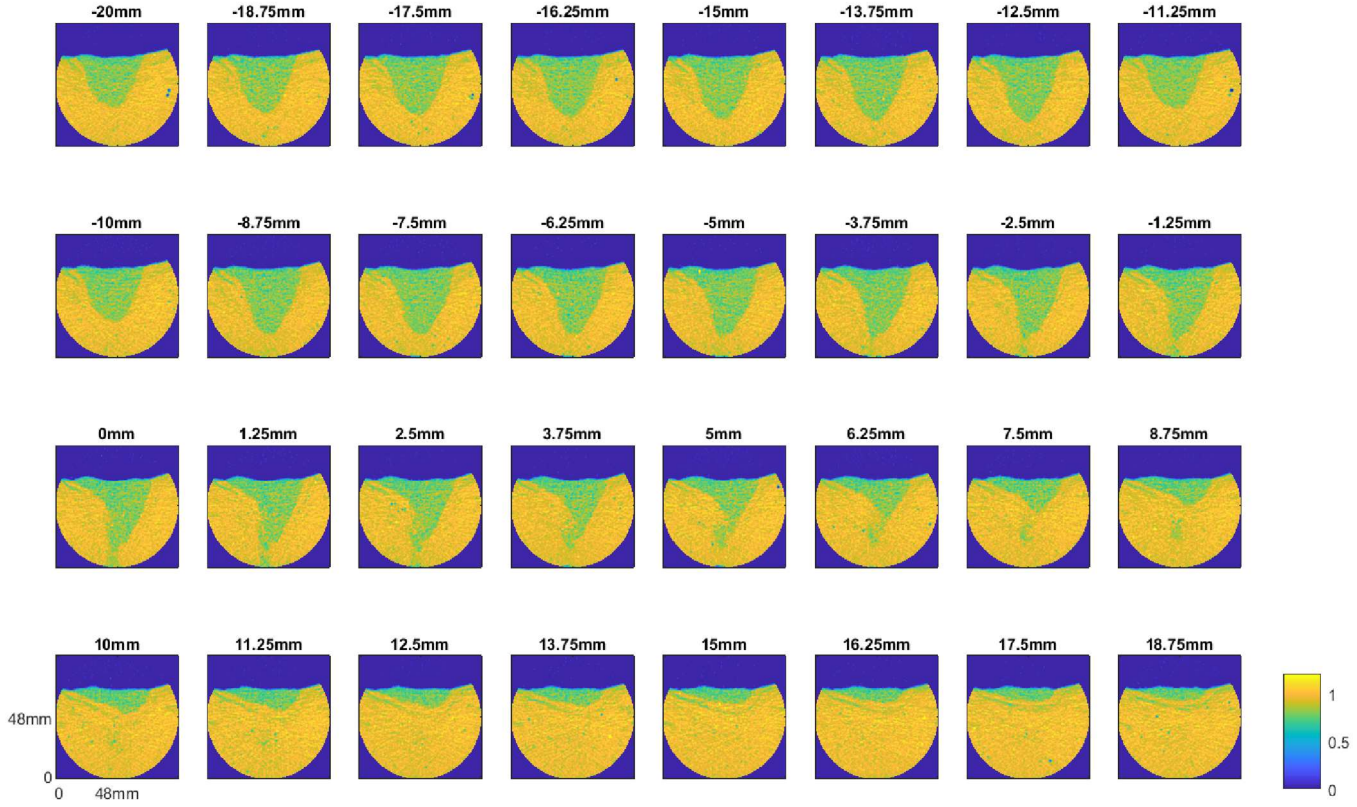

Figure 4-20 Axial scan of the residual morphology for the low porosity run that captured 20 – 30 mm volume during fluidisation.

4.2.4.3 Interior structure of residual morphology –high porosity bed mixture

The high porosity residual morphologies and the very high porosity cases (Figures 4-21 to 4-23 and 4-26 to 4-28) have been plotted with a restricted range of values to aid the visibility of the residual structures; values shown range between 0.6 and 1.2 of the original mean bed value. For the high porosity residual beds (Figures 4-21, 4-22 and 4-23) there is a visible residual structure in each case, similar to the low porosity residual morphologies, showing an upward flaring funnel. The transition between the region that has been fluidised and the undisturbed bed is much more gradual than in the low porosity case. The transition is in fact only distinguishable from the surrounding bed because of the value clamping. However, this is still indicative of a region of higher porosity than the undisturbed bed as blue values represent 0.6 or less of the mean unfluidised bed value. This means that there is a region of higher porosity evident in the remaining bed as a result of the fluidisation event.

Figure 4-22 shows lamination structures in the residual morphology. That is layers of higher porosity and lower porosity sequentially surrounding the central fluidised zone. Figure 4-24 shows an example of these structures after the cessation of flow during the qualitative experiments; blue particles form 20% of the large particle class. It should also be noted that the bed is 25 cm deep in the qualitative runs. Although the laminations in the experiment are not regular they show definitive regions of varying grain sizes. Such layers of varying porosity are reflected in the normalised bed concentrations shown in Figure 4-25. As the bed depth is much smaller for the concentration

experiments, the regions are significantly smaller than in the qualitative experiment.

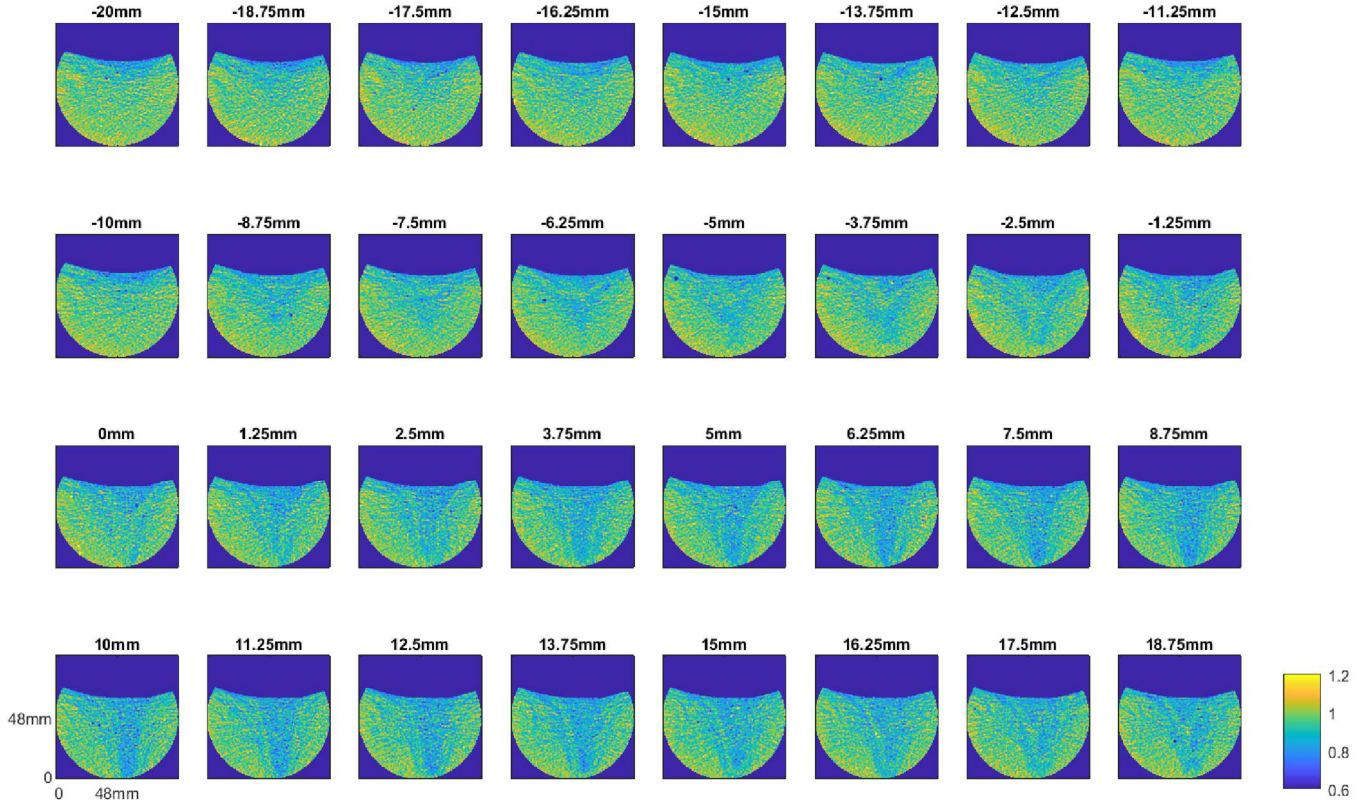

Figure 4-21 Axial scan capturing the residual morphology of the high porosity run that captured 0-10 mm volume during fluidisation.

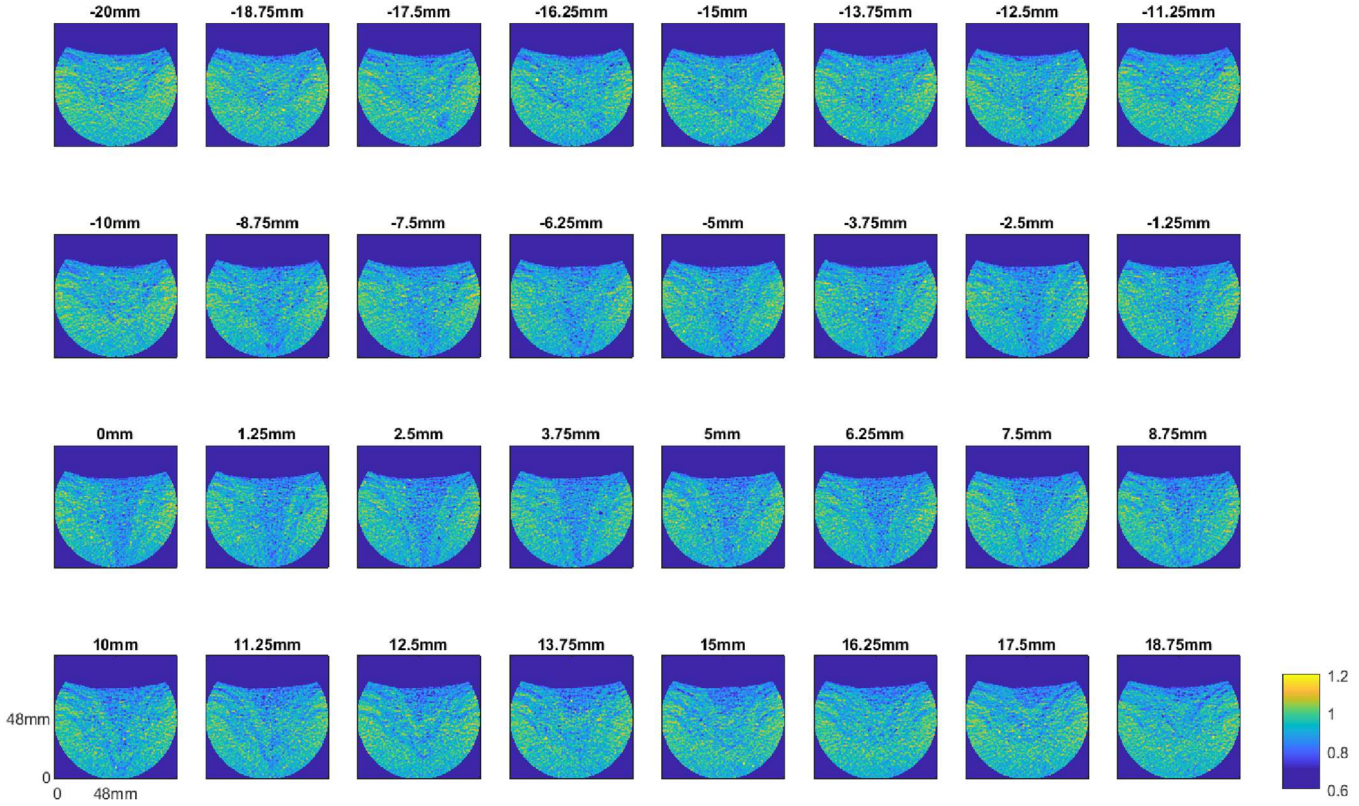

Figure 4-22 Axial scan capturing the residual morphology of the high porosity run that captured 10-20 mm volume during fluidisation.

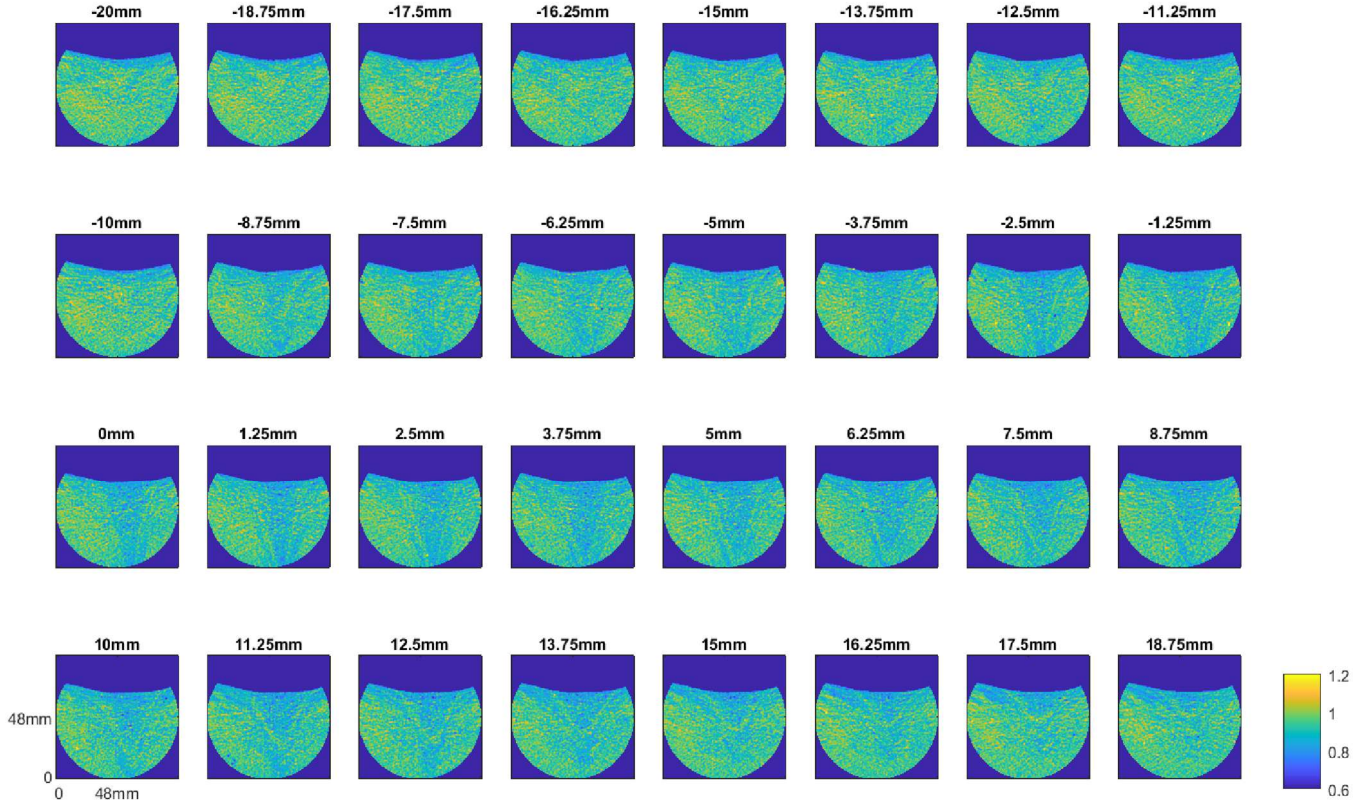

Figure 4-23 Axial scan capturing the residual morphology of the high porosity run that captured 20-30 mm volume during fluidisation.

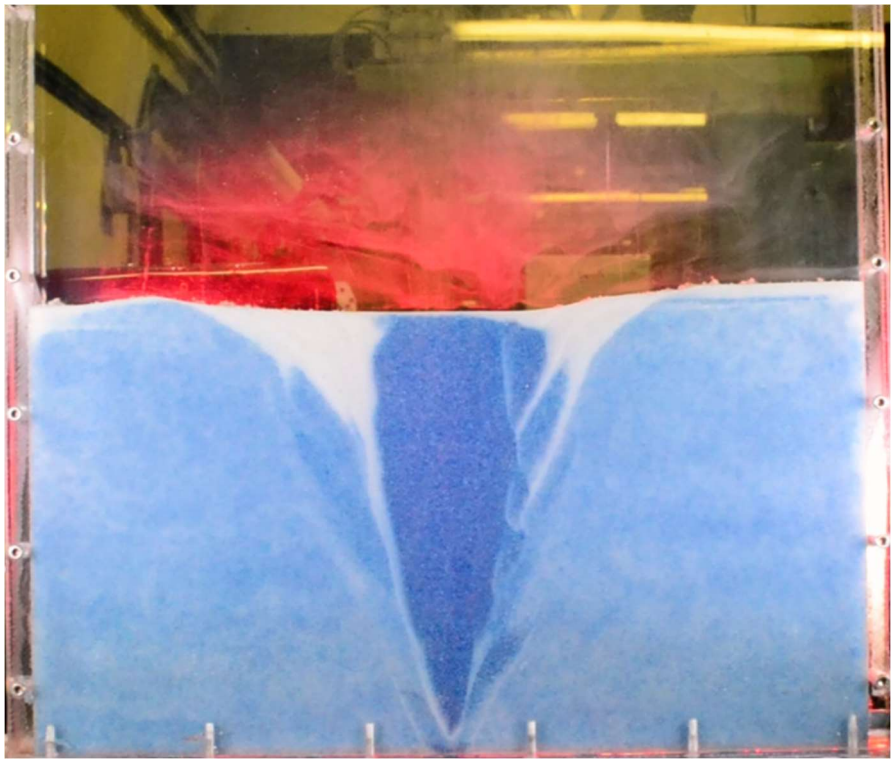

Figure 4-24 Qualitative Experimental Image of laminations formed for a high porosity bed mix.

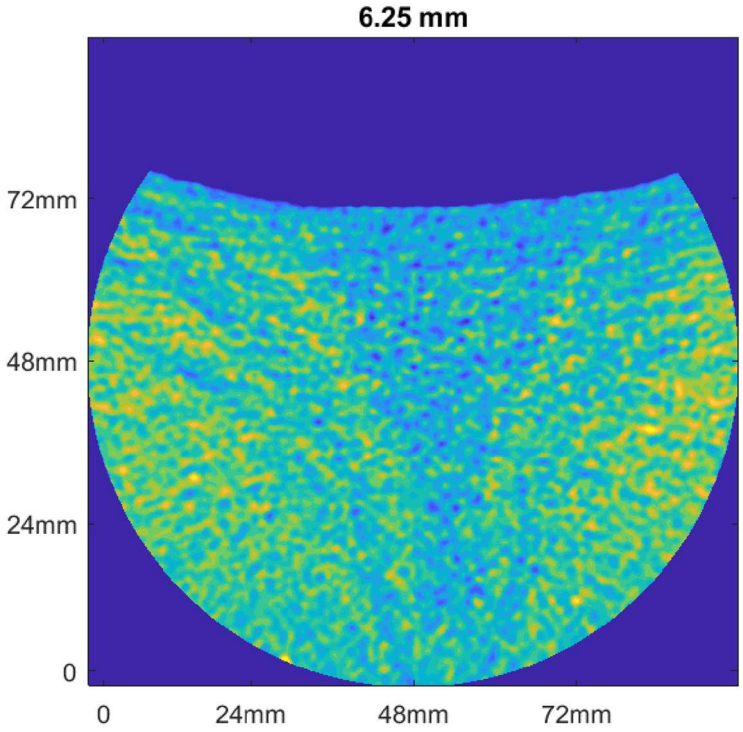

Figure 4-25 Residual Bed morphology for a high porosity mix showing normalised bed concentration.

4.2.4.4 Interior structure of residual morphology – very high porosity bed mixture

Plots of the bed interiors showed no discernible differences in the fluidised region and the undisturbed bed post-fluidisation for the very high porosity mix in the axial scans taken for the bed mixes that collected data for the volumes 10 – 20 mm and 20 – 30 mm (Figures 4-27 & 4-28). The CT numbers across the bed remained largely homogenous indicating the bed largely resembles its initial state in terms of bed density. This bed behaved much like a monodisperse bed (Mena et al., 2017) and it is likely that the overlap in the class sizes is such that the smaller particle class cannot migrate through void spaces as the smaller class does when the ratio of particle classes is greater. However, there was a very slight residual morphology detectable in the HU data for the bed that recorded data from 0 – 10 mm (Figure 4-26). Between 0 mm from the centre of the inlet to -20 mm from the centre of the inlet in the longitudinal direction a very wide funnel outline is slightly visible and for the qualitative experimental runs there was a visible residual morphology (Figure 4-29). There is evidently a small layer of segregated particles from the smaller particle class which, if this also occurred in the three dimensional runs is not detectable in the recorded Hounsfield Units.

The porosity for the very high porosity sediment mix is 0.377, the fine particle class has a porosity of 0.434 and the coarse particle class has a porosity of 0.431, representing a difference in porosity between the mixed bed and the segregated particle classes of 5.4-5.7% making it difficult to distinguish between mixed and unmixed sediments when averaging over pixel spaces and imperceptible if particle sizes have fully segregated from each other.

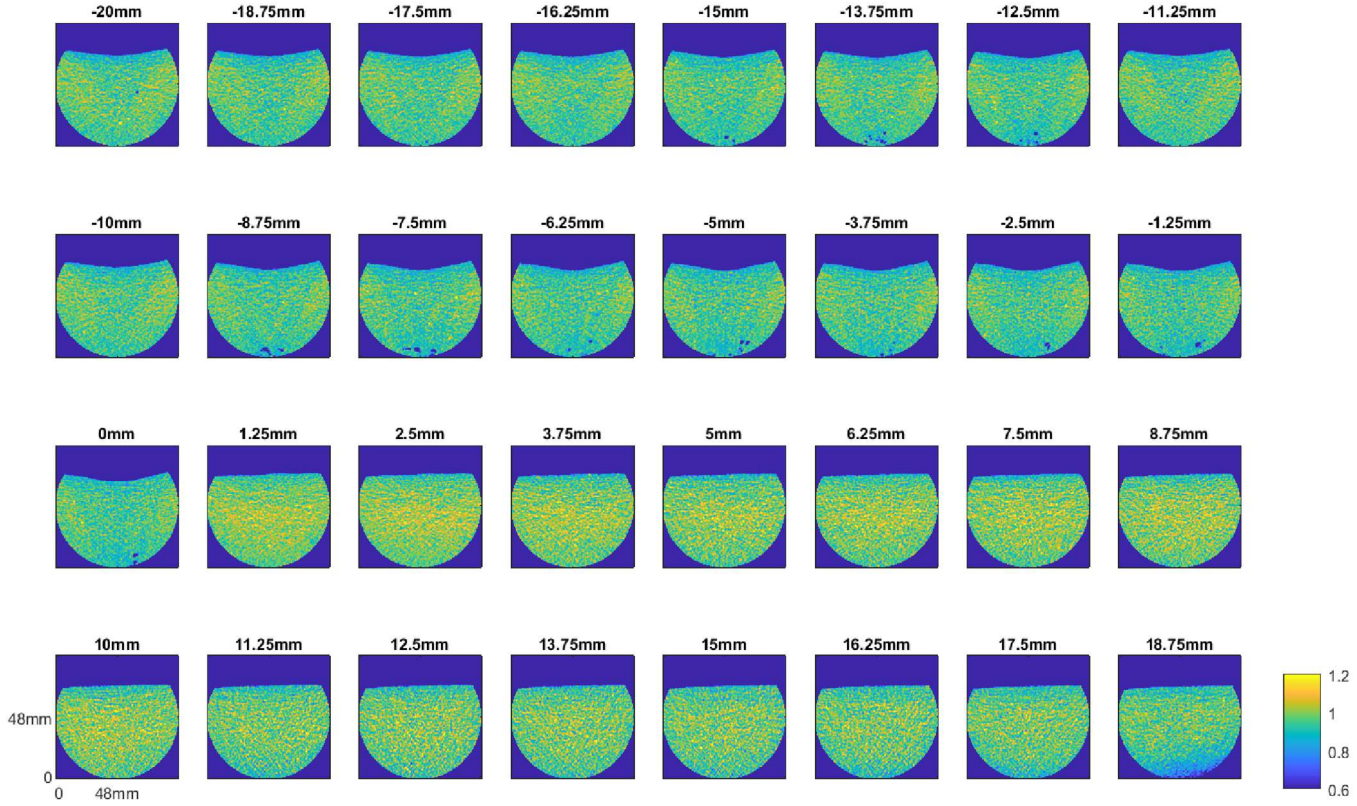

Figure 4-24 Axial scan capturing the residual morphology of the very high porosity run that captured 0-10 mm volume during fluidisation.

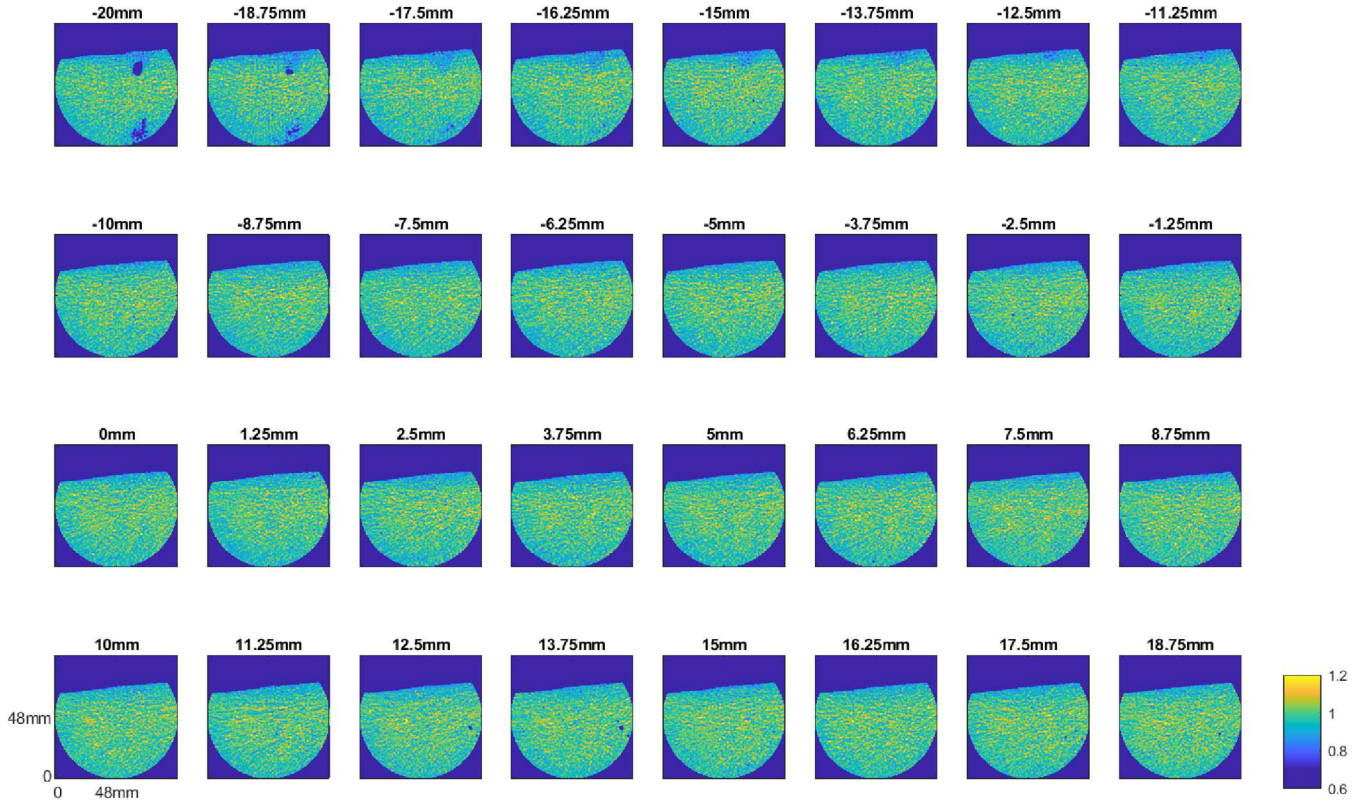

Figure 4-25 Axial scan capturing the residual morphology of the very high porosity run that captured 10-20 mm volume during fluidisation.

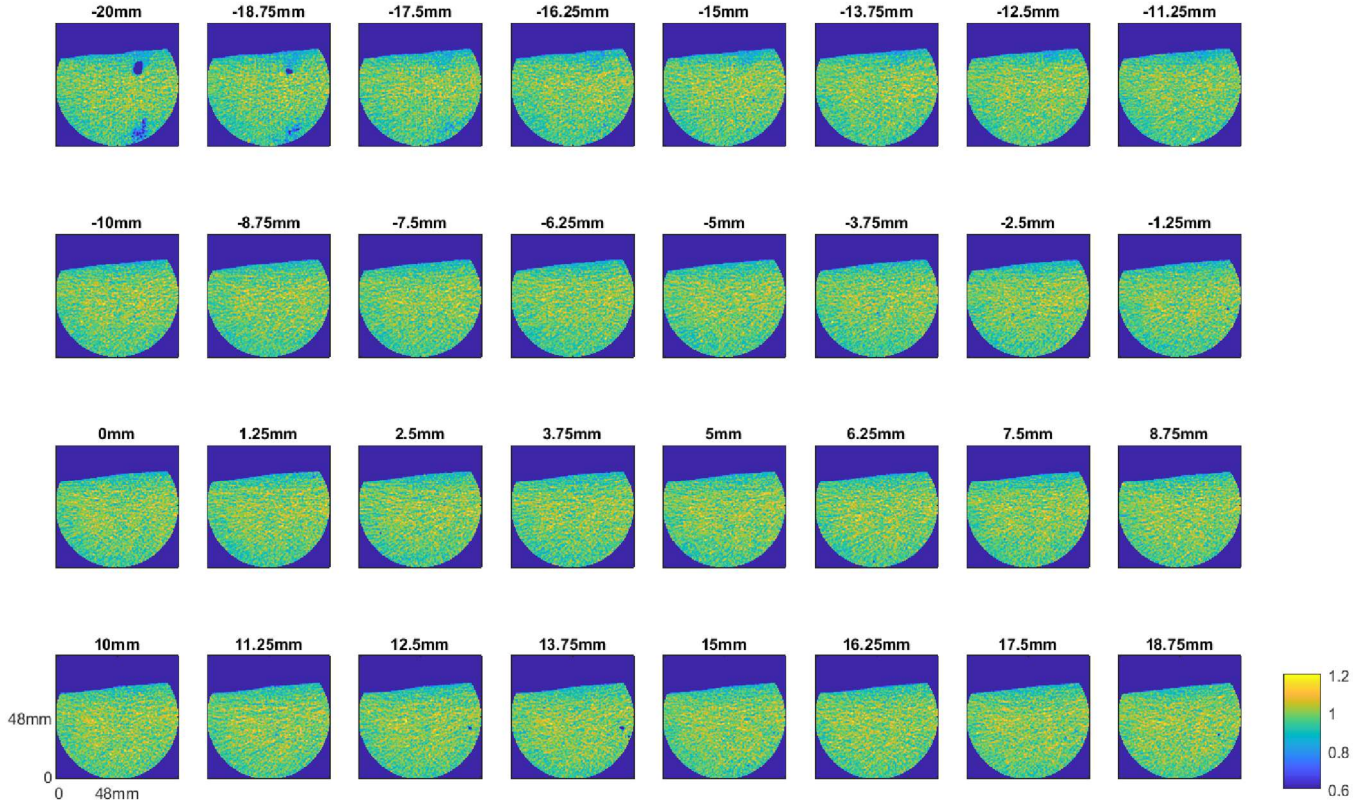

Figure 4-26 Axial scan capturing the residual morphology of the very high porosity run that captured 20-30 mm volume during fluidisation.

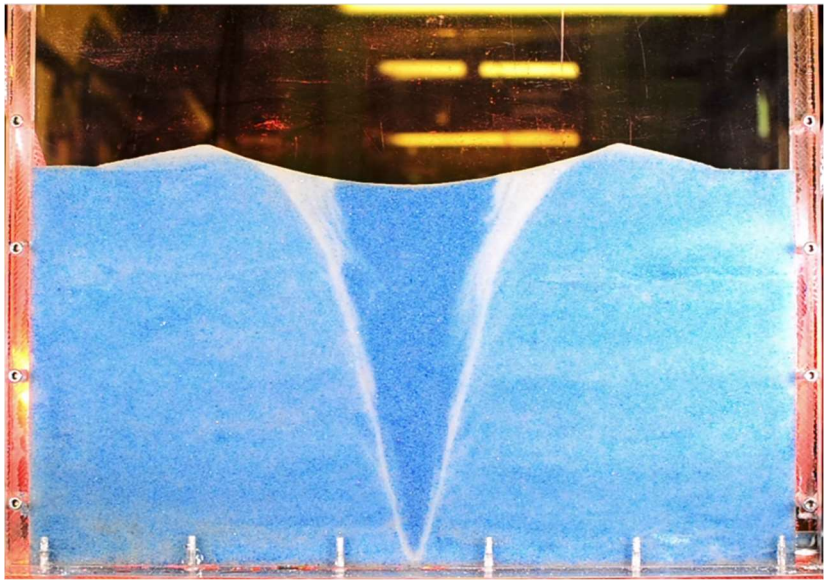

Figure 4-27 Residual morphology of a very high porosity qualitative experiment

4.2.5 Three dimensional morphology during fluidisation

The data slices were concatenated in order to create volumes of CT data and plot isosurfaces of specific HU-values (Figures 4-30 – 4-33). The mean HU-value for the unfluidised bed mixture was plotted in cyan, a HU-value approximately 3 standard deviations lower than the mean unfluidised bed value was plotted in yellow, and the mean HU-value of water was plotted in blue. By selecting a Hounsfield Unit outside of the range of values within the unfluidised bed, distinct regions of higher concentrations of particles, than the dilute region, but less concentrated than the unfluidised bed are identified.

These volume sections show 0 – 10 mm from the centre of the inlet with the centre of the inlet furthest from the field of view and 10 mm closest to the viewer. It is also noted that the vertical scale here is reversed in comparison to previous plots, with vertical measurements taken from the top of the slice (note this is not the top of the tank) and 96 mm representing the location of the inlet in the vertical direction.

This approach identifies the settling zone for each run and likely characterises the wall formation for each sediment mix. Blank zones are caused by the choice of discrete values in such plots and indicate that there are no data in that region exactly corresponding to one of the chosen isosurface numbers.

If the dilute zone were completely devoid of particles it would be expected that this region would show up as blue on the isosurface plots. However, the dilute region in the centre of each pipe shows as white for the very high porosity and high porosity cases (Figures 4-30 and 4-31 respectively). This indicates that no pixel in that region has the exact HU value of water and therefore must have a particle wholly or partially present in that particular pixel.

At 2 s the high porosity case shows the fluidisation event immediately prior to extrusion (Figure 4-30, 2 s). Interestingly two separate regions of dilute particles are advancing towards the surface with a chunk of undisturbed bed visible between the two advancing turbulent jets. As this is not visible in the time series presented for the centre of the inlet this must occur offset from the centre point In the longitudinal direction. At 3 s the turbulent mixing has eroded the undisturbed bed and has entrained much more of the upper portion of the bed. At 4 s however, there again appears to be large sections of particles with the same HU as the undisturbed bed (Figure 4-30, 4 s, right of the fluidisation pipe). As the previous time stamp (3 s) shows this location to be in motion, this indicates that when this bed is not actively fluidised it returns to the same HU value and thus porosity of the undisturbed bed very quickly. Therefore for this bed mix, there is little hysteretic effect of the fluidisation on the porosity of the bed even at small timescales.

The chaotic nature of the jet is once again evidenced across the timesteps for the high porosity bed and it is interesting to note that regardless of the location and timestamp the central dilute zone is always flanked by a less dilute zone immediately before transitioning to stationary bed (Figure 4-30, yellow zones). It is proposed that the regions shown in yellow in Figure 4-30 represent settling particles. As it has been observed that stationary particles appear return to the HU of the undisturbed bed, it follows that these regions must have a higher fluid content than a corresponding stationary bed. These regions are likely to be slow moving particles falling under their own weight after the chaotic jet is further from this location than some critical length scale.

In agreement with the corresponding time series (Figure 4-13), the very high porosity case (Figure 4-31) shows no evidence of fluidisation prior to 7 s. However at 7 s, a wide region of more dilute bed is observed close to the inlet and this is not evident in the time series. This could perhaps suggest that as this bed begins the process of fluidisation, there is a much wider region of dilute bed than would be expected to be directly influenced by the jet dynamics. These dilute regions at the base of the bed could be representative of a wider region of liquefaction, where the bed has dilated in response to the inflow of fluid but only expanded enough to show as more dilute in the recorded HU (as could be expected with a loss of grain to grain contact). It is noted however that it is unlikely that the fluid influx that caused such an expansion would be sufficient to push all the particles in this region into motion, as there is no evidence of wide fluidised regions at the base of pipes in corresponding qualitative data. At 8 s, extrusion has occurred and the wide region of expanded bed has shrunk significantly, indicating a loss of the previously mentioned excess fluid. In the following timesteps this liquefaction zone persists at a reduced size. It is likely that the presence of a liquefaction zone is a result of the very high porosity of this bed allowing some fluid flow in all directions as it is expelled from the inlet. In comparison to the other sediment mixes, the very high porosity bed presents the least resistance to fluid flow through the bed and so it is likely that fluid migrates, albeit at a slower velocity than is observed in the fluidised jet, in all directions.

As observed in the high porosity case, the very high porosity case shows a region of more dilute particles surrounding the dilute fluidised zone in all

timestamps where the bed has been fluidised. It is again assumed this represents the fraction of particles settling at the margins of the fluidised zone.

The high and very high porosity cases show no discernible pixels of pure water in the volume sections (fluidised zone is blank indicating no pixels with the HU value of pure water). In contrast, the low porosity case does demonstrate regions completely devoid of particles. Once again the extrusion event occurs out of the focus of the scanner, however at 5 s a blank zone has emerged above the bed surface, indicating particles are now present in this region, and a dilute bed zone is beginning to become visible (Figure 4-32, 5 s, yellow regions). At 6 s the fluidised pipe is visible with a small bulb at the base and blue regions already visible indicating that there are pixels of clear water in the fluidised pipe. 7 - 12 s shows the bulb expanding steadily. With increasing bulb size fewer pixels of water are visible, implying that more particles are being entrained into the bulb as it expands. Above the bulb is a dilute bed zone outlining a funnel shape overlying the bulb, again the yellow regions are interpreted as falling particles. In this case the recirculation zone appears to meet the top of the bulb which would imply that the particles recirculate in the upper bed and few recirculated particles fall into the lower bulb.

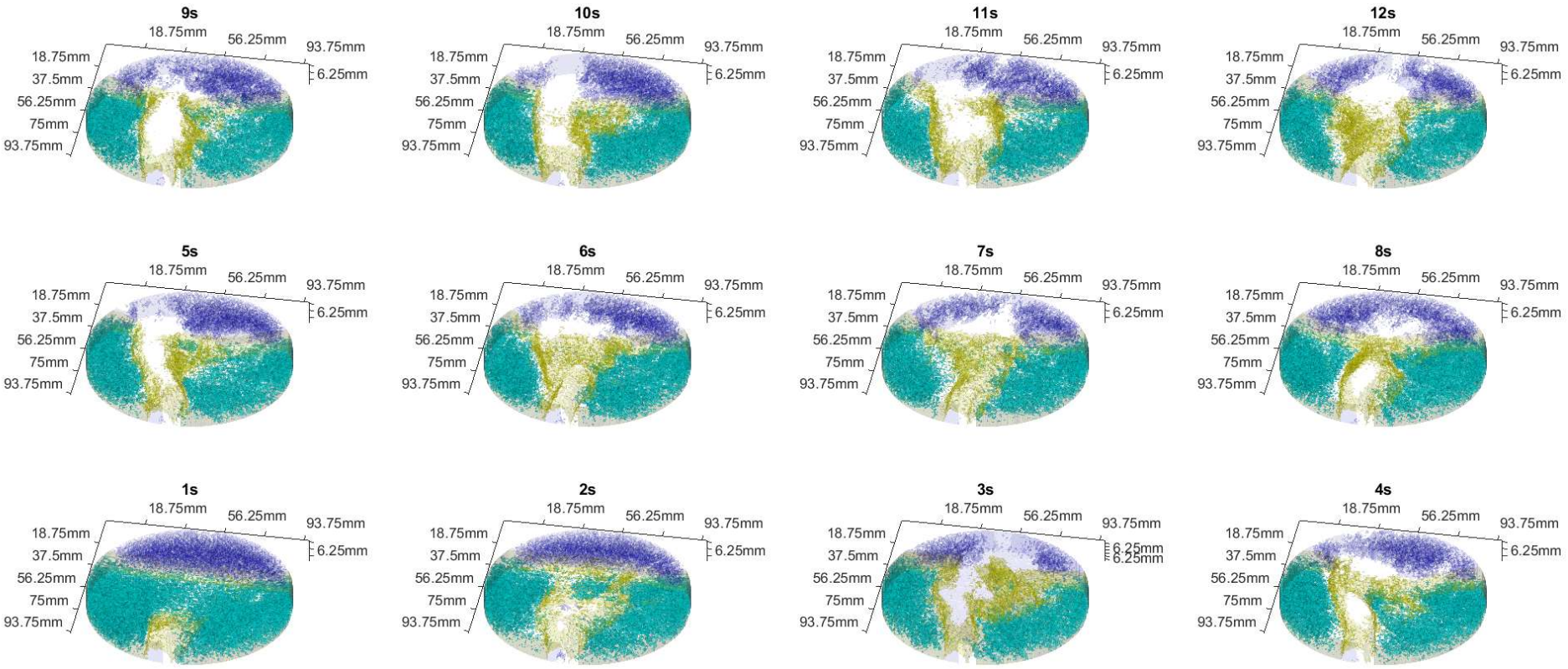

Figure 4-28 High porosity volume 0-10 mm, 10 mm is closest to the viewer - time series of isosurfaces at 980HU (blue) representing the HU of water, 2245HU (yellow) representing the HU value 3 standard deviations lower than mean HU value of the undisturbed bed and 2650HU (cyan) representing the mean HU value of the undisturbed bed value for this high porosity mix.

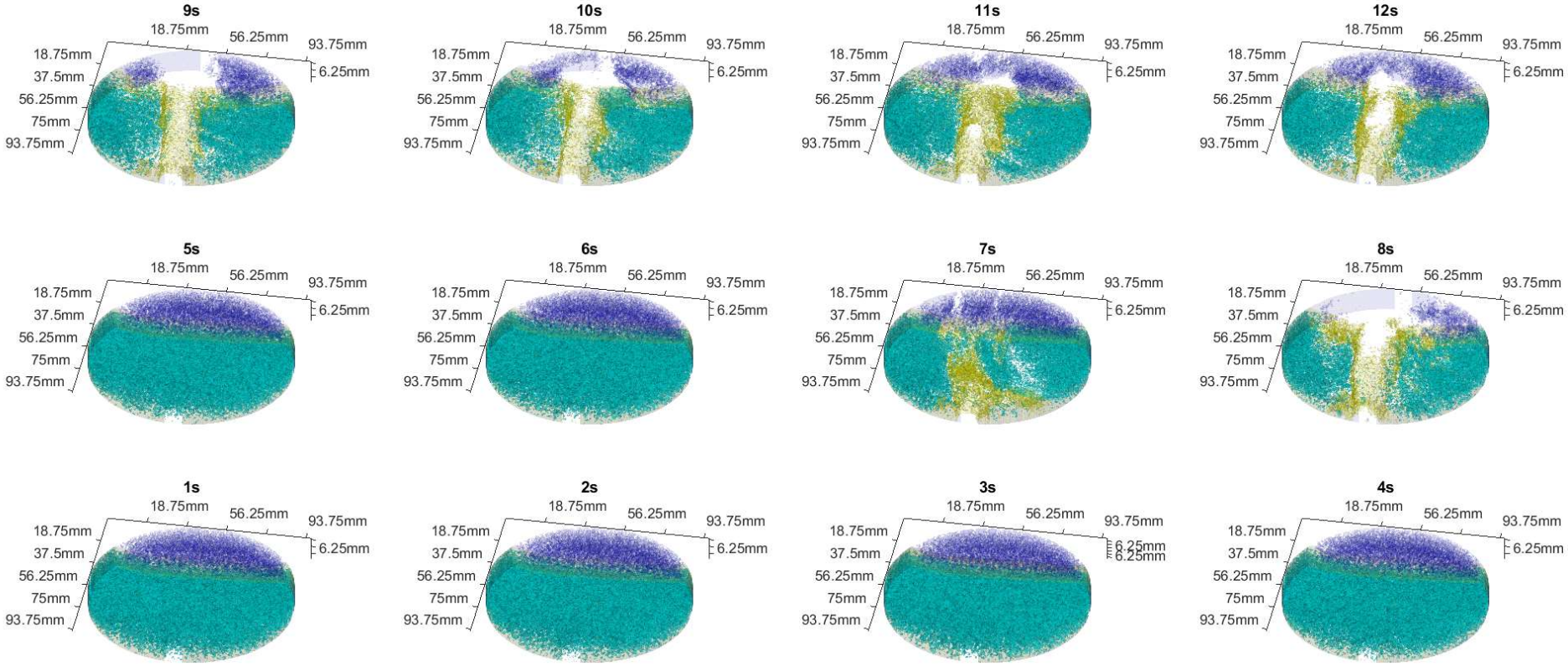

Figure 4-29 Very high porosity volume 0-10 mm, 10 mm is closest to the viewer - time series of isosurfaces at 980HU (blue) representing the HU of water, 2185 HU (yellow) representing the HU value 3 standard deviations lower than mean HU value of the undisturbed bed and 2500HU (cyan) representing the mean HU value of the undisturbed bed value for this high porosity mix.

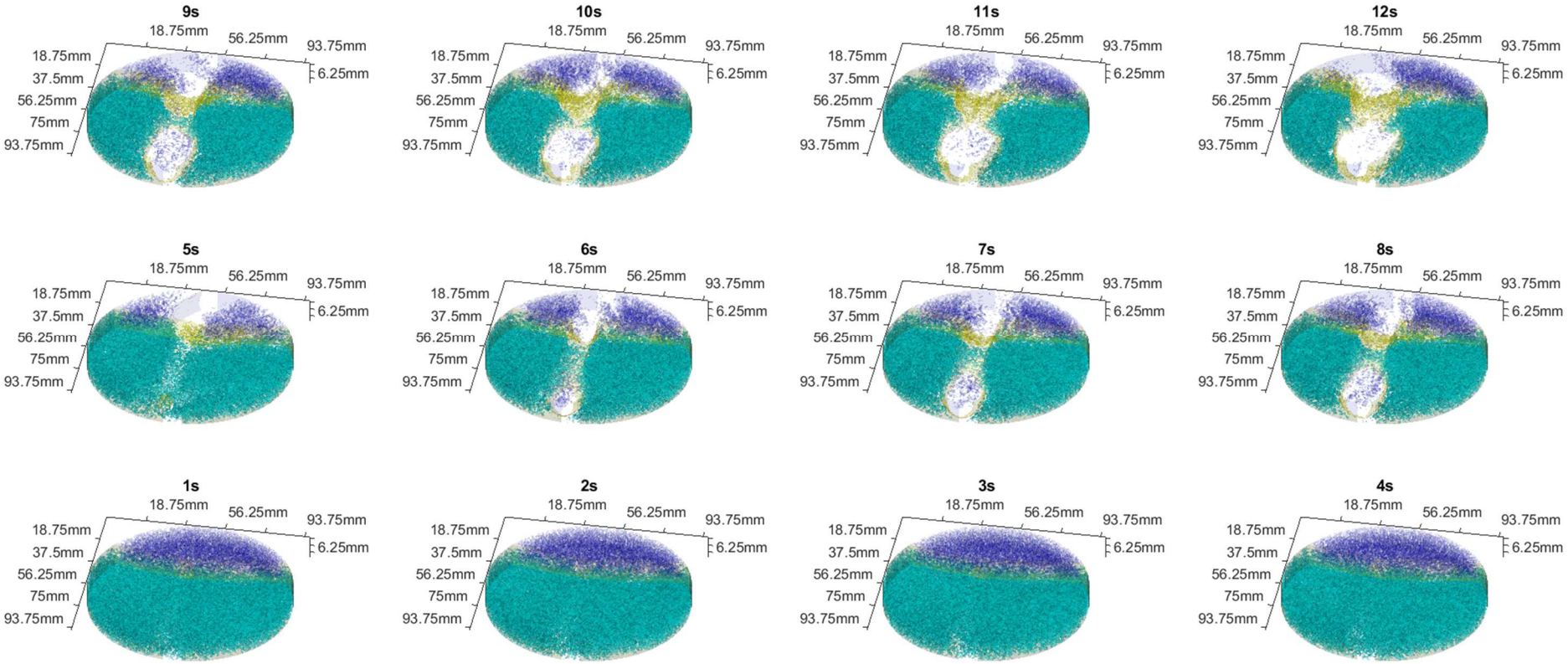

Figure 4-30 Low porosity volume 0-10 mm, 10 mm is closest to the viewer - time series of isosurfaces at 980HU (blue) representing the HU of water, 2200HU (yellow) representing the HU value 3 standard deviations lower than mean HU value of the undisturbed bed and 2750HU (cyan) representing the mean HU value of the undisturbed bed value for this low porosity mix.

4.2.6 Analysis of regions of fluid flow and particle content

In order to quantify the content of the dilute region, plots of the particle volume fraction at the location at the centre of the inlet in both the longitudinal and lateral directions, against height above the inlet are shown in Figure 4-33 for 6, 8, 10 and 12 s after the onset of fluid pumping. The volume fraction is calculated by multiplying the relative bed concentration (calculated from the HU data) by the particle volume fraction of the unfluidised sediment mix (Table 4-2).

All of the beds and time stamps in Figure 4-33 show significant fluctuations in the particle volume fraction; this is due to the largest particles (which are consistent across all runs) being larger than the pixel resolution. However larger features of the concentration profiles are still observed. At 6 s after the onset of fluid pumping the very high porosity bed (Figure 4-33, 6 s, blue triangles) has not yet been fluidised at the location plotted and so the particle volume fraction is steady, aside from the fluctuations previously mentioned. The original bed height is marked with a black dashed line. In comparison the high porosity bed has been fully fluidised at 6 s. Interestingly at the base of the flow the particle volume fraction is between 0.45 and 0.5 and shows a decreasing volume fraction to 0.28 approximately 30 mm above the inlet. Above 30 mm, the particle volume fraction remains steady at 0.33 mm for a further 12 mm displaying only the particle size fluctuation seen in the unfluidised bed. Above 42 mm the variation in the particle volume fraction increases indicating the volume fraction is less homogenous in this region. The low porosity bed shows an initially very high particle volume fraction, 0.8, very close to the inlet, at 7 mm above the inlet the particle volume fraction

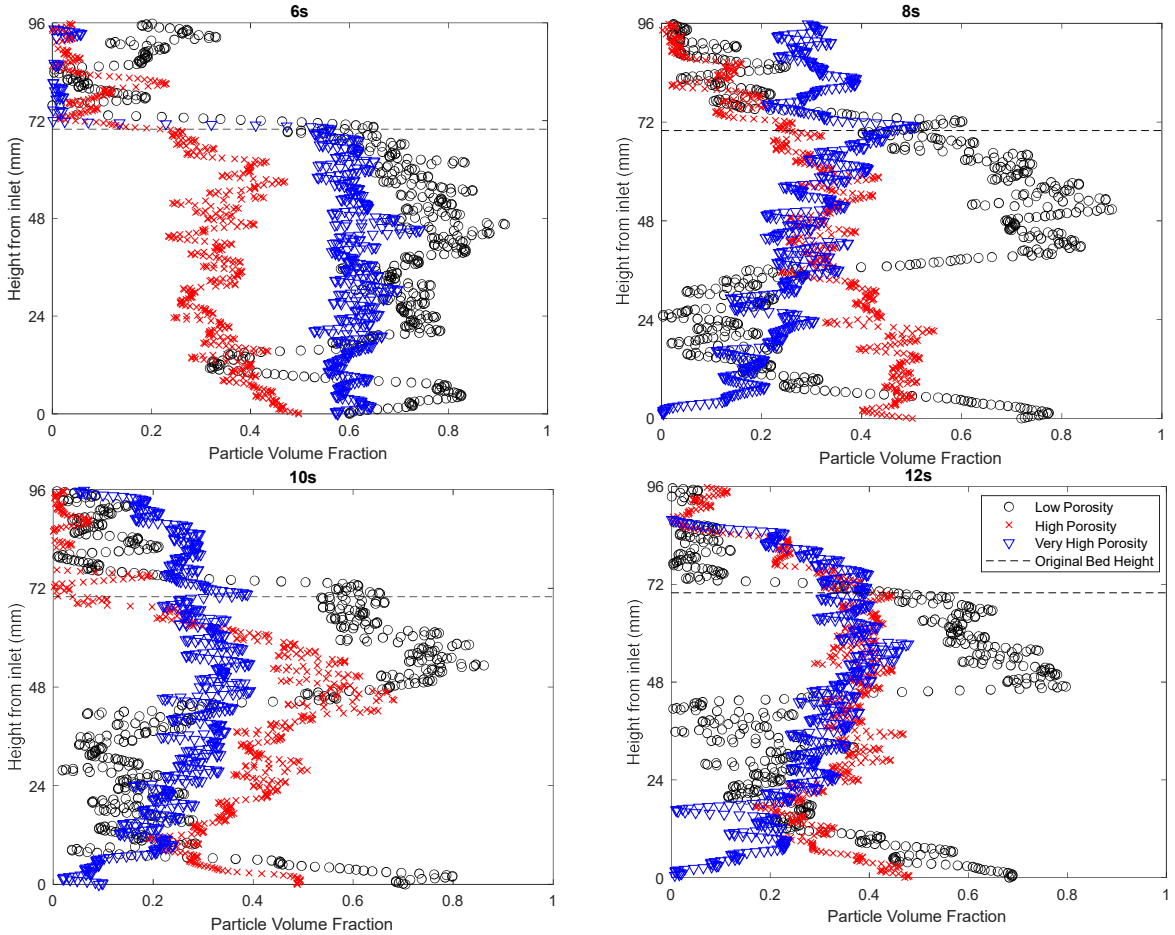

Figure 4-31 Particle volume fraction against height for each run measured at 6, 8, 10 and 12 s after the onset of fluid pumping in the centre of the inlet. Black circles - low porosity bed, red crosses - high porosity bed, blue triangles - very high porosity bed, dashed line represents the location of the original bed height.

drops significantly to around 0.33 before increasingly steeply again to 0.7 at 19.6 mm above the inlet. This dilute zone represents the particle volume fraction in the dilute bulb discussed in Section 4.2.2. At the top of the bulb there is a region of higher concentration that could be undisturbed bed that is not yet eroded into the flow. This is likely as the particle volume fraction is very high at around 0.73. The particle volume fraction is then approximately steady for the next 12.3 mm up to 31.9 mm above the inlet. Between 41 mm and the original bed height (dashed black line) the particle volume fraction shows a steadily decreasing profile. Indicating that the fluidised zone has fewer particles with increasing distance from the inlet. This would indicate that in this region (41 mm and 70 mm) the bed is no longer undisturbed and we are observing the overlying funnel where there is a recirculation of larger falling particles.

At 8 s after the onset of fluid pumping the fluidised zone for the low porosity bed has expanded and this is reflected In the profile of the particle volume fraction (Figure 4-33, 8 s, black circles). The dilute bulb begins at around 8 mm above the inlet and persists to 37.5 mm above the inlet with the particle volume fraction fluctuating around at 0.12. Above 39.9 mm the particle volume fraction is fluctuating around approximately 0.8 and above 58 mm from the inlet the particle volume fraction displays the same steadily decreasing profile with distance from the inlet as at 6 s, indicative of a recirculating region. The high porosity bed (Figure 4-33, 8 s, red crosses) also displays this decreasing profile in the upper bed above 22.1 mm, decreasing from a particle volume fraction of 0.49 to 0.25 at the interface with the overlying water column. However the concentration profile for this bed differs from the low porosity

case in that the most concentrated part of the bed is closer to the inlet and is relatively steady at 0.48 for the first 22.1 mm above the inlet. By comparing the vertical concentration profiles with the equivalent contour plot (4-10 8 s) we can see that at 8 s the dilute zone has been deflected away from the centre-line. As such, this region of higher volume fraction is likely to be the falling particles which will then recirculate back into the flow as the jet moves again. At 8 s the very high porosity bed once again shows the steadily increasing volume fraction with height which could be representative of the velocity diffusion observed in the supra-jet regions in Chapter 4 or, as this is still early in the pipe development, could be indicative of recirculating particles typical of the turbulent mixing stage discussed in Chapter 6.

It is interesting to note that the very high porosity case has increasing particle volume fractions with distance from inlet whereas, in the upper flow region of the high porosity and low porosity fluidisation events there is a decreasing volume fraction with height from the inlet. This could be due to the number of particles elutriated from each system. Very few particles can be elutriated from the very high porosity case as the particles are much larger and therefore require greater velocities to be fully removed from the system. In comparison the low porosity case has very fine particles in the fine particle class and, as previously discussed, many particles in this class can be elutriated, therefore in the upper bed the particles that persist in the system are of the coarse particle class. This would suggest that the high concentrations observed in the upper bed are recirculated in this region as fluid velocities are not exerting sufficient drag force to carry the particles away from the fluidisation pipe.

At 10 s after the onset of fluid pumping the dilute bulb In the low porosity case has expanded again and now persists to 44.6 mm above the inlet but the profile largely follows the same characteristics as at 8 s (Figure 4-33, 10s, black circles). However the more variable high porosity case shows a different particle volume fraction profile again (Figure 4-38, 10 s, red crosses). From 3 mm to 16 mm above the inlet is a dilute zone with a particle volume fraction of around 0.35, the particle volume fraction then steadily increases to around 0.55, 54.9 mm above the inlet. Above this point the particle volume fraction steeply decreases back to the clear water zone. The very high porosity case shows a slight change in profile in that instead of increasing in particle volume fraction for the full height of the fluidisation pipe the concentration becomes relatively steady at 43.3 mm above the inlet, the particle volume fraction fluctuates around 0.34 and this persists into the water column up to 87 mm above the inlet.

The very high porosity case continues these profile characteristics and remains largely unchanged at 12 s (Figure 4-33, 12 s, blue triangles), similarly there is little development between the 10 s profile and the 12 s profile for the low porosity case (Figure 4-33, 12 s, black circles). Once again however for the high porosity case (Figure 4-33, 12s red crosses) the particle volume fraction profile has changed. The initial dilute zone profile largely remains the same as for 10 s, however above this there is a less steep increase in particle volume fraction which becomes relatively steady above 36 mm fluctuating around a volume fraction of 0.38 which continues to the interface with the overlying water column.

4.3 Discussion

4.3.1 Comparison to the two dimensional case

By comparing the time series generated in this run of experiments to the two dimensional experiments (See Chapter 5 for qualitative images), it is clear that the two dimensional experiments are a comparable analogue for the three dimensional system. Geometrically there is only a small difference between the 3D measurements of the residual geomorphology and the two dimensional scans. Measurements were taken on the residual morphologies after the cessation of flow as there can be no further change in the morphology after this point and it is no longer subject to the temporal variation in the fluidisation process. The two dimensional high porosity bed yields a residual fluidised morphology diameter of 62.6 mm at a height approximately 70 mm above the inlet (Figure 4-22, 0 mm) and the equivalent three dimensional case is 68 mm. The low porosity three dimensional fluidisation event has a diameter at the top of the fluidisation pipe in the centre of the inlet approximately 70 mm above the inlet of 66.2 mm (Figure 4-18, 0 mm) and in the two dimensional fluidisation event there is a 72.5 mm diameter residual fluidised morphology. This represents an 8.7% variation between the two pipe diameters. This could perhaps be considered a significant difference, however the same measurement from the subsequent three dimensional runs yields a residual fluidised morphology diameter of 44 mm (Figure 4-19) and 64 mm (Figure 4-20) as such the variation between the two dimensional and three dimensional morphologies appears to fall within the expected variation of the pipe geometry. The time taken for the fluidisation pipe to reach the surface

necessarily varies between the three dimensional and two dimensional examples as the initial bed height varies between the two sets of experiments. The initial bed height for the two dimensional experiments is 250 mm and for the three dimensional experiments is 70 mm.

The high porosity case is seen in the time series of the CT data to fluidise through chaotic mixing (Figure 4-10), qualitatively this is incredibly similar to the fluidisation process seen in the qualitative and quantitative data in the two dimensional experimental runs, examples of which are shown in Figure 4-34 (left and middle).

The low porosity case however is observed in the two dimensional system to fluidise by hydraulic fracture followed by erosion of the undisturbed bed and turbulent mixing (Figure 4-35, left and middle). As the initial fluidisation happened outside of the range of the scanner (i.e offset from the centre location – Figure 4-7 particle extrusion evident at 5 s), it is unclear if a hydraulic fracture also occurred in the three dimensional cases. However an offset of the initial fracture is also evident in the 2D image (Figure 4-35 left). The three dimensional concentration images are characterised by an expanding dilute bulb with low particle concentrations and a narrow dilute pipe connecting the flow with the surface for one fluidisation event in the low porosity sediment mix (Figure 4-7) and a highly stable dilute pipe in another (Figure 4-8). Two dimensional runs were characterised by an expanding void space – which could be analogous to the bulb in three dimensions – and a channelised pipe reaching the surface. An example of how the narrow pipe in Figure 4-35 expands over time to a wide channel, via a dilute bulb is shown in Figure 4-36.

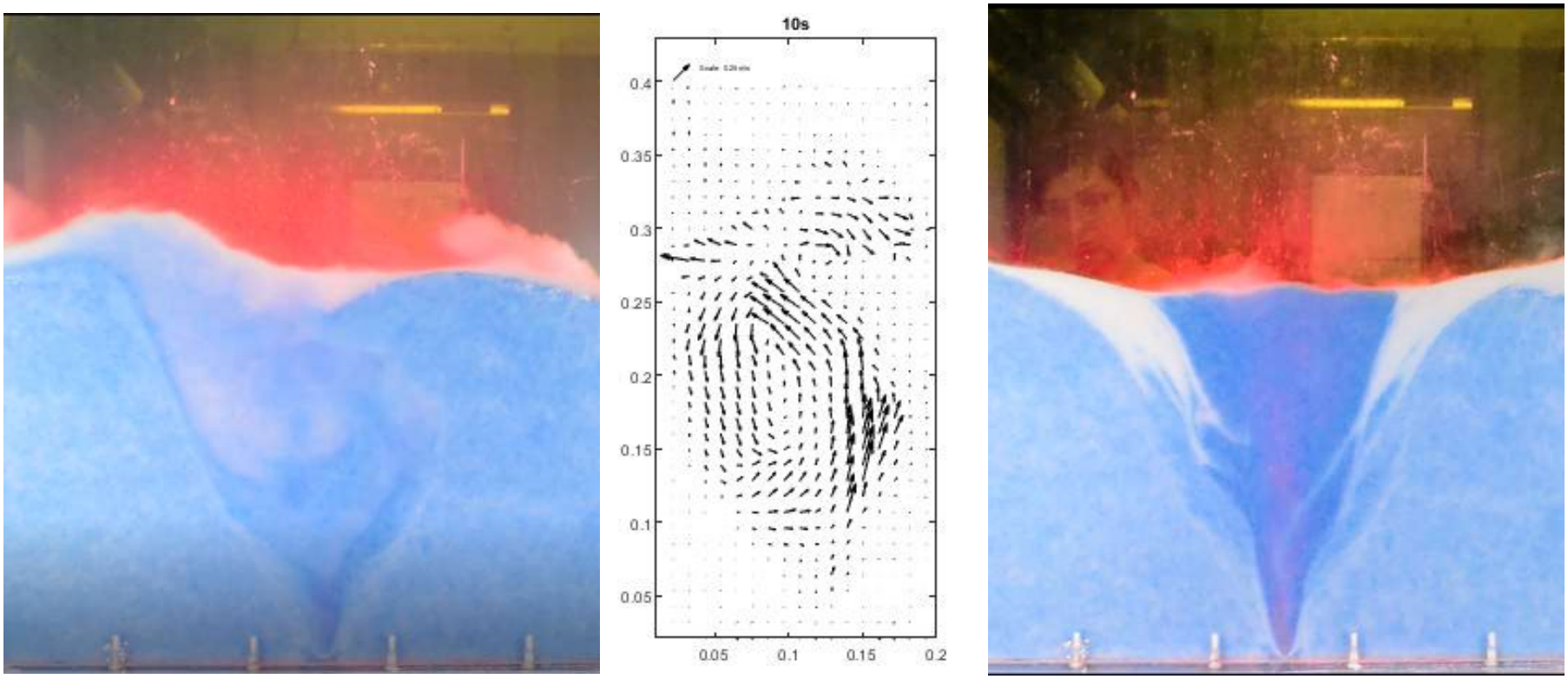

Figure 4-32 Qualitative image at approximately 10 s after the onset of fluid pumping for the High Porosity bed (left), corresponding PIV data at 10 s for the high porosity bed (middle), qualitative image at approximately 150 s after the onset of fluid pumping for the High Porosity bed (right)

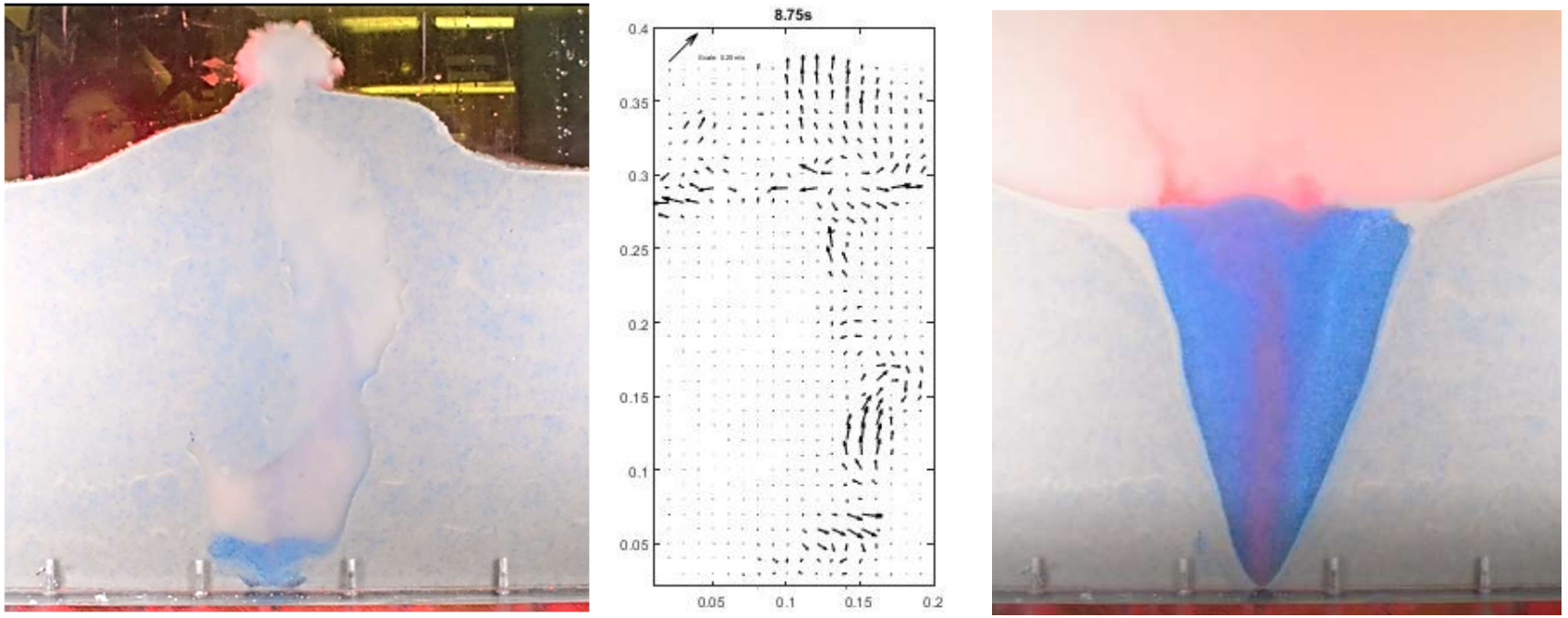

Figure 4-33 Qualitative image at approximately 9 s after the onset of fluid pumping for the Low Porosity bed (left) corresponding PIV data at 8.75 s for the low porosity bed (middle), qualitative image at approximately 150 s after the onset of fluid pumping for the Low Porosity bed (right)

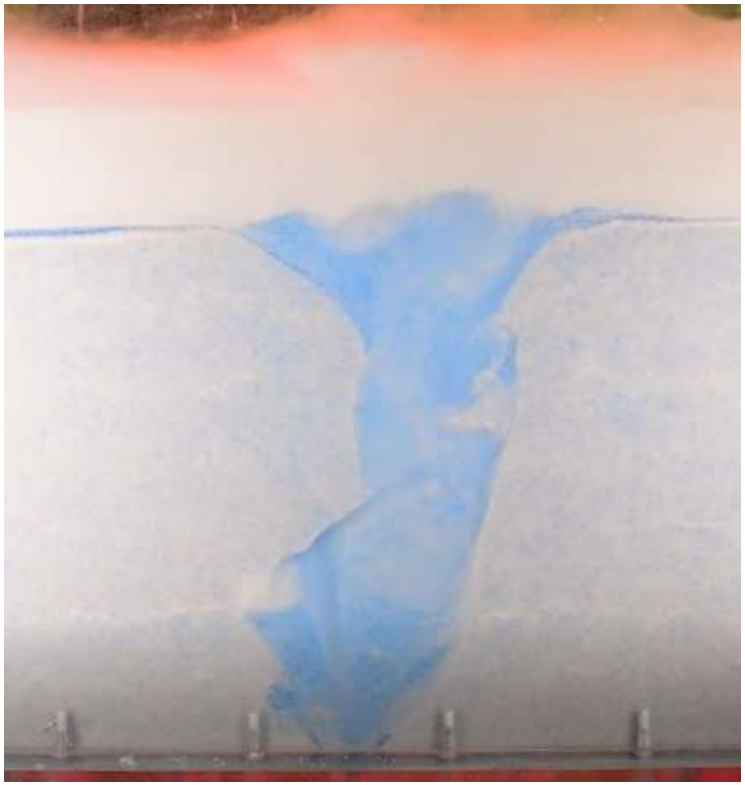

Figure 4-34 Qualitative two dimensional image showing geometry and fluidisation similar to concentration time series shown in Figure 4-7. Wider fluidised bulb is overlain by undisturbed bed to the left of the fluidisation zone, to the right a chunk of undisturbed bed is falling into the bulb. The fluidisation zone is observed to narrow above the bulb before widening into a typical funnel shape.

An interesting feature of the qualitative two dimensional data is that the segregation of the particle classes is very evident in the high porosity case (Figure 4-34, right), however this is not as clearly evident in the CT data. As discussed in Section 4.2.4, this could be due to the very similar porosities between the two particle classes which is difficult to discern when averaging over pixel spaces. It is also possible that due to the much smaller bed height in the three dimensional experiments the segregation is significantly less pronounced. Alternatively the accumulation of large volumes of segregated particles in the qualitative data could itself be a result of a two dimensional arrangement and the corresponding segregated particles are, in fact, spread more widely around the circumference of the pipe. The argument for the latter two options is perhaps made more robust when considering the low porosity case. In Figure 4-35, right, accumulations of particles are visible at the edges of the top of the funnel. Such accumulations of segregated particles would be expected to be evident in Figures 4-18 to 4-20. As such accumulations are absent, it can be assumed that they are either a result of the two dimensional arrangement or a result of a much deeper initial sediment bed (or perhaps both).

4.3.2 Concentration characteristics of bidisperse beds

These data provide the first estimates of concentration during a fluidisation event and represent the influence of the porosity of an undisturbed bed on the concentration profiles observed during a fluidisation event. It is evident from the fluidisation events represented in these data that there is no “typical” concentration or even concentration profile that characterises a fluidisation event. As observed in the velocity data presented in Chapter 4, the profile or

concentration at a particular location in a fluidisation event is influenced significantly by both the porosity of the undisturbed bed, the time of the desired profile, and the degree of recycling of material in the supra-jet regions.

The most predictable concentration profile was observed in the very high porosity bed. The fluidisation mechanism was that of an advancing erosive jet, and after the jet had reached the surface there was very little change in the pipe morphology (Section 4.2.2) or the profile of the particle volume fraction (Figure 4-33, blue triangles). The particle volume fraction varied from 0.2 to 0.4 falling within the previously extremely broad estimates of pipe concentration used in velocity predictions (Scott et al., 2009; Ross et al., 2014).

After extrusion, the concentration was shown to steadily increase with height from the inlet (Figure 4-33, blue triangles, 8, 10 and 12 s). The higher concentration persisted for approximately 15 – 20 mm above the original bed height before dropping off dramatically back towards 0. The increasing concentration with height is indicative of a flow that does not have sufficient energy to elutriate particles away from the system. It is interesting to consider how this would develop for a much taller pipe. If the concentration profile were to continue in such a manner the fluidisation pipe could conceivable reach a point where it becomes “self-plugging”. Where far from the inlet the velocities have dissipated to the point where the fluid velocity no longer exerts sufficient drag force the particles will no longer be fluidised and could remain in a state of liquefaction (grain-to grain contacts but no shear strength in the bed) or form a static bed. Such cases of fluidised zones overlain by static particles have been observed in monodisperse beds and are classed as beds in a

“cavity regime” (Philippe and Badiane., 2013; Mena et al., 2017). However, it is considered that such a regime cannot be stable over long time periods (demonstrated by Mena et al., 2017). In a fluidisation pipe setting, the “plugged” region will necessarily cause a build-up in pore pressure closer to the fluid inflow. In such a case it is suggested that fluidisation could become episodic, and periods of active fluidisation, plugging, pressure build up and re-fluidisation follow on in sequence. Alternatively, the pressure build up from a plugged fluidisation pipe could cause fluidisation to occur elsewhere in the same region of the over-pressured fluid. Regions of multiple extrusion events or pockmark fields in proximity to a known source of injection are not uncommon (Moss and Cartwright, 2010; Moss et al, 2012) and it is postulated here that these may, at least in part, be the product of some new fluidisation events undergoing self-plugging and finding new ways to the surface.

The low porosity mixture shows more temporal and spatial variation than the very high porosity case. As was observed in the velocity data the concentration profile can be split into two distinct regions, the dilute bulb, and the flow region overlying it. The concentration in the bulb is very dilute varying from 0.1 – 0.2 (corresponding to the lower bound of the concentration estimates used in Ross et al., 2014), however in the region overlying the bulb the particle volume fraction is significantly higher than previous estimates (maximum 0.54 in Ross et al., 2014). The porosity of the unfluidised bed for the low porosity sediment mixture is 0.753 (especially high as smaller particles are able to largely fill the pore spaces between larger particles), therefore in regions where the porosities are around the value of the unfluidised bed it is likely that the concentration data is capturing an uneroded “chunk” of the bed

or a portion of the bed currently being eroded. An example of such a “chunk” falling into the fluidised pipe is seen on the right hand side of the fluidisation pipe in Figure 4-41. It is noted then, that the highest concentrations are likely to represent undisturbed bed and the decreasing profile above this, represents the recirculating flow.

Where maximum data points exceeding 0.8, it should be noted that the coarse class of the particles is greater than the pixel size and so particle fractions of 0.8 represent a pixel with a large area inhabited by a particle.

The high porosity case produces no characteristic profiles during the fluidisation event. The high porosity bed is highly changeable due to the chaotic jet and turbulent mixing (Figure 4-39 left and middle) which does characterise the fluidisation events observed for this bed mix. Therefore it can be expected that the particle volume fraction profiles for this bed mix will continue to be unpredictable and show greatly varying values of particle volume fraction until a quasi-steady state is reached. The velocity data in Chapter 5 show that over a long period of time the chaotic nature of a fluidisation event in a high porosity bed does dissipate. Future work capturing the concentration profiles in the steady state would provide further insight into the particle volume fractions in the quasi-steady flow field.

These first data of concentration in fluidisation events show that the broad range of 0.2-0.4 is a reasonable estimate of the concentration in a dilute flowing region that breaches the surface. The ranges may of course be different for cases which do not reach the surface, as discussed by Cobain el al. (2015), however such cases are not addressed herein. The first order estimates can then be used in a broad sense to constrain the velocity

estimates calculated from outcrop data and based on particle size and concentration estimates. For example, the estimates given in Ross et al. (2014) span two orders of magnitude, and suggest a velocity of 0.01 m s^{-1} at a concentration of 54% concentration , 0.21 m s^{-1} at 30% concentration and 0.87 m s^{-1} at 15% concentration. It is likely the representative concentration is somewhere near the 30% estimate in a dilute flowing region.

Whilst these results may provide a first order estimate of concentration to constrain velocity estimates using the pseudo-fluid approach, they also reveal that there are significant spatio-temporal variations in concentration, particularly during this initial period of fluidisation. The pseudo-fluid approach relies on ascribing fluid properties to the fluid and particle volume and treating the mixture as a continuous fluid. The density of the fluid is averaged over the volume based on the concentration of particles and the viscosity is also augmented accordingly (Di Felice, 2010). Such an assumption could reasonably be applied to the very high porosity case to provide a rough estimate of the flow, however for the other cases the variation and temporal instability is much more significant and perhaps an approach accounting for this variation is more appropriate. It is not clear from the present study what is the porosity at which the characteristic behaviours in the concentration changes from one profile to another. Furthermore, it is not clear if over longer timescales as the flow moves to an equilibrium morphology (as seen qualitatively in the form of a funnel geometry, Figures 4-34 and 4-35), whether the concentration characteristics may become more homogenous.

4.3.3 Residual morphologies, outcrops and seafloor observations.

The residual morphologies presented in Section 4.2.4 show both surface views (Figure 4-17) and internal porosity characteristics for fluidisation events that are no longer undergoing active fluidisation (Figures 4-18 to 4-26). The surface morphologies are observed to bear a striking resemblance to seafloor geological features known as “pockmarks”. Often ascribed to migrating gasses, smaller pockmarks have been acknowledged as the result of pore-water seepage (Hovland et al., 2009) although this may be induced by unerupted gasses. Forwick et al. (2009) observe a range of pockmarks on the seafloor noting varying characteristics of the pockmarks in the region, such as sharply outlined, less sharply outlined and pockmarks with raised rims. Forwick et al. (2009) assume that raised rims are upward vented debris. They further suggest that the cause of the variations between the smooth-rimmed and sharply rimmed pockmarks is due to the age of the pockmark; with smooth rims representing older pockmarks that have since been reworked and sharp rims newer or active pockmarks. Whilst this may be the case where sediment beds are well known and consistent across the study area, herein we observe similar features that occur as a result of the varying compositions of the sediment mixes (Figure 4-17). Therefore, it is suggested that the range of observable pockmark morphologies is a function of bed type, sediment size and the distribution of particles in the vent relative to the applied seepage characteristics, such as velocity.

Surprisingly, the internal residual morphology of both the high porosity and very high porosity beds (Figures 4-21 to 4-26) are extremely difficult to

observe and data clamping was required to observe the structures that were there. This indicates there is a very small difference between the porosity of the unfluidised bed and the previously fluidised zone in these cases. It is also noted from the volumetric timeseries of the high porosity case (Figure 4-31), that the timescale to return to a porosity similar to that of the undisturbed bed is less than a second from the active jet moving away from the region under consideration. For examples with similar porosity variations, the present work suggests that fluidised features may not be detectable in cases such as seismic data sets and the difference between the undisturbed bed and the remaining morphology of the fluidisation event would have to be significantly more obvious such as in the low porosity examples (Figure 4-18 to 4-20).

The residual morphologies visible in Figures 4-18 to 4-20 bear very little resemblance to the geometry observed during initial fluidisation. It would appear that the bed has slumped into a typical funnel shape with a very wide opening at the surface in comparison to the diameter at the surface during initial fluidisation. This also has implications for predictions made based on outcrop data, where residual morphologies are used to justify assumptions based on the pipe geometry. It may be assumed in these cases that the final morphology resembles the likely structure during all phases of fluidisation and this may not be the case.

4.4 Conclusions

These first estimates of concentration during a fluidisation event show that, in addition to the velocity data the concentration profiles are highly variable both spatially and temporally during a fluidisation event. However, a means of constraining first order estimates of concentration for outcrop data is now provided for the first time, thus enabling more accurate estimates of likely flow velocities and regimes. The three porosities investigated during this set of experiments show distinct fluidisation processes with equally distinct concentrations profiles corresponding to the particular bed. Thus a range of field porosities can be better understood and the fluidisation characteristics estimated with greater accuracy. As a result of highly spatially and temporally varying concentration profiles it is observed that a pseudo-fluid approach to characterising a complete fluidisation event cannot accurately portray the event particularly during the onset and early evolution of fluidisation within a bed. However the dilute fast flowing region can now be estimated and the recirculating regions and behaviours understood and interpreted. Concentration profiles of high porosity beds are presented as a mechanism for episodic pipe growth or regionally extensive pockmark fields. The final preserved morphologies of the three cases tested are observed internally and from the surface and show that the morphologies of pockmarks observed on the seafloor may be indicative of the bed porosity, particle size and velocity characteristics of the formative event.

Whilst the three dimensional experiments reveal the full 3D structure of the fluidisation zone, they also show that in many respects the two dimensional

experiments used to observe the velocity field provide a good analogue. For instance, the 3D experiments here corroborate the findings of regions of less dilute flow at the margins of the fluidisation zone, observed to be settling particles in qualitative data sets.

5 Formation sequences of fluidisation pipes for a range of porosity beds and the implications for in-situ injectites

As discussed in Chapter 2.2, fluidisation events are necessarily observed from surface or seafloor observations (Loseth et al., 2011; Cobain et al., 2020 and refs therein), or as outcrop examples after dewatering and many other geological processes ultimately expose the fluidisation pipe (Mount, 1993; Loseth et al., 2011; Ross et al., 2014; Duarte et al., 2020). As a result the vast majority of the information available about fluidisation pipes is observed after the event is no longer active. Therefore experimental analogues are the only way to directly observe fluidisation events.

Previous chapters have shown that the velocity fields in active fluidisation events have significant spatial and temporal variation (Chapter 3) and that this is intrinsically linked to the concentration features at each spatio-temporal location (Chapter 4). This chapter observes the physical processes occurring during each fluidisation sequence and determines the implications for resulting characteristics of geological fluidisation events through the development of a new sequence based model.

5.1 Methodology

5.1.1 Experimental arrangement and procedure

The experiments described in this chapter were performed using the same set up described in Chapter 3.2. For brevity the reader is referred there for a detailed description. As before, each sediment bed type was fluidised using two different inlet velocities in separate experiments, corresponding to the

Reynolds laminar and Reynolds turbulent regimes, to assess the influence of flow regime on fluidisation dynamics (Section 3.2.3). Three bi-disperse bed mixtures of solid glass spheres (40% fine particle class, 60% coarse particle class) were tested to consider the effect of varying porosity on fluidisation (Section 3.2.3, Table 3-2). The bed was built up using the method outlined in section 3.2.2. Each configuration was repeated a minimum of three times and a maximum of 12 times, depending on the variability between repeat runs. Alongside, measurements of the fluidised flow as detailed in previous chapters, the qualitative development of the fluidisation event was captured at 24 frames per second using a Nikon D7200 and an Omega PX409-030GUSB pressure transducer recorded pressure in the manifold from before the onset of pumping to the cessation of flow at a frequency of 1 Hz.

Before the onset of fluid pumping, the pressure transducer and the qualitative camera started recording. In all cases, fluidisation was evident within a few seconds of the onset of pumping. Each experiment continued for at least 310 s and then the fluid flow ceased and residual morphology was captured.

5.2 Results

5.2.1 Sequence of fluidisation and pipe formation

For low porosity bed mixtures, the sequence of fluidisation was: (i) hydraulic fracture, (ii) void formation and expansion, (iii) propagation of an erosive jet towards the surface, (vi) extrusion and transportation of some fine particles away from the vent site, (v) collapse of the overbed and turbulent mixing, (vi) unstable jet propagation, (vii) jet stabilisation (Figure 5-1 and 5-2). Conversely, for the three higher porosity cases (very high porosity – fast inlet velocity,

Figure 5-3, high porosity – fast inlet velocity, and high porosity – slow inlet velocity Figure 5-4 and 5-5), the sequence of fluidisation was: (i) erosive void formation, (ii) turbulent mixing within a propagating zone of reduced particle numbers, (iii) extrusion, (iv) collapse of the overbed and turbulent mixing, (v) wall formation and unstable jet propagation, (vi) gradual stabilisation of the extrudite geometry. It is important to note that the sequence of fluidisation remained the same regardless of the inlet velocity of the fluid injection, demonstrated in the fast and slow inlet velocity sequences shown side-by-side in Figures 5-1, 5-2 and 5-4, 5-5. However, although the inlet velocity did not influence the sequence of fluidisation, it did control the rate at which it progressed; fluidisation rates were significantly accelerated for faster inlet velocities (Table 5-1, Figures 5-1,5-2 and 5-4,5-5).

Table 5-1 Expansion ratio and time to extrusion

Configuration ID	Expansion Ratio*	Time to extrusion (s)
Low porosity – slow velocity	14.4	24
Low porosity – fast velocity	24.1	9
High porosity- slow velocity	10.9	15
High porosity – fast velocity	21.3	8
Very high porosity – fast velocity	13.8	5

* Expansion Ratio is calculated as the ratio of the diameter of the fluidised zone at the top of the bed to the diameter at the inlet.

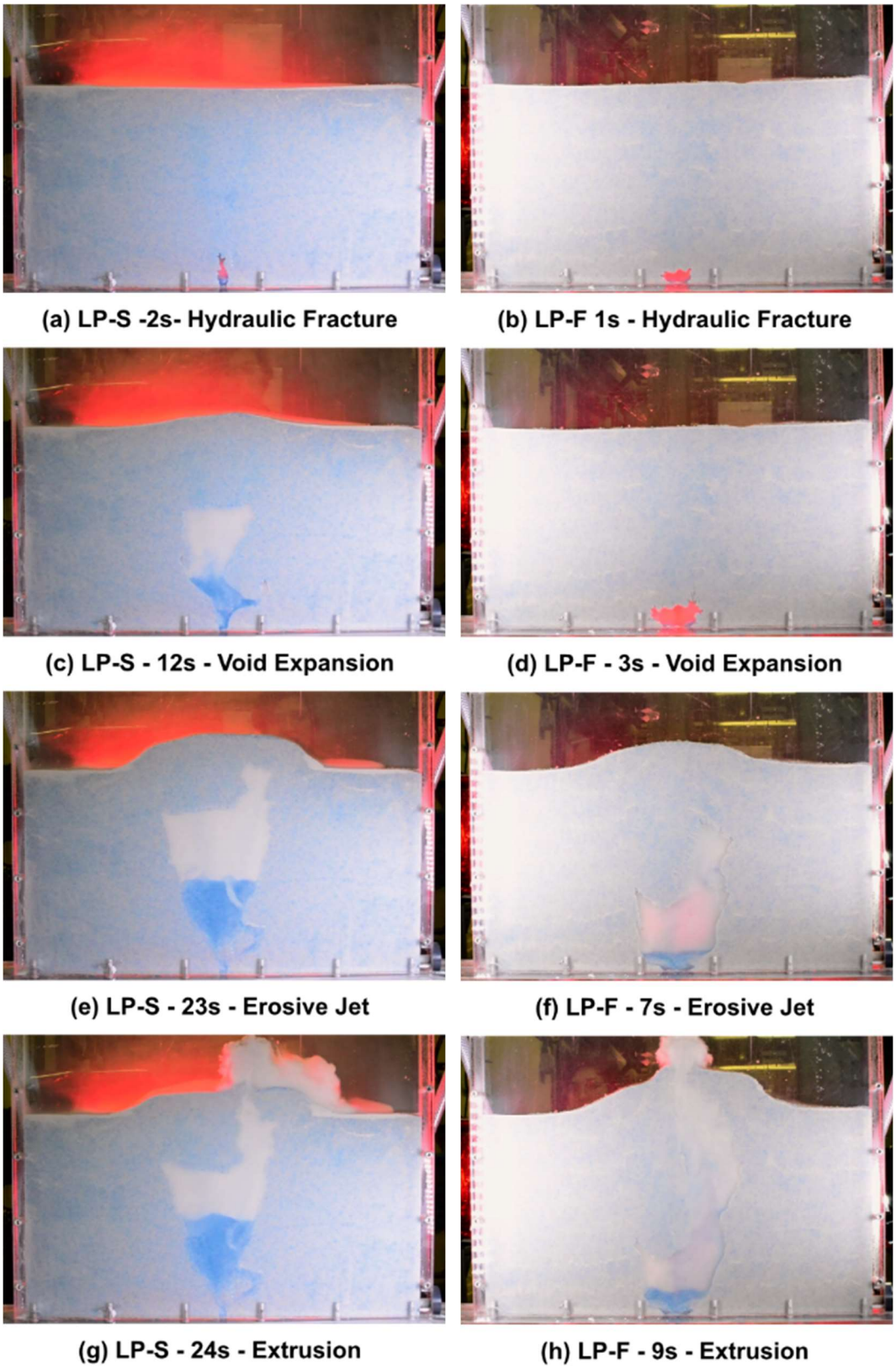

Figure 5-1 Qualitative images of the fluidisation sequence for the low porosity cases, low porosity - slow inlet velocity (LP-S), left, low porosity - fast inlet velocity (LP-F), right.

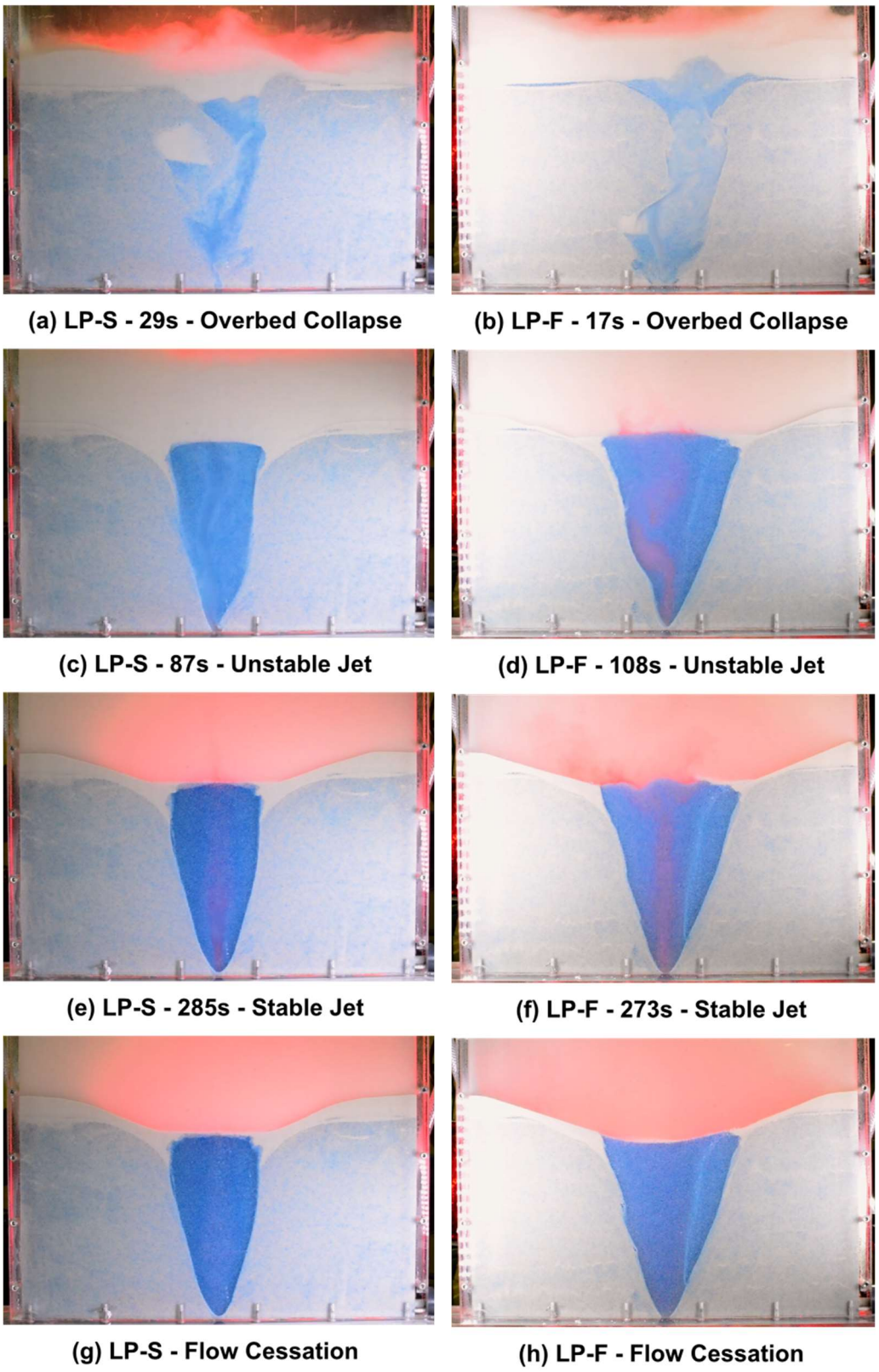

Figure 5-2 Images of the fluidisation sequence for the low porosity cases, low porosity - slow inlet velocity (LP-S), left, low porosity - fast inlet velocity (LP-F), right.

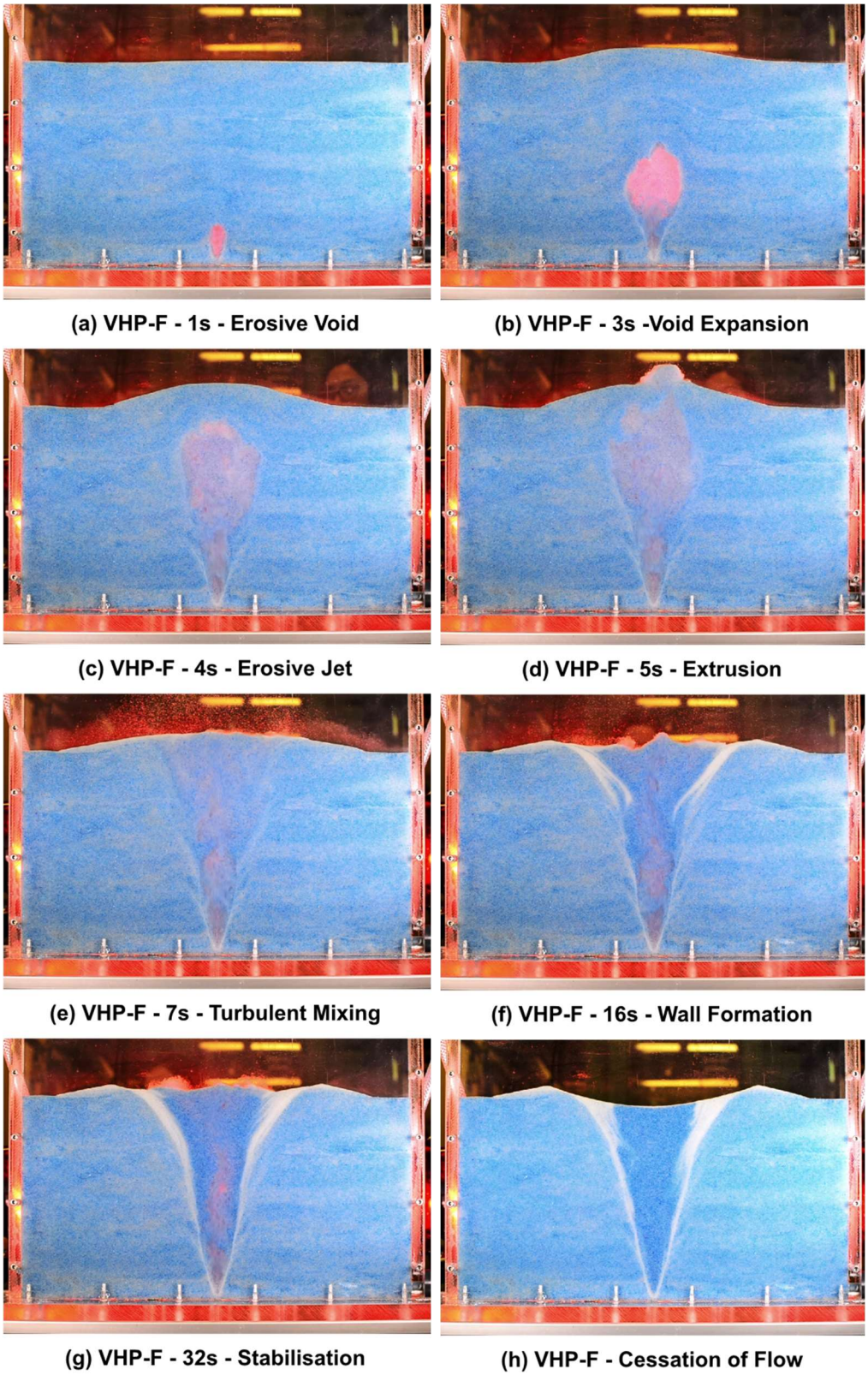

(a) VHP-F - 1s - Erosive Void

(b) VHP-F - 3s -Void Expansion

(c) VHP-F - 4s - Erosive Jet

(d) VHP-F - 5s - Extrusion

(e) VHP-F - 7s - Turbulent Mixing

(f) VHP-F - 16s - Wall Formation

(g) VHP-F - 32s - Stabilisation

(h) VHP-F - Cessation of Flow

Figure 5-3 Images of the fluidisation sequence for the very high porosity - fast inlet velocity case (VHP-F)

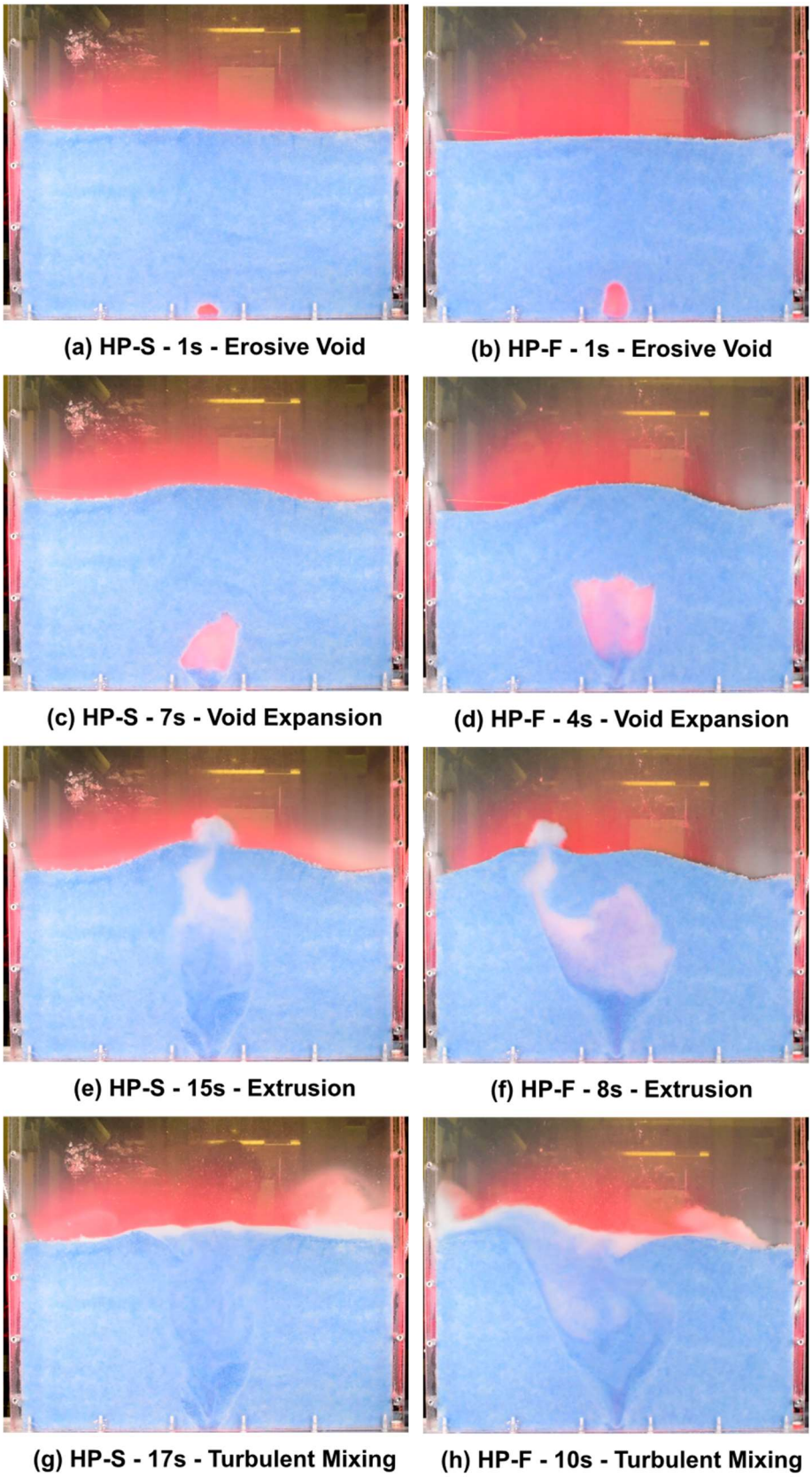

Figure 5-4 Images of the fluidisation sequence for the high porosity cases, high porosity - slow inlet velocity (HP-S), left, high porosity - fast inlet velocity (HP-S), right.

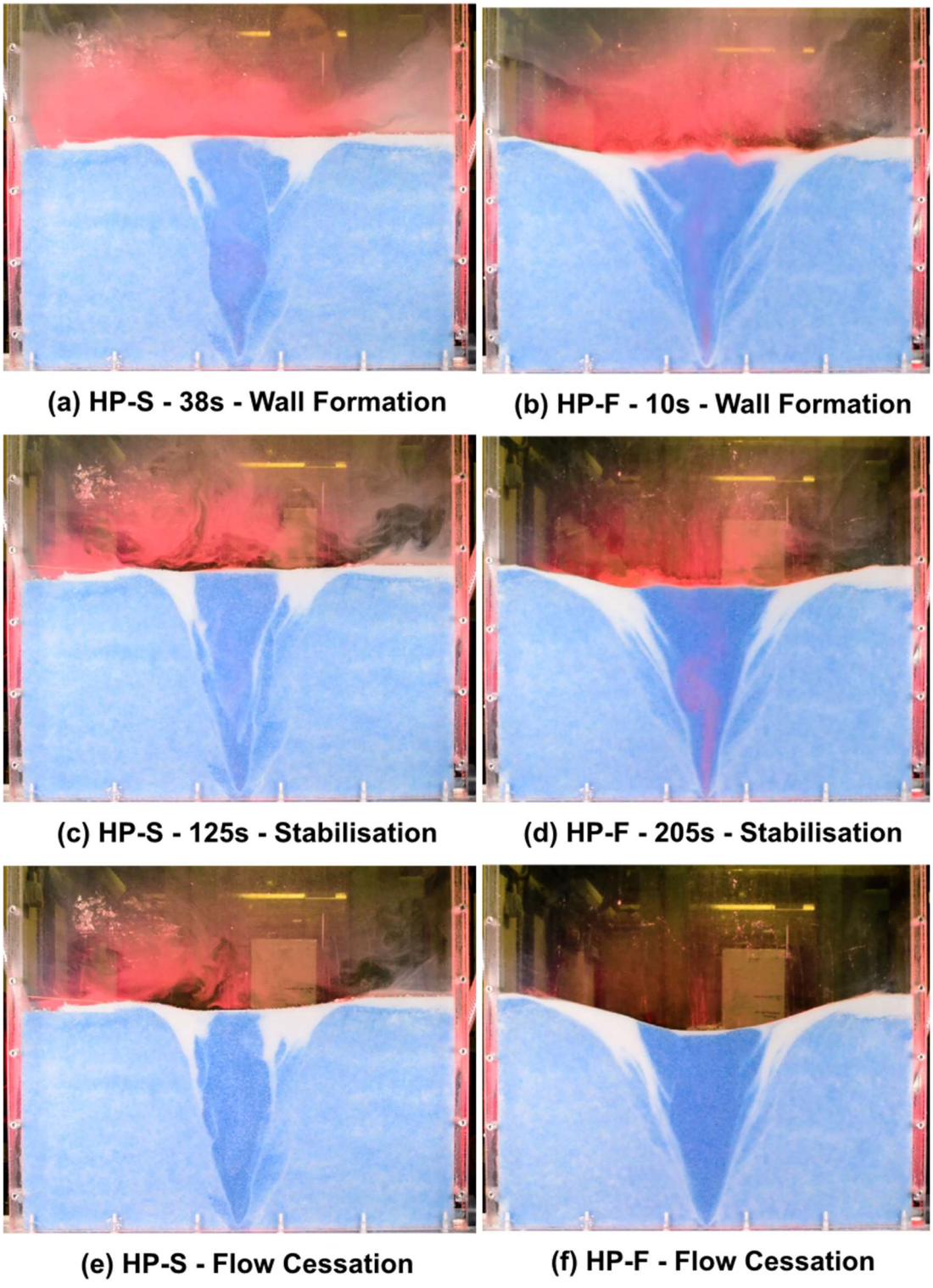

Figure 5-5 Images of the fluidisation sequence for the high porosity cases, high porosity - slow inlet velocity (HP-S), left, high porosity - fast inlet velocity (HP-S), right.

5.2.2 Onset of fluidisation

Within each experiment, pressure increased initially as a result of input of fluid into the base of the system. In all cases, fluidisation occurred within a few seconds of opening the valve. The pressure data shown in Figure 5-6 begins at the onset of fluidisation, not the onset of pumping. The induced overpressure begins to dissipate immediately following the onset of fluidisation, rapidly in the high porosity cases (Figure 5-6, C and D) and at a reduced rate in the low porosity cases (Figure 5-6 A and B). Note that Figure 5-6 presents multiple pressure data sets for each sediment bed mix as all of the sediment bed mixes were repeated multiple times. The numbers in the

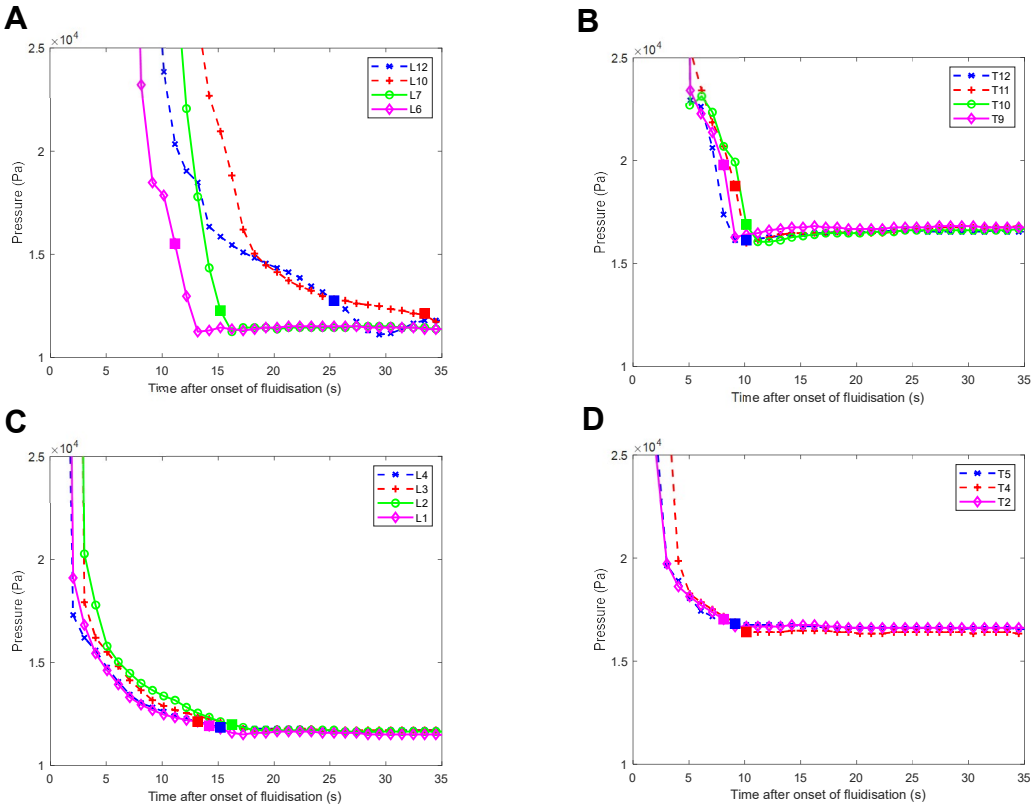

Figure 5-6 Pressure data for multiple runs for A, low porosity - slow inlet velocity, B low porosity - fast inlet velocity, C, high porosity - slow inlet velocity, D, high porosity - fast inlet velocity. Each bed type has pressure data for multiple runs presented with the experimental number of that run identified in the legend. For each run the solid filled square represents the point of extrusion.

legends in Figure 5-6 refer to the pressure data collected for that run number for that particular sediment mix.

The response of the bed at the onset of pumping was immediate in all cases. For the very high porosity and high porosity cases (very high porosity – fast inlet velocity, Figure 5-3, high porosity – fast inlet velocity, Figure 5-4 and 5-5 and high porosity – slow inlet velocity Figure 5-4 and 5-5), porosity of 0.325 and 0.377 respectively, the bed was forced to expand by an erosive jet that propagated rapidly (Figure 5-3 a, 5-4 a and b). The surface area of the jet increased with time, entraining more of the overbed. Conversely, for low porosity cases (porosity of 0.247), onset of fluidisation caused a hydraulic fracture to form (Figure 5-1 a and b). Due to the lower porosity, the bed behaved as if there was a small amount of tensile strength due to the inter-particle friction and the lithostatic load. This caused the failure to display features more common of a cohesive bed. The fracture formed when the forcing of the fluid into the bed exceeded the residual strength of the bed. The fracture was purely fluid and contained very few particles. It was not possible to quantify the rate of entrainment of the overbed in the different experiments but it appeared qualitatively similar in all cases, despite the porosity being varied from 0.247 to 0.377.

5.2.3 Void expansion and erosive jet

The propagation and surface expansion of the void caused the overbed to form a mound directly above the erosive jet in high and very high porosity cases (Figures 5-3 b, 5-4 c and d). The height of bed expansion caused by the turbulent erosive jet was smaller for the very high porosity bed than for the

other high porosity cases (Figure 5-4 c and d) because more fluid was able to pass through the void spaces in the intact bed. In the low porosity beds, the mound was exaggerated due to the reduced porosity hindering the passage of fluid through the bed (Figure 5-1 e and f). Greater numbers of bed particles were observed to be entrained into the void space in the low porosity cases than for the higher porosity mixtures, but only fine particles persisted in the void. Coarse particles were dislodged from the overbed and fell through the void, forming a persistent region of coarse particles near the inlet. As with the high and very high porosity beds, the void space expanded laterally with increasing height. The rate of expansion of the void space reduced once a propagating erosive jet formed.

5.2.4 Extrusion and elutriation

Upon reaching a critical point, a narrow erosive jet formed in the low porosity bed. Although the void space continued to expand, this jet separated from the void and propagated at a much faster rate to the bed surface (Figure 5-1 e and f). Upon breaching the bed surface (Figure 5-1 g and h), venting of the jet caused the immediate collapse of the overbed into the void space and particles were immediately elutriated from the system. In the low porosity high inlet velocity, the particles were transported much further from the vent site than in the slow inlet velocity case and the rate and transport distance of elutriation continued to correspond to the fluid injection velocity through the subsequent stages of fluidisation. For low porosity beds, the jet most commonly formed to one side of the propagating void space and a second weaker jet often formed simultaneously at the other side of the void space (Figure 5-1 e, f and g). The formation of the dominant and weaker jets formed

much earlier after the onset of fluidisation for the fast inlet velocity case than for the slow inlet velocity case. The erosive jet did not separate in the very high porosity case (Figure 5-3), but instead an expanded turbulent mixing zone began to entrain the undisturbed bed particles at a greatly increased rate. In comparison to the low porosity cases, the high and very high porosity cases (very high porosity – fast inlet velocity, high porosity – fast inlet velocity and high porosity – slow inlet velocity) exhibited an increased rate of bed entrainment and mixing as the void expanded. However some cases also demonstrated the branching of an erosive jet that propagated more rapidly towards the surface (Figure 5-7). In all cases, the fluidised region continued towards the surface, showing an increase in the rate of propagation with decreasing overbed thickness. Irrespective of the bed porosity, the magnitude of the extrusion event and the rate of elutriation of particles was dependent on the inlet velocity: slower velocity injections were not able to transport particles from the vent site and significantly fewer particles were elutriated from the system.

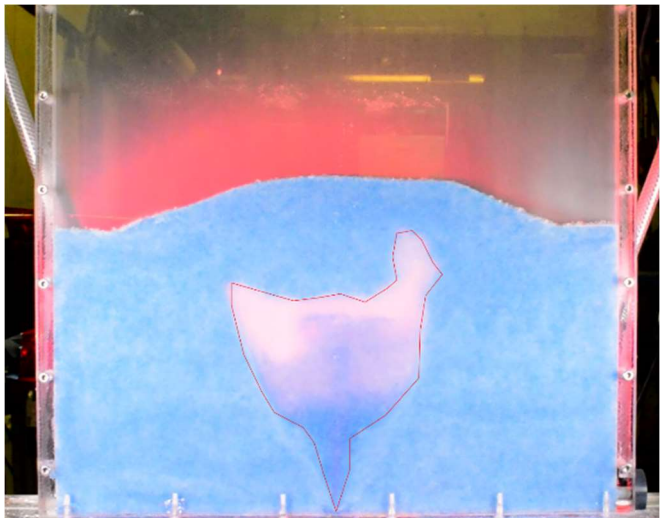

Figure 5-7 - High porosity fast inlet velocity case showing the advancing erosive jet "branching" and propagating more rapidly to the surface. Jet and dilute zone outlined in red for visibility.

5.2.5 Turbulent mixing

Following extrusion, a period of turbulent mixing commenced where the fluid jet was unsteady and frequently deflected by the inhomogeneous nature of the bed structure. Following extrusion, the mound that formed during preceding stages collapsed back into the fluidised region in all cases. In high porosity beds that had already been extensively mixed due to the erosive jet, mixing continued but with a narrowed region of fluidised particles (Figure 5-4 g and h). In low porosity beds, the overbed remained intact throughout the void formation and expansion and so the overbed collapsed back into the void space on extrusion, with sections of bed falling largely intact (Figure 5-2 a and b). It took significantly longer for these initially intact parts of the overbed to become completely remixed into the fluidised region in both these cases. These observations are reflected in the pressure data, which show that, after extrusion (shown as a solid square in Figure 5-6 A to D), pressures took longer to reach a stable equilibrium for the low porosity beds than high and very high porosity beds. There was also an inlet velocity control on the rate of pressure equilibration: for the low porosity - slow inlet velocity case (Figure 5-6 A), this took up to 3 seconds in some examples, but occurred much faster in the fast inlet velocity examples (Figure 5-6 B). For the high porosity cases, however, the pressure was at the equilibrium point at the time of extrusion and both the reaching of a pressure equilibrium and the point of extrusion appear to coincide (Figure 5-6 C and D). The dissipation of the overpressure in the system occurs significantly faster in the higher porosity beds (C and D) since the initial mounding caused by the expanding void space is less in comparison to the low porosity beds.

5.2.6 Wall formation and stabilisation of geometry

For the high porosity cases, the geometry immediately following extrusion is largely irregular and dictated by the advancement of the erosive jet (Figures 5-3 e and 5-4 g and h). In several cases, these irregular bed features were erased as the chaotic active jet eroded the structures formed earlier in the sequence. As the jet migrated back and forth across the fluidisation zone, particles were continually entrained, transported, deposited and re-entrained into the chaotic jet. Particles were falling in areas far from the jet, but were entrained and transported to the bed surface in areas near to the jet. Smaller particles were transported a greater distance than larger particles, forming regions of exclusively fine particles at the extremes of the fluidized zone (Figure 5-3 f and 5-5 a and b). Gradually these fine particles formed stable walls. As the walls formed thicker layers of fine particles, they became increasingly difficult for the jet to entrain and so gradually stabilised. The stabilisation occurs as the walls of fine particles are less permeable and therefore more resistant to the fast moving fluid flow than the central dilute zone, as the fluid takes the “path of least resistance” the flow becomes more focussed in this central region.

In all cases, the final stabilised geometry resembled an upward-flaring funnel (Figure 5-3 g and 5-5 c and d). Higher velocity injections showed a wider flare angle and greater diameter of the fluidised region (Figure 5-5 c and d). Coupled to the formation of the stable walls, small mounds of fine particles lateral to the vent site formed in all cases. As the accumulated fine particles exceeded their ability to self-support, they fell back towards the active fluidised

zone. In some cases, this would form alternating layers, with regions of mixed particle classes and layers exclusively formed of fines (Figure 5-8).

For the lower porosity bed, the fine particle class was significantly smaller than the other tested cases. As such more of the fines class was able to be supported by the flow and ultimately elutriated from the system. Therefore in these cases the mounds to either side of the vent were more laterally extensive, spreading along the entire bed.

In the low porosity - slow inlet velocity case, a deep layer of fines covered the bed because the jet imposed insufficient force to transport the fine particles high into the overlying ambient fluid (Figure 5-2 e). Conversely, in the low porosity - fast velocity case (Figure 5-2 f), the layer of fines was thinner because fines were transported further into the ambient fluid and were then removed from the system by the drain tubing.

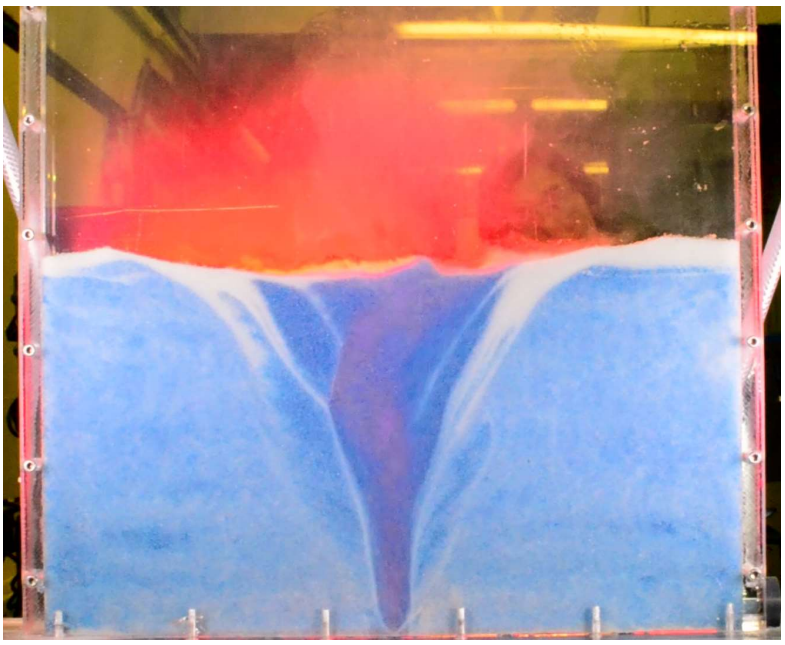

Figure 5-8 A high porosity fast inlet velocity example showing the formation of alternating mixed and exclusively fine particle layers.

All investigated cases exhibit features formed from the passage of a widened fluidised region early in the flow sequence and later cessation of the flow in that region (Figure 5-9). The high porosity cases tended to form erosive structures lower in the bed and then formed size-segregated layers higher in the bed (Figure 5-9 a and b). The coarse and fine particles segregated and formed layers with the passage of the void space, with fines falling at the margins and coarse particles forming the rest of the feature. Following the initial passage of the void, a static bed formed and fluid flow could not be detected in these regions, although there may have been some small-scale Darcian flow within the bed. The low porosity cases tended to develop regions of irregular bed structure discordant with both the surrounding bed and the active fluidised zone (Figure 5-9 c and d). As with the other flow features seen in the development of the sequence, the flow velocity at the inlet did not exert a large control on the spatial form of the observed formations. In some cases, the erosive features or early size-segregated structures were erased following re-entrainment into a fluidised zone, while in others they persisted after the cessation of flow (notably, residual structures remain visible in Figure 5-5 e and f) . Features were more likely to persist in low inlet velocity cases, since the steady fluidised zone is generally smaller in those cases. The diameter of the fluidised zone increased with inlet velocity. This can be characterised for each fluidisation event after the cessation of fluid flow through an expansion ratio , calculated as the ratio of the diameter of the fluidised zone at the top of the bed to the diameter at the fluid inlet. The fluidised zone was characterised as the central region where the bed is composed of coarse particles since this

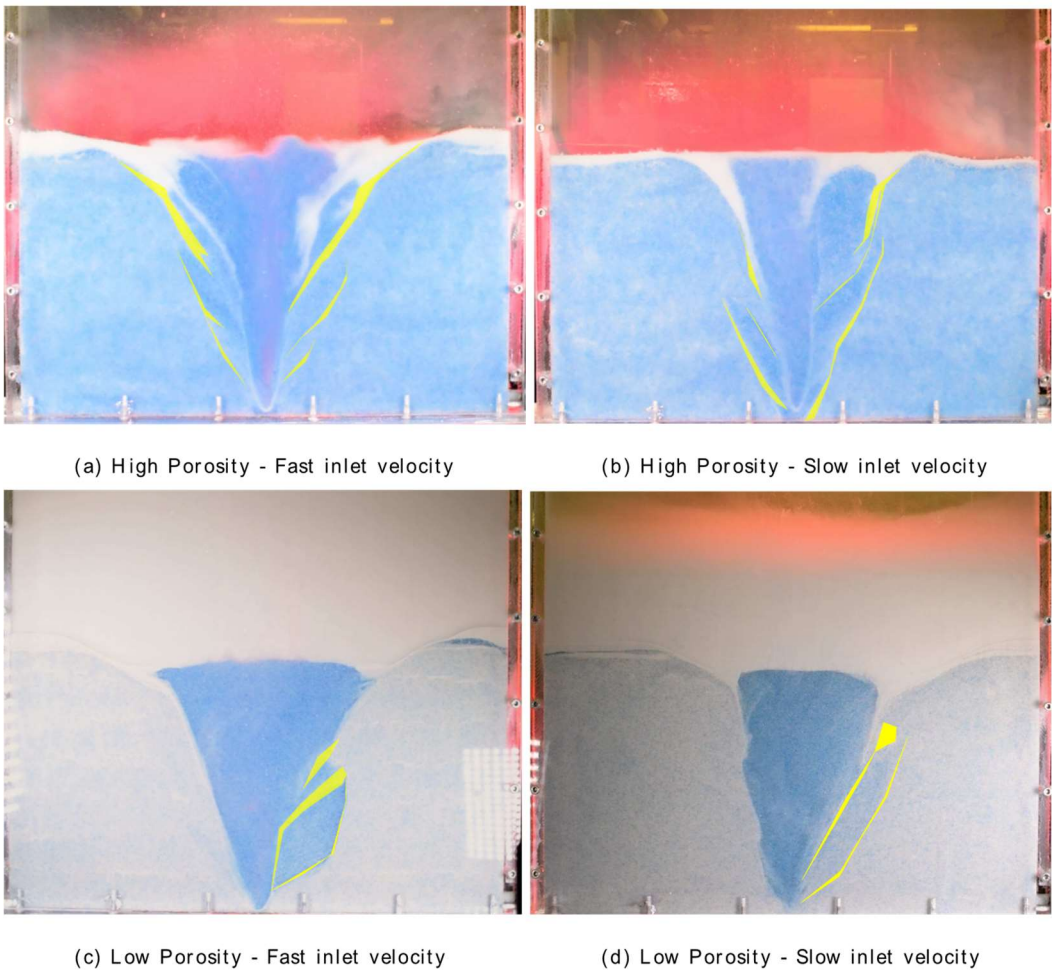

Figure 5-9 Residual features from the original passage of the fluidised zone highlighted in yellow for each case.

was easily identifiable across all cases. Although this does not capture the full variability in the final geometry in each example, the expansion ratio does show a dependence with both inlet velocity and bed porosity. Notably, increasing porosity results in a narrower coarse fluidised zone profile while increasing velocity gives a wider profile (Table 5-1).inlet velocity and bed porosity. Notably, increasing porosity results in a narrower coarse fluidised zone profile while increasing velocity gives a wider profile (Table 5-1).

5.3 Flow regime

Injectite evolution for comparable bed compositions but different injection velocities was strikingly similar. Comparing the same element of the fluidisation sequence across Reynolds number-based regime classifications show the same qualitative behaviours and characteristics. It is evident from the fluidisation events reported herein that many of the fluidisation stages can neither be categorised as wholly-laminar nor wholly-turbulent. Instead, at any instant in time, active regions of the bed exhibit elements of laminar or turbulent flow but the spatial locations of these regions are not necessarily constant nor clearly defined. This is especially clear after extrusion, where, regardless of inlet velocity, bed regime or duration of fluid flow, a highly turbulent, dilute jet is flanked by slow moving, dense, falling particle regions that circulate back into the jet, forming a continuous recirculation loop of particles. In the experiments reported herein, the falling-particle regions furthest from the jet were often composed exclusively of fine particles.

The flow through the bed is not homogeneous and although the bed had some interaction with the fluid motion, it did not act to dissipate or damp the heterogeneity caused by the injected fluid. In contrast, the bed often acted to increase channelisation of the jet or redirect the flow path. Streams of falling fine particles deflected the dilute turbulent jet on several occasions. Often, a chaotic jet with a migrating path was evident. Further, in the high porosity cases, regions of little or no flow formed and persisted within the initially fluidised zone when the chaotic jet was active far from that region.

5.4 Discussion

5.4.1 Flow regime

As previously addressed, the chimney regime in a fluidized bed system is the case where a region of particles move exclusively upwards breaching the surface of the bed (Phillippe and Badiane, 2013). This definition of a “chimney” can be applied to the turbulent jet observed herein: a clear, stable upward-directed jet is easily identifiable using the PIV data (Chapter 4, Figures 4-7 and 4-13, for example). Additionally, a continuous particle feed to the chimney is provided by downward moving particles surrounding it.

Mena et al. (2017) tested the influence of a range of parameters on the established fluidised bed regimes outlined in Section 2.5.2, including bed thickness, particle diameter, minimum fluidisation velocity, chimney diameter, and flow velocities. They showed that the threshold flow velocity for cavity and chimney regimes is dependent on bed thickness, the critical values of which are strongly dependent on particle size. Although Mena et al. (2017) tested particles with diameters between 3 mm and 11 mm, significantly larger than those assessed herein, critical bed thickness at which the behaviour of the bed becomes independent of bed height was below 50 mm for their smallest particle sizes. This critical height increased with particle size. This would imply, by extrapolation, that the bed thickness used herein, 250 mm, is adequate to render the flow regime independent of bed thickness. However, Zoueshtiagh and Merlen (2007), Philippe and Badiane (2013) and Mena et al. (2017) all used mono-sized spheres for their porous medium and as such, report no chaotic characteristics of the jet and no instabilities caused by the

falling of particles. Each of these studies using mono-sized spheres reached a steady state, where the cavity or chimney was clearly defined.

Through the use of bidisperse particle size distributions, this study has explored the influence of particle size segregation on the bed fluidisation process for the first time. The low porosity cases (Figures 5-2 e and f) formed a stable jet much more easily and consistently than the high porosity cases (Figure 5-5 c and d). This is likely because the fine particles in the low porosity cases are small enough to pass through the pore spaces of the coarse particle class. Therefore, the fine particles are much easier to transport to the margins of the fluidised zone, leaving a narrowly distributed, uniform coarse fraction in the central fluidised zone. As a result, in the low porosity cases, the behaviour within the central fluidised zone is much closer to the behaviour of a coarse-grained mono-disperse bed. Conversely, as discussed further in the next section, the high porosity cases display more interesting behaviours as a result of particle size segregation within the fluidized zone.

It was not possible to replicate the cavity regime (defined as a dilute cavity with fluidized particles overlain by a static bed governed by Darcy bed flow) in the course of these experiments. Although in some low velocity runs movement in the upper regions of the fluidised zone was small and slow (for example, Chapter 3, Figures 3-10 and 3-12), particles were still observed to be in motion and did not make up a static bed above the inlet at any height. It is possible that the varying local porosities caused by introducing multiple particle diameters narrows the range of particle sizes at which it is possible to

observe the cavity regime even further or possibly prohibits the formation altogether.

The influence on fluidisation pipe dynamics of whether flow is laminar or turbulent is often debated in geological literature. Specifically, studies have often considered whether the preserved lithology visible in outcrop examples shows characteristics that indicate laminar or turbulent flow (Peterson, 1968; Taylor, 1982; Obermeier, 1998; Duranti, 2007; Scott et al., 2009, Ross et al., 2014, Cobain et al., 2015). In this study, it has been observed that only laminar flow is visible at the margins of the fluidisation pipe, regardless of the flow regime calculated using traditional Reynolds numbers. The present experiments suggest that the walls of a fluidisation pipe will always form from laminar flow processes while the central region will always be turbulent, correlating well with the assertion of Cobain et al. (2015) that flow in clastic injections is either dilute and turbulent or concentrated and laminar. However, the experiments herein demonstrate that both regimes coexist within the same system, simultaneously. More strikingly, these characteristics of laminar flow propagation will be in the opposite direction to the predominant and driving flow direction in the vertical pipe. These findings suggest that many studies that have inferred flow regime from observations of outcrop data (Duranti and Hurst, 2004; Scott et al., 2009; Sherry et al., 2012; Ross et al., 2014), are flawed.

5.4.2 Pipe mobility

Within a monodisperse bed, particles are more easily re-entrained and beds more easily re-fluidised after a fluidisation event (Mena et al., 2017). This

hysteretic effect of fluidisation is key to considering the lithology remaining at any instant in time during fluidisation. Particle segregation, winnowing and wall formation all exacerbate the dependence of a polydisperse bed on its fluidisation history. The present experiments demonstrate that size segregation occurs within polydisperse beds, since the jet is able to transport fine particles further both laterally and vertically than coarse particles. Fluidisation thus evacuates fines from the central region of pipes, yielding a uniform, coarse, funnel-shaped deposit. In the high and very high porosity cases, the residual funnel is flanked by fine-grained walls that are formed by fines settling at the pipe margins (Figures 5-3 h, 5-5 e and f). In the low porosity case, there is no fine-grained wall in the lower bed, only an abrupt change between the undisturbed bed and a funnel depleted of fines (Figure 5-2 g and h). However, there is a layer of deposited fine particles on the undisturbed bed to either side of the fluidised zone (Figure 5-2 e, f, g and h). The formation of lower porosity walls relative to the previously fluidised funnel will deter any further pipe mobility. Thus, in comparison to a previously unfluidised bed that could allow some fluid to dissipate through the unconfined bed, the formation of fine-grained walls around the coarse-grained funnel will act to concentrate any future fluidisation episodes through this path. This will provide permeability conduits even after cementation, providing preferential dissipation of fluid overpressure by this route.

In some respects, the two-dimensional data shown in this chapter compare well to the three-dimensional experimental results shown in Chapter 5. For example, the low porosity cases exhibit an abrupt change between the fine-grained, low porosity wall and a coarser-grained, higher porosity funnel.

However the 3D concentration data (Figures 5-18 to 5-26) do not appear to show the accumulations of elutriated fines that are visible to the eye in the present qualitative data. It is likely that, in three-dimensions, segregation still occurs as is visible in the two-dimensional data but the difference in porosity between exclusively fine-grained regions and the undisturbed bed is very small. Similarly, the high porosity CT data do not clearly show funnel formation without “value clamping” of the data set. Nevertheless, wall formation was visible for the very high porosity and high porosity cases during fluidisation because the difference in porosity between the slow moving falling particles forming the walls and the dilute zone is more pronounced (See Chapter 5 Figure 5-16).

In some cases during pipe formation, fines accumulated in sufficient quantities to form a falling stream. These streams of fine particles have a higher suspended sediment concentration and thus a significantly reduced permeability relative to their surroundings and therefore can “deflect” the turbulent jet. In the higher porosity cases, the fluid is not able to transport the fine particles away from the fluidised zone and so fine particle accumulation is more likely thus causing more jet deflections and decreasing the stability of the jet in the higher porosity cases. In the present experiments, the jet has a fixed inlet and so deflections are variable in time but often revert to a central jet location. Ross et al. (2011) observe migrating jet behaviour but do not determine why some jets migrate and others stabilise. It is hypothesised that bed heterogeneity caused by particle segregation is a driving force for jet migration when the fluid flow inlet is not fixed.

5.4.3 Sequence of fluidisation

It is apparent that the mechanisms for fluidisation proposed by Cartwright and Santamarina (2015) are too simplistic to appropriately capture the range of fluidisation behaviours catalogued in the present experiments (see Figure 5-10). Although there is evidence for both hydraulic fracture and erosive fluidisation within the behaviours, the observed sequences of fluidisation differ according to the respective porosities of the tested beds. Therefore, two new models for fluidisation are now presented. These models will be compared to existing models in section 6.4.5.

5.4.4 New models of fluidisation

The consistency of the sequence of fluidisation across nominal flow regimes necessitates the development of new models for identifying a range of geological features observed in outcrop and seismic data. Herein, it has been shown that the geometry of the intrusion shows a much stronger dependence on the stage of the formation process relative to the intrusion velocity rather than the intrusion velocity alone. Furthermore, the sequence and mechanism of fluidisation is dependent on the porosity of the bed. As such, a range of complex geometries can be developed from a single set of inlet parameters. Figure 5-11 demonstrates the range of possible geometries from a high porosity bed and Figure 5-12 demonstrates the range of possible geometries from a low porosity bed.

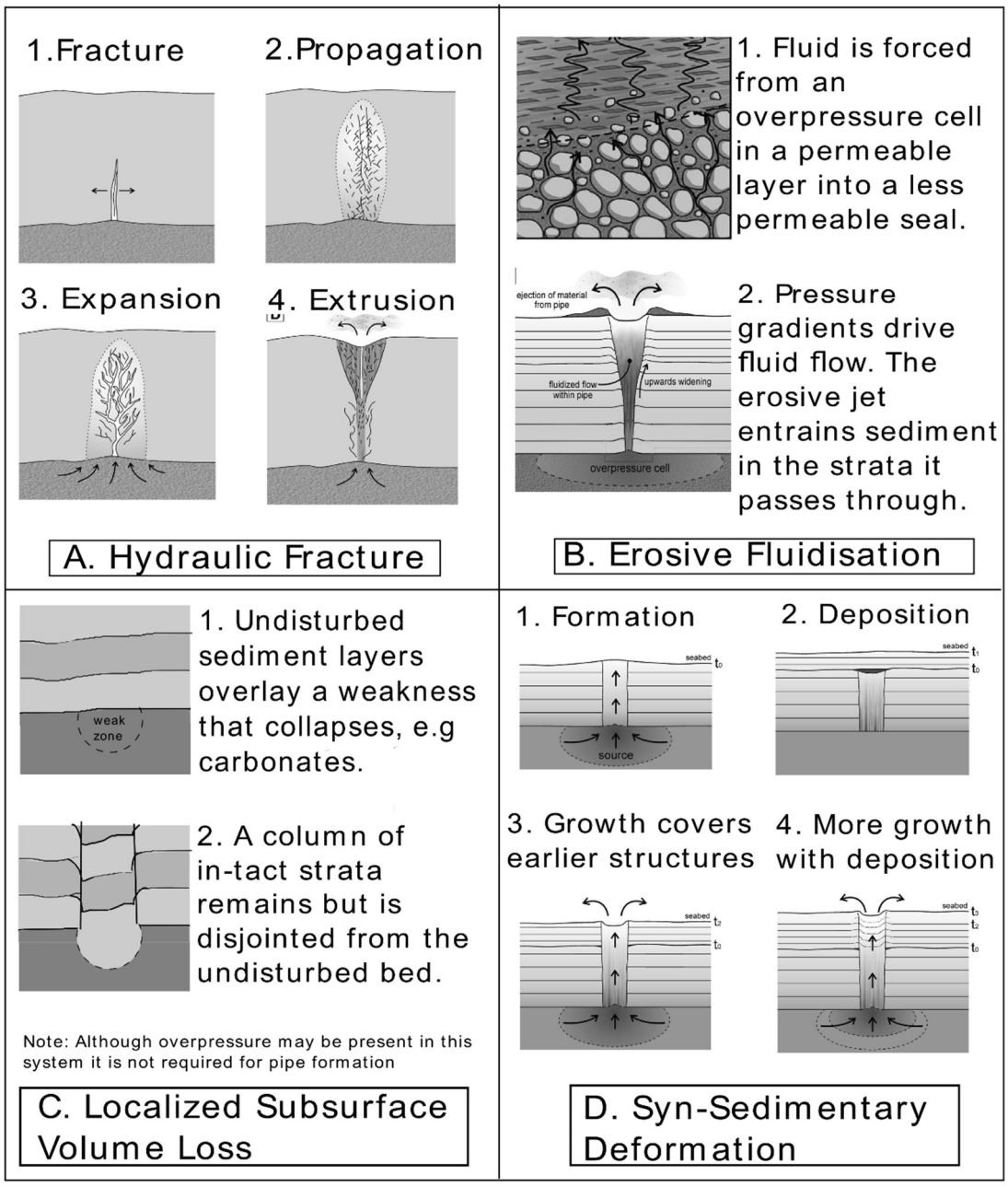

Figure 5-10 Summary of fluidisation mechanisms proposed by Cartwright and Santamarina (2015). A. Hydraulic fracture. A.1 - The overpressure exceeds the tensile strength of the bed and a fracture occurs, fluid rushes into the fracture expanding the fracture. A.2 the overpressure causes more fractures surrounding the initial fracture and a network of fractures propagates. A.3 The network of fractures expands as more fluid is pushed in. A.4 The network reaches the surface and extrusion occurs. B. Erosive fluidisation. C. Localised sub-surface volume loss. D Syn-sedimentary deformation.

5.4.5 The effect of the fluid content on the residual structure

In the low porosity model, fluidisation initiates with a small hydraulic fracture that expands to a void space. The bed is raised intact. If a dilute fluid flow were to cease at this point, the fluid in the void space would dissipate slowly, most likely through weaknesses formed where the undisturbed bed meets the disturbed bed that has been raised by the temporary formation of the void. The previously raised bed will fall downwards after fluid dissipation, still intact but disjointed from the original, unfluidised, strata. It is likely that the fluidised column will settle back down lower than the original strata because of the particle segregation and transportation out of the system due to the fluidisation process. Thus, such features could easily be misinterpreted as a localised sub-surface volume loss. However, if the injection is a multiphase mixture of sediment and fluid, the overlying sediment bed will remain raised upon dewatering and a region of injected sediment will sit below the raised, disjointed bed. This mechanism of sand remobilisation and subsequent mounding of the bed has been proposed by Wild and Briedis (2010) as the formation mechanism for the Palaeocene mounds observed in the Balder and Ringhorne Tertiary oil fields of the Utsira High. In line with their model, this would cause a convex doming effect directly over the injected sand (see Fig. 14 of Wild and Briedis, 2010). Therefore the concentration of the particles in the injected fluid is crucial to the residual structures observed. Future work modelling the influence of injecting high concentration slurries would provide evidence for formation of such structures by this mechanism.

5.4.6 Established mechanisms of fluidisation

The established formation mechanisms for fluidisation pipes are summarised in Figure 6.10 (adapted from Cartwright and Santamarina, 2015). Hydraulic fracture is the most commonly cited mechanism for fluidisation pipe genesis (Davies et al., 2012). Hydraulic fracture is described as a propagating network of fractures finally resulting in a widening, linkage of the network with increasing flow that eventually results in an expulsion at the seafloor (Figure 5-10 A). Other cases purported to propagate via hydraulic fracture propose a more rapid and explosive fracture mechanism (Loseth et al., 2011; Davies et al., 2012). Erosive fluidisation is established as a necessary and widely observed phenomenon (Nermoen et al., 2010) but cannot explain some features of *in-situ* pipes such as continuity of stratigraphy across the pipe (Cartwright and Santamarina, 2015). Localised sub-surface volume loss could explain a continuous stratigraphy across a fluidisation pipe but then a mechanism for such a loss must be identified (Quilang et al., 2013). The model of fluidisation proposed herein differs from previous models in that, rather than looking to single mechanisms to explain the characteristics observed in *in-situ* fluidisation pipes, the interaction between the well-established mechanisms and the stage in the flow sequence is considered.

It is demonstrated in these experiments that a range of processes and sediment reworking occurs in the formation of fluidisation pipes. The likelihood of any one fluidisation event reaching the stabilised state is heretofore unconsidered and therefore unquantified. A fluidisation event can only last as long as the overpressuring mechanism persists and has not dissipated (Davies et al., 2012). Once the overpressure has dissipated fluidisation must

necessarily cease and so the duration of the fluidisation event relative to the stage in the sequence is the key determining factor in the geological features observed both on the seafloor and in outcrop. This model extends the model proposed by Ross et al. (2011), by establishing the range of likely characteristics that could be observed following the fluidisation event and considering the interaction of the particle segregation effects on the wall formation features, although in contrast to the Ross et al., (2011) model the inlet of the fluid was deliberately fixed to prevent pipe migration so that the quantitative data collection could be optimised.

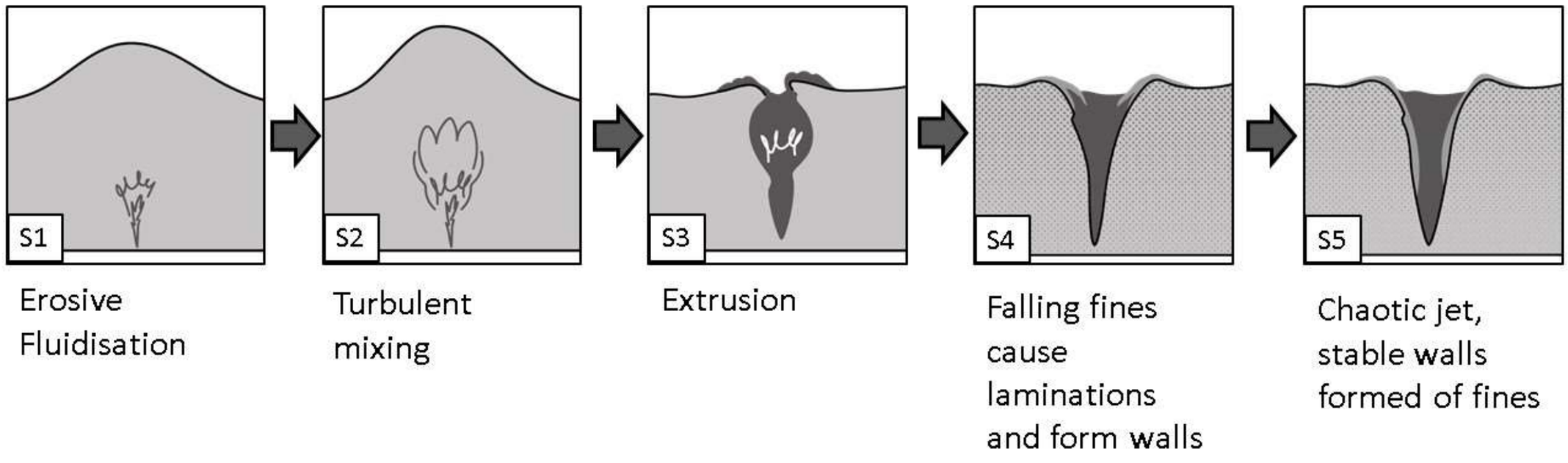

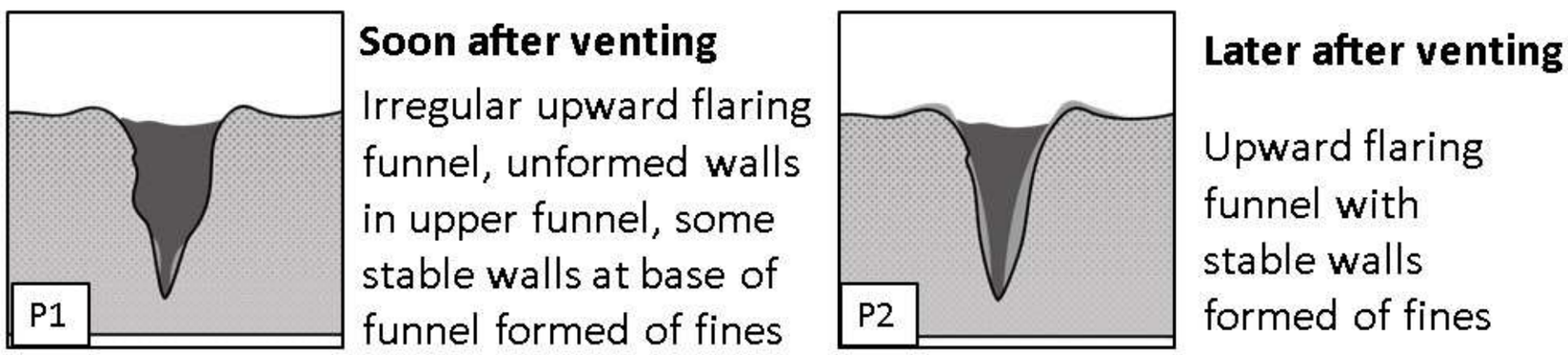

Figure 5-11 - Model of fluidisation for high porosity sediment beds. S refers to stage in the fluidisation sequence and P refers to the potential morphology that could be produced as a result of the cessation of flow at each stage in the fluidisation sequence.

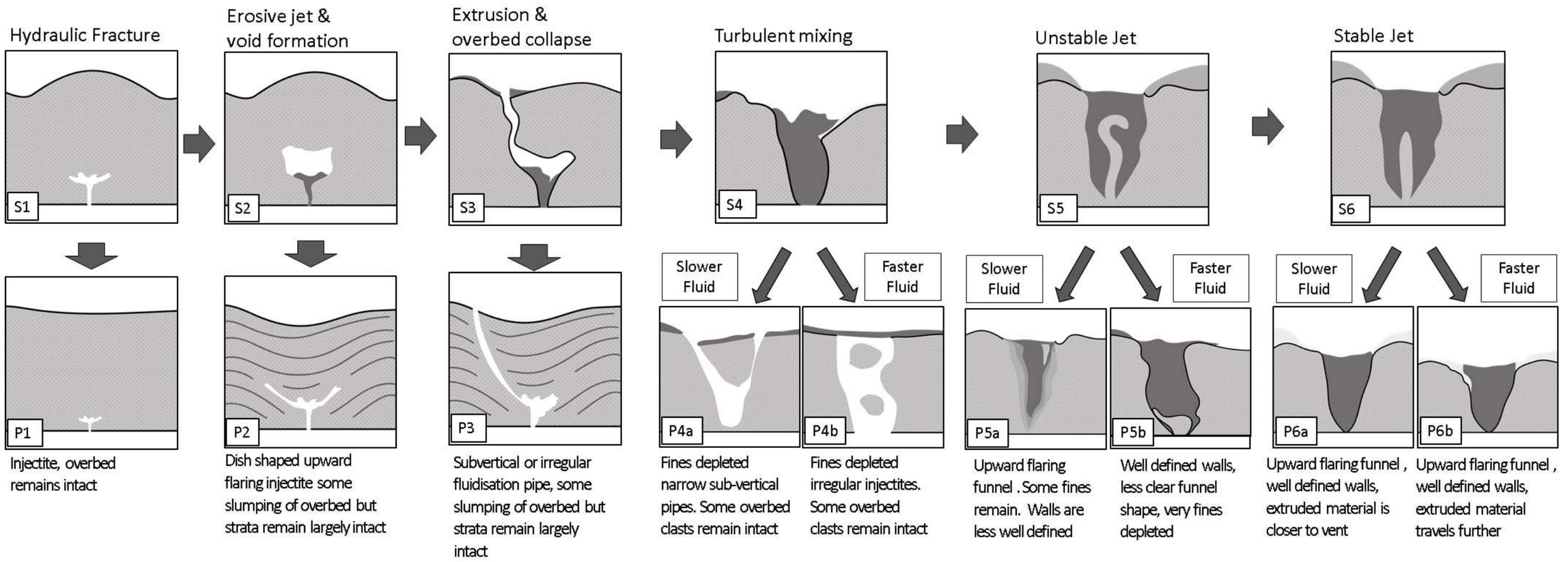

Figure 5-12 Model of fluidisation for low porosity sediment beds. Qualitative images of the fluidisation sequence for the low porosity cases, low porosity - slow inlet velocity (LP-S), left, low porosity - fast inlet velocity (LP-F), right.

5.5 Conclusions

An experimental model of the fluidisation of a sediment bed has been used to demonstrate the fluid dynamics of fluidisation pipe and extrudite formation. It has been shown that the porosity of the bed determines the initial mechanism for fluidisation but that the duration of fluidisation is of critical importance in determining the remnant geomorphology after the cessation of fluid flow and de-watering. It was observed that the nominal flow regime of the fluidisation event calculated as a Reynolds number *a-priori* bore no influence on the flow dynamics observed in the formation of the extrudite. In all cases, a central, dilute turbulent jet propagated upwards and a slow-moving laminar re-circulation of the particles was observed to either side of the central jet. The ratio of the particle size to the flow velocity governed whether winnowing or particle segregation was observed in the fluidisation pipe. In the cases where particles were too large to be elutriated from the system, they were segregated and in some cases were observed to interact with the upward moving jet, causing it to become more mobile within the fluidised zone. New models of fluidisation that capture the dynamics observed and documented herein have been presented for both low and high porosity cases. The likely geomorphological features that could be formed as a result of the fluidisation stages are proposed.

6 Numerical simulations of a bidisperse bed using a two-way coupled approach

In Chapter 3, experimental data were used to investigate particle motion through the flow field during a steady state fluidisation event (section 3.5.2). The data collected experimentally were used to make estimates about the capacity of a flow to support a given particle. This chapter seeks to use numerical modelling to investigate the particle behaviours at the onset of fluidisation and the coupling between the fluid and the particle velocities. The use of a Momentum Exchange Method (Ladd, 1994) facilitates coupling of the discrete phases and estimation of the forces exerted from the fluid to the particle and vice versa. This produces a simulation that is qualitatively and quantitatively comparable to the experimental analogue in the early stages of fluidisation.

Preceding chapters have established concentration as a critical parameter during fluidisation events. A numerical model of the flow field allows the definition of the exact locations of particles. The experimental modelling in previous chapters used particles to measure the velocities of the flow field but assumed that the particle had the same velocity as the fluid. This chapter will quantify the velocity of the fluid and the particles separately and outline progress towards modelling the full fluidisation sequence. The chosen approach is flexible in terms of permitting increased domain scale, bed thickness, and complexity in the form of polydisperse beds and non-spherical particles.

6.1 Methodology

Two approaches were used to model the fluidisation of a bidisperse bed: 1.) a commercial software suite, DigiPac produced by Structure Vision; and 2.) a freely available open source code, waLBerla produced by researchers at Friedrich-Alexander University, Germany. Both approaches rely on the Lattice Boltzmann Method implemented over a D3Q19 lattice model (Figure 6-1,taken from Iglberger et al., 2008) to model the fluid phase coupled to a model to solve for particle-particle interactions. The D3Q19 model uses 19 particle distribution functions (PDFs) to represent the 19 modelled directions possible from each node. For brevity, only the implementation of the two approaches through the software used and the computational architecture on which they were implemented are outlined here; both the underlying numerical codes and the computational architectures on which they were implemented were vastly different. Although the DigiPac suite is presented for completeness, it became apparent that it was not possible to use DigiPac to model the fluidised beds studied herein because it was impossible to scale the model domain to the size needed.

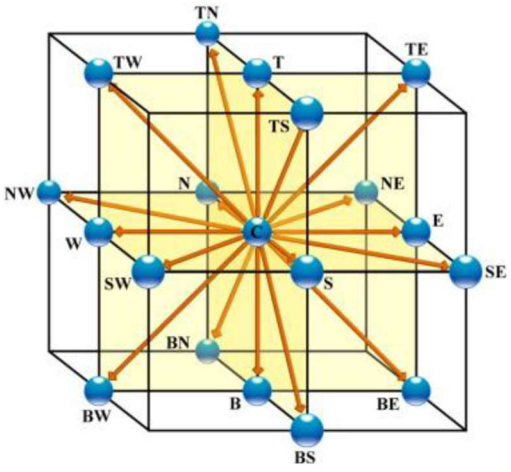

Figure 6-1 D3Q19 Lattice (Iglberger et al., 2008)

6.1.1 Structure Vision DigiPac software suite

The DigiPac software suite relies on multiple interacting modules that model different parts of the domain. First, the DigiUtility module – a module specifically used for creating the necessary .bin geometric input files – was used to build digital representations of the solid phase structures (e.g., particles, boundary walls; see examples in Figure 6-2). Second, the DigiDEM module was used to simulate particle motion. DigiDEM employs the Discrete Element Method (DEM) to model particle interactions as a “soft collision model” such that individual particles are permitted to overlap other particles when a collision occurs (DigiDEM user guide, 2012). It is then assumed that contact forces that result during collision are proportional to the degree of overlap of the particles. In order for simulations to run effectively within DigiDEM, each modelled particle must be composed of at least the minimum permissible number of voxels. Since the maximum permitted overlap in DigiDEM is 10% of the particle diameter (DigiDEM user guide, 2012), the minimum recommended diameter of particles is therefore 10 voxels to ensure a minimum permitted overlap of 1 voxel.

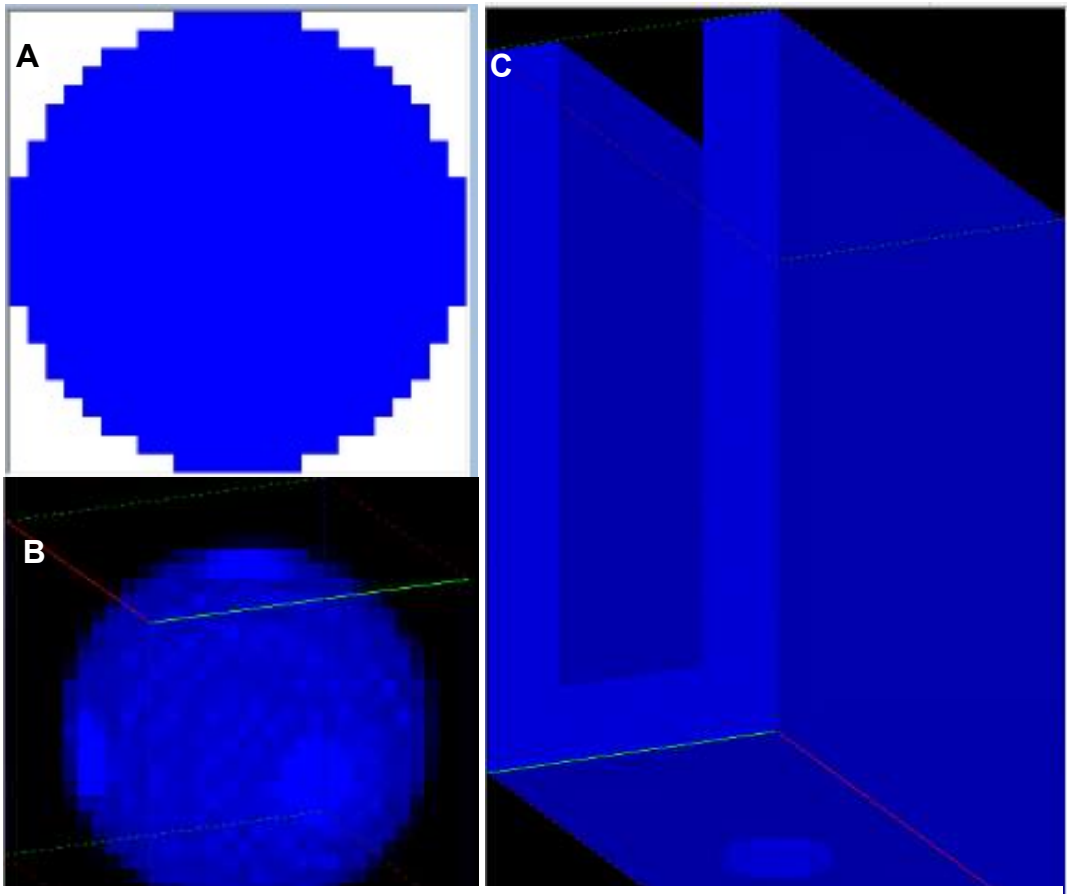

Figure 6-2 Representations of a sphere produced in DigiUtility with a diameter of 25 voxels rendered in two (A) and three (B) dimensions and a digitised tank (C).

It is not necessary to model the spheres and inlet at the scale of the experimental models, however it is important that the whole system is geometrically similar to allow a reasonable comparison between the experimental and numerical models. Therefore, the ratio between the diameters of the modelled coarse and fine spheres should approximate the ratio between the diameters of the coarse particle class and the fine particle class in the experimental analogue and the ratios between the diameters of the inlet and the particles should also be similar. The domain is configured so that Z represents the vertical direction corresponding with the positive fluid flow direction, X is the cross-stream direction across the width of the tank and Y represents the cross-stream direction corresponding with the depth of the tank, arranged to align with the experimental configurations in

preceding chapters. However, owing to computational limitations, it was not possible to ensure geometric similitude for the bed height because the number of particles in the model would be prohibitive.

The general process for running a DEM simulation in DigiDEM was:

1. Fill the virtual tank with a specified number of particles (e.g., Figure 6-3);
2. Allow the virtual bed to computationally settle to a (quasi) static state;
3. Pause the simulation. Add a drag force model by changing the selected drag force model from “none” to “LBM-Two way coupled”. Set X boundaries as periodic boundaries and Z boundaries as virtual boundaries in order to allow fluid to flow into and out of the domain and to more appropriately model the lateral bed properties. Specify the inlet velocity in the drag force model parameters;
4. Resume the simulation.

It was only possible to use the DigiPac software suite on a computer with a Windows-based Operating System, which somewhat limited the usability of the software in terms of scaling up the number of particles involved in the simulation. Initial simulations were run on a high-powered Windows Server 2012-based system comprising 2 × 18 core Intel Xeon E5 2699v3 processors with 512 GB of RAM (system name Wylye; see Table 7.1 for system architecture). It should be noted that DigiPac was not parallelisable across multiple processors so even though Wylye had two processors and 36 cores available, only 18 cores were available to the software at any one time. Executing simulations within DigiPac thus necessitated reaching a compromise between the desired domain size and the CPU and RAM

available. In addition, simulation run time was limited owing to IT-administration imposed policies that forced system restarts every 7 days. Furthermore, since DigiPac is a commercial package it was not possible to view, analyse or edit the underlying code. This proved problematic when encountering errors and problems with the implementation of the fluid phase

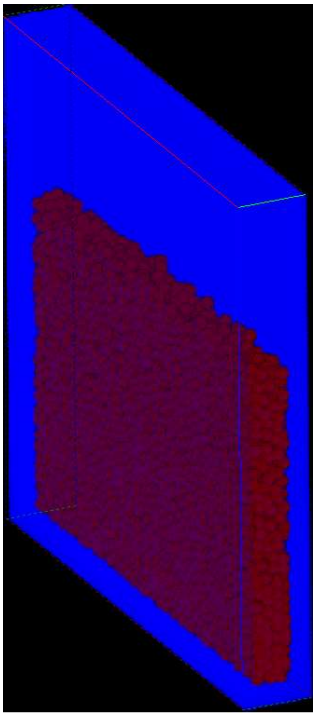

Figure 6-3 Example bed composed of 5,000 25 voxel particles produced by the DigiDEM DEM software.

model within the domain. After several months of trials and meetings with the software developers, it became apparent that these limiting factors would not permit the investigation of the research questions. As such, the decision was taken to use an open source implementation of the LBM suitable for use on a larger, Linux-based, High Performance Computing architecture

Table 6-1 Details of the computational architectures employed for simulations using both DigiPac and waLBerla

	Wylye	**Viper compute nodes***
Operating System	Windows	Linux
Processing cores	2x18 core Xeon E5 2699v3 processors	180 compute nodes each with 2x14-core Xeon E5-2680v4 processors (5040 potential processes)
Processing speed	2.3-3.6 GHz	2.4-3.3 GHz
RAM	512 GB	128 GB DDR4 per node

* The simulations reported herein were executed on the standard compute nodes, but Viper has a range of other nodes also available.

6.1.2 waLBerla and physics engine (pe) theory

The **w**idely **a**pplicable **L**attice **B**oltzmann framework from **Erla**ngen (waLBerla) is an open source numerical code created and maintained by the Friedrich-Alexander University, Erlangen, Germany. The code is highly parallelisable as it has been designed to run on the largest research computers available (Bauer et al., 2020). waLBerla and physics engine is implemented mostly in C++. Computational load is shared across the computational architecture though the partitioning of the simulation domain into a number of “blocks”; each process is then assigned to one or more blocks. Limiting data transfer between processes is important for high levels

of efficiency in a parallel environment (Bauer et al., 2020). The “BlockForest” part of the code monitors the distribution and load balancing amongst blocks and ensures that each process only “knows” about its assigned block and essential data from neighbouring blocks. The ability to parallelise simulations over large numbers of processes meant that it was possible to significantly increase the domain size and number of particles in the proposed simulations and increase the real-time computation output while still reducing computational time in comparison to DigiDEM.

The domain was modelled on a cuboid lattice, with each lattice node designated as solid or fluid. The fluid was approximated by Particle Distribution Functions (PDFs), the number of which was determined by the selected lattice; similar to DigiDEM, waLBerla uses a D3Q19 lattice by default (Figure 6-1), although this can be changed if required. The D3Q19 lattice results in 19 PDFs per lattice node (Figure 6-1, taken from Iglberger et al., 2008). The fluid field is calculated in two steps. First, the collision step, which has the effect of relaxing the PDFs towards their local equilibrium values, is computed as:

$$\widetilde{f_q}(\boldsymbol{x}, t) = f_q(\boldsymbol{x}, t) + \Omega_q(f) \tag{6.1}$$

where $\tilde{f}(\boldsymbol{x}, t)$ is the post-collision PDF at node location $\boldsymbol{x}$ and time t, $f(\boldsymbol{x}, t)$ is the pre-collision PDF at node location $\boldsymbol{x}$ and time t, $\Omega(f)$ is the inter-particle collision operator, and the subscript q (1 to 19) represents the direction of the PDF (Figure 7-1). The simplest collision operator available in this implementation is a single relaxation time approach first proposed by Bhatnagar et al. (1954):

$$\Omega_q(f) = \frac{f_q^{eq}(\boldsymbol{x},t) - f_q(\boldsymbol{x},t)}{\tau} \tag{6.2}$$

where f^{eq} is the local equilibrium PDF and τ represents a characteristic collision time. The local equilibrium PDF is given by:

$$f_q^{eq}(\boldsymbol{x},t) = w_q \left[\rho(\boldsymbol{x},t) + \rho_0 \left(\frac{3(\boldsymbol{c}_q \boldsymbol{u}(\boldsymbol{x},t))}{c^2} + \frac{9(\boldsymbol{c}_q \boldsymbol{u}(\boldsymbol{x},t))^2}{2c^4} - \frac{3\boldsymbol{u}(\boldsymbol{x},t)^2}{2c^2}\right)\right] \tag{6.2}$$

where $\boldsymbol{u}(\boldsymbol{x},t)$ is the fluid velocity, $\rho(\boldsymbol{x},t)$ is the macroscopic fluid density, ρ_0 is set to 1 in lattice units, c is the lattice speed $\Delta x/\Delta t$, Δx is the grid spacing, Δt is the timestep, $\boldsymbol{c}_q$ is the lattice velocity for the direction q, and w_q represents the weighting factors. The weighting factors for the D3Q19 stencil are:

$$w_q = \begin{cases} \frac{1}{3}, \boldsymbol{c}_q = (0,0,0) \\ \frac{1}{18}, \boldsymbol{c}_q = (\pm c,0,0),(0,0,\pm c),(0,\pm c,0) \\ \frac{1}{36}, \boldsymbol{c}_q = (\pm c,\pm c,0),(\pm c,0,\pm c),(0,\pm c,\pm c) \end{cases} \tag{6.3}$$

However, equation 7.2 is known to cause slip at no-slip boundaries (Ginzburg et al., 2008; Rettinger et al., 2018). Therefore, a two relaxation time collision operator is implemented (Ginzburg et al., 2008; Rettinger et al., 2018) that splits the PDFs and the equilibrium values into symmetric and asymmetric parts with $\bar{q}$ representing the inverted direction q:

$$f_q^+ = \frac{1}{2}\left(f_q + f_{\bar{q}}\right) \tag{6.5a}$$

$$f_q^- = \frac{1}{2}\left(f_q - f_{\bar{q}}\right) \tag{6.5b}$$

$$f_q^{eq+} = \frac{1}{2}(f_q^{eq+} + f_{\bar{q}}^{eq+}) \tag{6.5c}$$

$$f_q^{eq-} = \frac{1}{2}(f_q^{eq-} - f_{\bar{q}}^{eq-}) \tag{6.5d}$$

This gives the collision operator:

$$\Omega(f) = -\frac{1}{\tau_+}\left(f_q^+ - f_q^{eq+}\right) - \frac{1}{\tau_-}\left(f_q^- - f_q^{eq-}\right) \tag{6.6}$$

with the two relaxation times, τ_+ and τ_- related by $\frac{3}{16} = (\frac{1}{2} - \tau_+)(\frac{1}{2} - \tau_-)$

(Ginzburg et al., 2008; Rettinger et al., 2018).

Second, the streaming step, which acts to translate the particle distribution functions to the neighbouring lattice cells, is computed as:

$$f_q\left(\boldsymbol{x} + \boldsymbol{c}_q \Delta t, t + \Delta t\right) = \widetilde{f_q}(\boldsymbol{x}, t) \tag{6.7}$$

where $\boldsymbol{c}_q$ is a discrete lattice velocity associated with each node direction q and Δt is the timestep (Rettinger et al., 2017). Emboldened variables in equations 7.1 to 7.6 are vector quantities with three spatial dimensions (X, Y and Z).

The solid particles are mapped onto the fluid domain by means of a "FlagField" where each cell is designated as either solid or fluid. The interaction between the two fields is modelled by means of a Momentum Exchange Method (Ladd, 1994). This method asserts that the total hydrodynamic force exerted on a particle can be estimated as the sum of all of the momentum contributions from the fluid to the solid along the boundary between the solid and the fluid. Multiple LBM steps can be averaged before executing the rigid body solver to reduce fluctuations due to the solid bounce back condition at the boundary between the solid and fluid. After the force on

the particles is calculated they are streamed throughout the computational domain and the new locations of the particles updated. For this to be appropriate, a suitable boundary condition must be employed along the boundary between the fluid and the solid. Necessarily the flag field is updated with the new fluid and solid locations and the nodes will change from solid to fluid and vice versa. Where a solid cell has become a fluid cell the fluid field must be reconstructed in this location and this is done simply by setting the fluid field to the equilibrium function, f_q^{eq}.

The rigid body solver can be changed in waLBerla depending on the system at hand. The first sets of simulations employed a DEM solver as used in the Structure Vision software, but this caused errors in the code execution due to the very large numbers of overlapping particles and large contact forces from the high fluid velocities tested. Therefore, a Hard Collision Semi Implicit Time Stepping solver (HCSITS) was employed which prevents particle overlap and calculates the contact forces at the point of a collision using small time steps and a semi-implicit Euler method (see section 3.3.2 and equations and implementation in Rettinger et al., 2017). The HCSITS solver executes multiple iterations before passing the collision and particle mapping data back to the LBM field, and uses a different time step to the global time step. This collision solver allowed longer simulations and for the simulation to execute throughout the available run time without error.

The outline algorithm employed for the simulations is shown in Algorithm 6-1 (adapted from Schuster, 2017 for this implementation).

6.1.3 waLBerla and physics engine (pe) inputs

6.1.3.1 Initialising a packed bed

Algorithm: One time step of LBM coupled with rigid body solver

1. **for** *each time step* **do**
2. **for** *each body* **do**
3. Map body into lattice domain
4. Reconstruct missing PDFs in case of cell changes
5. **end for**
6. **for** *two LBM time steps* **do**
7. **for** *each lattice cell* **do**
7. *Apply boundary conditions and execute communication between blocks*
9. *Stream and collide PDFs and evaluate forces on moving obstacles*
10. **end for**
11. **end for**
15. **for** *each body* **do**
16. Add gravitational and buoyancy forces
17. end for
1 7. **for** *each rigid body solver time step* **do**
19. **for** *each body* **do**
20. *Calculate displacement and resolve collisi*ons
21. **end do**
22. **end do**
23. **end do**

Algorithm 6-1 Algorithm showing the coupling between the fluid-field model and the solid phase collision model (adapted from Schuster, 2017)

In a similar manner to the DigiPac software, waLBerla requires a bed to be initialised before the onset of fluid flow. The first challenge is to make a well mixed bed with the correct amount of particles of the two chosen radii. The bed is created in the physics engine module of the implementation. The specification of the spheres required for the simulation was based on the number of spheres of each species, their respective radii, the initial distance between them and a small initial velocity. The initial distance and initial velocity choices determine how quickly the particles settle into a packed bed.

The bidisperse packed bed is generated sequentially. First a particle of species A is created at the first location. The location was then incremented and the code determined the species (A or B – properties of each species assigned in the input file) of the new particle. The species (A or B) was chosen by ascertaining the ratio between number of particles already created for each species and comparing to the total ratio between species specified in the input file. The particle was then assigned the properties (diameter and density) for the chosen species (See Table 6.2). Finally the location was incremented by the specified distance between particles. This process was repeated until the total number of particles had been created. The packed bed simulation commenced by releasing all the particles from the initial location with an initial velocity and allowing them to settle. The simulation creating the packed bed terminated when all of the particles had a velocity below a threshold velocity. At this point, the locations and properties of all of the particles were transferred to the LBM blocks and the main fluidisation simulation commenced. As there was a run-time limit on the computational architecture, it was important to minimise the duration of the packed bed simulation.

Generally, it was found the initial distance between spheres needed to be greater than the diameter of the largest sphere to avoid initial large collisions. The settling check velocity needed to be much greater than the initial velocity or the LBM simulation would commence before the packed bed formed. After several trials, it was found that an initial velocity of 0.001 ms^{-1}, an initial spacing between particles equal to the median diameter of the largest particle class, and a packed bed particle termination velocity of 0.002

ms^{-1}, built a reliable packed bed structure; these parameters were used for all subsequent simulations.

6.1.3.2 Distributed computing architecture and simulation parameters

waLBerla and physics engine were implemented on the Viper high performance computing (HPC) facility at the University of Hull (see Table 6.1 for architecture details). The simulations reported herein used between 30,000 and 120,000 particles and 153.6 million and 640 million cells, utilising between 160 and 320 processors, or 44-89% of the entire compute node capability of VIPER. As each node has 128 GB of RAM available, simulations were utilising between 10.24 TB and 20.48 TB of RAM. Distributed computing within waLBerla and physics engine employed Open-MPI as implemented in gcc compiler version 6.3.0.

waLBerla and physics engine were executed by means of a batch processing script instructing the HPC how many processors were required and an input file with the simulation details. The inlet conditions were adapted from the default waLBerla settings (waLBerla Framework, n.d) by adding in a circular inlet and a parabolic velocity profile calculated from the inlet velocity specified in the input file. The boundary conditions were set to solid with a no slip condition for the boundaries simulating the front and sides of the tank. The top of the tank was designated an outlet and the bottom boundary was solid with a no slip condition but also had a circular spot inflow to correspond to the experimental tank inlet. Initial simulations aimed to produce an output comparable in geometry to the experimental analogue and to be able to run for a sufficient amount of simulation time to reflect the full process of fluidisation. Therefore, multiple domain sizes and

numbers of particles were trialled with varying numbers of processors, dependent on the availability of the HPC facilities. In order to model the same initial conditions as the laboratory example, all of the simulations set the inlet velocity to 0.9 ms^{-1}, 0.02 in LBM units, the lattice cell size was 50 μm and the time step 1.1 x 10^{-6} s, giving a scaling factor of 45 between the lattice speed and the SI velocity. The largest particle class had a diameter of 750 μm, approximating the median diameter of the coarse particle class in all of the experiments documented herein (both two dimensional – Chapters 3 and 5, and three dimensional – Chapter 4), and the fine particle class had a diameter of 300 μm, approximating the median diameter of the fine particle class in the very high porosity experiments (Chapters 4 and 5). This gave a bed mixture analogous to the very high porosity cases in the experimental work however, here was no variation in particle diameter across the particle class (compare with section 5.2). Using a cell size of 50 μm, particles in the fine class thus have a diameter of 6 lattice cells and particles in the coarse class have a diameter of 15 lattice cells. The parameters employed in the simulation that completed the most time steps in the available computation time had the input parameters specified in Table 6-2. Results from this simulation are discussed in the next section.

Results were outputted as a collection of “vtk” files, with selected data characterising the fluid fields and the particles field. The vtk files were then opened and post-processed in the open-source software, Paraview. As the domains tested were often of the order of hundreds of millions of cells the output files were correspondingly large (~5 GB per timestep of fluid field recorded), making data transfer, storage and management challenging.

6.2 Results

6.2.1 Influence of bed thickness on void space development

The development of the void spaces for simulations of a range of bed thicknesses is shown in Figures 6-4 A-D. All of the simulations used the same inlet velocity and simulation parameters as shown in Table 6-2. The domain parameters were changed for each simulation and these are shown in Table 6-3.

The expansion of the void space has the same geometric properties for each bed regardless of the number of particles for the timesteps 10,000, 20,000. Table 6.4 shows that at 10000 timesteps the height of the top of the void from the inlet ranges from 4.32 to 4.50 mm. A maximum difference in height of 180 μm, this is less than the smallest particle diameter. Similarly, the maximum width of the void space varies by a maximum of 300 μm between the narrowest and widest void space across the range of particle beds. This indicates that across the range of bed heights tested numerically at 10000

timesteps (or 0.01 s) the void development is the same to within a particle diameter. At 20000 timesteps (0.02 s), the range in height of the void space is 280 μm, and the range in width is 650 μm. The smallest bed of 30,000 particles (Figure 6-4 D) then appears to grow faster in terms of height of void from the inlet for the following timesteps. The range in void heights begins to increase and is broadest between the thickest bed (120000 particles) and the smallest bed (30000). However it is noted that at 40000 timesteps the hight difference between the two void spaces has reduced again. This is likely because the differences in heights observed are to within a small

Table 6-2 Input parameters for simulation with 30,000 particles and 153.6 million cells

Width	40 mm
Depth	10 mm
Height	48 mm
Cell size	50 µm
Blocks width	10
Blocks depth	2
Blocks height	15
Inlet diameter	8.0 mm
Diameter Particle A	750 µm
Diameter Particle B	300 µm
Number of Particle A	18000
Number of Particle B	12000
Density Particle A	2.6
Density Particle B	2.6
Density fluid	1
Gravity	9.81 ms^{-2}
Inlet velocity	0.9 ms^{-1}
LBM velocity	0.02

Table 6-3 Domain parameters for particle beds compared in Figure 7-4 A-D

Run Name	Number of particles	Cells in domain	CPUs used for simulation (RAM in brackets)	Maximum number of LBM timesteps
1.2	120000	640 000 000	320 (20.48 TB)	41000
1.3	60000	640 000 000	160 (10.24 TB)	44000
1.10	45000	160 000 000	160 (10.24 TB)	32400
1.11.2	30000	153 600 000	300 (19.20 TB)	120000

number of particles and thus are not representing any meaningful differences between the void space developments of the bed thicknesses tested.

The diameters of the growing void spaces are remarkably similar between bed heights and at corresponding timesteps. Therefore it is concluded that the diameter of the void space in the very early stages of development is governed by the inlet geometry rather than the bed geometry. This could be further investigated by testing the influence of particle geometry on the void development in the system.

Despite the similarities in the void formation in these early timesteps, the overlying bed characteristics do show differences between bed thicknesses. For the 120000 particle bed (Figure 6-4 A) there is no detectable deformation of the interface of the bed with the overlying water column. At 40000 timesteps the height of the bed surface has increased by approximately 5 mm, but the bed surface remains level. At 40000 timesteps the 60000 particle bed (Figure 6-4 B) shows a small amount of “mounding”. There is a difference in the height of the bed surface at the centre (above the developing void) and the height of the bed surface at lateral tank walls of approximately 1.2 mm. At 45000 particles (Figure 6-4 C) and 30000 timesteps the mounding is even more pronounced, despite 10000 fewer timesteps than the other modelled beds. The bed surface height above the void is 2.5 mm higher above the base of the tank than at the walls. The 30000 particle bed (Figure 6-4 D) shows significantly more pronounced

mounding than is observed in the other beds. The mounding is visible at all plotted timesteps following the onset of fluid flow. At 40000 timesteps the

difference in height of the bed surface over the void to at the walls is approximately 6.5 mm. The bed deformations produced by the numerical model demonstrate that the model is able to qualitatively replicate the bed behaviour observed in the experimental work.

Table 6-4 Geometry of void spaces for each particle bed in Figure 7-4 A-D

Timestep	**10000**		**20000**		**30000**		**40000**	
Number of particles	height (mm)	diameter (mm)	height (mm)	diameter (mm)	height (mm)	diameter (mm)	height (mm)	diameter (mm)
120 000	4.5	12.9	6.8	15.5	9.2	17.35	10.8	16.6
60 000	4.45	12.65	7.1	15.35	9.6	17.66	10.2	21.7
45 000	4.4	13.6	7	15.5	9.75	17.4	-	-
30 000	4.32	12.3	6.82	14.85	10.32	17.1	11.42	17.09

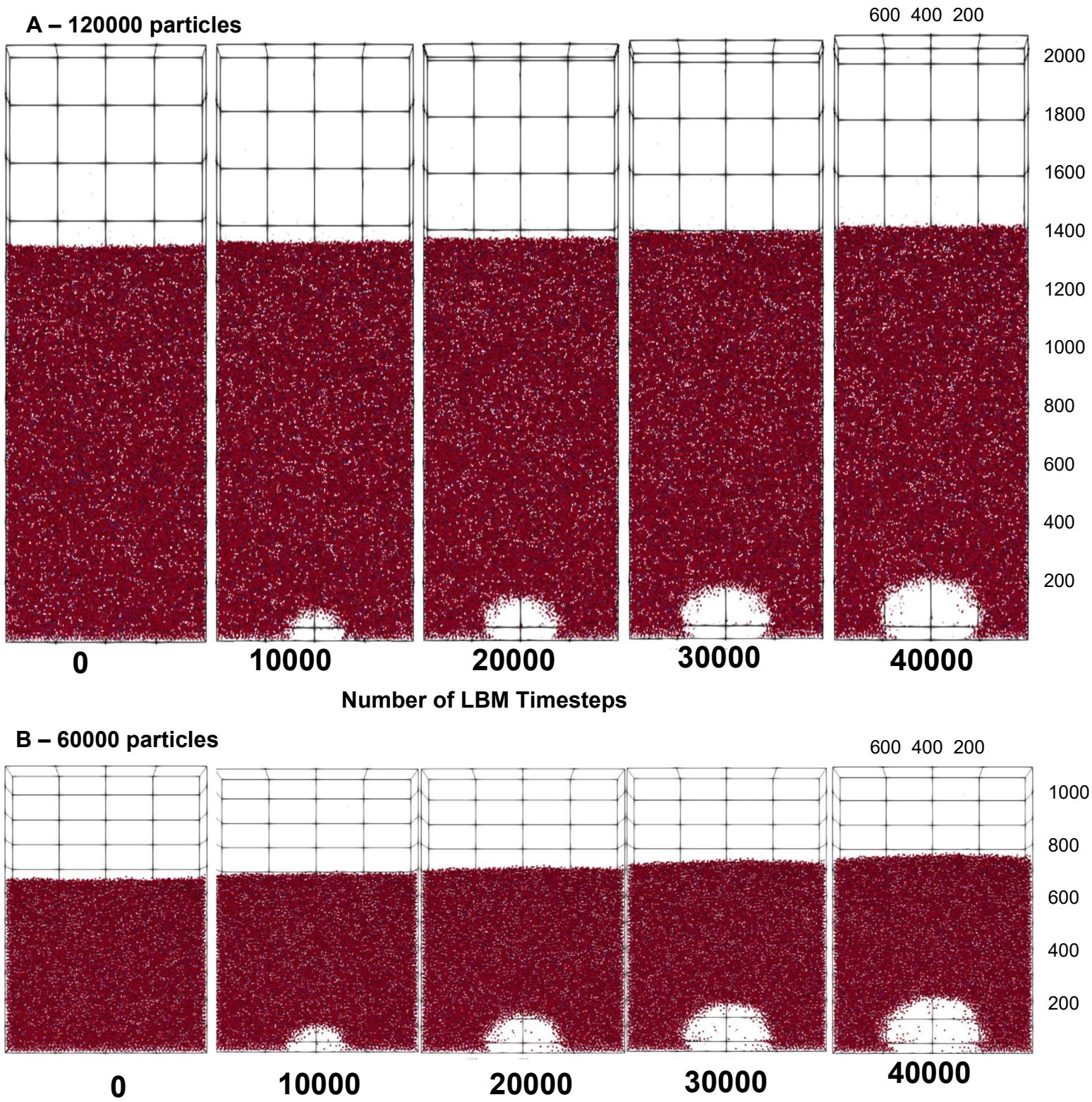

Figure 6-4 Results of multiple simulations showing the development of the void space during the initial stages of fluidisation. A - 120000 particles, B - 60000 particles, C- 45000 particles & D - 30000 particles. Where possible results are shown representing up to 40000 timesteps equating to 0.04 s of real-time simulation.

6.2.2 Onset of fluidisation

Results are shown from the simulation that completed the most timesteps, which comprised 30,000 particles, 153.6 million cells and ran to 122000 time steps (0.14 s of simulation time). The sequence is shown in Figure 6-5. The fluid velocity contours represent a slice through the centre of the tank and inlet (Y plane). The spheres shown are not clipped and show all of the particles in the domain coloured by velocity in the direction of fluidisation (Z), the particle velocity values have been clamped (-0.0014 to 0.11 ms^{-1}) here for clarity between the fluid and particle fields, however are shown unclamped in the sequence included in Figure 6-6.

Interestingly, the sequence in Figure 6-5 shows that after an initial period of expansion, from 0.066 s onwards the diameter of the void space remains at around 24.8 mm, approximately 3 times the diameter of the inlet. The fluid field also appears largely invariant from 0.044 s onwards. The velocity profiles in Figure 6-6 also reflect that the fluid field remains mostly invariant after 0.044 s.

Within the central jet region, velocity profiles plotted at multiple heights from the inlet show that once the void has passed a particular height, velocity profiles reach an equilibrium form (e.g., compare the profiles at 3 mm from the inlet in Figures 6-7 b-g, or those at 12 mm from the inlet in Figures 6-7 e-g).

The initial bed thickness for this simulation was approximately 17 mm. In the first captured data set at 5000 LBM timesteps (0.005 s), the void space had begun to develop and was 3 mm above the inlet. The fluid had a velocity of around 0.9 m s^{-1} close to the inlet but decreased approximately linearly to

around 0.18 m s^{-1} immediately beneath the particles (Figure 6-7, 0.005 s, right). The particle velocity in the region immediately above the void space was around 0.16 m s^{-1}, showing that the particles immediately above the void space were very slightly lagging the fluid velocities. Even at the first recorded dataset, the void space had expanded to the front and back faces of the simulated tank (20 mm wide), and had a diameter in the x direction of 10.4 mm.

At 0.022 s from the onset of fluidisation, the void space had expanded to 6.84 mm from the inlet in the vertical direction, and had a diameter in the X direction of 14.4 mm. The velocity profile still showed a linear decrease in velocity magnitude with height from the inlet to 0.14 m s^{-1}. Some particles from the largest size class were falling within the void space with a very low fall velocity (Figure 6-7, 0.022 s).

The void space had reached a maximum diameter of 24.8 mm by 0.066 s and was 17.6 mm vertically above the inlet, having now expanded past the original bed thickness (Figure 6-7, 0.066 s, left). The fluid filled void still supported the largely intact overlying bed which had a thickness of 10.2 mm. Above the particle bed, the fluid velocity remained constant at 0.098 m s^{-1} for the remaining height of the domain (Figure 6-7, 0.066 s, right).

The void space continued to grow until the final recorded dataset at 0.133 s (120,000 LBM timesteps), but appears to become asymmetrical towards the right of the void space (Figure 6-7, 0.133 s, left). At timestep 120000, the void space was 31.4 mm in height from the inlet at the centreline. At 6 mm to the right of the centre of the inlet the void space reached 32.3 mm in height from the inlet, indicating that the void space is beginning to become

asymmetric. The asymmetric void development possibly represents the beginning of jet branching as observed in sections 5.2.5 and 6.2.4.

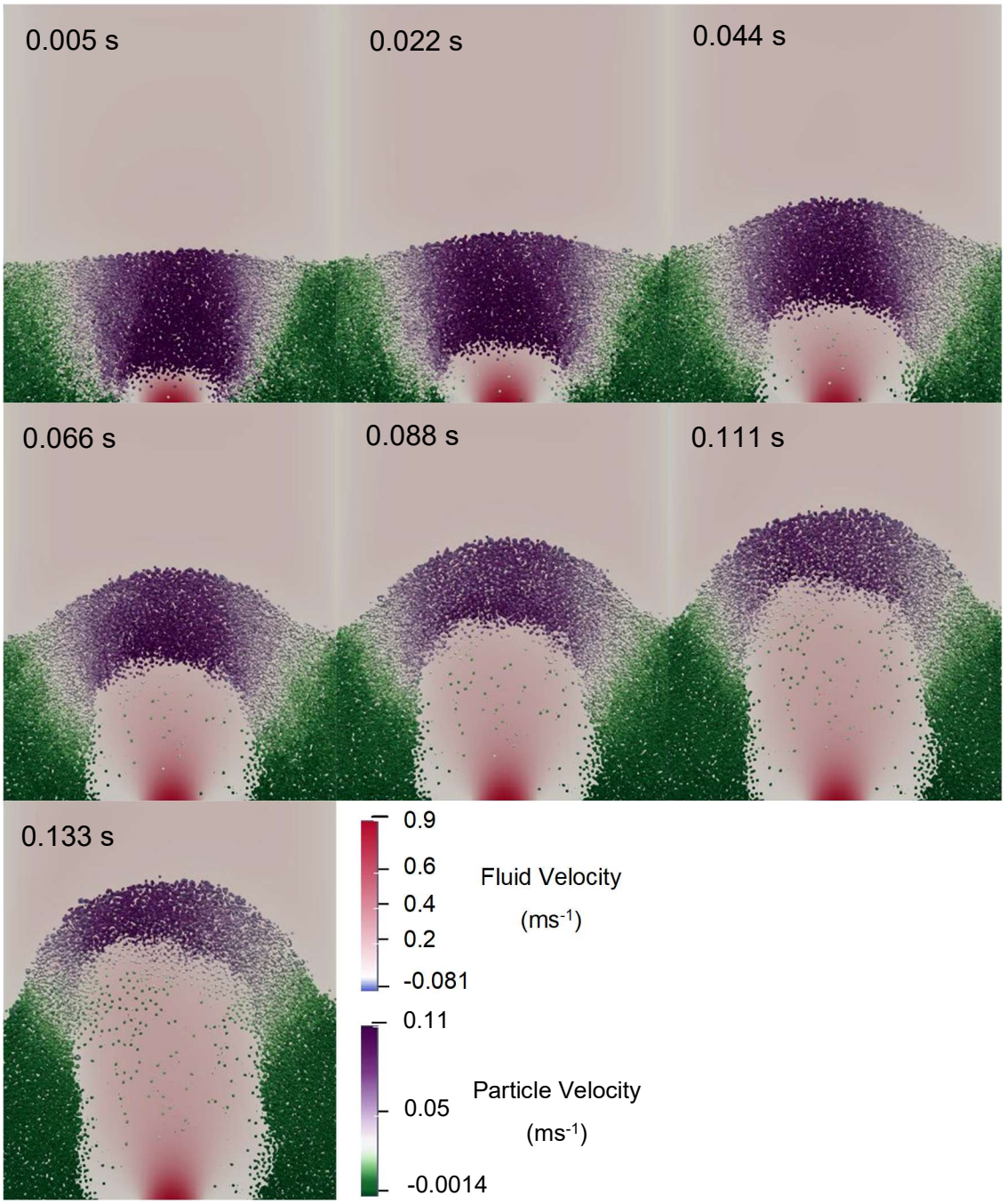

Figure 6-5 Fluidisation sequence for 30000 particles

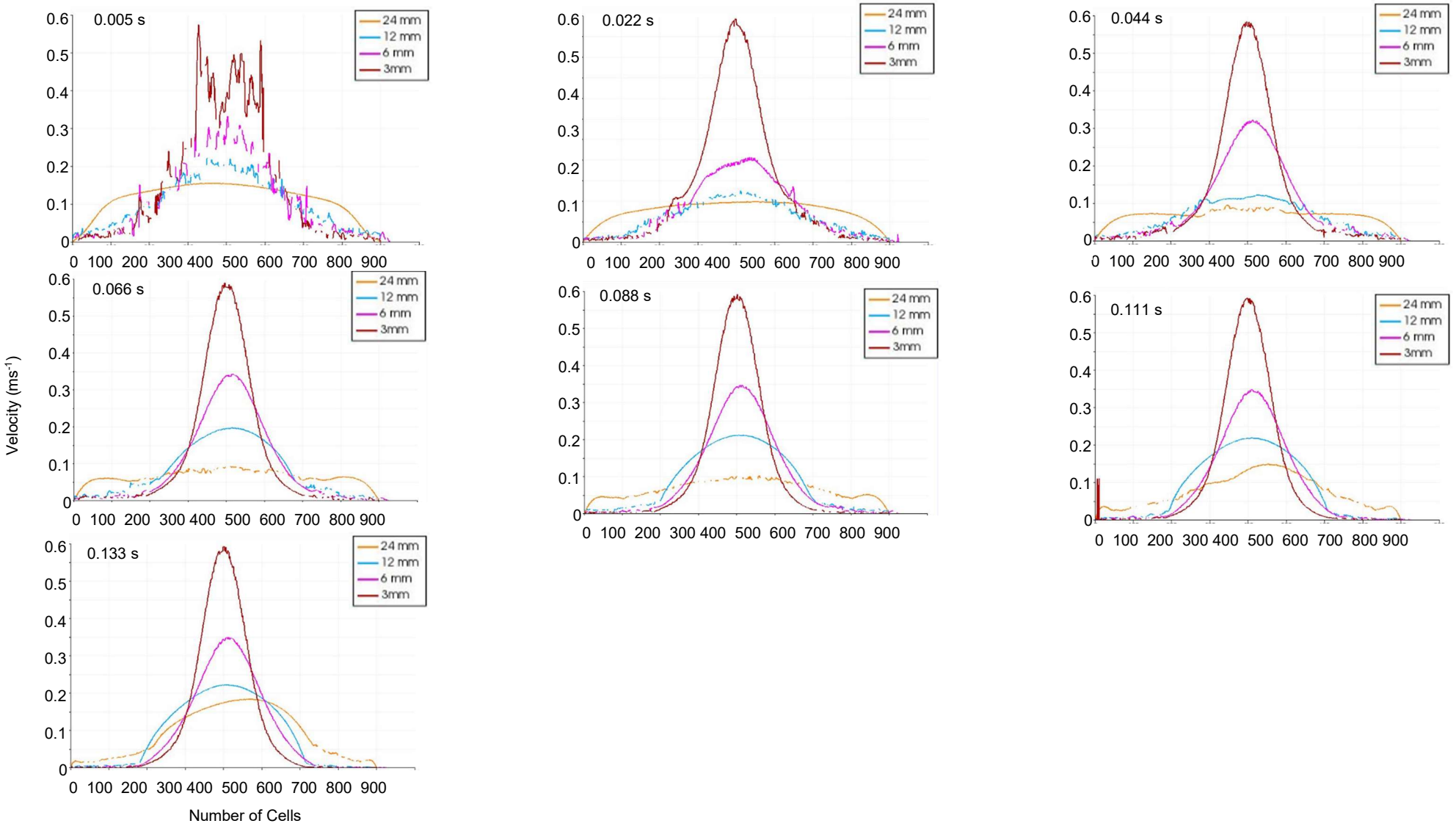

Figure 6-6 Velocity profiles for 3 mm, 6 mm, 12 mm and 24 mm from the inlet

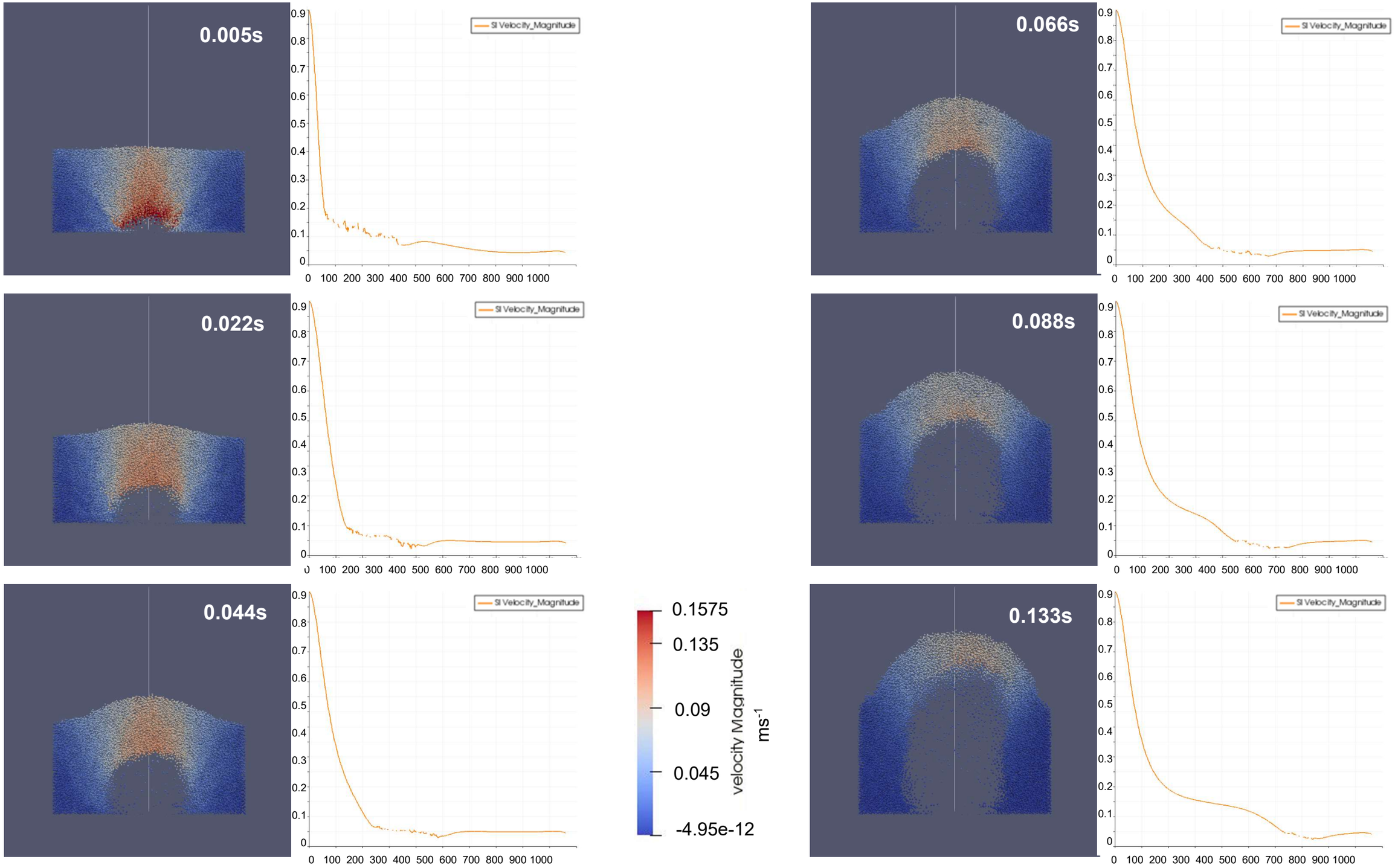

Figure 6-7 Particle field coloured by velocity of particle (left image of each timestep) and velocity plot of the fluid field (right image of each timestep), showing how the fluid velocity varies with height from the inlet along the centreline of the domain (line shown in the particle images).

6.3 Discussion

6.3.1 Comparison to experimental work

The numerical work herein simulate only a tiny amount of the data that was modelled experimentally, however it is still valuable to compare the data sets as an indicator of the potential of the model to be further developed in the future. Qualitatively the numerical model appears to be a good analogue for a fluidisation event. The qualitative analysis in Chapter 6 shows that all of the fluidisation events modelled begin with the formation of a void space in the bed, and this is replicated in the models shown in section 7.2.1 for multiple bed heights. The fluidisation sequence for the bed with a

Figure 6-8 Zoomed in image of comparable experimental analogue. The distance between the screws is 100 mm.

comparable porosity, particle sizes, and inlet diameter and velocity is shown in Figure 5-4, that is the very high porosity run detailed in section 5.2.3. Figure 6-11 shows the equivalent experimental analogue at approximately 0.5 s. The numerical model herein does not have equivalent tank dimensions, the depth of the tank in the experiments is 0.02 m and in the numerical models this is 0.01 m. So although Figure 6-8 shows a void diameter of 12 mm the void is only visible further from the inlet than is visible in the numerical model. The experimental analogues were also

characterised by mounding developing above the void as it formed and expanded, which is also seen in the numerical models. The three dimensional experimental data set showed a columnar fluidised zone, while the two dimensional experimental data set has a much more exaggerated funnel shape. However in the numerical case the bed height is significantly smaller so it is difficult to say exactly how the model compares to either case. It is likely that with greater computational power a deeper bed would resemble more closely the two dimensional analogues as the domain has been specified in this quasi-two dimensional way.

The velocity profiles presented in the quantitative data sets in Figure 3-19 share the same general profile, however in the numerical model the velocities appear to dissipate much more with increasing height than is seen in the steady states in Chapter 3. This could be due to the much reduced bed heights tested in the numerical simulation or alternatively could be due to the differences in permeability between the experimental bed mixture and the numerical bed mixture or a combination of both. As the numerical bed mixture is made up of spheres with no variation of particle diameter with spheres in the same class. This means that the pore throats will be larger between particles in the bed and thus it is significantly easier for the fluid velocities to dissipate through the bed. This has the implication then that the numerical model may never reach extrusion. If the fluid velocities have dissipated beyond the minimum fluidisation velocities the bed could remain in a quasi-steady state of a void overlain by the raised particle bed. This would appear similar to the cavity regime observed by Mena et al., (2017). Additionally, the much smaller bed thickness will allow more fluid to pass through as the flow path to clear water is much shorter. Future models could

test how increasing bed heights affect dissipation of velocities in the fluidised zone.

It is noted that even directly above the propagating void space there is a slight lag between the fluid and particle velocities (Figure 6-7). The difference between the two velocity fields is more pronounced away from the centreline of the velocity field. Figure 6-5 shows that the fluid field does not have any areas of negative fluid velocities, although there are very small fluid velocities, whereas falling particles are expected at the margins of the fluid flow and in the void space. This would imply that the velocities measured in the PIV data, which are measured by tracking the larger particles in the flow field, are affected by the particle drag forces and particle interaction forces during the fluidisation event. Further work could develop the numerical model to be able to quantify the lag between the two velocity fields more exactly and thus quantify the drag coefficients appropriate for high concentration fluidisation events.

As was also observed in the experimental work, it appears the propagation of the void space accelerates with proximity to the free surface. In this chapter it was observed that this appears to happen at the half-thickness of the bed. However, it is likely this is related to the small scale of the numerical experiment. In qualitative experiments of ‘very high porosity beds’ the void did not persist to the half-thickness of the bed. After a relatively small height the mechanism changed from a void propagation mechanism to an erosive turbulent mixing mechanism that entrained the bed as the fluidisation advanced towards the surface. It is unclear at this stage in the simulation if the model would have replicated this behaviour on the deeper beds or at

extrusion. It is noted however, that the instantaneous velocity profiles are comparable to the mean velocity profiles of the experimental data. This would imply that the fluid flow field in the numerical model displays fewer turbulent fluctuations than is observed experimentally, thus some kind of turbulence model could be required to increase the turbulence behaviour in the fluid in the void and central core.

6.3.2 Further model development

The model presented in this Chapter shows what is possible to simulate on approximately 160 processing cores on the Viper HPC facility (full capacity outlined in Table 6-1) (some simulations were able to use more due to quiet periods on the HPC facilities) and using a code that has been optimised for parallelisation. With access to a greater number of processing cores or longer simulation times the models used here would be capable of producing much greater insight into the fluidisation processes. The waLBerla and physics engine numerical models scale linearly with particle numbers and so by improving the number of blocks and simulation time much larger beds would be able to be modelled. Increasing the computational power would allow more timesteps and therefore enable simulation of the full fluidisation process. It would be beneficial to determine if the model displays the same turbulent mixing features observed higher in the fluidising bed as seen in Chapter 5.

The original aim of using the numerical model in this work was to investigate how a greater range of polydispersivity in the particle classes affects the fluidisation and segregation features observed in fluidisation events. waLBerla and physics engine are able to achieve this (Eibl and Rüde, 2018;

Schruff et al., 2018), but again this was not possible with the limited run times and processing power available during this work. It is possible to specify a particle class by a mean and standard deviation in the input parameters selected and so, this would be a relatively simple adaptation to the model arrangements presented here. For details of how waLBerla and physics engine are optimised for polydisperse simulations see Eibl and Rüde (2018).

The physics engine module stores multiple data fields for the particles and the orientation field and flag field allows for angular and asymmetrical particles to be modelled (Fischermeier et al., 2014; Bartuschat et al., 2018). Future models could take advantage of these features and investigate how the angularity of the particles affects the fluidisation features of the bed as this will likely induce more local variations in porosities.

Although waLBerla has the in-built functionality to create checkpoint files (Bauer et al., 2020), thereby allowing a simulation to be stopped and restarted (accounting for run time limits often employed on HPC systems), it was not possible to successfully restart simulations on the Viper architecture (Table 6.1). The initial simulation was able to run successfully however restarts failed at the first timestep, the error messages cited stability issues, and unfortunately these were unable to be resolved in the time available. Further work would resolve issues that prevented the interruption and temporary pausing of simulations, facilitating much longer run times.

This work models the highest porosity sediment mix that was modelled experimentally in Chapters 4 and 5 however, the sediment classes were modelled without any variation of diameter. This sediment mix was chosen

as it allowed for the smallest number of cells in the domain and thus optimised the available compute time and capacity. Future work should could expand the cases tested to the high porosity and low porosity cases and thus allow a direct comparison between the PIV velocity profiles and those produced by the numerical model. Such numerical models would require an even smaller cell size, further increasing the number of cells in the domain and thus the compute capacity and run time required.

6.4 Conclusions

This study is the first to demonstrate that LBM and rigid body modelling can be used to examine fluidisation processes within sediment beds. The numerical model and resulting simulations modelled a fluidisation event that is qualitatively comparable to the experimental analogue. The model successfully replicated the development of a void space, the mounding of the overbed and the beginning of an asymmetry in the upper part of the void something that has been observed experimentally prior to larger-scale failure. The difference in permeabilities between the experimental analogue and the numerically simulated bed is expected to be the driver behind the greater dissipation of the velocity field observed in the numerical model. The void space generated by the model also appeared to have fewer falling particles than the experimental model, however this could be due to the difference in domain size. It has been demonstrated that, when using between 160 and 300 cores, it is possible to use numerical modelling to further investigate the fluidisation behaviour of bidisperse beds. By comparing multiple bed heights it is demonstrated that in the very early stages of fluidisation the geometry of the fluidisation event is independent of

the bed thickness. Further development of the numerical model offers a potential avenue to investigate the effect of adding more complexity to the models herein. There is a detectable difference in the velocities of particles and the fluid field in close proximity (Figure 6-7) providing a mechanism to quantify drag coefficients in high concentration events with further development. This initial demonstration of the power of LBM based models to simulate fluidisation events, has the potential to open up a whole field of study where velocity and concentration can be examined in detail for all the particles within a system and for a broader range of parameters.

7 Synthesis and Conclusions

This thesis has examined the processes and products of fluidisation events through both physical and numerical modelling. In Chapter 3 velocity data were captured using a two dimensional experimental arrangement. In Chapter 4 the novel use of Computed Tomography provided the first concentration data of a fluidisation event and also provided justification for the use of two dimensional arrangements for data capture. Chapter 5 utilised the qualitative data produced in the two dimensional arrangement to provide detailed sequences and processes of fluidisation and propose new models of the geological features that can be produced in fluidisation events. Chapter 6 used numerical modelling to elucidate the processes of void development and demonstrated that a numerical approach can improve understanding of sedimentological processes and form a basis for further investigations. This chapter will synthesise these data and contextualise the results, new models and understanding generated from these experimental and numerical models with the wider literature.

7.1 Initial stages of fluidisation

7.1.1 Initiation of fluidisation via shock or gradual onset

The present experiments (Chapters 3, 4 and 5) and those of Frey et al. (2009) and Ross et al. (2011) used a sudden onset of fluid flow to initiate fluidisation. This resulted in a sudden increase in the overpressure that the bed responded to by forming an expanding void space. In the present experiments, the cases where small void formation occurred were the very high porosity cases (Figure

5-3). In contrast, in the experimental arrangements of Philippe and Badiane (2013) and Mena et al. (2017), the fluid velocity was gradually increased until fluidisation of their monodisperse beds occurred and they did not report void formation. A further example is Mörz et al. (2007) who investigated fluidisation of a selection of natural and artificial soils and sands, covering a range of grain sizes. They also gradually increased inlet fluid velocity until fluidisation and did not observe the formation of voids, instead observing a gradual dilation of the bed until fluidisation.

This raises the question of whether the porosity of the bed governs the presence and magnitude of void formation or is the presence of voids related to a sudden onset of inlet fluid velocity? When the fluid velocity is gradually increased, the bed responds to small increases in pressure by dilating slowly, expanding the pore spaces between grains and causing a gradual transition from Darcian flow to dilation, liquefaction and finally fluidisation once the fluid velocity exceeds the minimum fluidisation velocity of a single particle. As such, the bulk density of such systems changes slowly and gradually in a homogeneous manner. If allowed sufficient time and the inlet velocity is only slowly increased, this behaviour is theoretically achievable for all beds irrespective of porosity. However, when a sudden onset fluid flow is used, the porosity of the bed is necessarily critical to the production of a void space. For a low porosity bed, the fluid flow cannot pass through the bed quickly enough to dissipate the induced overpressure. As such, a void forms that is capable of supporting a bed. Void formation may also be exaggerated by the two dimensional configuration of the present experiments, but although void formation was not visible for the low porosity cases in the three dimensional experimental runs due to the initial fluidisation occurring outside of the focus

of the CT scanner, void formation was captured in the high porosity cases (Figure 4-10, 3.5 - 4.5 s and 4-11, 3.5 – 5s). The very high porosity case was less dilute in the forming fluidised zone and also showed a more cylindrical geometry and so may not have formed a void space but a propagating erosive jet (Figure 4-13 7 s). Void formation was observed to occur in all of the tested numerical cases (Figure 6-4). At early timesteps, the geometry of the developing void was observed to be independent of the bed thickness, indicating that bed thickness is not a control on the geometry of the developing void (see Section 6.2.1).

As a direct result of the inability of the excess fluid to dissipate, the present experiments demonstrate that larger void spaces are generated by low porosities and large inlet flow velocities (Figures 5-1 and 5-4). The very high porosity bed was observed to expand through turbulent expansion and the bed could not be fluidised at a lower inlet velocity (Figure 4-13, 5-3). Therefore, the existence and magnitude of a void space is both a function of the bed porosity and the timescales of the change in fluid velocity. This raises further questions about the probability of seeing void behaviour in geological water escape systems. An analysis of the timescales and fluid velocities needed specifically to form void features is beyond the scope of this work.

7.1.2 Formation mechanisms of voids in early fluidisation

The formation of voids has been recognised in previous experimental work (Mörz et al., 2009; Ross et al., 2011; Bureau et al., 2014) but neither the sensitivity of formative mechanism to porosity nor the extension of voids to either form fluidisation pipes or steady-state fluidisation features have been identified previously. It was observed in Chapter 5.2.1 that all bed porosities and inlet velocities show some form of void development. The voids were

observed to initiate by mechanisms described by Cartwright and Santamarina (2015), but their models were developed to describe entire fluidisation pipes, not the void formation process specifically. The porosity of the bed was seen to be the controlling factor for the formative mechanism (Chapter 5.2.1), with the inlet velocity observed as a secondary control dictating the timescale of development and to a lesser degree the maximum size of the void space formed (see Figures 5-1, 5-3 and 5-4). The initiation of the fluidisation in the two dimensional cases is shown in Figure 7-1. Qualitative observations did not capture the initial liquefaction of the very high porosity bed (Figure 4-31), as this is very difficult to observe visually. Liquefaction is the process of the pore fluid pressure becoming sufficient to remove the grain-to-grain contacts and thus shear strength of the bed, but not sufficient for full fluidisation. Di Felice (2010) therefore identified liquefaction as a potential preceding step to full fluidisation, when the drag force exerted by the fluid exceeds the inertia of particles and causes entrainment. Pore-scale dilation of the bed resulting from liquefaction (Figure 6-2, H) could only be observed in the concentration data of the very high porosity case (see Chapters 4.2.5 and 5.2.5) immediately prior to the void development by erosive fluidisation (Figure 7-2, G-I). The wider liquified zone persisted through the erosive void formation and only regained the structure of an unfluidised bed several seconds after extrusion (Figures 4-31 6 – 11 s, 7-2 I). The present study is the first to observe a liquified base surrounding the fluidised region in a fluidisation zone.

The formation mechanisms for void spaces are shown in Figure 7-2. Erosive fluidisation is the simplest mechanism, shown in Figure 7-2, D-F. First, an initial erosive jet forms the void and entrains the bed. Second, as the void grows, the bed can be seen to mound over the expanding void and particles fall to the bottom of the void space and are re-entrained into the jet (Figure 7-2 E and 7-2, F). Erosive fluidisation was also simulated numerically in section 6.3 for a high porosity bidisperse bed but each particulate class was assigned a specific constant grain size without any deviation from the assigned diameter. It was therefore proposed that it is possible that the permeability of this bed may be large enough that the fluidisation may never reach extrusion (Chapter 6.3.1).

The formation of voids via hydraulic fracture was observed in low porosity beds. This mechanism was also addressed in Cartwright and Santamarina (2015), although after initial fracture the development process differed significantly. Cartwright and Santamarina (2015) posed that the initial fracture expanded slightly, leading to more fractures that would expand a little and so on, propagating as a network of fractures. Herein, the initial fracture was either

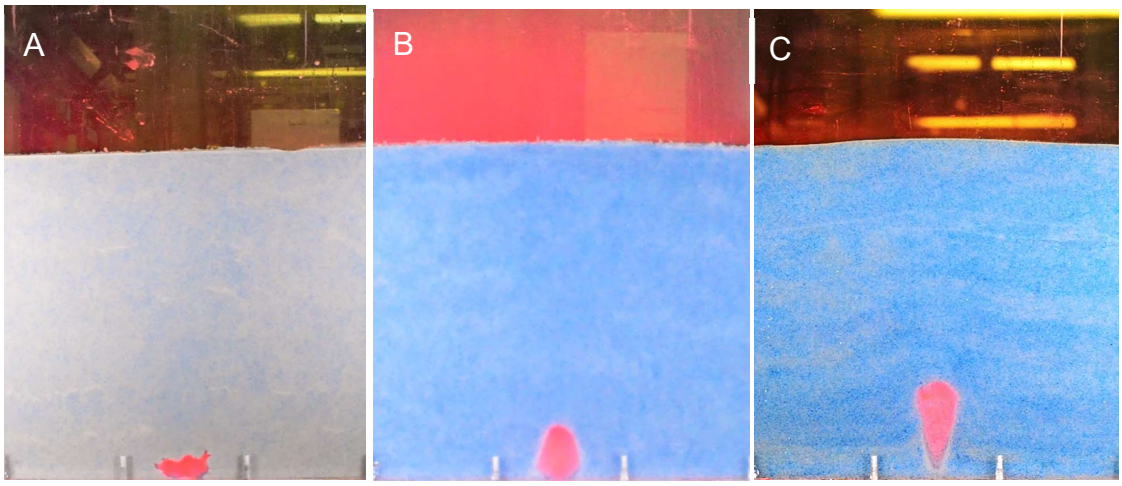

Figure 7-1 Formation of void space. Hydraulic fracture is observed for the low porosity case (A), and Erosive void propagation for high porosity (B) and Very High Porosity (C).

initially oriented in a quasi-perpendicular direction to the fluid propagation direction (low porosity, fast inlet velocity case, Figure 7-1 A), or was initially vertical before rotating to a quasi-perpendicular orientation at some elevation within the bed (Figure 7-1 a and c). In all observed cases of the low porosity mixture, at some stage the bed had a quasi-perpendicular fracture from which the void space expanded (Figure 7-2 A). As more fluid was pumped into the system, the void further expanded in the vertical direction, causing mounding above the void space and the formation and near-vertical propagation of two planes of weakness from the upper lateral edges of the propagating void to the edges of the mounded bed surface (Figure 7-2, B, dashed lines). When a jet propagated to the surface from the void space it would always be along one (or both) of these planes of weakness (Figure 7-2, C), providing a mechanism for the bowl structures seen in many seismic studies (for example Cobain et al. 2020). The difference in the hydraulic fracture mechanism observed herein and that described by Cartwright and Santamarina (2015) might be caused by a difference in the intruding fluid; experimental work injecting gas into saturated beds identified a propagating network of fractures (see Varas et al., 2011 and Varas et al., 2015), reflecting the Cartwright and Santamarina (2015) mechanism.

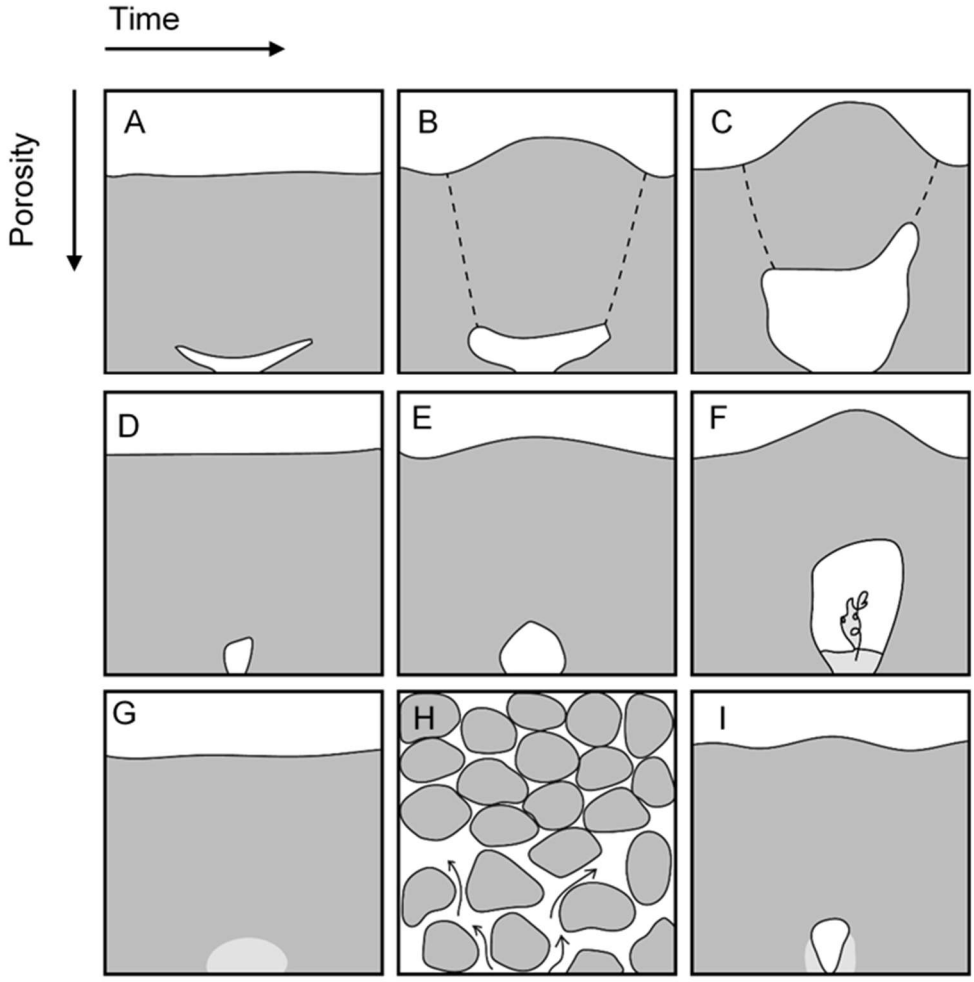

Figure 7-2 Formation mechanisms of void spaces shown for increasing porosity top-bottom and over time left - right. A-C hydraulic fracture: A is the initial fracture in quasi-perpendicular orientation to the lithostatic load, B shows expansion, mounding and planes of weakness, C shows further expansion and the formation of a jet along one of the planes of weakness. D - F erosive void formation: D shows initial formation, E widening of the void and mounding of the overbed F much larger mounding and recirculation of particles within the void space. G-I shows the very high porosity case where erosive formation sequence is preceded by the liquefaction of the bed region close to the inlet. G shows formation of a liquefaction zone H is a close up of the liquefaction process showing fluid supporting the grains overlain by the undisturbed bed and I shows erosive void passing through the liquefied sediment.

7.1.3 Presence of heterogeneities/faults/weak spots to exploit

Nichols et al. (1994), Frey et al. (2009) and Ross et al. (2011) observed that extrusions occurred at the apex of a regularly expanding void space. For a fixed inlet position, this occurs directly above the inlet. This behaviour is also observed in some cases herein, but this is not the case in all experimental arrangements, nor the case consistently within a set of experimental parameters. For low porosity cases, it was observed that an erosive jet or sometimes two erosive jets formed (Figures 5-1), and the dominant jet would propagate to the bed surface. The formation of such jets is intrinsically related to the exaggerated void formation and subsequent mounding of the overbed observed alongside this behaviour. Since the bed resists the passage of the fluid, the bed is pushed upwards en masse by the expanding void space. The kinetic energy of the jet is not dissipated in this manner, instead the force of the jet from the velocity of the fluid is partly deflected by the overbed and so propagates sideways along the roof of the void space until a point of lesser resistance is found. This weak point coincides with where the bed is already fractured from the upwards movement of the overbed (Figure 7-2 B and C) and so an erosive jet forms along these planes of weakness and propagates to the surface. Interestingly jet formation along a plane of weakness due to void-induced fracturing was not observed in the three dimensional configuration. However, one three dimensional low porosity run did form and stabilise away from the centreline equilibrium position (Figure 4-8), indicating that heterogeneities in the low porosity beds are the preferred location of fluidisation events. This mechanism of an injection exploiting bed heterogeneities is addressed by Cobain et al. (2015) for propagating injections in mudstones (Figure 2 of Cobain et al. 2015). Herein we observe that, in

addition to mudstones, a plane of weakness will also be the preferred location of fluidisation in a low porosity sand bed.

In higher porosity cases, extrusion is also observed to occur through an erosive jet. The high and very high porosity beds do not have such easily exploitable weak zones. However, there are still instances of jet deflection caused by a lower porosity heterogeneity, for example the jet splits around an undisturbed bed zone in Figure 5-30 at 2 s after initiation of fluid flow, demonstrating that even in high porosity cases small heterogeneities can influence fluidisation locations. It was also observed that in the higher porosity cases, void expansion is much less regular, demonstrating that the system is very sensitive to small scale heterogeneities.

7.2 Development of geomorphological features

7.2.1 Wall formation and particle transport in fluidisation pipes

In all cases observed herein, the steady-state stabilised walls in the upper part of the funnel were formed and shaped by the slow-moving, high concentration, particle flow to either side of the dilute turbulent jet (Figures 3-7, 3-9, 3-11 and 3-13). This is in direct agreement with the observations of Frey et al. (2009) and provides a logical explanation for the downward dipping laminations often seen in seismic and outcrop studies (Obermeier, 1996; Kawakami and Kawamura, 2002; Macdonald and Flecker, 2007) on the flanks of in-situ fluidisation pipes (see also Figures 4-24 and 4-25). In all cases, the walls are clearly identifiable and, after sufficient time has passed, relatively stable. In low porosity beds, sharp transitions between undisturbed bed and regions of mainly coarse particles with very few fine particles are characteristic; the

presence of the walls of the fluidisation pipe are only evident by these discordant margins with the undisturbed bed (Figures 4-16 C, 5-3 e and f). Both particles classes are transported upward in the central jet (Figure 7-3 left, red and blue arrows). At the interface with the overlying fluid the fine particle class is elutriated away from the fluidisation event (Figure 7-3 left – blue arrows). The three dimensional cases showed that recirculating coarse particles were located above the “bulb” (Section 4.2.2.1). The walls of the bulb had a sharp interface with the undisturbed bed, interpreted as forming via erosion by the upward moving jet (Figure 4-32 and 4-33). Therefore, in these low porosity cases, walls in the lower pipe would display evidence of turbulent upward erosion while walls in the upper pipe would display evidence of laminar falling particles (Section 4.2.5 and Figure 7-3 left). In the two-dimensional low porosity beds falling laminar particles formed the walls for the full height of the fluidisation event (Section 4.3.1). As it was not possible to collect three dimensional data for the steady state it is not clear from this data set if the upward moving erosive wall formation continues into the steady state or if recirculating particles migrate further down the pipe walls over time. Future work measuring the three-dimensional steady state could establish if this phenomena is time-dependent or a feature of the geometry of low-porosity fluidised beds.

For the high porosity cases, walls are lined with fine particles (Figures 4-16 A and B, 5-6 c and d and 5-4 h). When the absolute size of the finest particle class is greatest, the walls are most clearly defined (see Sections 5.2.6). This is due to the mechanism of formation: small particles are more easily elutriated from the system and have more potential to filter into the pore spaces of the coarse particles. In the highest porosity case, the particle size ratio between

the two classes is smallest. At high densities, fine particles cannot filter through the spaces in the coarse particle class. This is further evidence that the walls are formed by falling particles. Smaller particles can be transported further by the energy of the dilute turbulent jet, so they are translated further from the turbulent region and group together on the flanks of the sand volcano (Figure 7-3 right, blue arrows represent fine particle class, red arrows represent coarse particle class). When enough particles have accumulated, they slow the flow of the recirculating coarse particles and fall downwards, lining the fluidised zone. This layer is less permeable and less easily remobilised by the slow moving, larger particles and so stable walls are formed. Radial flow properties or turbophoresis (the inertial migration of particles away from a central region of turbulence) is a possible mechanism for the lining of fluidisation pipes with fine particles (Segre and Siberberg, 1962a, 1962b; Hogg, 1994; Ross et al., 2014). However, there is no evidence

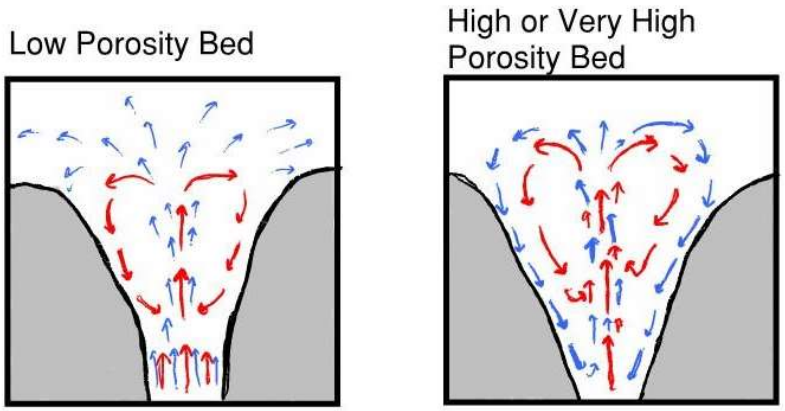

Figure 7-1 Sediment transport and erosion mechanisms in fluidisation events. Red arrows represent the coarse particle class and blue arrows represent the fine particle class. Low porosity beds (left) display erosion of the walls in the upward direction in the lower bed, elutriation of the fines particle class and downward erosion at the walls by falling coarse particles in the upper bed. High or very high porosity beds (right) have slow downward-moving fine particles forming the walls of the pipe as the fine particles are not able to escape the fluidisation pipe but are transported further from the central jet.

that either of these mechanisms apply in the cases observed herein. In fact, the identification of a shear zone indicated by very high velocity gradients between upward and downward flow regions would imply that it is impossible for a wall of fines to form in this way in the present geometries (Figures 3-23 to 3-30). It is more likely that the fines in the walls are formed by the recirculation cell and the smaller fluidisation velocity required by smaller particles of the same density. The formation of walls by falling particles means that when using the interface between the pipe walls and undisturbed bed in outcrop data, the propagation direction identified could be the reverse of the true propagation direction in a vertically oriented injection system. In all cases, more recirculating particles were accumulating in the upper funnel of the pipe (Figures 4-30 to 4-32 and also observed in Figures 5-1 to 5-5). Further, the wall formation in the steady-state is unequivocally laminar, as identified by the PIV data in Chapter 3 and the qualitative data in Chapter 6. It is noted that as there is no steady-state three dimensional data it is unclear if the falling particles in a laminar regime would recirculate from the free surface back to the inlet if there were a pipe circumference where deposition is possible (ie not made smaller by the two-dimensional tank geometry). Nevertheless, it was impossible to fluidise any of the beds without the formation of a turbulent core (see sections 3.4.1 and 3.5.1). Therefore, when interpreting laminar wall formations this is also likely to lead to unrepresentative assumptions of the whole pipe.

Chapter 5.2.6 identified that, in some cases, the passage of the void space and turbulent mixing of the bed as it propagated left residual structures in the bed (Figure 5-9). Interestingly, Ross et al. (2014) identified structures in outcrop interpreted to have formed by some sort of vortical structure (Figure

7-4). The structures appear similar, although in contrast to Ross et al. (2014) who interpreted the vortical structures to indicate that flow was likely from right to left, here a similar structure has been shown to form through vertical flow. The vortical formation process is likely similar to the two dimensional rotational vectors seen in the PIV data (Figure 3-3, repeated here in Figure 7-4, right).

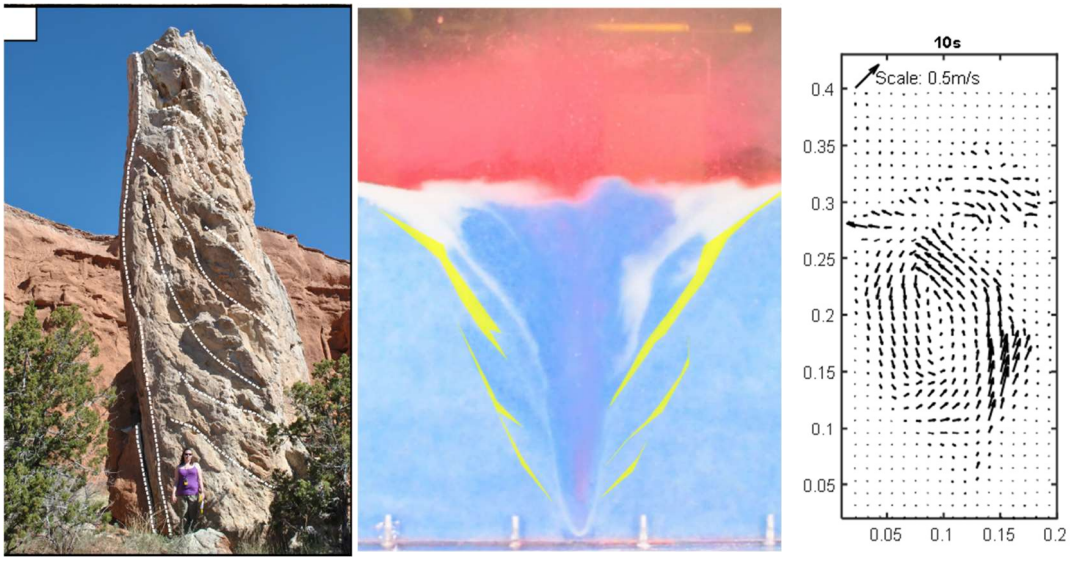

Figure 7-2 Columnar intrusion (left) taken from Ross et al. (2014) with vortical structures. Middle image shows similar structures created in two dimensional experiments formed by passing of a void and resulting turbulent mixing in the early stages of formation. Right image shows turbulent vectors during the passing of an erosive void space.

7.2.2 Flow regimes

The flow regimes of fluid injections have often been discussed (Peterson, 1968; Taylor, 1982; Obermeier, 1998; Duranti, 2007; Hubbard et al., 2007; Hurst et al., 2011; Ross et al., 2014; Cobain et al., 2015). The PIV data show that both laminar and turbulent regions of flow occur in the same fluidisation event when the steady-state has been reached (Figure 7-5) and this is true for both high and low porosity beds and fast and slow inlet velocities. It was not possible in the present experiments to form a fluidisation event without the formation of a turbulent core. The local Reynolds numbers calculated in

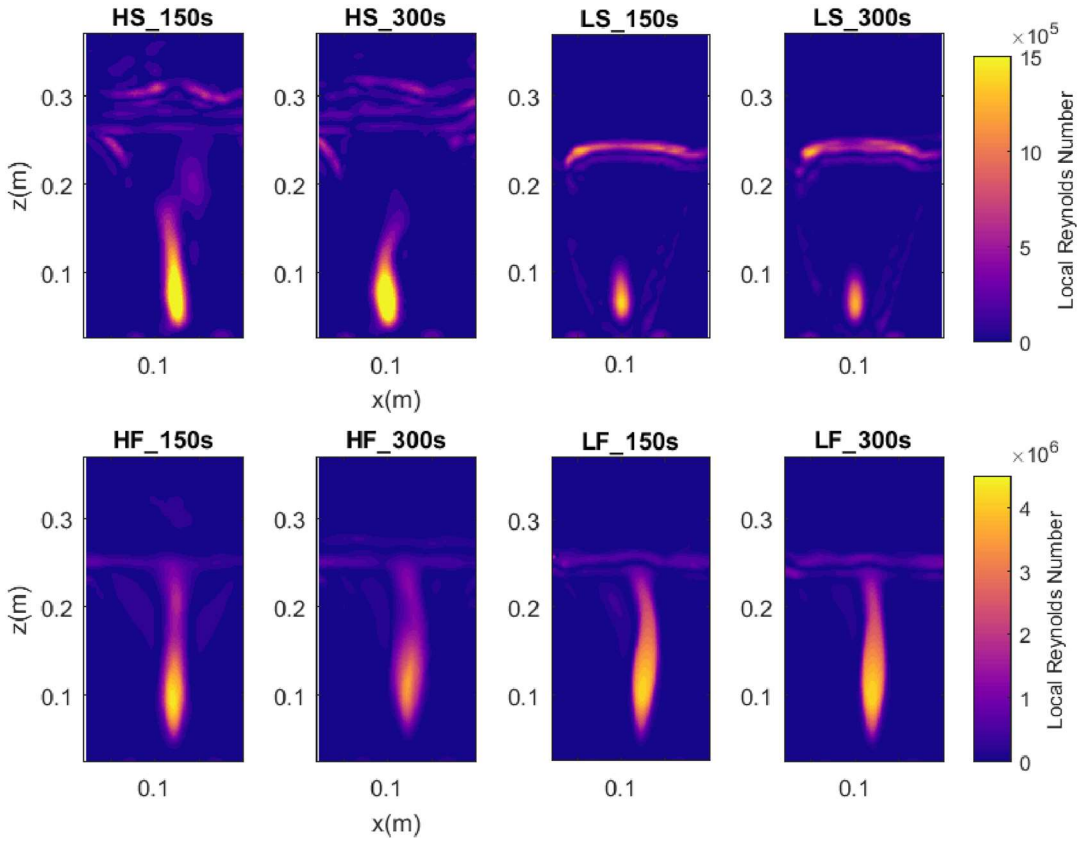

Figure 7-3 Local Reynolds numbers for steady-state two dimensional data sets as presented in section 4.4.1.

section 3.4.1 were calculated using the viscosity of the fluid in the system (i.e., water). However, using a pseudo-fluid approach to characterise the system as described by Di Felice (2010) would require using an augmented viscosity and density to account for the concentration of particles in the system. Herein it is observed that after extrusion and even in the steady-state, the pseudo-fluid properties of the fluidised suspension vary spatially (see Section 4.2.1). However, these first observations of concentration data in a fluidisation event and comparable velocity data provide a basis to further understand outcrop and seismic pipes, and the likely regimes within the anatomy of the injection at each fluidisation stage.

The velocity and concentration data presented herein further support the assertion of Cobain et al. (2015) that the flow regime of an injection is critically

dependent on the concentration of the fluidised injection. The high concentrations of particles in the supra-jet region act to damp the turbulence of the upward moving fluid and dissipate the high fluid velocities (Figures 3-7 to 3-14). In the recirculation zones, downward-moving particles have significantly reduced velocities and it is noted that, by comparison with the numerical data, it is highly likely that in these regions the particulate phase is fully decoupled from the fluid phase (Figure 6-7). In light of these observations, it is therefore interesting to consider how the central core would present if a slurry was injected at high pressure instead of a single-phase fluid. Future work could address this and, by capturing the velocities of the separate phases in three dimensions, compare the dynamics of fluid-only injections to multiphase slurry injections.

7.2.3 Timescales

The laboratory scale experiments show that the time to extrusion on the laboratory scale beds is of the order of seconds (Chapters 4 and 5). The two dimensional beds were 250 mm thick and the three dimensional beds were 70 mm thick (Chapter 3.1, 4.1 and 5.1). However, the formation of stable, well-defined, walls and stabilisation of the jet took significantly longer (Figures 5-1 to 5-5). The mechanisms controlling the timescales of formation should then be considered. Necessarily the total bed thickness will be a major control on total time to extrusion, but this does not appear to affect the rate of propagation of the void space in early fluidisation as demonstrated by the numerical model in section 6.2.1. The rate of propagation of the void space is observed to be non-linear, increasing with proximity to the surface. Cathles et al. (2010) provided a quantitative analysis of the growth rate of a gas fluidised pockmark

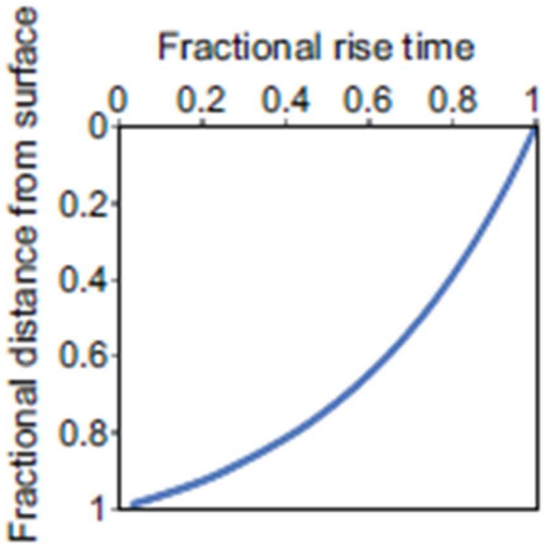

Figure 7-4 Modelled propagation rate of a gas chimney rising from the top of a gas pocket to the ground surface (reproduced from Cathles et al., 2010)

(Figure 7-6). It was proposed therein that the total time for the gas chimney to traverse the bed from the gas reservoir to the surface of a sediment bed was a function of the ratio of the thickness of the overlying bed to the height of the gas reservoir, the ratio of bed porosity to bed permeability, the density difference between the gas and water, the viscosity of water and the radius of the gas chimney (Cathles et al., 2010). This system derived by Cathles et al. (2010), is modelled on the driving system for a gas-fluidised pockmark, i.e. the buoyancy of the gas in the system. Herein, we do not have a system driven by the buoyancy of gas but a system driven by the migration of water pumped into the system. However, the buoyancy of that system does not change with the advancement of the gas chimney and, comparably, herein a constant rate of fluid pumping is used. Therefore, it could be argued that merely with a substitution of a suitable parameter as the driver of this system, the model of Cathles et al. (2010) would also be applicable to a water-fluidised system. As proposed in section 7.3.1, it is observed by Cathles et al. (2010), that the point at which the fluidisation rate increases is half the total bed thickness as this is the point at which the excess fluid pressure equals the buoyant weight of the

overlying sediments. The sediment density or particle size is not considered in the Cathles et al. (2010) model, rather they are likely captured in the ratio of the porosity to permeability. If such a model is considered applicable to a water-fluidised bed it is noted that the timescale for the formation of an in-situ pipe should scale linearly with the bed thickness and substituting an appropriate descriptor of the driving mechanism. Although this makes it possible to quantitatively model time-to-extrusion, the parameters involved do rely on homogeneity of the overlying bed as the fluid propagates. Bed heterogeneities have been demonstrated in Chapters 3, 4 and 5 to strongly influence the fluidisation process and so while such a model may provide a good approximation for fluidisation timescales it may not adequately simulate cases of localised low permeabilities.

The time to reach a quasi-steady state and the formation of stable walls cannot be quantified in such a simple linear model as these stages of fluid flow are driven by relative inhomogeneities of the bed caused by particle size segregation. Future work could investigate the rate of propagation of the water fluidised-pipe through a bed and modify the Cathles et al. (2010) model to provide an estimate of timescales of injection for active sea-floor fluidisation events.

7.3 Residual features

7.3.1 The influence of fluidisation stage on residual structures

The qualitative data in Chapter 6 demonstrated that fluidisation processes are critically time dependent and are described by a sequence proposed in Figures 5-11 and 5-12. It was also concluded that the residual flow features

observed after the cessation of fluid flow will be determined by the stage in the flow process at which fluidisation ceased (see Section 5.4.6). The integration of numerous discrete mechanisms across the fluidisation sequence differs from the mechanisms proposed by Cartwright and Santamarina (2015) in that only one mechanism is proposed therein for the formation of a pipe. Herein, it was observed that multiple mechanisms occur in sequence and, crucially, multiple directions of particle transport and regions of flow regimes are present at the same time.

The formation of void spaces is recognised in multiple data sets with polydisperse beds (Bons and van Milligen, 2002; Nermoen et al., 2010; Ross et al., 2011) and the mechanisms of void formation are addressed in section 7.1.2. The passing of the void space through the bed is also recognised to leave residual features within the fluidised bed (see section 5.2.6 and Figure 5-9). The residual features of the passing void space are formed by downward oriented vectors at the walls of the void in the early stages of fluidisation (Figure 7-7).

The void space is wider than the stabilised pipe and so the particle segregation that occurred within this wider mixing zone is preserved in the early stages of fluidisation and in some cases indefinitely (Figure 5-9). The residual features of passing void spaces are not visible in the CT data, which may be due to fluidisation voids forming out of the focus of the scanner or the (un)detectability of such features in porosity and density data (see section 7.3.4).

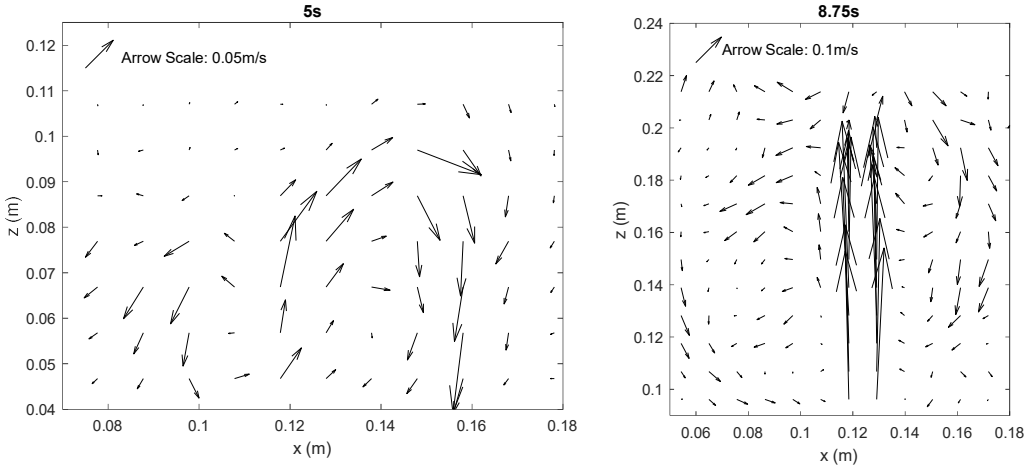

Figure 7-5 Velocity vectors captured during the formation of a void space for a low porosity bed (left) and a high porosity bed (right)

As posed in section 5.4, if fluid flow ceases during void formation there are two possible residual bed structures. First, if fluid flow was as modelled herein, it is likely that the overlying bed would collapse back into the void space in high porosity cases. As the lithostatic load of the overbed would no longer be supported by the overpressure, the porosity of the bed is such that the fluid could migrate out as the bed sinks. This would likely present as a structure that appears similar to subsurface volume loss (see section 5.4.6). If the sediment bed were of low porosity, seepage of the void fluid could take much longer as only small fractures caused by the raising of the bed could be easily used for fluid migration. However, if the injected fluid were a slurry, upon the cessation of flow the collapse into the void space would be significantly reduced since the grain structure emplaced by the slurry would support the lithostatic load of the raised bed. Such mounds would likely be visible on the sea floor, even after the cessation of flow.

In both the qualitative two dimensional observations (Chapter 5) and the three dimensional data (Chapter 4), fluidisation events showed a tendency to form the typical funnel shape after the cessation of flow (Figures 4-18 to 4-23 and

5-1 to 5-5). This shape is partly formed by the recirculation of particles at the edges of the fluidised zone (see sections 3.5.1.3, 4.2.5, and 5.4.3) and likely exaggerated due to a slumping of the bed into the dilute zone central jet region.

7.3.2 Pockmarks and mud volcanoes

Pockmarks are described as the seafloor expression of vertical focussed flow, result from explosive fluid venting (Judd and Hovland, 2009; Andresen, 2012) and are observed in a variety of contexts (Judd and Hovland, 2009, Pau et al., 2014) . Often, they are interpreted to be formed by gas fluidisation of sediments in methane rich environments. However, the term has also been used to describe water fluidised events (Judd and Hovland, 2009). Pockmarks are identified by the imprint left on the seafloor. They display a range of geometries, including ellipsoidal or asymmetrical geometries, sharp sided or shallow depressions (Forwick et al. 2009; Judd and Hovland, 2009). Figure 4-17 (reproduced here as Figure 7-8) demonstrated that the surface of water-fluidised event is largely indistinguishable from a gas-fluidised event (Figure 7-8). Further, the differences in geometry such as steep angled ridges as outlined in observations by Forwick et al. (2015) can be a result of the bed grain characteristics.

In the three dimensional experiments, it was also observed that high porosity beds had a concentration profile that increased with height. It was suggested that this could be indicative of fluidisation events that would eventually “self-plug”, leading to episodic pipe growth or perhaps a complete plug. If this is true, excess pressure would need to dissipate by fluidising elsewhere. This self-plugging behaviour of pipes could also be a mechanism for the formation

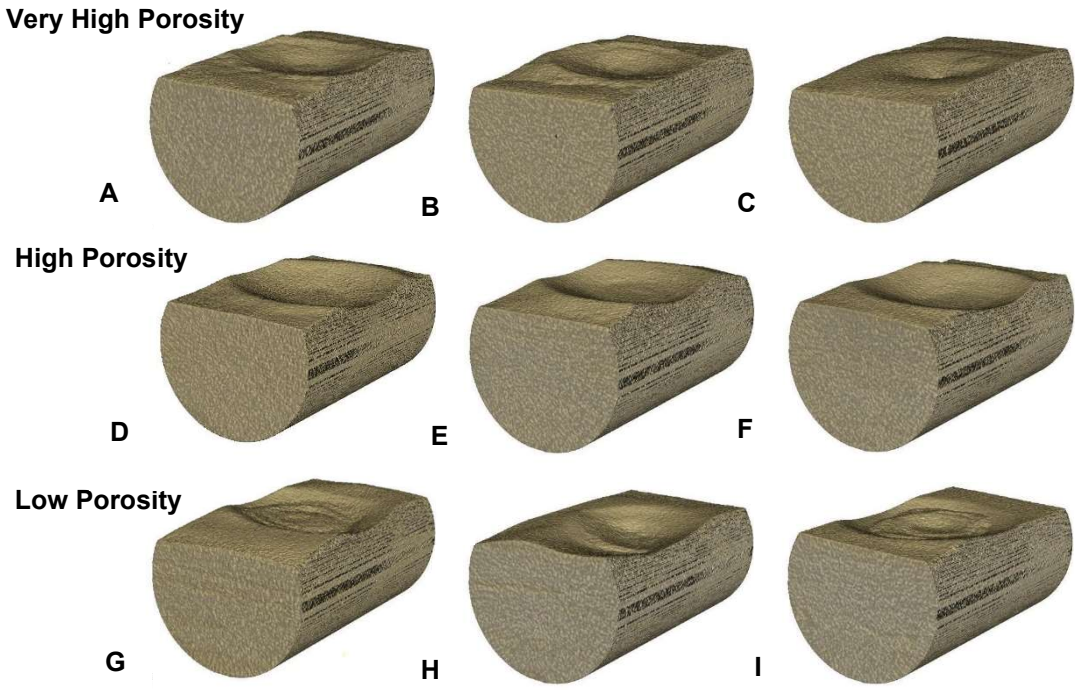

Figure 7-6 Reproduction of Figure 4-17 showing the surface presentation of the three dimensional experiments after the cessation of fluid flow.

of pockmark fields (Figure 7-9 right). However, plugging of pockmarks and formation of new pockmarks would not explain the coeval formation a pockmark field (e.g., as suggested by Ross et al., 2013).

Mud-volcanoes form by the extrusion of mud-slurries and tend to form ridges of extruded material that can form classical conical shapes and grow with self-channelisation and continuing extrusion (Mazzini and Etiope, 2017). However, it is recognised that the formation of such vertical conical volcanoes relies on frequent viscous eruptions; short explosive blasts result in morphologies much more comparable to a typical pockmark (Figure 3 of Mazzini and Etiope, 2017). Mud volcanoes are able to self-channelise easily because the cohesion in the sediment produces a highly viscous slurry and resists the fluidisation mechanisms observed herein. As the channel resists erosion and entrainment much more than a fluidisation event in a non-cohesive bed, the system is able to grow with the continuing flow of the slurry. The non-cohesive, high porosity

beds observed herein show a decoupling of the sediment from the fluid flow in the upper bed and so the system becomes self-organising. The funnel widens as the sediment is reworked and little growth or development is seen once the steady state is reached.

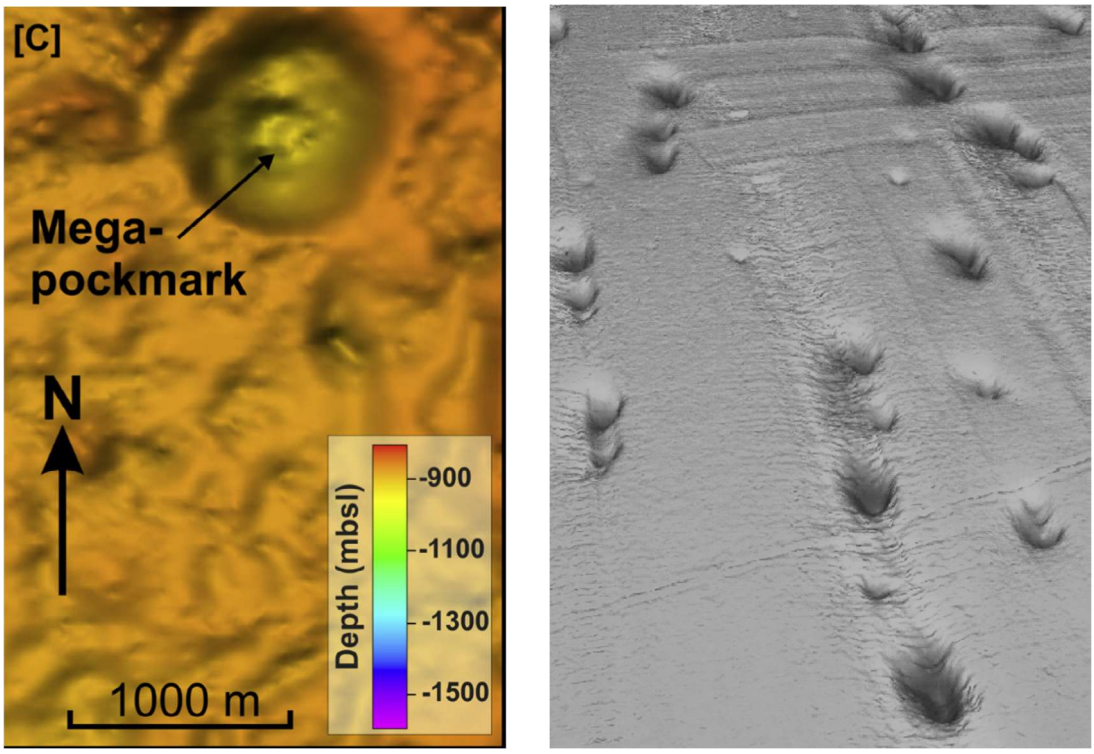

Figure 7-7 Images of pockmarks on the seafloor. Left - mega pockmark on the western Niger Delta slope taken from Benjamin et al., (2015). Right pockmark field on the Witch Ground Basin, UK North Sea taken from Judd and Hovland, (2009).

7.3.3 Extrudites

Extrudites form as material is elutriated from the fluidised system and occur in a wide range of deposits (Ross et al., 2013 and references therein). The experiments presented herein have shown that both high porosity and very high porosity systems do not easily remove material from the system (section 5.2.4). The velocity data in section 3.3.1 showed that velocities were barely detectible in the upper bed of the low inlet velocity cases, while velocities were significantly slowed near to the surface in high inlet velocity cases. The supra-

jet region was characterised as having a diffuse flow field (section 3.5.1.2) and the numerical model echoed this finding, showing significantly slowing velocities with distance from the inlet (Figure 6-6). The qualitative data showed characteristic funnel-shaped formations in all cases, but high porosity cases showed very little elutriation and all of the particles were recirculated within the system, tending to a quasi-steady state. These observations identify the presence of feedback loops and self-organisation during the formation of fluidisation pipes in high porosity beds (see Bons and Milligen, (2001) for further examples feedback and self-organisation in sedimentology). High particulate concentrations in the upper bed cause enhanced dissipation of fluid velocities. This encourages previously entrained particles to fall out of suspension until the supporting fluid is able to exert sufficient drag to re-entrain them. Thus, particles recirculate between two zones of relatively high concentration and enhanced velocity damping . If particles are unable to be carried out of the system, extrudites cannot form. In both the high porosity and very high porosity cases, at high velocities particles were able to be carried into the overlying water column (Figures 4-10 and 4-13) but were observed to fall back into the system relatively quickly. If currents were active in the overlying water column, it is likely that more material would be transported out of the system. In contrast, the low porosity system was able to elutriate significant amounts of material from the system, in some cases forming layers exclusively of fines on the surface of the bed (Figure 5-2), directly modelling the formation of an extrudite sheet. The elutriation of particles was only possible to such an extent because the presence of the fine particles in the bed provided reduced porosity in the undisturbed bed (Figure 4-16 C). The channelling of the flow caused higher velocities in the low porosity fast inlet

velocity beds (Figure 3-13) than in the beds with a higher porosity that allowed more diffuse flow (Figure 3-19). Although the channelisation mechanism provides a means for greater elutriation in the early flow stages, soon after extrusion, these analogues also quickly reached a steady state where elutriation was minimal. This suggests that all of the particles capable of being carried away by the fluid velocities had been elutriated. It is likely then, that there are two requirements for large scale extrudite formation. First, a sufficient number of fine particles are needed in the bed to provide the reduced porosities for channelisation and thus the reduced dissipation of the flow field. Second, a sufficient supply of material to be extruded, i.e. the injection of a particulate flow. However, it is noted that the suspension itself would have to be of a form able to be carried by the focussed flow.

7.3.4 Detectability of dewatered structures on the sea floor

It has long been recognised that detection of fluidisation events on the seafloor is challenging and impossible below the scale of the seismic data capture (Hurst et al., 2011; Ross et al., 2011). In the three dimensional experiments presented in Chapter 5 it was observed that only the low porosity system left easily detectable differences in the CT data after the cessation of flow (Figures 4-18 to 4-20). The residual structures of the higher porosity beds were much more difficult to detect in the CT data (section 4.2.4.3). This is due to the CT data detecting density differences caused by the presence of particles and water in each sampled cell. If the difference in porosity is not great enough to provide a big enough contrast between the residual pipe structure and the undisturbed bed it is simply not visible through such a means of detection. Figure 7-10 B shows a high porosity bed with the HU values clamped between

0.6 and 1.2. Conversely, qualitative observations identified very visible residual structures from the fluidisation event (Figure 7-10, A), including a distinct region of segregated particles at the walls. Such structures are visible in outcrop examples (such as Ross et al., 2014). Therefore, it is likely that when using data collection techniques reliant on distinct differences in porosity or resulting density differences between the injection and the undisturbed bed, such as seismic data collection, only injections into low porosity beds with high fines content will be detectable. This is likely the reason for the paucity of sand injectite detection into sand beds evidenced in the sea floor datasets in the literature to date (Palladino et al., 2020).

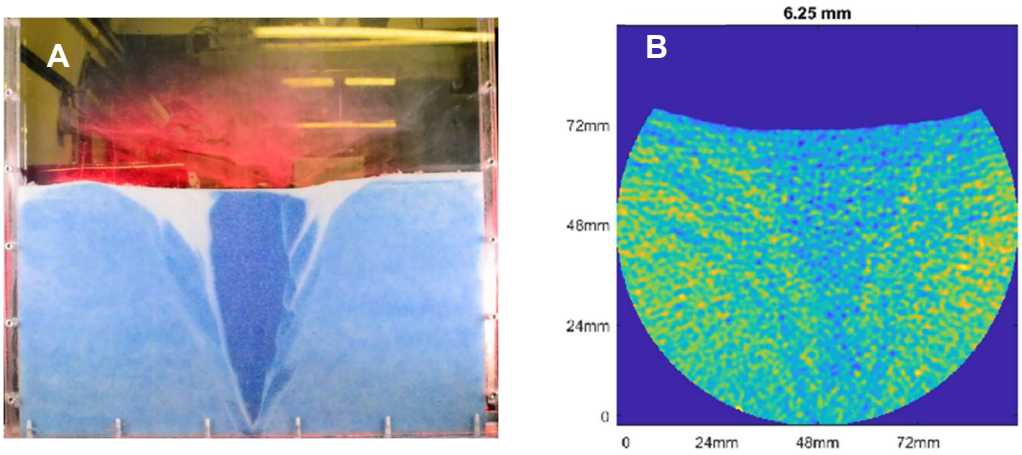

Figure 7-8 Residual structures of high porosity beds in qualitative data (A) and as detected by computed tomography (B).

7.4 Further work

A number of areas provide opportunities to further advance the analyses and conclusions derived in this work. In Chapter 5.4, it was observed that some structures could be formed by the injection of slurry instead of clear fluid, and thus this presents a particularly interesting field of research. Injection of

slurries would likely impact the range of residual morphologies observed and also the typical formation mechanisms. It may also provide material to enable more extensive extrusions. However, it would also introduce complexities typically observed in slurry flows, such as jamming and plugging flows and it would be fascinating to observe how the injection of a slurry behaves in unconfined beds.

Much of the pockmark literature identifies methane seeps and other gaseous injections to be the fluidising medium in many geological examples (Judd and Hovland, 2009; Forwick et al., 2009; Hovland et al., 2010; Pau et al., 2014). Varas et al. (2011) and Varas et al. (2015) injected gas into a saturated bed and observed hydraulic fractures. Observations of the interaction of a water-fluidised system with trapped gases would help extend current knowledge of the dynamics involved in fluidisation events and also explore the influence of the additional buoyancy on the system.

The present experimental work could be further advanced by developing a method of measuring both the velocities of the fluid and the particle classes simultaneously and quantifying the concentration in three dimensions. One possible approach for the synchronized measurement of both the fluid and particle phases is Planar Laser Induced Fluorescence (PLIF) coupled with refractive index matching (RIM) as employed by Phillipe and Badiane (2013) and Mena et al., (2017) for monodisperse fluidisations. Although this technique allows for the simultaneous tracking of the fluid field (through the Fluorescence induced by the laser) and the particle trajectories (using Particle Image Velocimetry on the “dark spots”), this has yet to be developed for use over multiple particle size classes. Such synchronized datasets would allow

the true drag coefficients of the high concentration flows to be calculated and lead to further understanding of multiphase interactions. The observation of angular particles and particles with cohesive properties, which are likely to behave differently to pure spheres, would expand the range of systems thus far observed. In such systems, porosity will become even more heterogeneous, possibly increasing channelization and resistance to fluidisation.

Numerical modelling has been presented as a means to understand the influence of different parameters on the system. Further work in this field could investigate the influence of particle shape such as highly ellipsoid or plate-like particles and parameterise the polydispersivity of the particle classes. Development in numerical modelling would greatly enhance the understanding of the flow in fluidisation pipes. The numerical model adopted herein is capable of such parametrisations but is currently restrained by the availability of computational power and run time.

7.5 Conclusions

This thesis has presented the results of multiple methods of investigation into the flow processes and dynamics of water fluidisation events in bidisperse beds

This thesis has presented the results of multiple methods of investigation into the flow processes and dynamics of water fluidisation events in bi-disperse beds. The physical mechanisms of particle segregation and transport, and processes documented herein are applicable to a number of fields.

The findings of the three-dimensional experiments demonstrate that the preserved geological feature can be difficult to detect through geophysical methods based on density contrasts within sediments. This has implications across wider geological fields as fluidisation pipes are known to behave as permeability pathways. In the petroleum industry this means the fluidisation pipe can act as a reservoir seal bypass (Hurst et al., 2011). In the developing field of carbon storage and sequestration leakage through caprock is also critical (Song and Zhang (2013), and characterisation of the sealing lithology of paramount importance to identifying suitable sites. These experiments demonstrate that there is a risk of not detecting these potential seal bypasses in the conventional seismic mapping approach.

The numerical modelling demonstrated a viable approach for the modelling of bi-disperse beds across a range of scales and turbulent regime inlet velocities. This presents an additional approach to the advancing field of fluidised bed modelling which has previously only investigated fixed bi-disperse beds or mono-disperse beds at low Reynolds numbers (Duan et al., 2020). Modelling in this field is used to optimise the drag on the particles in fluidised bed reactors.

The geometries and formation mechanisms of the resulting fluidised structure can be used to inform the likely resulting bed geometries and refine required injection velocities in sea-floor piling (de Brum Passini et al., 2018) as these are known to be underpredicted quantities in this field. Furthermore, the resulting geometries observed herein bear obvious similarities to a number of other geological processes such as pockmarks (Forwick et al., 2009, Andresen and Huuse., 2011), sand blows after seismic activity (Quigley et al.,

2013, Mazzini et al., 2017) and even pyroclastic flows (Roche et al., 2001). Although each of these scenarios demonstrate deviations from the prototypes modelled here comparisons around the spatio-temporal variation of flow regimes during formation and wall formation processes can be used to inform the likely processes in these broader fields.

The main outcomes are summarised as:

Two dimensional experimental modelling provided comprehensive velocity data across flow regimes investigating the influence of both inlet velocity and porosity on the flow fields within the bed. Multiple characteristic regions (jet, supra-jet, recirculation) were quantified and described. Evidence of multiple flow regimes, more specifically both laminar and turbulent flow regions, within the same fluidisation event were presented for the first time. It was demonstrated that the surrounding bed is not a good indicator of likely flow concentrations during a fluidisation event as low porosity beds were shown to behave more like a monodisperse bed than high porosity beds.

It was shown that the largest clast size observed in a deposit is unlikely to yield sufficient understanding of the flow field, as the minimum fluidisation velocity is dependent on a number of factors. The capacity of a fluidisation pipe to elutriate particles has been demonstrated to be significantly lower than previously expected due to the diffusion of the flow velocities in the supra-jet region. It is proposed that this is likely the reason there are less examples of large extrusion events in the field than would be expected.

Qualitative data from the two dimensional experimental arrangement were used to interpret flow regimes and propose new models of processes and products for sediment beds of different characteristic porosity. It was observed

that the nominal flow regime of the fluidisation event calculated as a Reynolds number *a-priori* bore little influence on the flow dynamics observed in the formation of the extrudite. Alternative formation mechanisms for wing-like structures, bowls, sub-vertical pipes, jack-up structures and laminations were proposed.

Three dimensional experiments demonstrated the novel use of Computed Tomography to further understanding of fluidisation events and presented the first concentration data for fluidisation pipes in bidisperse beds. As was observed with velocities, concentration profiles were demonstrated to be both spatially and temporally variable and, due to the differences in fluidisation sequences, showed a dependence on the porosity of the undisturbed bed. The concentration data provide a means of constraining first order estimates of concentration for outcrop data for the first time enabling more accurate estimates of likely flow velocities and regimes. Concentration profiles of high porosity beds are presented as a mechanism for episodic pipe growth of regionally extensive pockmark fields.

The novel use of a fully two-way coupled Lattice Boltzmann Method and rigid body solver to model fluidisation in a bidisperse bed was demonstrated. Qualitative agreement was observed between the experimental and the numerical analogues by successfully replicating the formation of voids, mounding of the overbed and development of asymmetry in the late void formation stage. The development of the early stages of void formation were seen to be independent of bed height. The approach was shown to be a promising avenue for future development and will permit exploration of the various influencing parameters on fluidisation events.

The residual structures and detectability of fluidisation pipes were discussed in light of the data presented and the impact on the observation of such structures considered. The final preserved morphologies of the three cases tested are observed internally and from the surface, showing that the morphologies of pockmarks observed on the seafloor may be indicative of the bed porosity, particle size and velocity characteristics of the formative event.

New models of the formation of void spaces in water-fluidised pipe formation were developed based on experimental and numerical data and the void formation mechanisms observed to be dependent on bed porosity. For the first time quantitative data showing void formation through a liquified zone was presented.

The data and interpretations presented in this thesis provide comprehensive evidence for the flow processes, characteristics and mechanisms of the formation and quasi-steady state of fluidisation pipes across bed heights and fluid injection velocity. The evidence presented herein can be used to support improved interpretation of common geological features observed in outcrop and seismic data and can be used to justify the inferences made on data sets collected after the cessation of flow on in-situ and ancient fluidisation events.

References

Adrian, L., Adrian, R.J. and Westerweel, J., 2011. Particle image velocimetry (No. 30). *Cambridge university press.*

Aidun, C. K. and **Clausen**, **J. R.** 2010 Lattice-Boltzmann method for complex flows. *Annual review of fluid mechanics*, 42, p. 439-472.

Albertson, M.L., Dai, Y.B., Jensen, R.A., Rouse, H., 1950. Diffusion of a submerged jet. *Transcript of the A.S.C.E., Paper No. 2409, 115*, 639–697.

Andresen, K.J. and **Huuse, M.,** 2011. 'Bulls-eye'pockmarks and polygonal faulting in the Lower Congo Basin: relative timing and implications for fluid expulsion during shallow burial. *Marine Geology*, 279(1-4), pp.111-127.

Barnes, H.A., 1989. Hutton. JF and Walters, K., An Introduction to Rheology. *Rheology Series*, *3*.

Bartuschat, D., Fischermeier, E., Gustavsson, K. and **Rüde, U.,** 2016. Two computational models for simulating the tumbling motion of elongated particles in fluids. *Computers & Fluids*, 127, pp.17-35.

Batchelor, G.K. and **Green, J.T**., 1972. The determination of the bulk stress in a suspension of spherical particles to order c 2. *Journal of Fluid Mechanics*, *56*(3), pp.401-427.

Bauer, M., Eibl, S., Godenschwager, C., Kohl, N., Kuron, M., Rettinger, C., Schornbaum, F., Schwarzmeier, C., Thönnes, D., Köstler, H. and **Rüde, U.,** 2020. waLBerla: A block-structured high-performance framework for multiphysics simulations. *Computers & Mathematics with Applications*.

Best, J.L., 1989. Fluidization pipes in volcaniclastic mass flows, Volcan Hudson, Southern Chile. *Terra Nova*, *1*(2), pp.203-208.

Bhatnagar, P.L., Gross, E.P. and **Krook, M.,** 1954. A model for collision processes in gases. I. Small amplitude processes in charged and neutral one-component systems. *Physical review*, *94*(3), p.511.

Bolliger, S.A., Oesterhelweg, L., Spendlove, D., Ross, S. and **Thali, M.J.,** 2009. Is differentiation of frequently encountered foreign bodies in corpses possible by Hounsfield density measurement?. *Journal of forensic sciences*, *54*(5), pp.1119-1122.

Bons, P.D. and van **Milligen, B.P.,** 2001. New experiment to model self-organized critical transport and accumulation of melt and hydrocarbons from their source rocks. *Geology*, 29(10), pp.919-922.

Boyer, F., Pouliquen, O. and **Guazzelli, É.,** 2011. Dense suspensions in rotating-rod flows: normal stresses and particle migration. *Journal of Fluid Mechanics*, *686*, p.5.

Briedis, N. A., D. Bergslien, A. Hjellbakk, R. E. Hill, and **G. J. Moir**, 2007, Recognition criteria, significance to field performance, and reservoir modeling of sand injections in the Balder field, North Sea, in A. Hurst and J. Cartwright, eds., Sand injectites: Implications for hydrocarborbon exploration and production: *AAPG Memoir 87*, p. 91–102.

Brumby, P.E., Sato, T., Nagao, J., Tenma, N. and **Narita, H.,** 2015. Coupled LBM–DEM micro-scale simulations of cohesive particle erosion due to shear flows. *Transport in Porous Media*, *109*(1), pp.43-60.

Bureau, D., Mourgues, R. and **Cartwright, J.,** 2014. Use of a new artificial cohesive material for physical modelling: Application to sandstone intrusions and associated fracture networks. *Journal of Structural Geology*, *66*, pp.223-236.

Cartwright, J. and **Santamarina, C.,** 2015. Seismic characteristics of fluid escape pipes in sedimentary basins: implications for pipe genesis. *Marine and Petroleum Geology*, *65*, pp.126-140.

Chan, M.A., Hasiotis, S.T. and **Parrish, J.T.,** 2019. Enigmatic clastic pipe swarms and implications for fluidization dynamics in aeolian deposits. *Sedimentology*, 66(2), pp.513-535.

Chavan, P.V. and **Joshi, J.B.,** 2008. Analysis of Particle Segregation and Intermixing in Solid− Liquid Fluidized Beds. *Industrial & engineering chemistry research*, *47*(21), pp.8458-8470.

Chen, L., Duan, Y., Pu, W. and **Zhao, C.,** 2009. CFD simulation of coal-water slurry flowing in horizontal pipelines. *Korean journal of chemical engineering,* 26(4), pp.1144-1154.

Chidsey, T.C., Sprinkel, D.A., Willis, G.C. and **Anderson, P.B.,** 2012. Glen Canyon National Recreation Area and Rainbow Bridge National Monument, Utah–Arizona. *Utah Geological Association*, *29*, pp.1-81.

Chien, L.K., Oh, Y.N. and **Chang, C.H.,** 2002. Effects of fines content on liquefaction strength and dynamic settlement of reclaimed soil. *Canadian Geotechnical Journal*, 39(1), pp.254-265.

Cobain, S.L., Peakall, J. and **Hodgson, D.M.,** 2015. Indicators of propagation direction and relative depth in clastic injectites: Implications for laminar versus turbulent flow processes. *Bulletin*, *127*(11-12), pp.1816-1830.

Cobain, S.L., Hodgson, D.M., Peakall, J. and **Silcock, S.Y.,** 2020. Relationship between bowl-shaped clastic injectites and parent sand depletion: implications for their scale-invariant morphology and composition. *Geological Society, London, Special Publications*, *493*, pp.SP493-2018.

Cosgrove, J.W., 1995. The expression of hydraulic fracturing in rocks and sediments. *Geological Society, London, Special Publications,* 92(1), pp.187-196.

Cosgrove, J.W., 2001. Hydraulic fracturing during the formation and deformation of a basin: A factor in the dewatering of low-permeability sediments*. AAPG bulletin*, 85(4), pp.737-748.

Craig, R.F., 2004. *Craig's soil mechanics*. CRC press.

Cundall, P.A. and **Strack, O.D.,** 1979. A discrete numerical model for granular assemblies. *geotechnique,* 29(1), pp.47-65.

Cushman-Roisin, B., in prep. Turbulent Dispersion*. Mathematics of Marine Modeling,* to be published by Springer, submission under review.

Davies, R.J., Mathias, S.A., Moss, J., Hustoft, S. and **Newport, L.,** 2012. Hydraulic fractures: How far can they go?. *Marine and petroleum geology*, *37*(1), pp.1-6.

Di Felice, R., 1995. Hydrodynamics of liquid fluidisation. *Chemical engineering science, 50*(8), pp.1213-1245.

Di Felice, R., 2007. Liquid suspensions of single and binary component solid particles—an overview. *China Particuology*, *5*(5), pp.312-320.

Di Felice, R., 2010. Liquid–solid suspension theory with reference to possible applications in geology. *Basin Research*, *22*(4), pp.591-602.

Diggs, T.N., 2007. An outcrop study of clastic injection structures in the Carboniferous Tesnus Formation, Marathon basin, Trans-Pecos Texas. *in* A. Hurst and J. Cartwright, eds., Sand injectites:

Implications for hydrocarbon exploration and production: AAPG Memoir 87, p. 209-219.

Dott, R.H., 1966. Cohesion and flow phenomena in clastic intrusions. *AAPG Bulletin*, *50*(3), pp.610-611.

Duarte, S.K., Hartmann, L.A. and **Baggio, S.B.,** 2020. Fluidized sand effusion over successive basalt flows of the northwestern Paraná volcanic province. *Journal of South American Earth Sciences*, *99*, p.102505.

Duranti, D. and **Hurst, A.,** 2004. Fluidization and injection in the deep-water sandstones of the Eocene Alba Formation (UK North Sea). *Sedimentology*, *51*(3), pp.503-529.

Duranti, D. and **Mazzini, A.,** 2005. Large-scale hydrocarbon-driven sand injection in the Paleogene of the North Sea. *Earth and Planetary Science Letters*, *239*(3-4), pp.327-335.

Eibl, S. and **Rüde, U.,** 2018. A local parallel communication algorithm for polydisperse rigid body dynamics. *Parallel Computing*, 80, pp.36-48.

Eichhorn, R. and **Small, S.,** 1964. Experiments on the lift and drag of spheres suspended in a Poiseuille flow. *Journal of Fluid Mechanics*, *20*(3), pp.513-527.

Einstein, A., 1905. Über die von der molekularkinetischen Theorie der Wärme geforderte Bewegung von in ruhenden Flüssigkeiten suspendierten Teilchen. *Annalen der physik*, *4*.

Epstein, N., 2005. Teetering. *Powder Technology*, *151*(1-3), pp.2-14.

Esteghamatian, A., Hammouti, A., Lance, M. and **Wachs, A.,** 2017. Particle resolved simulations of liquid/solid and gas/solid fluidized beds. *Physics of Fluids,* 29(3), p.033302.

Ferreira, J.M. and **Diz, H.M.,** 1999. Effect of solids loading on slip-casting performance of silicon carbide slurries. *Journal of the American Ceramic Society*, *82*(8), pp.1993-2000.

Fischer, H.B., List, E., Koh, R., Imberger, J. and **Brooks, N.,** 1979. Mixing in inland and coastal waters *Academic Press. New York,* pp.229-242.

Fischermeier, E., Bartuschat, D., Preclik, T., Marechal, M. and **Mecke, K.,** 2014. Simulation of a hard-spherocylinder liquid crystal with the pe. *Computer Physics Communications*, 185(12), pp.3156-3161.

Fontana, D., Amoroso, S., Minarelli, L. and Stefani, M., 2019. Sand liquefaction induced by a blast test: New insights on source layer and grain-size segregation mechanisms (Late Quaternary, Emilia, Italy). *Journal of Sedimentary Research,* 89(1), pp.13-27.

Forwick, M., Baeten, N.J. and **Vorren, T.O.,** 2009. Pockmarks in Spitsbergen fjords. *Norwegian Journal of Geology/Norsk Geologisk Forening,* 89.

GE Medical Systems, 2018. Brivo CT385 User Manual. https://customer-doc.cloud.gehealthcare.com/copyDoc/5491782-1EN/5

Gibilaro, L.G., 2001. *Fluidization dynamics*. Elsevier.

Gibilaro, L.G., Gallucci, K., Di Felice, R. and **Pagliai, P.,** 2007. On the apparent viscosity of a fluidized bed. *Chemical engineering science*, *62*(1-2), pp.294-300.

Ginzburg, I., Verhaeghe, F. and **d'Humieres, D.,** 2008. Two-relaxation-time lattice Boltzmann scheme: About parametrization, velocity, pressure and mixed boundary conditions. *Communications in computational physics, 3(2)*, pp.427-478.

Goldman, L.W., 2007. Principles of CT: radiation dose and image quality. *Journal of nuclear medicine technology*, *35*(4), pp.213-225.

Götz, J., Iglberger, K., Stürmer, M. and **Rüde, U.,** 2010, November. Direct numerical simulation of particulate flows on 294912 processor cores. *In SC'10: Proceedings of the 2010 ACM/IEEE International Conference for High Performance Computing, Networking, Storage and Analysis* (pp. 1-11). IEEE.

Guadarrama-Lara, R., Jia, X. and **Fairweather, M.,** 2015. A meso-scale model for fluid-microstructure interactions. *Procedia engineering,* 102, pp.1356-1365.

Guadarrama Lara, R., 2017. Modelling Fluid-Structure Interaction Problems with Coupled DEM-LBM (*Doctoral dissertation, University of Leeds).*

Guhman, A.I. and **Pederson, D.T.,** 1992. Boiling sand springs, Dismal River, Nebraska: agents for formation of vertical cylindrical structures and geomorphic change. *Geology*, *20*(1), pp.8-10.

Han, M., Kim, C., Kim, M. and **Lee, S.,** 1999. Particle migration in tube flow of suspensions. *Journal of rheology*, *43*(5), pp.1157-1174.

van der Hoef, M.A., van Sint Annaland, M., Deen, N.G. and **Kuipers, J.A.M.,** 2008. Numerical simulation of dense gas-solid fluidized beds: a multiscale modeling strategy. *Annu. Rev. Fluid Mech.*, *40*, pp.47-70.

Hogg, A.J., 1994, The inertial migration of non-neutrally buoyant spherical particles in two-dimensional shear flows. *Journal of Fluid Mechanics, 272*, p. 285–318

Hounsfield, G.N., 1973. Computerized transverse axial scanning (tomography): Part 1. Description of system. *The British journal of radiology*, *46*(552), pp.1016-1022.

Hovland, M., Heggland, R., De Vries, M.H. and **Tjelta, T.I**., 2010. Unit-pockmarks and their potential significance for predicting fluid flow. *Marine and Petroleum Geology*, *27*(6), pp.1190-1199.

Hu, Y., Gan, Q., Hurst, A. and **Elsworth, D.,** 2018. Evolution of permeability in sand injectite systems. *International Journal of Rock Mechanics and Mining Sciences*, 106, pp.176-189.

Hubbard, S.M., Romans, B.W. and **Graham, S.A.,** 2007. An outcrop example of large-scale conglomeratic intrusions sourced from deep-water channel deposits, Cerro Toro Formation, Magallanes basin, southern Chile. *in* Hurst, A., and Cartwright, J., eds., Sand Injectites: Implications for Hydrocarbon Exploration and Production: *American Association of Petroleum Geologists Memoir 87*, p. 199–207.

Hubbert, M.K., 1937. Theory of scale models as applied to the study of geologic structures. *Bulletin of the Geological Society of America,* 48(10), pp.1459-1520.

Hurst, A., Scott, A. and **Vigorito, M.,** 2011. Physical characteristics of sand injectites. *Earth-Science Reviews*, *106*(3-4), pp.215-246.

K. Iglberger, N. Thürey, and **U. Rüde,** 2008. Simulation of moving particles in 3D with the Lattice Boltzmann method, *Computers & Mathematics with Applications, 55(7) ,* pp. 1461–1468.

Jeffrey, R.C. and **Pearson, J.R.A**., 1965. Particle motion in laminar vertical tube flow. *Journal of Fluid Mechanics*, *22*(4), pp.721-735.

Jolly, R.J. and **Lonergan, L.,** 2002. Mechanisms and controls on the formation of sand intrusions. *Journal of the Geological Society*, *159*(5), pp.605-617.

Jonk, R., 2010. Sand-rich injectites in the context of short-lived and long-lived fluid flow. *Basin Research*, *22*(4), pp.603-621.

Kawakami, G. and **Kawamura, M.,** 2002. Sediment flow and deformation (SFD) layers: Evidence for intrastratal flow in laminated muddy sediments of the Triassic Osawa Formation, northeast Japan. *Journal of Sedimentary Research,* 72(1), pp.171-181.

Kidanemariam, A.G. and **Uhlmann, M.,** 2014. Interface-resolved direct numerical simulation of the erosion of a sediment bed sheared by laminar channel flow. *International Journal of Multiphase Flow*, 67, pp.174-188.

Kidanemariam, A.G. and **Uhlmann, M.,** 2017. Formation of sediment patterns in channel flow: minimal unstable systems and their temporal evolution. arXiv preprint arXiv:1702.06648.

Klinkmüller, M., Schreurs, G., Rosenau, M. and **Kemnitz, H.,** 2016. Properties of granular analogue model materials: A community wide survey. *Tectonophysics*, 684, pp.23-38.

Ladd, A.J., 1994. Numerical simulations of particulate suspensions via a discretized Boltzmann equation. Part 1. Theoretical foundation. *Journal of fluid mechanics*, *271*, pp.285-309.

Lade, P.V. and **Yamamuro, J.A.,** 1997. Effects of nonplastic fines on static liquefaction of sands. *Canadian Geotechnical Journal,* 34(6), pp.918-928.

Li, Y., Craven, J., Schweig, E.S. and **Obermeier, S.F**., 1996. Sand boils induced by the 1993 Mississippi River flood: Could they one day be misinterpreted as earthquake-induced liquefaction?. *Geology*, *24*(2), pp.171-174.

Loope, D.B., Elder, J.F., Zlotnik, V.A., Kettler, R.M. and **Pederson, D.T.,** 2013. Jurassic earthquake sequence recorded by multiple generations of sand blows, Zion National Park, Utah. *Geology*, 41(10), pp.1131-1134.

Løseth, H., Wensaas, L., Arntsen, B., Hanken, N.M., Basire, C. and **Graue, K.,** 2011. 1000 m long gas blow-out pipes. *Marine and Petroleum Geology*, *28*(5), pp.1047-1060.

Loth, E., 2000. Numerical approaches for motion of dispersed particles, droplets and bubbles. *Progress in energy and combustion science*, *26*(3), pp.161-223.

Lowe, D.R., 1975. Water escape structures in coarse-grained sediments. *Sedimentology*, 22(2), pp.157-204.

Macdonald, D., and **Flecker, R**., 2007, Injected sand sills in a strike-slip fault zone: A case study from the Pil'sk Suite (Miocene), southeast Schmidt Peninsula, Sakhalin, *in* Hurst, A., and Cartwright, J., eds., Sand Injectites: Implications for Hydrocarbon Exploration and Production*. American Association of Petroleum Geologists Memoir 87*, p. 253–263

Maestrelli, D., Iacopini, D., Jihad, A.A., Bond, C.E. and **Bonini, M.,** 2017. Seismic and structural characterization of fluid escape pipes using 3D and partial stack seismic from the Loyal Field (Scotland, UK): A multiphase and repeated intrusive mechanism. *Marine and Petroleum Geology,* 88, pp.489-510.

Makse, H.A., Ball, R.C., Stanley, H.E. and **Warr, S**., 1998. Dynamics of granular stratification. *Physical Review E*, 58(3), p.3357.

Marchand, A.M., Apps, G., Li, W. and **Rotzien, J.R.,** 2015. Depositional processes and impact on reservoir quality in deepwater Paleogene reservoirs, US Gulf of Mexico. *AAPG Bulletin*, *99*(9), pp.1635-1648.

Matas, J.P., Morris, J.F. and **Guazzelli, É**., 2004. Inertial migration of rigid spherical particles in Poiseuille flow. *Journal of Fluid Mechanics*, *515*, p.171.

Matuttis, H.G. and **Chen, J**., 2014. *Understanding the discrete element method: simulation of non-spherical particles for granular and multi-body systems*. John Wiley & Sons.

Maxey, M.R. and **Riley, J.J.,** 1983. Equation of motion for a small rigid sphere in a nonuniform flow. *The Physics of Fluids*, *26*(4), pp.883-889.

van der Meer, J.J., Kjær, K.H., Krüger, J., Rabassa, J. and **Kilfeather, A.A.,** 2009. Under pressure: clastic dykes in glacial settings. *Quaternary Science Reviews*, *28*(7-8), pp.708-720.

Mena, A., Francés, G., Pérez-Arlucea, M., Aguiar, P., Barreiro-Vázquez, J.D., **Iglesias, A.** and **Barreiro-Lois, A.,** 2015. A novel sedimentological method based on CT-scanning: Use for tomographic characterization of the Galicia Interior Basin. *Sedimentary Geology*, *321*, pp.123-138.

Mena, S.E., Luu, L.H., Cuéllar, P., Philippe, P. and **Curtis, J.S.,** 2017. Parameters affecting the localized fluidization in a particle medium. AIChE Journal, 63(5), pp.1529-1542.

Mena, S.E., Brunier-Coulin, F., Curtis, J.S. and **Philippe, P.,** 2018. Experimental observation of two regimes of expansion in localized fluidization of a granular medium. *Physical Review E*, *98*(4), p.042902.

Mikhailov, M.D. and **Freire, A.S.,** 2013. The drag coefficient of a sphere: An approximation using Shanks transform. *Powder technology*, *237*, pp.432-435.

Monkul, M.M. and **Yamamuro, J.A.,** 2011. Influence of silt size and content on liquefaction behavior of sands. Canadian Geotechnical Journal, 48(6), pp.931-942.

Mörz, T., Karlik, E.A., Kreiter, S. and **Kopf, A.,** 2007. An experimental setup for fluid venting in unconsolidated sediments: New insights to fluid mechanics and structures. Sedimentary Geology, 196(1-4), pp.251-267.

Moss, J.L. and **Cartwright, J.,** 2010. The spatial and temporal distribution of pipe formation, offshore Namibia. *Marine and Petroleum Geology*, *27*(6), pp.1216-1234.

Moss, J.L., Cartwright, J., Cartwright, A. and **Moore, R.,** 2012. The spatial pattern and drainage cell characteristics of a pockmark field, Nile Deep Sea Fan. *Marine and Petroleum Geology*, *35*(1), pp.321-336.

Mount, J.F., 1993. Formation of fluidization pipes during liquefaction: examples from the Uratanna Formation (Lower Cambrian), South Australia. *Sedimentology*, *40*(6), pp.1027-1037.

Mourgues, R., Bureau, D., Bodet, L., Gay, A. and **Gressier, J.B.,** 2012. Formation of conical fractures in sedimentary basins: Experiments involving pore fluids and implications for sandstone intrusion mechanisms. *Earth and Planetary Science Letters*, *313*, pp.67-78.

Nermoen, A., Galland, O., Jettestuen, E., Fristad, K., Podladchikov, Y., Svensen, H. and **Malthe-Sørenssen, A.,** 2010. Experimental and analytic modeling of piercement structures. *Journal of Geophysical Research: Solid Earth*, *115*(B10).

Newman, K.R., Cormier, M.H., Weissel, J.K., Driscoll, N.W., Kastner, M., Solomon, E.A., Robertson, G., Hill, J.C., Singh, H., Camilli, R. and

Eustice, R., 2008. Active methane venting observed at giant pockmarks along the US mid-Atlantic shelf break. *Earth and Planetary Science Letters, 267(1-2),* pp.341-352.

Nichols, R.J., Sparks, R.S.J., and **Wilson, C.J.N.,** 1994, Experimental studies of the fluidization of layered sediments and the formation of fluid escape structures: *Sedimentology 41*, p. 233–253.

Nichols, R.J., 1995. The liquification and remobilization of sandy sediments. *Geological Society, London, Special Publications, 94(1)*, pp.63-76.

Nobach, H. and **Bodenschatz, E.,** 2009. Limitations of accuracy in PIV due to individual variations of particle image intensities. *Experiments in fluids*, *47*(1), pp.27-38.

Obermeier, S.F., Olson, S.M. and **Green, R.A.,** 2005. Field occurrences of liquefaction-induced features: a primer for engineering geologic analysis of paleoseismic shaking. *Engineering Geology*, *76*(3-4), pp.209-234.

Oh, S., Song, Y.Q., Garagash, D.I., Lecampion, B. and **Desroches, J.,** 2015. Pressure-driven suspension flow near jamming. *Physical Review Letters*, *114*(8), p.088301.

Özener, P.T., Özaydın, K. and **Berilgen, M.M.,** 2009. Investigation of liquefaction and pore water pressure development in layered sands. *Bulletin of Earthquake Engineering*, *7*(1), pp.199-219.

Palladino, G., Alsop, G.I., Grippa, A., Seers, T. and **Hurst, A.,** 2020. Sandstone intrusions along different types of faults and their effect on fluid flow in siliciclastic reservoirs. *Geological Society, London, Special Publications*, 493.

Paola, C., Straub, K., Mohrig, D. and Reinhardt, L., 2009. The “unreasonable effectiveness” of stratigraphic and geomorphic experiments. *Earth-Science Reviews,* 97(1-4), pp.1-43.

Papanicolaou, P.N. and **List, E.J.,** 1988. Investigations of round vertical turbulent buoyant jets. *Journal of Fluid Mechanics, 195*, pp.341-391.

Pau, M., Hammer, Ø. and **Chand, S.,** 2014. Constraints on the dynamics of pockmarks in the SW Barents Sea: evidence from gravity coring and high-resolution, shallow seismic profiles. *Marine Geology*, *355*, pp.330-345.

Peakall, J., Ashworth, P. and Best, J., 1996. Physical modelling in fluvial geomorphology: principles, applications and unresolved issues. *The scientific nature of geomorphology*, pp.221-253.

Peker, S.M. and **Helvaci, S.S.,** 2011. *Solid-liquid two phase flow*. Elsevier.

Peterson, G.L., 1968. Flow structures in sandstone dikes. *Sedimentary Geology*, *2*(3), pp.177-190.

Philippe, P. and **Badiane, M.,** 2013. Localized fluidization in a granular medium. *Physical Review E*, *87*(4), p.042206.

Philippe, P., Mena, S., Brunier-Coulin, F. and **Curtis, J.,** 2017. An experimental study of the transient regime to fluidized chimney in a granular medium. In *EPJ Web of Conferences (Vol. 140, p. 09030).* EDP Sciences.

Picano, F., Sardina, G. and **Casciola, C.M.,** 2009. Spatial development of particle-laden turbulent pipe flow. *Physics of Fluids*, *21*(9), p.093305.

Preclik, T. and **Rüde, U.,** 2015. Ultrascale simulations of non-smooth granular dynamics. *Computational Particle Mechanics,* 2(2), pp.173-196.

Prosperetti, A. and **Tryggvason, G., 2007.** Coupled methods for multi-fluid models. In *Computational Methods for Multiphase Flow*. Cambridge University Press.

Quigley, M.C., Bastin, S. and **Bradley, B.A.,** 2013. Recurrent liquefaction in Christchurch, New Zealand, during the Canterbury earthquake sequence. *Geology*, *41*(4), pp.419-422.

Ravier, E., Guiraud, M., Guillien, A., Vennin, E., Buoncristiani, J.F. and **Portier, E.,** 2015. Micro-to macro-scale internal structures, diagenesis and petrophysical evolution of injectite networks in the Vocontian Basin (France): Implications for fluid flow. *Marine and Petroleum Geology*, *64*, pp.125-151.

Reilly, B.T., Stoner, J.S. and **Wiest, J.,** 2017. Sed CT: MATLAB™ tools for standardized and quantitative processing of sediment core computed tomography (CT) data collected using a medical CT scanner. *Geochemistry, Geophysics, Geosystems*, *18*(8), pp.3231-3240.

Rettinger, C. and **Rüde, U.,** 2017. A comparative study of fluid-particle coupling methods for fully resolved lattice Boltzmann simulations. *Computers & Fluids*, *154*, pp.74-89.

Rettinger, C., Godenschwager, C., Eibl, S., Preclik, T., Schruff, T., Frings, R. and **Rüde, U.,** 2017, June. Fully resolved simulations of dune formation in riverbeds. *In International Supercomputing Conference* (pp. 3-21). Springer, Cham.

Richardson, J.F. and **Zaki, W.N.,** 1954. The sedimentation of a suspension of uniform spheres under conditions of viscous flow. *Chemical Engineering Science*, *3*(2), pp.65-73.

Roche, O., Druitt, T.H. and **Cas, R.A.,** 2001. Experimental aqueous fluidization of ignimbrite. *Journal of Volcanology and Geothermal Research*, *112*(1-4), pp.267-280.

Roco, M. C. *Particulate two-phase flow*. Butterworth-Heinemann, 1993.

Rodrigues, N., Cobbold, P.R. and **Løseth, H.,** 2009. Physical modelling of sand injectites. Tectonophysics, 474(3-4), pp.610-632.

Ross, J.A., Peakall, J. and **Keevil, G.M.,** 2011. An integrated model of extrusive sand injectites in cohesionless sediments. Sedimentology, 58(7), pp.1693-1715.

Ross, J.A., 2013. *Clastic injection: process to product*. University of Leeds.

Ross, J.A., Peakall, J. and **Keevil, G.M.,** 2013. Sub-aqueous sand extrusion dynamics. *Journal of the Geological Society*, *170*(4), pp.593-602.

Ross, J.A., Peakall, J. and **Keevil, G.M.,** 2014. Facies and flow regimes of sandstone-hosted columnar intrusions: insights from the pipes of Kodachrome Basin State Park. Sedimentology, 61(6), pp.1764-1792

Schruff, T., Liang, R., Rüde, U., Schüttrumpf, H. and **Frings, R.M.,** 2018. Generation of dense granular deposits for porosity analysis: assessment and application of large-scale non-smooth granular dynamics. *Computational Particle Mechanics*, 5(1), pp.59-70.

Schuster, Dominik: *Direct Numerical Simulation of Fluidized Beds with the Lattice Boltzmann Method*, 2017 (Download)

Sciacchitano, A. and **Wieneke, B.,** 2016. PIV uncertainty propagation. *Measurement Science and Technology, 27(8)*, p.084006.

Scott, A., Vigorito, M. and **Hurst, A.,** 2009. The process of sand injection: internal structures and relationships with host strata (Yellowbank Creek Injectite Complex, California, USA). *Journal of Sedimentary Research*, *79*(8), pp.568-583.

Segre, G. and **Silberberg, A.J.,** 1962a. Behaviour of macroscopic rigid spheres in Poiseuille flow Part 1. Determination of local concentration by statistical analysis of particle passages through crossed light beams. *Journal of fluid mechanics, 14*(1), pp.115-135.

Segré, G., and **Silberberg, A.,** 1962b, Behaviour of macroscopic rigid spheres in Poiseuille flow. Part 2. Experimental results and interpretation. *Journal of Fluid Mechanics*, v. 14, p. 136–157.

Seil, P., Pirker, S. and **Lichtenegger, T.,** 2018. Onset of sediment transport in mono-and bidisperse beds under turbulent shear flow. *Computational Particle Mechanics*, 5(2), pp.203-212.

Shampine, L.F. and **Reichelt, M.W.,** 1997. The matlab ode suite. *SIAM journal on scientific computing*, *18*(1), pp.1-22.

Sherry, T.J., Rowe, C.D., Kirkpatrick, J.D. and **Brodsky, E.E.,** 2012. Emplacement and dewatering of the world's largest exposed sand injectite complex. *Geochemistry, Geophysics, Geosystems*, *13*(8).

Silva, R., Garcia, F.A., Faia, P.M. and **Rasteiro, M.G.,** 2015. Settling suspensions flow modelling: a review. *KONA Powder and Particle Journal*, p.2015009.

Stickel, J.J. and **Powell, R.L., 2005.** Fluid mechanics and rheology of dense suspensions. *Annu. Rev. Fluid Mech.*, *37*, pp.129-149.

Sturkell, E.F. and **Ormö, J.,** 1997. Impact-related clastic injections in the marine Ordovician Lockne impact structure, Central Sweden. *Sedimentology*, *44*(5), pp.793-804.

Taylor, B.J., 1982. Sedimentary dykes, pipes and related structures in the Mesozoic sediments of south-eastern Alexander Island. *British Antarctic Survey Bulletin*, *51*, pp.1-42.

Tritton, D.J., 2012. *Physical fluid dynamics*. Springer Science & Business Media.

Varas, G., Vidal, V. and **Géminard, J.C., 2011.** Venting dynamics of an immersed granular layer. *Physical Review E,* 83(1), p.011302.

Varas, G., Ramos, G., Géminard, J.C. and **Vidal, V.,** 2015. Flow and fracture in water-saturated, unconstrained granular beds. *Frontiers in Physics*, 3, p.44.

WaLBerla Framework Website, n.d. Viewed 14/11/2020.

https://walberla.net/doxygen/classwalberla_1_1lbm_1_1DefaultBoundaryHandlingFactory.html

Wang, Y. and **Wang, Y.,** 2010. Study of effects of fines content on liquefaction properties of sand. In *Soil Dynamics and Earthquake Engineering* (pp. 272-277).

Wheatley, D.F., Chan, M.A. and **Sprinkel, D.A.,** 2016. Clastic pipe characteristics and distributions throughout the Colorado Plateau: implications for paleoenvironment and paleoseismic controls. *Sedimentary Geology*, 344, pp.20-33.

Wheatley, D.F., Chan, M.A. and **Okubo, C.H.,** 2019. Clastic pipes and mud volcanism across Mars: Terrestrial analog evidence of past Martian groundwater and subsurface fluid mobilization. *Icarus*, 328, pp.141-151.

Wieneke, B., 2015. PIV uncertainty quantification from correlation statistics. *Measurement Science and Technology, 26(7),* p.074002.

Wieneke, B. and Pfeiffer, K., 2010, July. Adaptive PIV with variable interrogation window size and shape 15th *Int. In Symp. on Applications of Laser Techniques to Fluid Mechanics* (Lisbon, Portugal, 5–8 July).

Xiong, Q., Li, B., Zhou, G., Fang, X., Xu, J., Wang, J., He, X., Wang, X., Wang, L., Ge, W. and **Li, J.,** 2012. Large-scale DNS of gas–solid flows on Mole-8.5. *Chemical Engineering Science*, 71, pp.422-430.

Yamamuro, J.A. and **Lade, P.V.,** 1999. Experiments and modelling of silty sands susceptible to static liquefaction. *Mechanics of Cohesive-frictional Materials: An International Journal on Experiments, Modelling and Computation of Materials and Structures*, *4*(6), pp.545-564.

Yang, G.C., Jing, L., Kwok, C.Y. and **Sobral, Y.D**., 2019. A comprehensive parametric study of LBM-DEM for immersed granular flows. *Computers and Geotechnics*, 114, p.103100.

Yeoh, G.H. and **Tu, J.,** 2019. *Computational techniques for multiphase flows*. Butterworth-Heinemann.

Yu, Z. and **Fan, L.S.,** 2010. Lattice Boltzmann method for simulating particle–fluid interactions. *Particuology,* 8(6), pp.539-543.

Zoueshtiagh, F. and **Merlen, A.,** 2007. Effect of a vertically flowing water jet underneath a granular bed. *Physical review E*, *75*(5), p.056313.